ELECTROOPTIC ELECTRIC FIELD SENSOR FOR DC AND EXTRA-LOW-FREQUENCY MEASUREMENT

A thesis submitted for the degree of Doctor of Philosophy

by

Michael Bordovsky

Department of Manufacturing and Engineering Systems, Brunel University, West London

June, 1998

For the attention of candidates who have completed Part A

i) Attention is drawn to the fact that the copyright of a thesis rests with its author.

ii) A copy of a candidate's thesis is supplied to the Library on condition that anyone who consults it is understood to recognise that its copyright rests with its author and that no quotation from the thesis and no information derived from it may be published without the prior written consent of the author or University, as appropriate.

Requests for such permission should be addressed in the first instance to the Head of Library Services.

ELECTROOPTIC ELECTRIC FIELD SENSOR FOR DC AND EXTRA-LOW-FREQUENCY MEASUREMENT

A thesis submitted for the degree of Doctor of Philosophy

by

Michael Bordovsky

Department of Manufacturing and Engineering Systems, Brunel University, West London

June, 1998

For the attention of candidates who have completed Part A

i) Attention is drawn to the fact that the copyright of a thesis rests with its author.

ii) A copy of a candidate's thesis is supplied to the Library on condition that anyone who consults it is understood to recognise that its copyright rests with its author and that no quotation from the thesis and no information derived from it may be published without the prior written consent of the author or University, as appropriate.

Requests for such permission should be addressed in the first instance to the Head of Library Services.

ELECTROOPTIC ELECTRIC FIELD SENSOR FOR DC AND EXTRA-LOW-FREQUENCY MEASUREMENT

A thesis submitted for the degree of Doctor of Philosophy

by

Michael Bordovsky

Department of Manufacturing and Engineering Systems, Brunel University, West London

June, 1998

BRUNEL UNIVERSITY

PUBLICATION OF THESES

Please complete in block capitals

NAME: MICHAL BORDOVSKY

DEPARTMENT: OF MANUFACTURING AND ENGINEERING SYSTEMS

TITLE OF THESIS: ELECTROOPTIC ELECTRIC FIELD SENSOR FOR DC AND EXTRA-LOW-FREQUENCY MEASUREMENT

PLEASE COMPLETE EITHER PART A OR PART B

A. I agree that the abstract of my thesis may be published by the University without further reference to me.

In accordance with the University's Handbook of Procedures, the Head of Library Services may allow my thesis to be copied in whole or in part without further reference to me. Such Authority shall apply only to single copies made for study purposes and shall be subject to normal conditions of acknowledgement.

(See notes overleaf)

Signature: Michal Bordovsky

Date: 25/07/98

B. I request that my thesis be held under confidential cover in the Library for a period of years for the following reasons:

_____

_____

_____

_____

Once the period of confidentiality has expired, I agree that the conditions set down in Part A will apply without further reference to me

Signature: _____

Date: _____

Please pass this form to your supervisor who should sign below indicating his/her agreement to the retention of the thesis under confidential cover.

Signature of Supervisor: _____

Additional comments _____

_____

_____

_____

If you have completed Part A please return this form direct to the Library.

Part B, when complete, should be returned to the Assistant Registrar.

Solomon Islands (a unique form of logging):

...if a tree is too large to be felled with an axe, the natives cut it down by yelling at it. Woodsmen with special powers creep up on a tree just at dawn and suddenly scream at it at the top of their lungs. They continue this for thirty days. The tree dies and falls over. The theory is that the hollering kills the spirit of the tree. According to the villagers it always works...

Abstract

The thesis reports the results of the research carried out towards the development of an electrooptic sensor for DC and extra low frequency electric field measurement.

Available cubic electrooptic crystals were compared from the sensor sensitivity point of view. A new figure of merit was used taking into account the attenuation of the electric field in the dielectric crystal and its shape. The effect of optical activity in 23 cubic crystals was analyzed using the concept of Poincare sphere. The cubic crystals were further characterised for the charge relaxation time constant to estimate their performance in DC field measurements. Crystals of Bismuth Germanate and Lithium Niobate were identified as suitable materials for the DC field sensor.

The selected crystals were found suitable at extra-low-frequencies. DC field measurements, without the rotation of the crystal, were possible only with Lithium Niobate. However, its performance was influenced to a great extent by the effect of stimulated conductivity. The quarter-wave plate and the crystal of Lithium Niobate were identified as the main sources of temperature instability. A new method of temperature compensation of the quarter-wave plate is proposed. Due to the temperature instability of Lithium Niobate, mainly attributed to the pyroelectric effect and natural birefringence, it is difficult to use the sensor in practical applications.

The performance of the sensor is significantly affected by the presence of an external space charge. The proposed method of its elimination using an artificial extension of the sensing element did not reduce the space charge effect adequately. The response of the sensor in a space charge environment was found to be linear and independent of the space charge density. This enabled measurements of static fields in a unipolar environment. The direct field measurements in bipolar environment suffered from a drift which is intolerable in practical measurements.

The minimum detectable electric field of this sensor in the frequency range from 1 to 200Hz was 1V/m, with a signal to noise ratio equal to 0dB and a resolution of 1V/m. The static field measurements were limited to measurements of pulses with a duration of 200s, due to a long term drift of photodetectors. The minimum detectable level of DC electric field was 2.4kV/m.

Acknowledgements

I wish to thank the following people, without whom this work would not have been possible: my supervisor Professor Wamadewa Balachandran, for invaluable guidance and for having me come work with him, and Franjo Cecelja for great understanding and support.

Special thanks to Silvio Hrabar and Zoran Djuric for invaluable discussions, their encouragement and friendship, and to my friend Lydia Herloffson for being here for me when I needed that.

The project was funded by EPSRC, whose financial support is appreciated.

THANKS...

Michael Bordovsky

June 1998

Contents

List of Figures

List of Tables

Notation

A	point on Poincare sphere representing linearly polarized light with plane of polarization at 45° to horizontal axis, or acceptor energy level [eV], as stated
A_n	point on Poincare sphere representing analyzer, or coefficients of Legendre's expansion of the potential V, as stated
$\mathbf{A}_n$, $\mathbf{A}_n^{st}$	Jones matrix of analyzer, superscript st denotes the standard form
a	major axis of polarization ellipse, diameter of the dielectric ball [m], or diameter of charged plates [m], as stated
B	magnetic flux density [T], or a point on Poincare sphere representing linearly polarized light with plane of polarization at 45° to horizontal axis, as stated
B_n	coefficients of Legendre's expansion of the potential V
b	minor axis of polarization ellipse
C	capacitance [F], or proportionality constant between the external and internal electric field [-]
$\mathbf{C}_r$	Jones matrix of crystal
C_l, C_r	points on Poincare sphere representing left-handed an right--handed circularly polarized light, respectively
$\mathbf{D}$, D_i	electric displacement vector and its components [Cm^{-2}]
D	donor energy level [eV]
d	distance between the electrodes [m], depolarisation factor [-]
d_i	depolarisation factor [-]
$\mathbf{E}$, E_i	electric field intensity vector and its components [V/m]
$\mathbf{E}_{in}$	electric field intensity in a dielectric ball [V/m]
E_{bi}	electric field inside a dielectric ball in a bipolar environment [V/m]
E_c	energy of the bottom of the conduction band [eV]
E_f	Fermi energy level [eV]
E_m	macroscopic field inside the crystal [V/m]
E_{m0}	macroscopic field inside the crystal at time $t = 0s$ [V/m]
E_r, E_θ	components of the electric field intensity in spherical coordinates [V/m]
E_v	energy of the top of the valence band [eV]
$\mathbf{E}_0, E_0$	electric field intensity of the measured field [V/m]
e_{kl}	strain tensor [-]
e_{rn}	coefficients of Legendre's expansion of the radial component of the electric field on the surface of a dielectric ball
er	extinction ratio of polarizer [-]
$\mathbf{F_r}, \mathbf{F}_\theta$	components of the force acting upon ions in spherical coordinates [N]
f	fast optical axis, or frequency [Hz]
f_{3dB}	limit frequency [Hz]
g	gyration factor [-]

H	point on Poincare sphere representing linearly polarized light with horizontal polarization
h	Planck's constant, $h = 6.627 \quad 10^{-34} Js$
I	light beam intensity $[Wm^{-2}]$
I_{SPCest}	estimated value of the space charge current between the electrodes $[A]$
I_c	corona current $[A]$
I_0	light beam intensity incident on the photodetector without applied electric field $[Wm^{-2}]$
$\tilde{I}_0$	fluctuating intensity of the light incident on crystal $[Wm^{-2}]$
I_1, I_2	light beam intensity incident on the photodetectors with applied electric field, tilde above the symbol expresses fluctuating outputs, $[Wm^{-2}]$
$\tilde{I}_{10}, \tilde{I}_{20}$	fluctuating outputs of the sensor without applied electric field $[Wm^{-2}]$
$J(t)$	current density $[Am^{-2}]$
$\mathbf{k}, \mathbf{k}_1, \mathbf{k}_2$	wave vector $[m^{-1}]$
k_1, k_2	square roots of principle transmittances of polarizer [-]
K_m	figure of merit for electrooptic modulators $[\mu radV^{-1}]$
K_s, K_s^1	figure of merit for electrooptic sensors $[\mu radV^{-1}]$
l	length of the crystal $[m]$
l_{optim}	optimum length of the crystal $[m]$
$\mathbf{L}_a$	Jones vector of the light behind analyzer
$\mathbf{L}_c$	Jones vector of the light behind crystal
$\mathbf{L}_{in}$	Jones vector of the input light
$\mathbf{L}_{out}$	Jones vector of the output light
$\mathbf{L}_p$	Jones vector of the light behind polarizer
$\mathbf{L}_q$	Jones vector of the light behind quarter-wave plate
$\mathbf{M}, \mathbf{M}^{st}$	general Jones matrix of an optical component, superscript st denotes the standard form
n	refractive index [-]
n_o, n_e	ordinary and extraordinary refractive indices in a uniaxial crystal [-]
n_1, n_2	refractive indices of the linearly polarized eigenwaves [-]
O	origin of the coordinate system
p_{ijkl}	elastooptical tensor [-]
$\mathbf{P}, P_i$	polarisation vector and its components $[Cm^{-2}]$
P	general point on Poincare sphere
$\mathbf{P}_{ol}, \mathbf{P}_{ol}^{st}$	Jones matrix of polarizer, superscript st denotes the standard form
$P_n(x)$	Legendre's polynomial of argument x
Q	polarizer representation on Poincare sphere, electric charge $[C]$
$\mathbf{Q}_{wp}, \mathbf{Q}_{wp}^{st}$	Jones matrix of quarter-wave plate, superscript st denotes the standard form
r, θ, φ	spherical coordinates
r_{ac}, r_{ca}	amplitude reflectance coefficients at the air-crystal interface [-]
r_{ijk}, r_{ij}, r	linear electrooptic coefficients $[mV^{-1}]$, superscripts T and S denote

	low and high frequency (clamped) coefficients, respectively
$\mathbf{R}, \mathbf{R}^{-1}$	rotation transformation matrix and its inverse matrix, or point on Poincare sphere
RI	relative imprecision [-]
R, R'	reflectivity and reflectivity corrected for absorption, respectively [-]
RS	relative sensor sensitivity [-]
s	slow optical axis
s_{ijkl}	quadratic electrooptic coefficients $[m^2V^{-2}]$
sns	sensor sensitivity $[Wm^{-1}V^{-1}]$
S/N	signal to noise ratio [-]
t	time $[s]$
t_{ac}, t_{ca}	amplitude transmittance coefficients at the air-crystal interface [-]
T, T'	temperature $[K]$, or transmissivity [-] and transmissivity corrected for absorption [-]
T_1, T_2	principle transmittances of polarizer [-]
U_e	energy density $[Jm^{-3}]$
V	Verdet constant $[rad\,m^{-1}T^{-1}]$
V	electric field potential $[V]$, or point on Poincare sphere representing linearly polarized light with vertical polarization
V_{out}, V_{in}	electric field potential outside and inside a dielectric ball $[V]$
V_{out}, V_0	output voltage of the sensor with and without applied electric field, respectively $[V]$
w	width of crystal $[m]$
x_1, x_2, x_3	cartesian coordinates
x'_1, x'_2, x'_3	transformed cartesian coordinates
x''_1, x''_2, x''_3	transformed cartesian coordinates
α	angle of rotation (general, analyzer) $[rad]$, factor characterising inhomogeneity of LN crystal, absorption coefficient $[m^{-1}]$, or intensity fluctuation factor [-]
α_{optim}	angle of analyzer $[rad]$
α_T	normalized temperature coefficient of sensor output $[K^{-1}]$. The second subscript specifies the cause of temperature instability (Γ-phase retardation due to electric field, nb-natural birefringence, Q-quarter-wave plate.
β	general angle of rotation $[rad]$, half of the sum of propagation constant of the eigenwaves $[m^{-1}]$, or asymmetry factor [-]
Γ	linear phase retardation $[rad]$
Γ_{nb}	linear phase retardation caused by natural birefringence $[rad]$
γ	rotation angle in Poincare spheres $[rad]$, phase retardation of quarter-wave plate $[rad]$
δ	linear phase retardation per unit length $[rad\,m^{-1}]$
δ_{mn}	Kronecker delta; $\delta_{mn} = 1$ if $m = n$, $\delta_{mn} = 0$ for $m \neq n$
Δ	composite phase difference $[rad]$, relative error of the sensor output [-]
ΔE_g	bandgap $[eV]$
Δn	linear birefringence [-]
$\Delta_{out-rel}$	relative uncertainty of the sensor output [-]

Δ_{rel}	ratio of an output change due to an electric field and output change due to intensity fluctuations [-]
Δ_0	composite phase difference per unit length $[radm^{-1}]$
$\underline{\epsilon}, \epsilon_{ij}$	permittivity tensor $[AsV^{-1}m^{-1}]$
ϵ_r	relative permittivity [-]
ϵ_0	permittivity of vacuum, $\epsilon_0 = 8.854 \quad 10^{-12} AsV^{-1}m^{-1}$
$\underline{\eta}, \eta_{ij}$	impermeability tensor [-]
λ	angle 2λ expresses longitude in Poincare sphere $[rad]$, optical wavelength $[m]$
λ_c	critical wavelength $[m]$
μ	material permeability $[VsA^{-1}m^{-1}]$
ν	frequency of optical oscillations $[Hz]$
π_{ijkl}	piezooptical coefficients $[N^{-1}m^2]$
ρ	specific rotatory power $[rad\,m^{-1}]$
σ	specific conductivity $[\Omega^{-1}m^{-1}]$, surface charge density $[Cm^{-2}]$
σ_{kl}	stress tensor $[Nm^{-2}]$
σ_n	coefficients of Legendre's expansion of surface charge density σ
τ	charge relaxation constant $[s]$
τ_c	coherence time $[s]$
θ	angle in spherical coordinates, general angle $[rad]$
φ	angle in spherical coordinates, general angle $[rad]$
χ, χ_{ij}	susceptibility and susceptibility tensor [-], respectively
ω	radian frequency $[s^{-1}]$, or angle of latitude in Poincare sphere $[rad]$
ζ	general angle of rotation $[rad]$

Abbreviations

ADP	Ammonium Dihydrogen Phosphate
Ba:PZT	Barium Piezoelectric ceramics
BG	Bismuth Germanate
BGO	Bismuth Germanium Oxide
BSO	Bismuth Silicon Oxide
EI	Electrical induction
ELF	Extra low frequency
EMC	Electromagnetic compatibility
EMI	Electromagnetic interference
ES	Electrostrictive effect
FP	Fabry-Perot interferometer
KDP	Potassium Dihydrogen Phosphate
LED	Light Emitting Diode
LD	Laser Diode
LHP	Left handed circularly polarized light
LN	Lithium Niobate
MZ	Mach-Zehnder interferometer
Nd:YAG	Neodymium Yttrium Aluminium Garnet
PE	Piezoelectric effect
PZT	Piezoelectric ceramics
RHP	Right handed circularly polarized light
YAG	Yttrium Aluminium Garnet ($Y_3Al_5O_{12}$)

Chemical Formulae

$Bi_4Ge_3O_{12}$	Bismuth Germanate
$Bi_{12}GeO_{20}$	Bismuth Germanium Oxide
$Bi_{12}SiO_{20}$	Bismuth Silicon Oxide
$CdTe$	Cadmium Telluride
$GaAs$	Gallium Arsenide
GaP	Gallium Phosphide
In_2O_3	Indium Oxide
$KNbO_3$	Potassium Niobate
$LiNbO_3$	Lithium Niobate
$LiTaO_3$	Lithium Tantalate
$NH_4H_2PO_4$	Ammonium Dihydrogen Phosphate
PVF_2, $PVDF$	Polyvinylidene Fluoride
$[P(VDF/TFE)]$	Copolymer of Vinylidene Fluoride and Tetrafluorethylene
$[P(VDF/TrFE)]$	Copolymer of Vinylidene Fluoride and Trifluorethylene
ZnS	Zinc Sulphide
$ZnSe$	Zinc Sellenide
$ZnTe$	Zinc Telluride

Chapter 1

Introduction

The measurement of electric fields has many wide ranging uses. These range from the assessment of the health hazards of electromagnetic radiation, to process industry where electrostatic charge can be present either beneficially or as a hazard, to communications where large electric fields may be generated in transmission of data through to the electronics industry in the design of electronic equipment. For example, it was found that complex electronic devices in medicine may interfere with electromagnetic fields. Even devices implanted in human bodies such as pacemakers may be influenced by surrounding fields. Furthermore, electric, magnetic and electromagnetic fields interact with biological systems. In medicine the interaction can be employed beneficially for diagnosis and therapy but can be harmful as well. Various studies were carried out concerning electric field emission from transmission lines and the effects on people living or working close to these sources. Nowadays the assessment of the electromagnetic compatibility of electric devices is required to satisfy stringent emission requirements. For more efficient and reliable operation of ultra high voltage power systems the electric field strength in high voltage machines must be accurately measured. In electrostatic applications it is mainly DC electric field which is applicable. The presence of electrostatic charges is a major concern in the process industry where a build up of the charge could lead to hazards to operators handling material or equipment or to a possible explosion or fire. In microelectronic industry the measurement of electric fields is important in the manufacture of silicon devices as stray charge can destroy sensitive circuits.

1.1 DC Field Measurement

The electric field is usually measured using field meters or potential probes. The simplest type of a field meter is the induction field meter (Figure 1.1). It consists of a metal sensing plate, a capacitor C, an amplifier and a voltmeter. The electric field E induces a charge on the sensing plate [3]. The same charge flows from the ground to the plate and charges the capacitance C. Thus the measurement of the

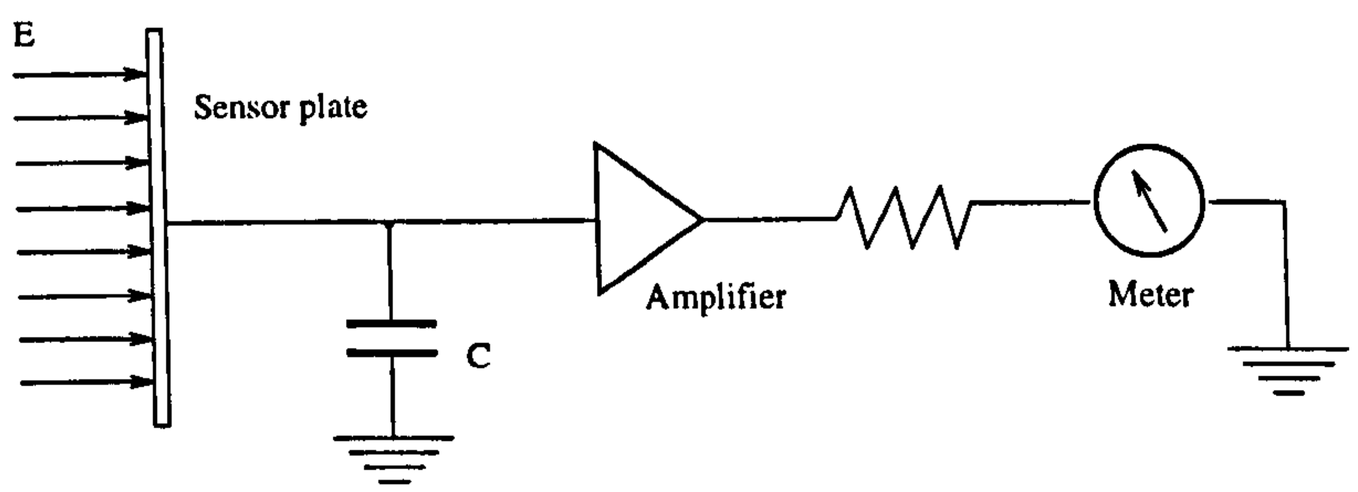

Figure 1.1: Induction field meter.

voltage across the capacitor enables to determine the electric field intensity E. This voltage is usually small and so the sensing plate is close to earth potential. A zero drift of the amplifier and a collection of free stray charge prevents this sensor to be used for continuous monitoring.

The most widely used field meter, the rotating vane field meter (Figure 1.2), exploits the principle of electrical induction as well [3]. The turning butterfly rotor in front of the sensing area which is normally several centimetres in diameter alternately exposes the sensor plate to the measured electric field. An alternating signal appears at capacitor C. Its peak voltage is proportional to the electric field and independent of the rotor speed. The rotating mill vane removes the drift problem of the induction meter because of its AC coupling to the amplifier. This kind of probe can be used even in a space charge environment because the amount of free charge able to reach the collector plate during one rotation of the butterfly motor ($< 0.01s$) is negligible.

In vibrating field meters the collector plate is screened by a grounded plate with an aperture. Either the aperture or the plate moves and thus provides an oscillatory

signal [3]. The induced charge depends on the spacing between the aperture and the sensing plate, on the size of the aperture and on the electric field. Vibrating field meters may have the sensing area as small as a millimetre across.

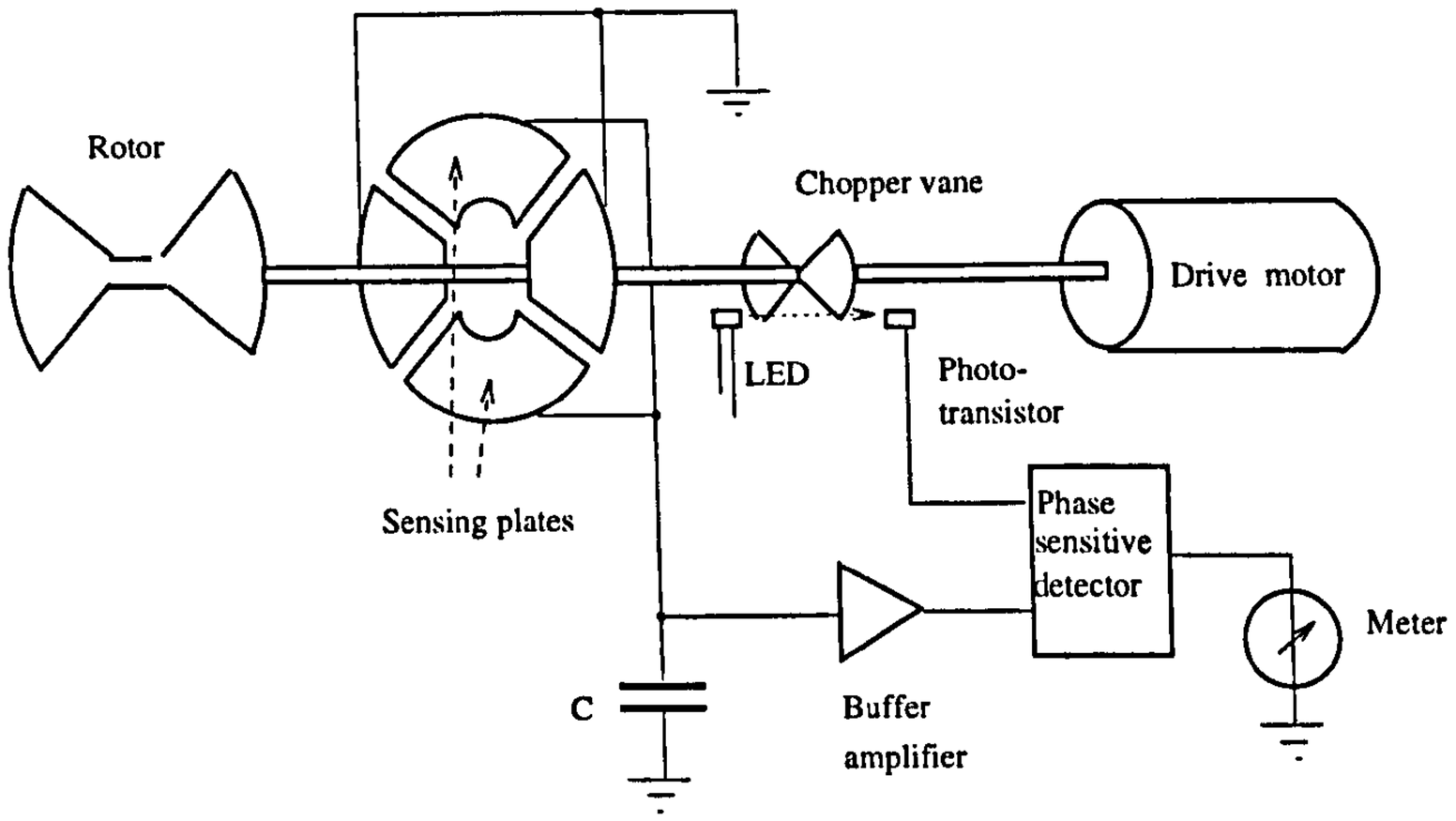

Figure 1.2: Rotating-vane field meter.

All three introduced field meters use the principle of electric induction. Typically, they measure field between 1 and 10^3kV/m [3] and can achieve high spatial resolution. However, because of their grounding they can disturb the original electric field unless they are not placed in a position of zero potential. The sensing area is connected to a measurement unit with an active source by conductive leads. These leads create equipotential lines and when an alternating signal is measured they radiate an electromagnetic field. Sometimes the electronics and the sensing plate are integrated in a small metallic box which, however, has to be grounded. In both cases a significant field distortion will take place. This has to be taken into account and often complex computer models are used to calculate the correct values of electric field from those measured if it is possible at all.

Apart from the field meters, potential probes (corona, potential and bipolar probes [3]) can be used to evaluate the potential distribution in space and then the electric field intensity can be calculated by numerical differentiation. Uncertainty introduced by numerical methods are accompanied by perturbation of the measured electric field by the conducting leads necessary to measure the induced current as

in the case of field meters.

1.2 Extra Low Frequency Field Measurement

Non-optical measurements of AC electric field are most frequently carried out by dipole probes, loop probes or free body meters. The dipole probes use a dipole antenna which is generally coupled to the voltage-measuring instrument. The coupling is realized by thermocouple element, diode or field effect transistor, followed by a filter network and a transmission line. For an optimal function of the probe the dipole dimension is required to be comparable to one tenth of the wavelength of the electromagnetic field. Thus at extra-low frequencies the required length becomes unrealistic and the dipole probes are typically used to measure electric fields from 100MHz [68]. Short dipole antenna are used for EMC (electromagnetic compatibility) measurements down to 1kHz [39]. Their frequency characteristics are very flat and broad-band, however, the sensitivity is decreased. The dipole probes are not used for ELF electric field measurement.

The loop probes are used for indirect measurements of electric field. They are similar to the dipole probes except that the dipole is substituted by a loop antenna. The loop probes measure directly the intensity of magnetic field and, therefore, their use is limited to measurements of plane wave electromagnetic fields where the relationship between magnetic and electric field intensities is known. This makes the probe unsuitable for near field measurements. In addition the loop probes work in the frequency range from 10 kHz to 300MHz which does not cover the ELF region [68]. The limitation for the low frequency measurement comes from the fact that the response of a loop antenna depends on the frequency of the incident magnetic field.

The third most popular probe for AC electric field measurement is a free body meter sometimes also called a balanced meter. This technique uses the principle of electric field induction. A current detector, placed between two electrodes which are usually plate like or hemispherical in shape, measures the AC current resulting from the potential difference caused by the electric field. This probe can measure

electric field of frequency from 20Hz to 1MHz [14]. However, such a probe is highly perturbing due to its metallic parts.

Recently, electric field sensors based on a dipole antenna in conjunction with optical techniques have been reported [46][25][18]. They used an electro-optic modulator in combination with an antenna and were reported to measure electric field of frequencies down to 50Hz. Using optical fibre connection with signal processing unit instead of conductive leads, the problem of interference due to extraneous electromagnetic fields is eliminated. Another great advantage of the reported probes is a very broad and flat frequency characteristic which extends to the extra-low-frequency region [68]. Some other reported optical sensors for low frequency electric field are described in the literature review.

The brief introduction of currently available techniques for DC and ELF electric field measurement indicates the need for a suitable sensing probe to measure both DC and ELF field in free space with increased accuracy and with negligible field distortion even in the presence of space charges.

1.3 Optical Techniques

Optical techniques enable to measure DC and low frequency electric field directly. Optical probes can be passive, without any active source of energy which would disturb the measured field. Conductive leads and grounded parts are often not necessary and probes can be made all dielectric which partly eliminates one of the major problems associated with the conventional field meters, the perturbation of the measured electric field. Optical probes, even if all dielectric, distort the electric field by its polarisation charge but the perturbation is relatively small. For example, a dielectric probe in the shape of a ball of a diameter a distorts the measured uniform field to a distance comparable with the diameter a from the surface of the probe. At distances farther away from the probe the field distortion can be neglected [6]. Another advantage of the optical techniques is the possibility to separate the probe from the signal processing unit by optical fibres which eliminates electromagnetic interference (EMI) and has the inherent advantage to be used in hazardous areas.

Additionally, optical probes can be made physically small compared to the field meters used at present which are often bulky [14].

Most of the optical techniques used for electric field measurement are based on linear electro-optic, nonlinear electro-optic, piezoelectric or electrostrictive effects. The electro-optic effect is a change in the refractive index of material caused by an electric field. It can be linear (Pockel's) or nonlinear (Kerr) effect ([9], section 3.2). The linear electrooptic effect is usually stronger than the nonlinear effect and offers a linear dependence of the sensor output. On the contrary, the output of sensors using Kerr effect is nonlinear, proportional to the square of the electric field intensity. If a sensor exploiting the Pockel's effect is well designed, an excellent temperature stability can be achieved (section 2.1). In the presence of an electric field some materials change their dimensions. This is called converse piezoelectric effect, if the change is linear with the electric field, or electrostrictive effect when it is nonlinear [7]. Sensors based on piezoelectric and electrostrictive effects usually use Mach-Zehnder fibre optic interferometer and can achieve high sensitivity (section 2.2). However, fibre optic interferometers are known for their temperature instability and furthermore once the interferometer is switched off, it has to be calibrated again upon switching on [36]. More about different types of sensors using optical techniques can be found in chapter 2.

1.4 Summary

As an introduction to the topic of DC and extra-low-frequency electric field measurements, the non-optical techniques for field measurement were briefly described. The main disadvantage of these techniques was found to be a perturbation of the measured field due to grounded conductive parts, low sensitivity to the measured field and quite often a bulky design. It was also pointed out that the standard techniques for AC field measurement do not cover the extra-low-frequency region. Apart from free body meter, all the techniques used at present are limited to higher frequencies. The advatages offered by optical techniques were outlined together with most frequently used effects in optical electric field sensors.

1.5 Organisation of the Thesis

The thesis is divided into chapters and structured as follows:

- Chapter 2 presents literature review on the DC and extra-low-frequency electric field sensors based on optical techniques. Reported ELF sensors based on piezoelectric, electrostrictive and electrooptic effects are discussed. A separate section deals with DC field sensors. The chapter ends with the aims and objectives of the project which follow from the literature review.

- Chapter 3 gives a summary of the fundamental physics which is essential for the understanding of the electrooptic sensor and the topics investigated in this study.

- Chapter 4 is divided into five sections. The first two sections presents an analysis of the electrooptic sensor and a mathematical and computer model which was developed. A separate section, which results in electrooptic crystals selection, deals with the analysis of the sensor sensitivity to electric field and internal space charge effect. It is followed by a section on experimental results of DC and extra low frequency measurements. The last section then comprises investigations of sensor isotropy.

- Chapter 5 presents a study of the external space charge influence on the electrooptic sensor. Theoretical results are compared with experiments in both unipolar and bipolar space charge environments. The efficiency of the artificial extension of the sensing element is discussed at the end of the section.

- Chapter 6 is focused on the problem of temperature stability of the electrooptic sensor. The effects of polarizers, quarter-wave plate, electrooptic crystals and their antireflection coating on sensor temperature stability are discussed.

- Chapter 7 summarises the main achievements of the research and its originality with recommendation for further work.

Chapter 2

Literature Review of Electric Field Sensors Using Optical Techniques

The following sections are focused on the literature review of electric field and voltage sensors using optical techniques. An effort was made to present the most frequently used principles and their practical exploitation in optical electric field sensing. The voltage sensors were also covered because in the literature, they are often considered as identical to electric field sensors. However, there is a difference between the two types of sensors. The electric field meters measure the electric field intensity directly. The voltage sensors are designed to measure potential difference between two places to which they are connected by conductive leads. The intensity of electric field is calculated from measured voltage assuming a uniform homogenous field. The metallic electrodes can disturb the measured field but most importantly once connected to a voltage source they eliminate the conductivity effect described in section 4.2.2. Therefore, the frequency characteristics of the voltage sensors do not generally coincide with those of the electric field sensors.

The first two sections describe sensors built on the basis of the electrooptic, converse piezoelectric and electrostrictive effects which at least partly cover measurements at extra low frequencies up to 100 Hz. A special attention is then paid to DC electric field sensors.

2.1 Electro-Optic Sensors

One of the first optical voltage sensors was reported by Susumu Namba in 1961 [59]. Its configuration is shown in Figure 2.1. Two crossed polarizers were used together with ammonium dihydrogen phosphate $NH_4H_2PO_4$ crystal (ADP) in the polarimetric setup (section 4.1) at 500nm. The voltage was applied via attached transparent electrodes. The sensor used the longitudinal electrooptic effect and the achieved accuracy was ±50V.

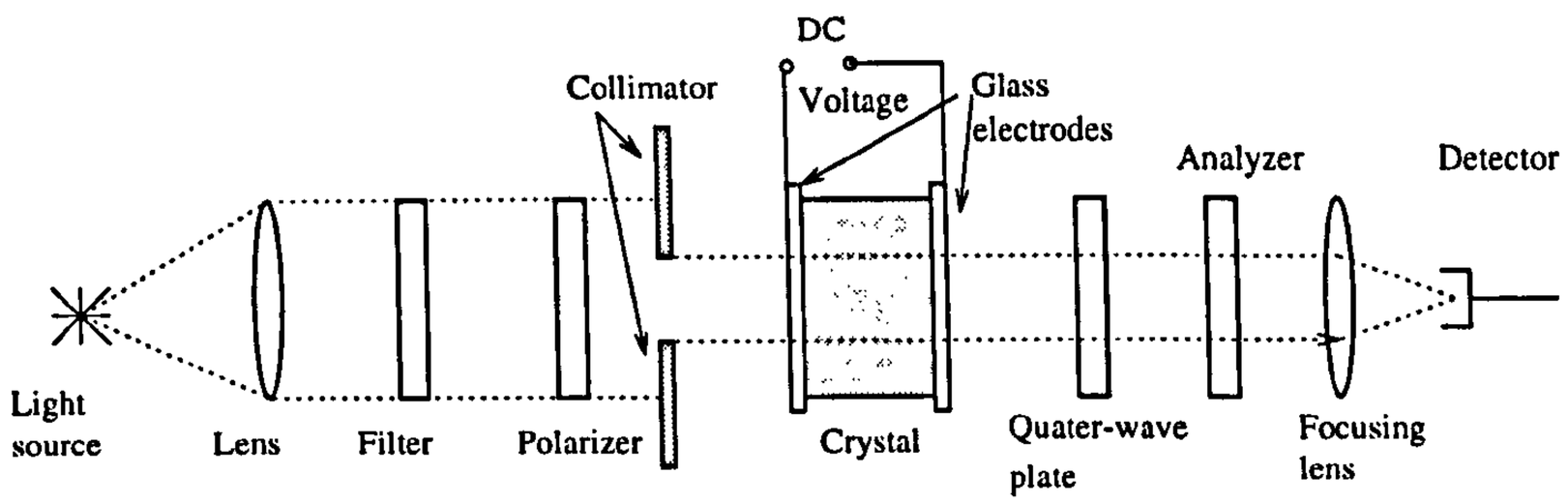

Figure 2.1: Voltage sensor by Namba.

During the next fifteen years new electro-optic materials such as bismuth silicon oxide (BSO) and bismuth germanium oxide (BGO) became available. Hamasaki realised the advantages of these isotropic cubic crystals and in 1980 introduced a high intensity electric field sensor based on BSO crystal [31]. Compared to uniaxial crystals (crystals with a rotational index ellipsoid and natural birefringence, see chapter 3), such as lithium niobate ($LiNbO_3$, LN), lithium tantalate ($LiTaO_3$) and potassium dihydrogen phosphate (KDP) group of crystals, the isotropic BSO and BGO crystals do not possess the natural birefringence or pyroelectricity (chapter 3) which significantly influences temperature stability. Thus a remarkable temperature stability of ±3% was achieved over the range from 15°C to 70°C. The electric field was measured in the range from 15 to 200kV/m with a linearity better than 1%. This sensor was improved by the same research group later in 1982 [44]. It was found that the temperature dependence of the crystal optical activity (chapter 3) can be decreased by properly choosing the length of the crystal. This improved the temperature stability to ±0.2% over the temperature range from 15°C to 70°C.

In 1983 Kyuma used BGO crystal for a fibre optic voltage sensor [47] (Figure 2.2). Transparent indium oxide (In_2O_3) electrodes were attached to 1 mm thick BGO crystal in a bulk setup with multimode incoming and outcoming fibres. It was shown that a decrease in sensitivity due to the optical activity of the crystal can be neglected if the crystal length is smaller than 1 mm. The sensor achieved an excellent temperature stability of $\pm 0.5\%$ over the range 25° to 85°C and a minimum detection level of 10^{-3}V. The linearity of the sensor was better than 0.5% and the bandwidth of about 1 kHz.

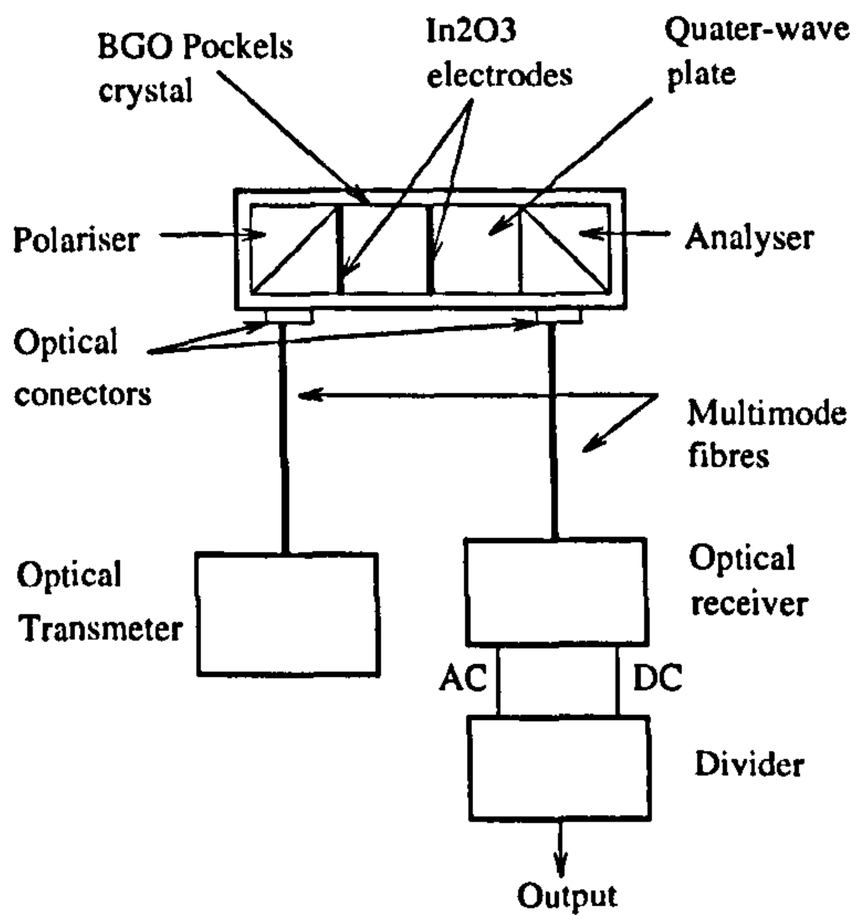

Figure 2.2: Voltage sensor by Kyuma.

Nevertheless all the mentioned sensors, developed in Japan, were designed to measure voltage, not the electric field directly. They used cubic crystals of 23 point group [7] and therefore had to deal with optical activity of BGO and BSO crystals. The first really electric field sensor was developed by Shibata in 1983 [65] (Figure 2.3). It was for the first time when a cubic crystal of $\bar{4}3m$ point group and its excellent features were applied. Bismuth Germanate ($Bi_4Ge_30_{12}$) has no natural birefringence, no pyroelectricity (e.g.$LiNbO_3$) and no optical activity (e.g.$Bi_{12}Ge0_{20}$, $Bi_{12}Si0_{20}$) and, therefore, no temperature dependence associated with these effects. The light emerging from the optical fibre is linearly polarized by the polarising beam splitter. Because of the light reflection at the reflecting film the light experiences a phase shift of $\pi/2$ due to the 1/8 wave plate plus a phase retardation induced by

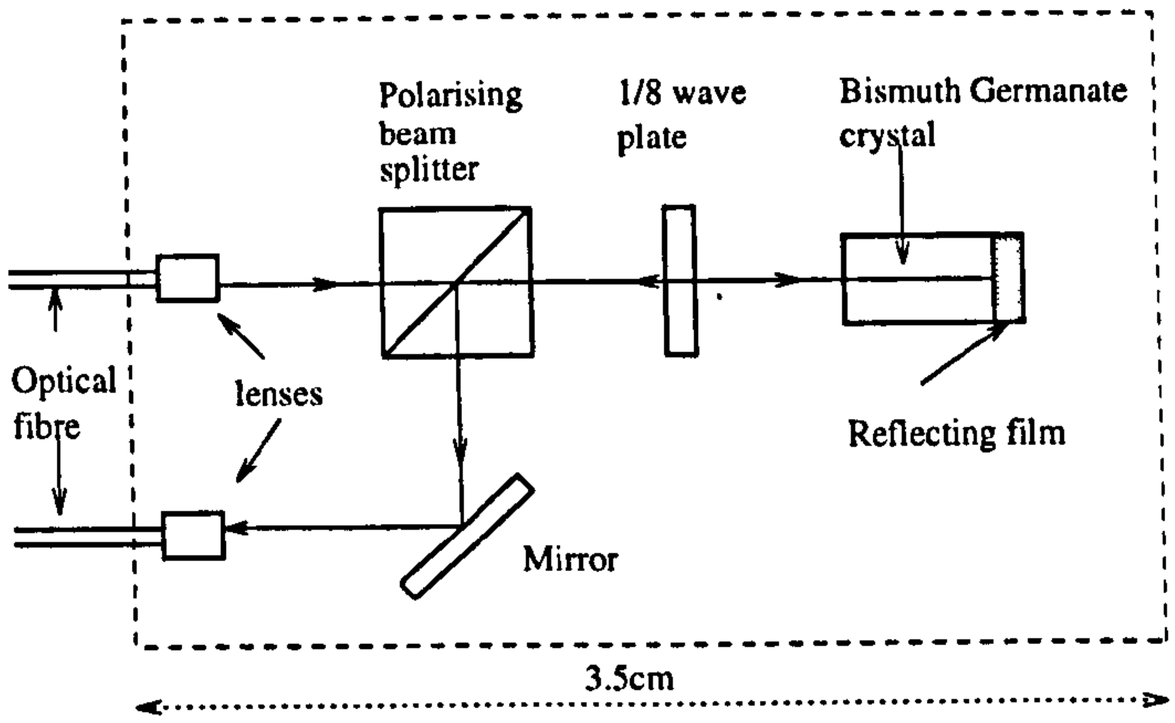

Figure 2.3: The first electric field sensor made by Shibata.

the electrooptic effect in the crystal. The beam splitter acts as an analyzer for the reflected beam. It reflects one linearly polarized component of the light letting it pass through a lens and an optical fibre to a photodiode. The sensor was designed to measure two dimensional AC electric field in the range from 1kV/m to 300kV/m. The probe of the sensor is ca 3.5 cm long and its temperature stability is $\pm 0.5\%$ in the range from 15° to 60°C.

Another electric field sensor was devised by Gulyaev et al. in 1984 [30], [45]. The sensor used the optical scheme similar to that of Kyuma [47]. Their studies were mostly concentrated on the effect of optical activity in BSO crystal on the electrooptic sensor. The lowest measured value of the electric field in the frequency range from 10Hz to 200kHz was 3kV/m. The frequency of 10Hz is probably the lowest frequency reported for the electrooptic sensor.

In 1987 another Pockel's effect voltage sensor was reported by Meyrueix et al.[55]. This sensor differed from the previous sensors in its output which consisted of the Wollaston prism splitting the output light beam into two orthogonal components. The separate detection and the final electronic processing, reported for the first time, enables to improve the accuracy and sensitivity of the sensor. The dynamic range of the sensor was from 0.9 to 18kV/m.

At the end of eighties, attempts were made to miniaturize field sensors using integrated optics technology. Compared to bulk electrooptic sensors integrated devices can offer some advantages like size reduction and simplicity of design. There is no need for lenses, quarter-wave plate and polarizers [37]. Since the piezoelectric

resonances can be shifted up to higher frequencies by decreasing size of devices, the integrated optics based sensors can work as a broad band device. These sensors do not use the polarimetric technique but are based on Mach-Zehnder integrated optic interferometer. A sensor developed in 1992 by Kuwabara [46] is representative in a number of aspects (Figure 2.4). It is based on $LiNbO_3$ integrated Mach-Zehnder interferometer and can measure the electric field strength in the range from 100Hz to 300MHz with almost flat frequency response characteristic. Two 50mm long metal rods which serve as an antenna are connected to the electrooptic modulator with halfwave voltage about 4V at $1.3\mu m$. The YAG laser pumped by a laser diode had 25mW output power. The minimum detection level of the sensor was 1 mV/m at 50MHz and 0.14mV/m at 750MHz and the lowest measured frequency of the electric field was about 100Hz. The overall length of the sensor element is 144mm. Since the sensor uses Mach-Zehnder interferometer based on optically anisotropic and pyroelectric material of Lithium Niobate, a low temperature stability can be expected. However, no results on the temperature characteristics of the sensor were reported.

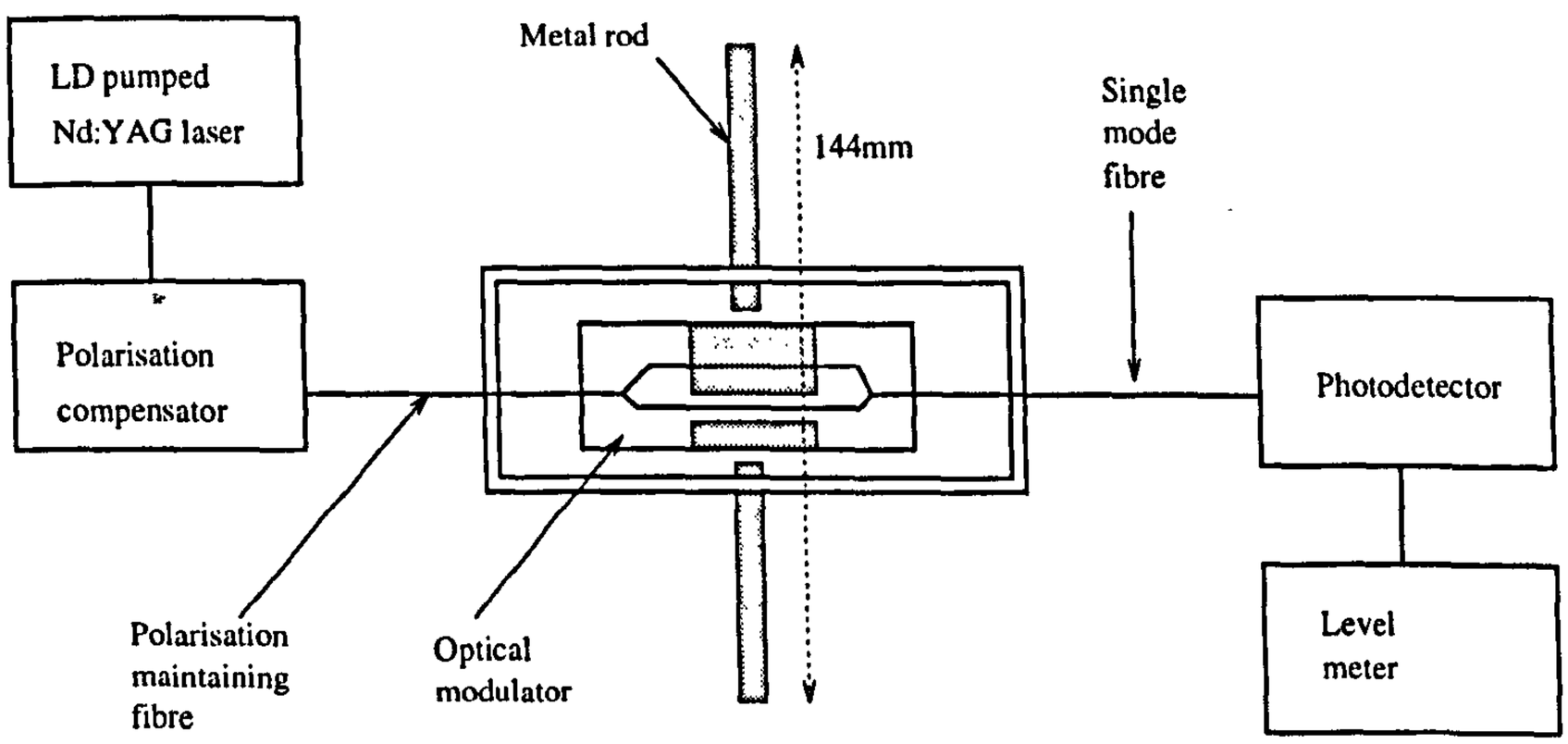

Figure 2.4: Electric field sensor using electro-optic modulator made by Kuwabara et al.

A similar sensor designed especially for low frequency measurement was made by Y.K.Choi et al. in 1993 [25]. It employed an asymmetric Mach-Zehnder interferometric amplitude modulator in combination with an antenna. Measurements

were performed in the range 10V/m to 6kV/m at frequencies from 60Hz through to 100kHz. These sensors based on the integrated Mach-Zehnder interferometer contain metallic antenna which disturb the measured field. In both cases no results were reported for measurements at frequencies lower than 50Hz.

2.2 Piezoelectric and Electrostrictive Effect Sensors

Sensors exploiting converse piezoelectric and electrostrictive effects use optical fibre Mach-Zehnder interferometers for a phase shift detection (Figure 2.5). In the signal arm of the Mach-Zehnder interferometer an electrostrictive material is used to extend the optical path and thus create a phase shift between the signal and reference arms which can be detected. The prolongation is a function of the ap-

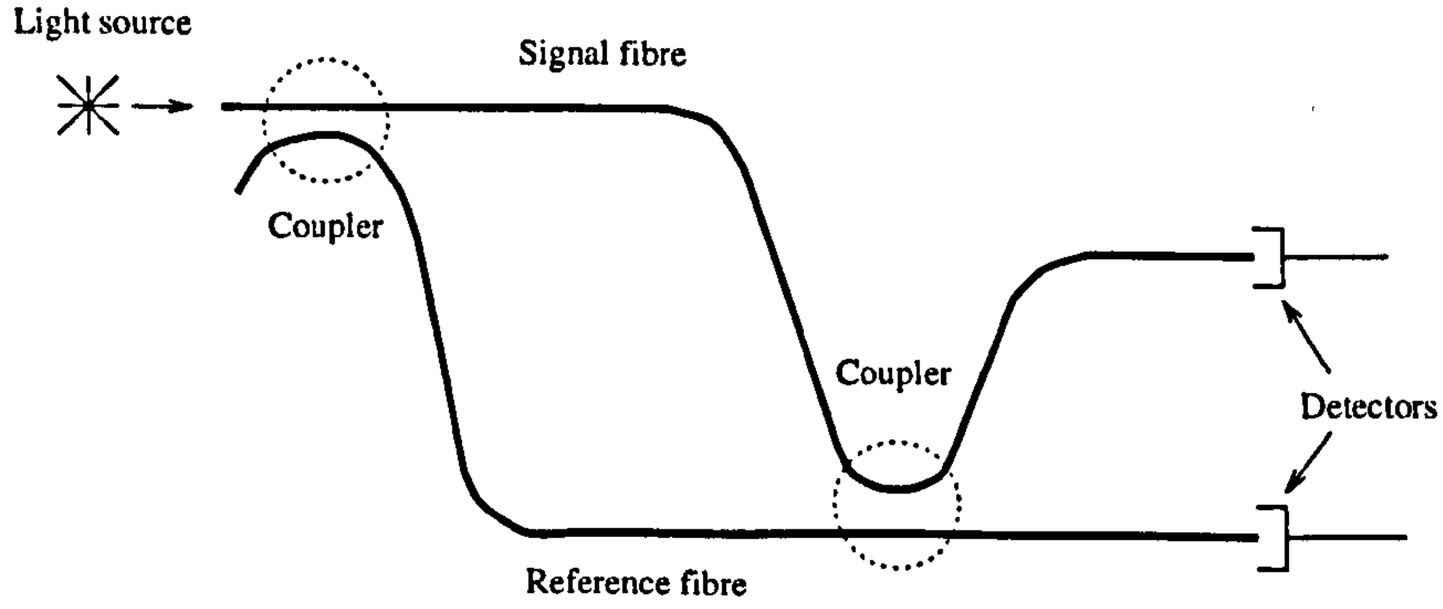

Figure 2.5: Mach-Zehnder interferometer.

plied electric field. The electrostrictive material is used as a jacket of an optical fibre [35] [28] or an optical fibre is firmly attached to a piece of the electrostrictive material [17] [71] [43] [54]. These sensors can be completely passive and their sensitivity can be simply regulated by the length of fibre which is in contact with the electrostrictive material. To achieve reasonable sensitivity, the fibre attached to a sensing material must be long enough to induce a sufficient phase retardation. Nowadays fibre optic interferometers can detect a phase shift of about 10^{-7} radians [28]. Thus, for example 1 km long fibre can theoretically detect an electric field

as small as $4\mu V/m$ [28]. The reported piezoelectric materials are mostly polymers as for instance polyvinylidene fluoride (PVF_2) [28], copolymer of vinylidene fluoride and tetrafluorethylene [P(VDF/TFE)] and copolymer of vinylidene fluoride and trifluoroethylene [P(VDF/TrFE)] [35].

However, due to strong sensitivity of optical fibre interferometers to environmental changes, as for example changes in temperature, these sensors show high environmental instability.

In 1988 Bohnert and Nehring demonstrated that sensors based on the piezoelectric effect can be used to measure spatial components of an electric field [17]. The sensor used symmetry properties of the converse piezoelectric effect [7]. The sensitivity to only one component of the electric field was achieved by a proper

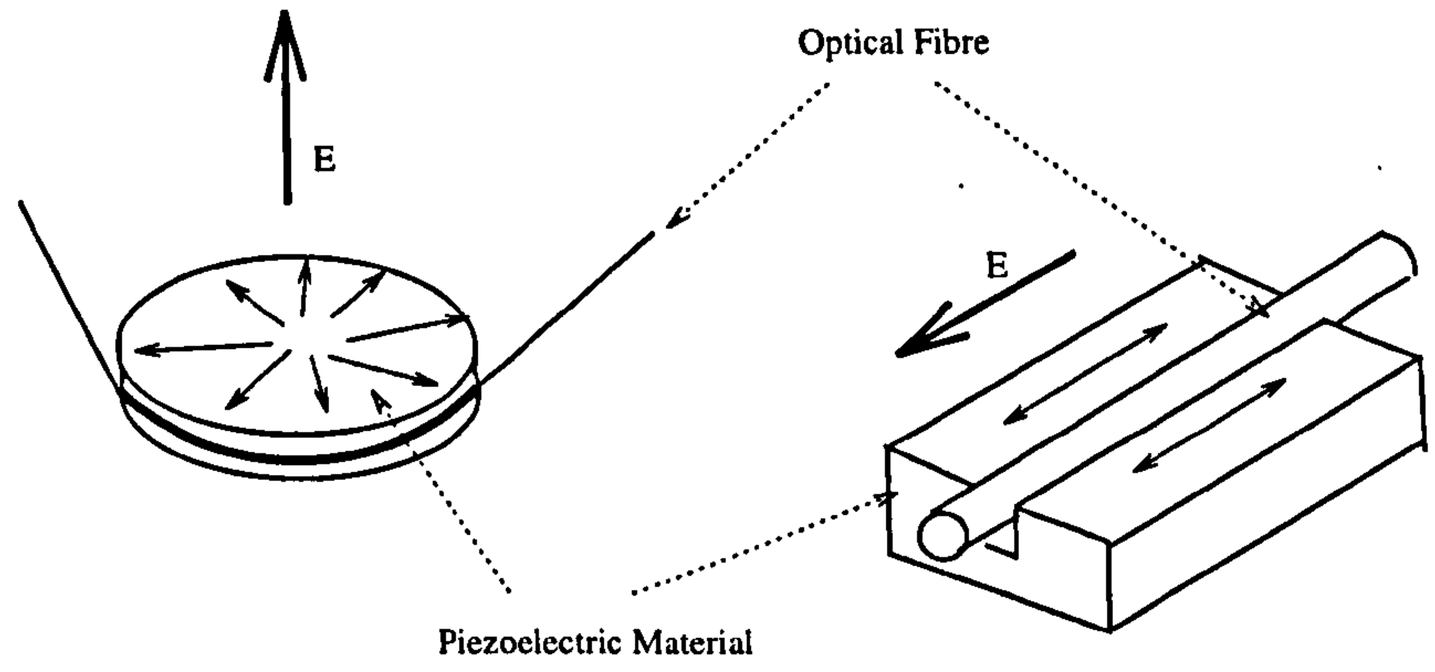

Figure 2.6: Sensing elements for individual field components measurement by Bohnert. *Electric field components E and the response are displayed.*

selection of a crystal and its orientation. Two shapes of the sensing element were suggested (Figure 2.6) and tested with quartz, polyvinylidene fluoride (PVDF) and piezoelectric ceramics (PZT). The fibre elongation was measured by Mach-Zehnder interferometer which operated in quadrature so that its output was directly proportional to the relative phase shift in both arms. The diameter of the sensing disk element was 10mm and its thickness 3mm. The bandwidth of the detection system was 50kHz and the signal of the mechanically isolated sensor was frequency independent. Vibrational resonances of the disk (quartz) are expected to affect the sensor above a few hundred kHz. Using appropriate geometrical dimensions it should be possible to shift the piezoelectric resonances into the MHz range. The lowest mea-

sured value of an electric field was 10V/m but it is possible to change the range simply by using more turns of the optical fibre on the disk. The temperature stability of Mach-Zehnder fibre optic interferometer, however, stays a problem for this kind of sensor.

2.3 DC Measurement

The DC electric field measurement has to solve problems of various drifts which can lead to errors. The drifts can be caused by space charges either inside or outside a sensing crystal, by temperature dependence of refractive indices or permittivity. The low frequency 1/f noise can be a problem as well. In electro-optic electric field sensors the space charges are the crucial problem. Space charges inside the crystal can influence the function of the sensor to such an extent that the sensor is not functional. The outside space charge can be deposited on the surface of the sensing crystal non-uniformly and thus create an electric field which is superimposed on the original field and causes errors in the measurement. The review shows that these problems were mostly solved by a rotation of the sensing element.

In 1982 Hidaka [33] used the linear electrooptic effect for measurements of an electric field distorted by a space charge. The measuring system (Figure 2.7) con-

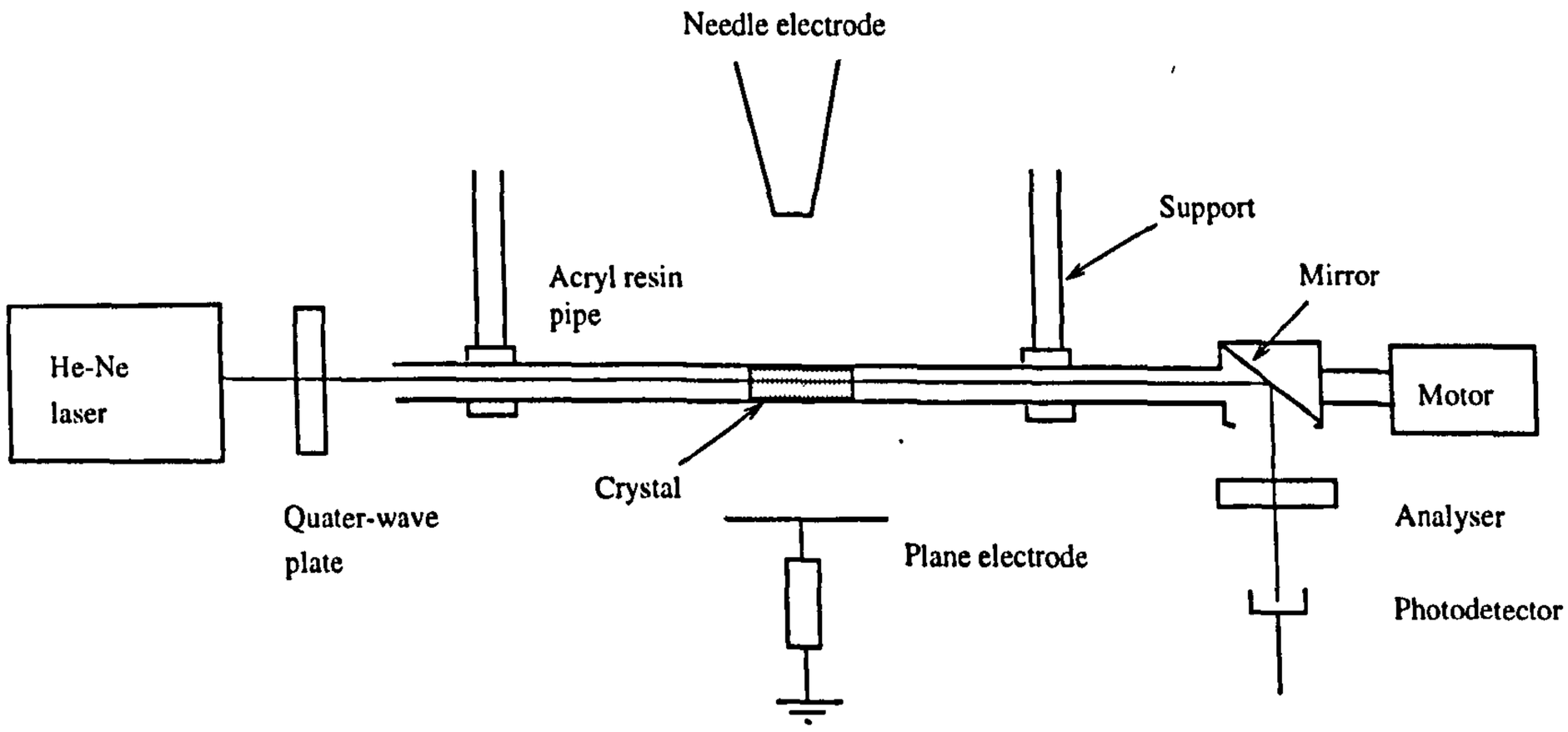

Figure 2.7: Schematic diagram of the electric field sensor for field measurements in corona discharge by Hidaka.

sisted of a laser source followed by quarter-wave plate which makes the light beam circularly polarised, Pockel's crystal and analyzer which were set up to maximize the sensor sensitivity to the electric field. The crystal was rotated to eliminate the space charge influence. The space charge can sit on the surface of the crystal or its housing non-uniformly creating an electric field which is superimposed on the measured field. The rotation of the sensing element causes the space charge to be attached to its surface uniformly. As a consequence, the internal electric field in the crystal due to the deposited charge is zero, and sensor is sensitive only to the measured electric field. The rotation also solves the problem of the space charge inside the crystal (crystal conductivity, see section 4.3.2). The advantage of this kind of sensor is that it is electrically isolated and completely passive. The sensor was successfully used in a measurement of the electric field distribution in a needle to plane gap of 0.1m with a positive DC corona and was able to measure electric fields of the order 10^5V/m.

In 1985 Robertson and Rogers introduced another DC electric field sensor [64] for measurements in the presence of space charge (Figure 2.8). Experiments were carried

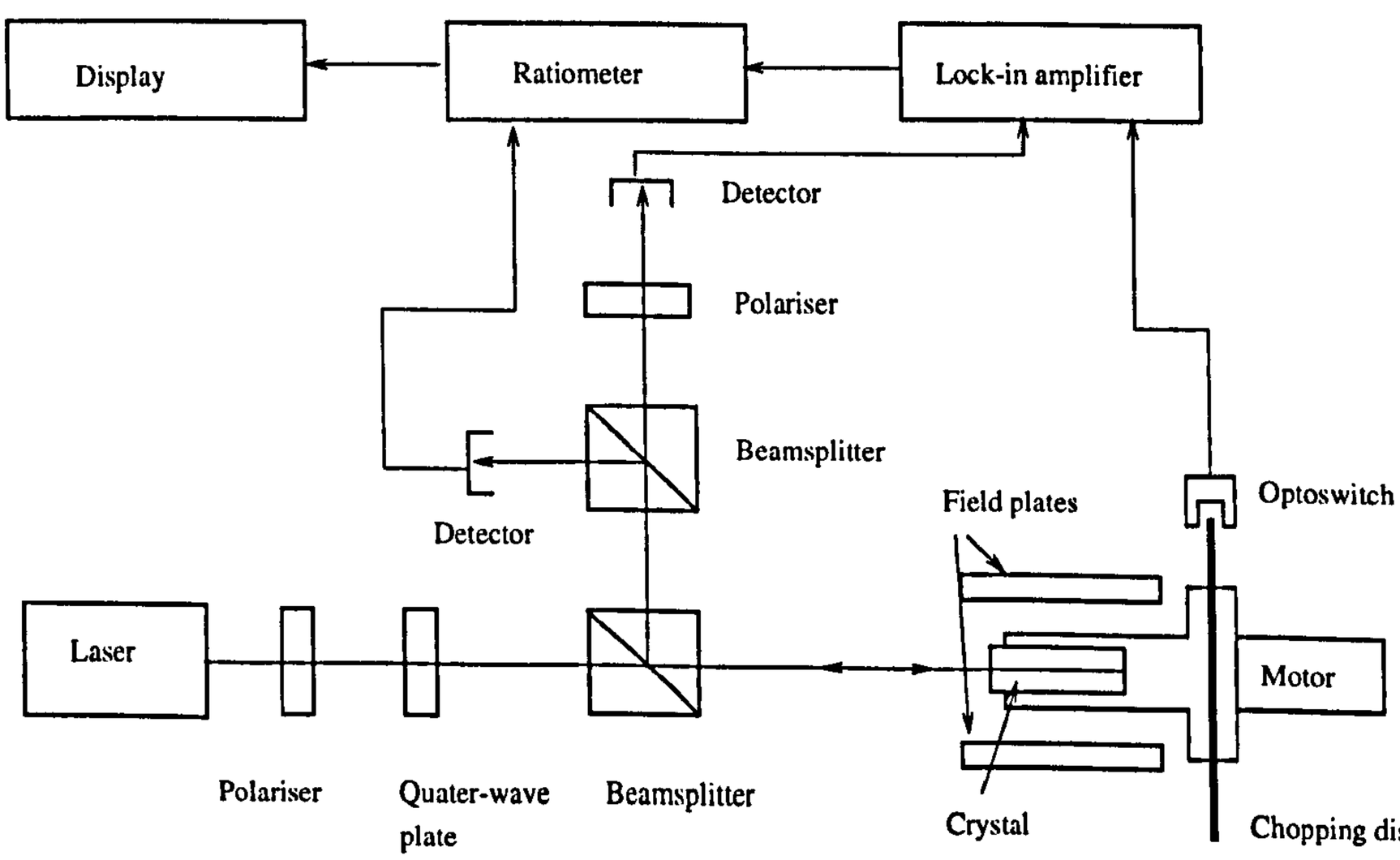

Figure 2.8: DC electric field sensor using the electro-optic effect by Rogers and Robertson.

out with lithium niobate $LiNbO_3$ and bismuth germanate $Bi_4Ge_3O_{12}$. The problem

of space charges attached to the surface of an electrooptic crystal was again solved by rotating the crystal. The circularly polarized light enters the crystal rotating with a frequency f, is reflected by a dielectric mirror at the back of the crystal and after passing through the analyzer, the photodetector provides a signal which is a mixture of two frequencies, $2f$ and $3f$. The signal at $3f$ frequency is proportional to the electric field induced birefringence, whereas the $2f$ signal is caused by fixed birefringence of the crystal. Thus the signal proportional to the applied field can be selected by filtering the output signal appropriately. The crystal was spun at 20Hz in order to satisfy two important criteria: the measured signal frequency must lie within the detection passband, and, secondly the crystal rotation frequency f must be sufficiently high for any surface charge to be effectively locked into place by its finite mobility. The minimum detection level of the sensor was equivalent to the noise level of $\approx$ 2.5kV/m, which is approximately the same as for the sensor made by Hidaka et al. [33]. The reason of such a high value was attributed to the disalignment of the sensor due to the rotation of the crystal and the induced stresses.

In 1991 Vohra, Buchholtz and Kersey [70] demonstrated an interferometric fibre optic dc and low frequency electric field sensor based on the electrostrictive effect (Figure 2.9). The quadratic relation between an applied electric field and the induced strain in an electrostrictive ceramics (Ba:PZT) allows for the detection of low frequency signals as sidebands of a high frequency carrier. A preliminary investigation of the sensor has yielded a minimum detectable electric field of $0.35(V/m)/\sqrt{Hz}$ for a sensor with 3cm of fibre. From calculations it follows that for 30m of fibre at-

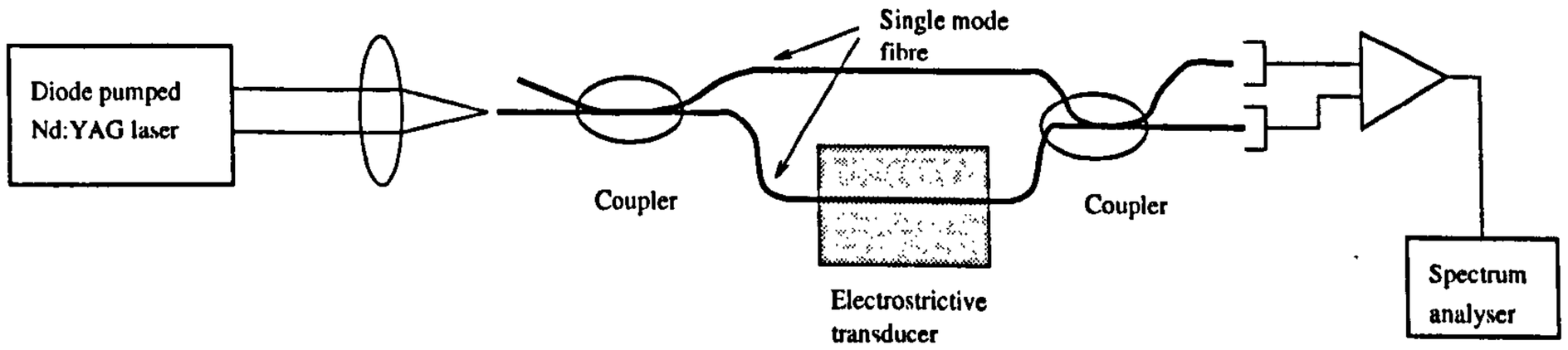

Figure 2.9: DC electric field sensor based on the electrostrictive effect.

tached to an electrostrictive ceramic, it should be possible to achieve a minimum detectable field of $10(\mu V/m)/\sqrt{Hz}$, limited by interferometer phase noise [70]. The disadvantages of this sensor are conductive electrodes and driving AC voltage source which disturb the original electric field. The use of Mach-Zehnder fibre optic interferometer makes it also highly sensitive to environmental changes.

Another DC probe for electric field distribution measurements was reported in 1991 [34] (Figure 2.10). Metal hemispheres with radius $R = 40$mm are separated

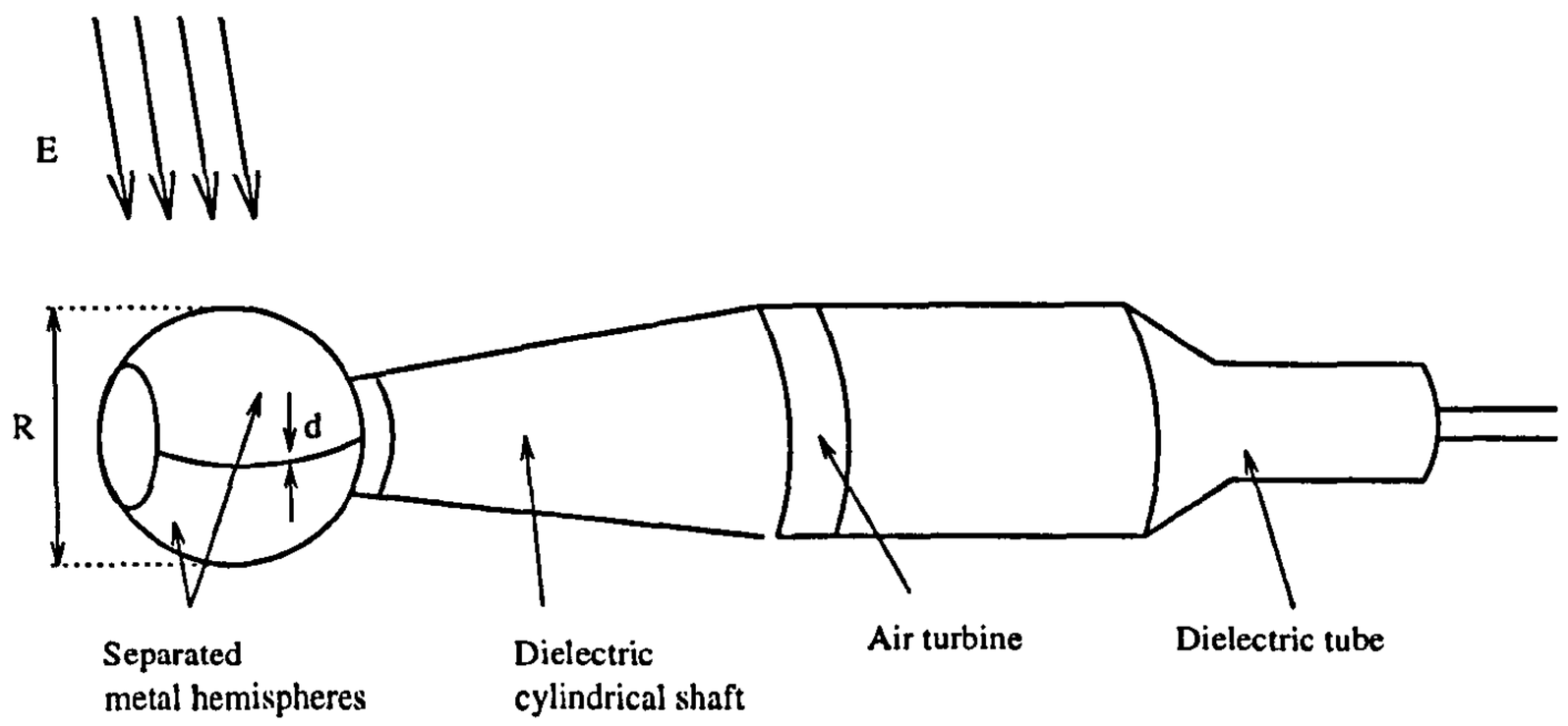

Figure 2.10: Electric field sensor by Hornfeld.

by a dielectric gap of width $d \ll R$ and rotated in an electric field by means of an air turbine to which they are connected by a dielectric shaft. The electrical induction induces an alternating signal proportional to the electric field. Several different methods were employed to measure DC field with this probe. For example, if the hemispheres are connected together by low impedance, the current is induced and detected by an electronic circuit inside the globe. With this system it was possible to measure fields from 30V/m to 500kV/m. Another method of measuring the signal induced by the rotating hemispheres, uses a Pockel's voltage sensor and optical fibre connection. In this arrangement the field intensities up to 600kV/m were measured. A disadvantage of this sensor is its metal head and conductive leads which are required to connect it to either a meter or a crystal.

The sensor developed by Hidaka in 1982 was further improved by Murooka and Nakano in 1992 [56]. Their work was exclusively concentrated on an improvement of the sensitivity of the sensor. A new measuring system was presented which uses an

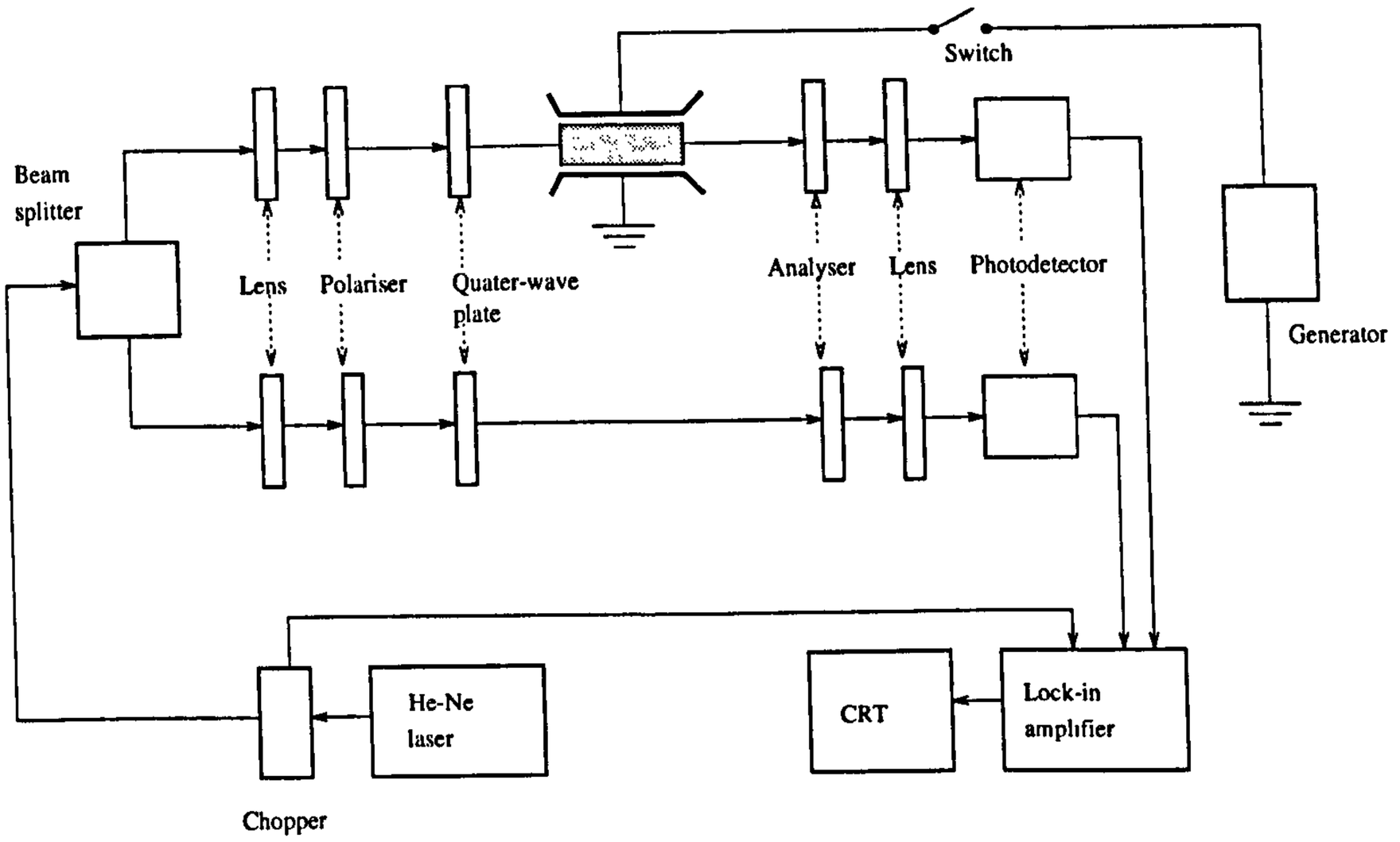

Figure 2.11: Schematic diagram of optical field measuring system by Murooka et al.

intensity difference method with an intensity modulated laser beam (Figure 2.11). To decrease the noise level, lock-in amplifier was used and two optical branches were created completely equivalent except for the Pockel's sensing head placed only in one of them. Signals from both branches were differentially added in the locking amplifier. In the range of the field strength from 6kV/m to 100kV/m, the researchers succeeded to improve the sensor sensitivity to AC electric field by 100 times compared to the previous system. The minimum detectable field was 750V/m with S/N ratio of 20dB. Further improvement of this measurement system was reported in 1994 [57]. The system was simplified using reflection mirror technique. The minimum measurable field strength was 500V/m at the S/N ratio of 10.2dB and 1V/m at the critical value of 0dB. The sensitivity of the sensor was improved immensely for AC field measurements. The crystal in these experiments was not rotated. However, all the experiments were done with AC electric field at 50Hz and with a commercially available Pockel's element which has electrodes attached directly to the electrooptic crystal. Therefore, the effects of the internal and external charge on the sensor (section 4.3.2 and chapter 5) were not addressed by this study, and the improvement in the sensor sensitivity should be considered only with the respect to AC field measurement.

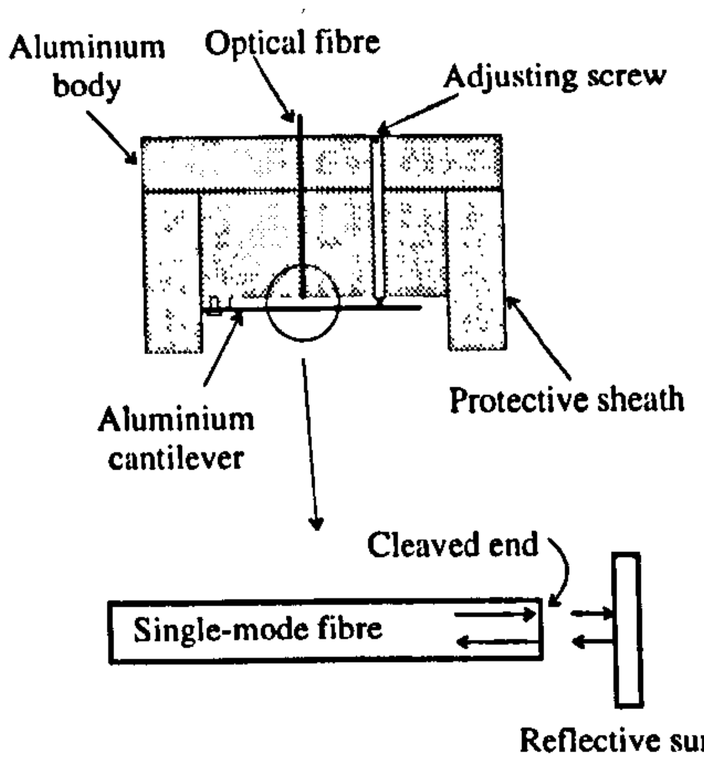

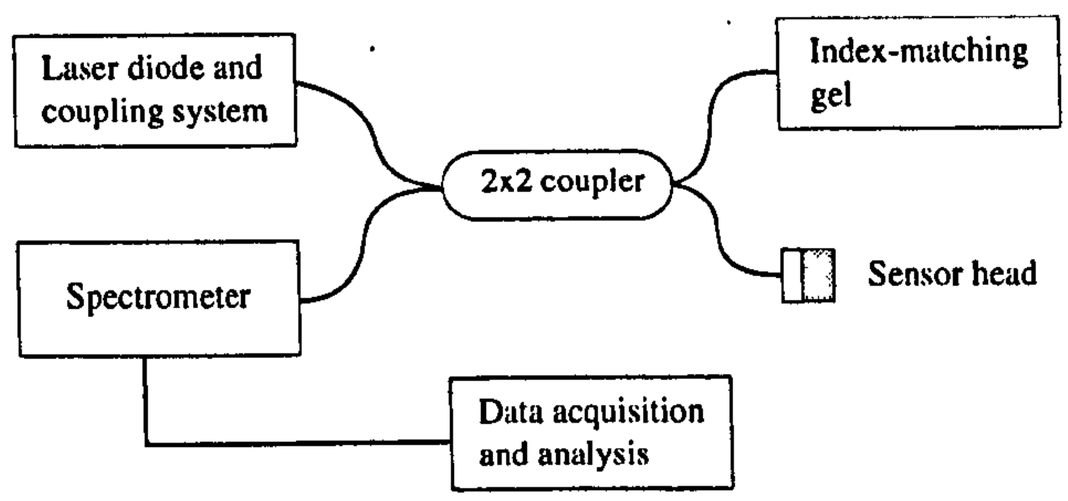

Figure 2.12: Schematic diagram of the electric field sensor by Priest et al.

A different type of an electric field sensor, designed especially for measurement of a static electric field and charge density in corona discharge, has been developed by Priest et al. in 1997 [62]. The sensor uses electrostatic charging either due to an electric field induction or environmental space charge to deform the flexible cantilever. In both cases the flexible surface and the surface adjacent to cleaved fibre end become charged and the electrostatic repulsion between the surfaces alters the cavity length. This is monitored by a low-coherence Fabry-Perot interferometer which enables an absolute measurement of the cavity length. The spectrum of the output light is obtained by the spectrometer and analyzed deriving its autocorrelation function. The relationship between the cavity length and the electric field or charge concentration, can be obtained either through calibration in known fields or concentration or from knowledge of the elastic properties of the flexible cantilever. This miniature sensor has a diameter of 20mm and was used to measure electric field in the vicinity of Van de Graaff generator in the range 13.5-65 kV/m with a resolution of 9kV/m.

The summary of the reported electric field probes is shown in Table 2.1. From the presented literature review, it can be concluded, that the techniques using converse piezoelectric and electrostrictive effect can achieve very high sensitivity compared to electrooptic probes which have inherently low sensitivity due to low values of electrooptic coefficients (chapter 3). However, because of the use of Mach-Zehnder

fibre optic interferometer the temperature stability is poor. It was also shown that the problem of electric field measurements in space charge environment was solved using the rotation of the sensing head. This rotation was identified as one of the main sources of the low sensor sensitivity.

For practical purposes the sensor should be relatively insensitive to environmental changes. It should be small and passive to achieve a high spatial resolution and to reduce the disturbance of the measured field to minimum. Ideally the sensor would measure also the electric field in a space charge environment with an improved accuracy. The polarimetric electrooptic sensor configuration can offer relatively small size, passive nature and not very complex output signal processing. Although its sensitivity to the electric field is not very high, the temperature stability of the reported probes was very good. Therefore, the polarimetric electrooptic arrangement has been chosen for the development of DC and ELF electric field sensor.

Table 2.1: Reported electric field probes; used effects - P Pockel's effect, EI electrical induction, PE piezoelectric effect, ES electrostrictive effect; Scheme - MZ Mach-Zehnder interferometer, FP Fabry Perot interferometer.

Year-Author	Frequency Range[1]	Voltmeter/ Metal part	Minimum measured value or *Range	Effect/ Scheme	Material
61-Namba[59]	dc/ac	y/y	-	P	ADP,KDP
75-Massey[53]	60Hz	n/n	$6V/m$	P	KDP
80-Hamasaki[31]	ac	y/y	*0-300V	P	BSO
82-Kuhara[44]	ac	y/y	*0-500V	P	BSO
82-Hidaka[33]	dc	n/n	-	P	LN
82-Donalds[28]	0.5-1.5kHz	n/n	-	PE/MZ	PVF2
83-Kyuma[47]	dc/ac	y/y	$10^{-3}V$	P	BGO
84-Shibata[65]	ac	n/n	$500V/m$	P	BG
84-Gulyaev[30]	0.01-200kHz	n/n	$3kV/m$	P	BSO
85-Kutsaenko[45]	dc/ac	n/n	$1kV/m$	P	BSO
85-Robertson[64]	dc	n/n	$2.5kV/m$	P	LN,BG
86-Kanoi[40]	dc/ac	y/y	*25-500V	P	BG
86-Imai[35]	0.02-5kHz	n/n	-	PE/MZ	P(VDF/ TrFE)
87-Meyrueix[55]	dc/ac	y/y	0.1-18kV/m	P	-
87-Jaeger[37]	60Hz	n/y	-	P/MZ	LN
88-Bohnert[17]	ac	n/n	*0.01-100kV/m	PE/MZ	quartz,P-VDF,PZT
91-Hoernfeldt[34]	dc	n/y	*0.03-500kV/m	EI	metal
91-Vohra[70]	dc/ac	n/y	$0.35V/(m\sqrt{Hz})$	ES	Ba:PZT
92-Vohra[71]	ac	n/y	$10\mu V/(m\sqrt{Hz})$	ES/MZ	PMN
92-Kuwabara[46]	100Hz -1GHz	n/y	$0.22mV/m$ @50MHz	P/MZ	LN
92-Bonek[18]	50Hz	n/y	$0.25V/m$	P/MZ	LN
93-Choi[25]	0.06-100kHz	n/y	*0.01-6kV/m	P/MZ	LN
94-Murooka[57]	ac	y/y	$1V/m$ $(S/N = 0dB)$	P	LN
94-Kingsley[42]	ac	n/n	$0.2V/(m\sqrt{Hz})$	P/MZ	LN
97-Priest[62]	dc	n/y	*13.5-65kV/m	E/FP	-

[1] where the frequency range was not available, either the frequency used in the reported experiments is stated or suitability of the probe for DC or ELF measurements is indicated using the symbols dc, ac , respectively.

2.4 Aim and Objectives of the Research

The aim of this research was to investigate the possibility of a precise measurement DC and extra-low-frequency electric field using a passive, all dielectric and ElectroMagnetic Interference (EMI) immune sensor. The sensor should use the linear electrooptic effect in a crystalline material, preferably cubic crystal. The measurements of DC field should be possible in environments both with and without a space charge, without the necessity to rotate the sensing head.

The specific objectives to be achieved were:

1. Material analysis and selection of the most suitable electrooptic material.
2. Theoretical and experimental study of the internal space charge effect in the electrooptic sensor (conductivity and photoconductivity effects)
3. Investigation of the external space charge effect and possibility of its elimination using an artificial extension of the sensing element.

2.5 Summary

The literature review revealed that the most common optical techniques for electric field measurements are based on the electrooptic and piezoelectric effects. The reported probes for DC and ELF field measurements were discussed separately. It was shown that the techniques using electrostrictive and piezoelectric effects in conjunction with the Mach-Zehnder interferometer can be very sensitive to DC and ELF field, however, their temperature stability is poor. On the other hand, probes based on the electrooptic effects may have a very good temperature stability. Their sensitivity is, however, lower. Taking into account the importance of the sensor stability to environmental changes, size of the sensor, disturbance of the measured field and complexity of the output signal processing design, the linear electrooptic effect was chosen for the DC and ELF sensor and the aim and objectives of the research were defined.

Chapter 3

Theoretical Background

The aim of this chapter is to summarise the material physics which is essential for the understanding of the electrooptic sensors. It covers the propagation of electromagnetic waves in a crystalline linearly birefringent medium, the electrooptic effect as the basic principle of the sensor, and a brief description of other effects in crystals which can influence the performance of the electrooptic sensors, such as optical activity, Faraday rotation, photoelastic and pyroelectric effects. The discussion of the electromagnetic wave propagation is extended at the end of the chapter to account for effects of both linear and circular birefringence.

3.1 Electromagnetic Waves in Anisotropic Medium

3.1.1 Permittivity Tensor

The concept of the electrooptic sensor is based on light propagation in a crystal, that, generally, is an optically anisotropic medium and its physical properties depends on the direction of the propagating light. Optical and dielectric properties of materials can be characterised by so called permittivity, a physical property which is indispensable for the description of electrooptic effect and, therefore, its origin is explained below.

An electric field applied to any material causes the redistribution of free and bound electric charges within the material [6], effect which is called polarization. In

an isotropic medium the induced polarization **P** and the electric field **E** are parallel and are related by a scalar factor χ called susceptibility

$$\mathbf{P} = \epsilon_o \chi \mathbf{E} \tag{3.1}$$

where ϵ_o stands for the permittivity of vacuum. In an anisotropic material, which is the case of most crystals, the induced polarisation depends on the direction of the electric field vector and it becomes necessary to define the susceptibility as a second rank tensor. Each of the polarization components P_i is dependent of all three components of the electric field E_i, and can be written using Einstein notation [1] as

$$P_i = \epsilon_o \chi_{ij} E_j, \quad i,j = 1,2,3 \tag{3.2}$$

The susceptibility tensor has clear physical origin and can be used to define the permittivity tensor ϵ_{ij} as follows

$$\epsilon_{ij} = \epsilon_o (1 + \chi_{ij}) \tag{3.3}$$

The permittivity tensor relates the electric field vector **E** and the electric displacement vector **D** [6]

$$D_i = \epsilon_{ij} E_j, \quad i,j = 1,2,3 \tag{3.4}$$

and thus defines the dielectric properties of the crystal. It is shown in the next sections that the permittivity tensor characterises optical properties as well.

If the medium is homogenous, non-absorbing and magnetically isotropic the permittivity tensor can be shown to be symmetric using the principle of the conservation of electromagnetic field energy [9]. The same analysis, applied to a non-absorbing optically active medium, shows more general result:

$$\epsilon_{ij} = \epsilon_{ij}^* \tag{3.5}$$

where ϵ_{ij}^* is a complex conjugate of the permittivity ϵ_{ij}. The symmetrical property of the permittivity tensor makes it possible to find a coordinate system in which the tensor has only its diagonal elements. The axes of such a coordinate system are called the *principal dielectric coordinate axes* and are of great importance for a description of the electrooptic effect.

3.1.2 Electromagnetic Wave Propagation in Anisotropic Medium Possessing Linear Birefringence

Electromagnetic wave propagation in an optically anisotropic medium is the starting point for an investigation of the electrooptic effect. Even if crystals are isotropic, under the influence of a disturbance, such as electric field or strain, they become optically anisotropic.

To determine how the electromagnetic waves propagate in an anisotropic medium it becomes necessary to solve Maxwell's equations. Electrooptic crystals can usually be considered as non-conductive and magnetically isotropic medium. Maxwell's equations then give the basic wave equation for crystal optics [9]

$$\mathbf{k} \times (\mathbf{k} \times \mathbf{E}) + \omega^2 \mu \underline{\epsilon} \mathbf{E} = 0 \tag{3.6}$$

In this equation $\underline{\epsilon}$ is the permittivity tensor, ω is the radian frequency, μ the permeability of the material, $\mathbf{k}$ and $\mathbf{E}$ are the wave and electric field vectors. The fact that the permittivity is the symmetric tensor and in principal coordinates can be expressed only by the diagonal elements ϵ_{ii} (section 3.1.1) simplifies the wave equation (3.6) and its analytical solution [9].

In a medium characterised by a symmetric permittivity tensor, there are two solutions which satisfy the wave equation (3.6). They correspond to propagation of two mutually orthogonal, linearly polarized electromagnetic waves with parallel wavefronts. In other words, if the direction of the phase velocity is given there are two linearly polarized orthogonal waves with different wave vectors $\mathbf{k_1}, \mathbf{k_2}$ or different refractive indices n_1, n_2 which satisfy the equation (3.6). These solutions are termed *eigenwaves* and the axes along directions of the polarization vector are called *optical eigenaxes*.

The propagation of the two eigenwaves is the key to understanding of the electrooptic sensor. The two waves propagate independently with different phase velocities given by different refractive indices n_1,n_2. The difference between the refractive indices $(n_1 - n_2)$ is called birefringence or often *linear birefringence* because the eigenwaves are linearly polarized compared to *circular birefringence* when the eigenwaves are circularly polarized waves. It can be either *natural birefringence*, which

is an inherent property of the crystal, or *induced birefringence*, when the difference in the refractive indices is caused by an external disturbance such as electric field, stress etc. The natural or the induced birefringence causes a phase retardation between the two eigenwaves and, therefore, the polarization of the light emerging from the anisotropic medium is generally changed. Such a change can be detected and this is the basic principle used in the electrooptic field sensor.

3.1.3 Index Ellipsoid

In the previous section it was pointed out that two independent linearly polarised eigenwaves can propagate in a linearly birefringent crystal, for a given direction. The determination of their refractive indices, directions of their polarisation and the birefringence are essential for the design of an electrooptic field sensor. These optical properties of the propagating waves can be obtained by solving the equation (3.6) or more conveniently, by using the method of the index ellipsoid. This method is also suitable for computer simulations of the electrooptic effect because only simple matrix operations are required to obtain the parameters of the propagating waves. The index ellipsoid and the way of using it to obtain the optical properties of an electrooptic material are explained in the following paragraphs.

The index ellipsoid is a geometrical construction, in the literature sometimes referred to as optical indicatrix. It can be obtained assuming that the electric field energy density can be written as [9]

$$U_e = \frac{1}{2}\mathbf{ED} \tag{3.7}$$

where $\mathbf{E}$ is the intensity of the electric field and $\mathbf{D}$ the electric displacement vector. Considering the principal coordinate axes as defined in section 3.1.1, the permittivity tensor has only the diagonal elements ϵ_{ii}. Then using the equation (3.4) and algebraic operations, the following equation can be derived:

$$2U_e = \frac{D_1^2}{\epsilon_{11}} + \frac{D_2^2}{\epsilon_{22}} + \frac{D_3^2}{\epsilon_{33}} \tag{3.8}$$

The equation (3.8) represents a surface of constant energy U_e in (D_1, D_2, D_3) space and it is an ellipsoid with axes parallel to the principal dielectric axes. Finally, the

substitution of $D_1^2/(2U_e)$ by x_i and ϵ_{ii}/ϵ_o by n_i^2 gives:

$$\frac{x_1^2}{n_1^2} + \frac{x_2^2}{n_2^2} + \frac{x_3^2}{n_3^2} = 1 \tag{3.9}$$

which is the equation of the index ellipsoid with major axes parallel to the principal dielectric axes x_1, x_2, x_3. The constants n_i are called the principle refractive indices and can be calculated from the permittivity tensor.

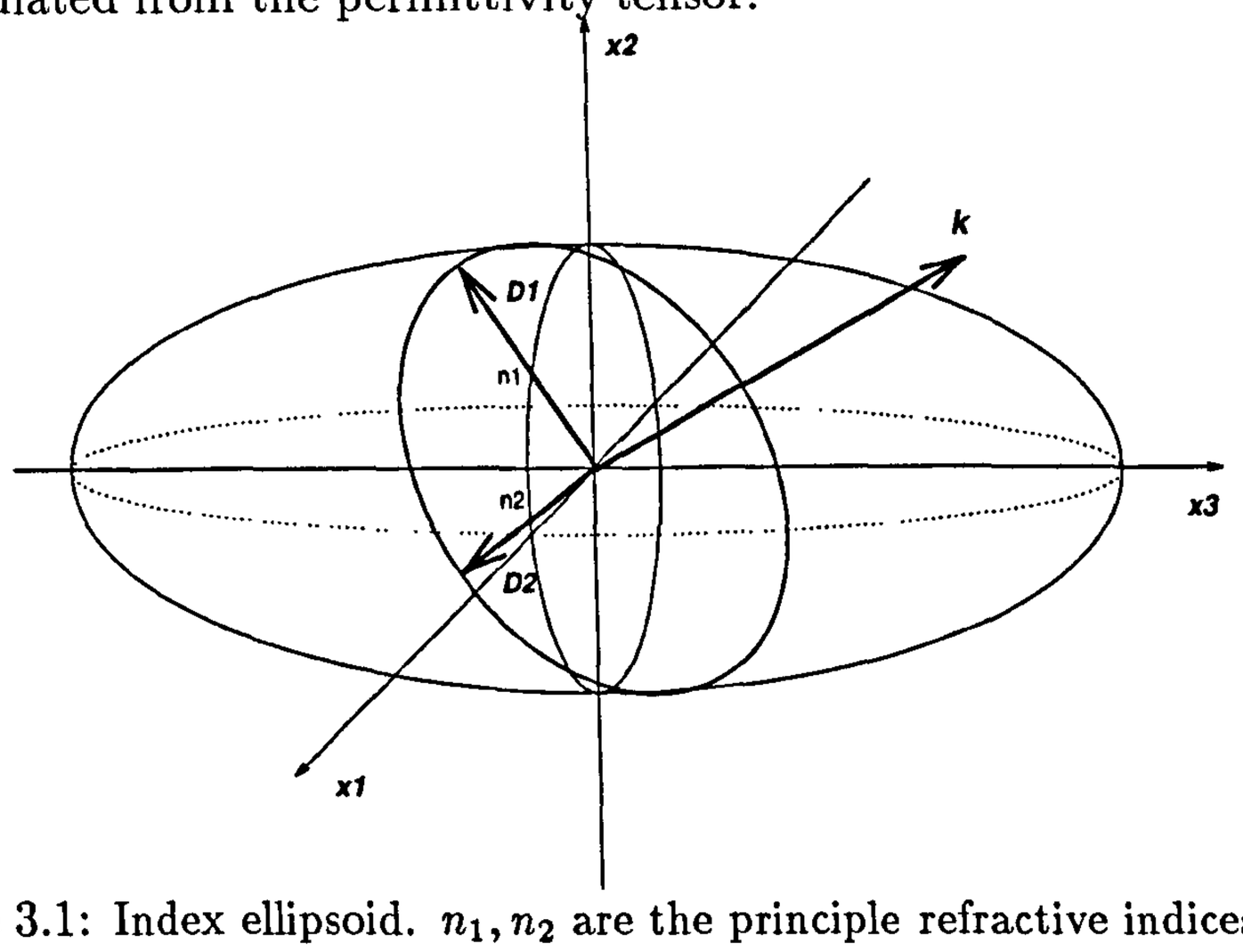

Figure 3.1: Index ellipsoid. n_1, n_2 are the principle refractive indices.

The index ellipsoid simplifies the determination of the refractive indices and directions of electric field displacement vectors of the two eigenwaves [5]. Provided that the normal vector of the wavefront (direction of the phase velocity $\mathbf{k}/k$) is given, the method of the index ellipsoid requires to find the intersection of the plane passing through the origin, which is normal to the phase velocity vector (parallel to $\mathbf{k}$), with the index ellipsoid (Figure 3.1). This intersection is an ellipse. Directions of the two major axes of the ellipse are the directions of the two independent electric displacement vectors D_1, D_2 and the length of these two axes are equal to the values of refractive indices n_1, n_2. Because the speed of light in a material increases with decreasing refractive index the shorter axis is called *fast optical axis* and the longer axis is called *slow optical axis*.

The introduced index ellipsoid is a powerful tool for a description of light propagation in crystals. It will be used later to describe the electrooptic effect and to determine the eigenwaves of propagation and refractive indices in a mathematical model of the electrooptic sensor.

3.1.4 Eigenwaves Separation in Anisotropic Media

The light incident in an anisotropic medium can be expressed by a linear combination of the two eigenwaves. These two eigenwaves generally have different refractive indices and, therefore, they can be refracted with different angles which leads to their separation in an anisotropic crystal. This effect is called the double refraction and its description can be found in the literature [5]. It may have unwanted consequences in the design of the sensor.

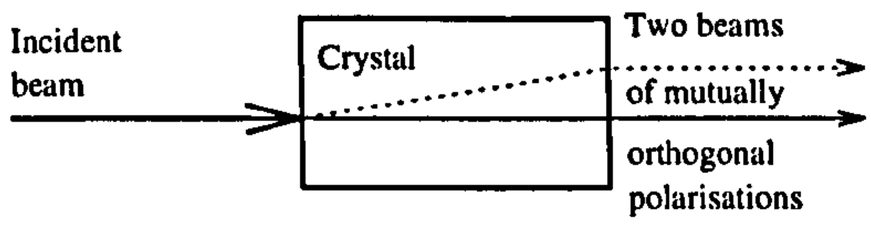

Figure 3.2: Separation of the eigenwaves in an uniaxial crystal.

In electrooptic sensors the light beam incident on a crystal is perpendicular to the face of the crystal. If the crystal is isotropic the light passes through the crystal without changing its polarization due to the absence of natural birefringence, and emerges from the opposite face of the crystal as a single beam. In an anisotropic medium, however, the beam can be divided into two beams corresponding to two eigenwaves [5]. Thus even for normal incidence two beams can be found on the opposite face of the crystal (Figure 3.2). This effect depends on the crystallographic orientation of the crystal incident face and on the type of the crystal. Generally, it can be said that if a normally incident light is parallel with one of the principal axes of the index ellipsoid, no separation of the eigenwaves occurs.

Since electrooptic sensors are based on the interference of the two eigenwaves, care should be taken to compensate the effect or to avoid the separation of eigenwaves by choosing an appropriate crystal orientation.

3.2 Electro-Optic Effect

The light propagation in an optically anisotropic medium and the way of using the index ellipsoid to obtain the optical properties of materials have been described in

the previous section. Now it is possible to describe the electrooptic effect using the concept of the index ellipsoid.

In some materials, an electric field induces changes in refractive indices. This effect is called the electrooptic effect, and it is caused by a redistribution of the bound charges and possibly a slight deformation of the ion lattice [9]. Such changes can be expressed by a change of the index ellipsoid. To do so, it is suitable to define an impermeability tensor η by the inverse tensor to the permittivity tensor

$$\underline{\eta} = \epsilon_o \underline{\epsilon}^{-1} \tag{3.10}$$

Using the η_{ij} tensor the index ellipsoid (3.9) can be written as [9]

$$\eta_{ij} x_i x_j = 1 \tag{3.11}$$

An applied electric field $\mathbf{E}$ causes changes in optical properties of the crystal which can be expressed by changes in the impermeability tensor using Taylor expansion as

$$\eta_{ij}(\mathbf{E}) - \eta_{ij}(0) = r_{ijk} E_k + s_{ijkl} E_k E_l + higher \quad order \quad terms \tag{3.12}$$

where r_{ijk} is the third rank tensor of linear (Pockel's) electrooptic effect, s_{ijkl} the fourth rank tensor of quadratic (Kerr) electrooptic effect. Both tensors are symmetric [9] in i and j and, therefore, Voigt' notation can be used. Thus using equations (3.11),(3.12) and Voigt's notation [7], and neglecting all nonlinear terms in (3.12) the index ellipsoid in an electric field is

$$\begin{aligned} (\frac{1}{n_2^2} + r_{1k}E_k)x_1^2 + (\frac{1}{n_2^2} + r_{2k}E_k)x_2^2 + (\frac{1}{n_3^2} + r_{3k}E_k)x_3^2 \quad + \\ 2x_2x_3r_{4k}E_k + 2x_3x_1r_{5k}E_k + 2x_1x_2r_{6k}E_k \quad = \quad 1 \end{aligned} \tag{3.13}$$

This is an equation of the index ellipsoid changed by linear electrooptic effect in the presence of an electric field. The values of the refractive indices and the orientation of the slow and fast axes can be found by the method introduced in section 3.1.3.

The equation (3.13) shows that an applied electric field changes the index ellipsoid. Therefore, the refractive indices and the polarisation direction of the two eigenwaves generally change as well. In the electrooptic sensors it is usually required that the directions of $\mathbf{D_1}$ and $\mathbf{D_2}$ vectors of the two eigenwaves do not change with

the applied electric field. Then the normally incident light can be expressed by the same linear combination of the unchanged eigenwaves both in the presence and in the absence of the electric field. Only a change in the principal refractive indices occurs. If the difference $(n_1 - n_2)$ of the refractive indices changes with the applied field, the polarization of the light emerging from the crystal is changed as well. In this case the electrooptic effect is detectable.

When the electrooptic coefficients r_{4k}, r_{5k}, r_{6k} are zero and an electric field is applied, the principal axes of the ellipsoid change their size but not the orientation (the mixed terms in the equation (3.13) are zero). When at least one of them is non-zero the ellipsoid undergoes a change in orientation of its principal axes and a change in shape. Therefore, the r_{4k}, r_{5k}, r_{6k} coefficient are sometimes called the *skew* coefficients. Some materials as for example Potassium Niobate ($KNbO_3$) possess very high skew coefficients and may seem to be very attractive for the sensor application. However, in most cases these materials are not isotropic and the use of their high skew electrooptic coefficients may lead to eigenwaves separation accompanied by a strong natural birefringence, effects which degrade the sensor performance as shown later. Therefore, if the crystals are not inherently isotropic it is better to avoid the use of the skew coefficients.

3.3 Unwanted Effects in Crystals

An ideal electrooptic field sensor should be sensitive only to the electric field and should have a linear output dependence on the electric field. However, in reality the electrooptic crystal is influenced not exclusively by the electric field but other environmental disturbances can change the optical properties of the crystal and hence influence the whole sensor. The crystal can be influenced by magnetic field (e.g.Faraday effect), by vibrations or other forces applied to the crystal (e.g.photoelastic effect) or by a change in temperature (e.g.pyroelectric effect). Some of the electrooptic crystals can possess inherent optical properties (optical activity) which affect the propagation of the light through the crystals which can differ from the propagation in a linearly birefringent medium described in the section 3.1.2.

3.3.1 Optical Activity

The optical activity is an inherent property of some non-centrosymmetric crystal classes [7]. The effect causes rotation of the polarization plane of a linearly polarized light. The phenomenon can be explain by means of two circularly polarized eigenwaves, right and lefthanded, which propagate with different phase velocities [7]. The optical activity is, therefore, often referred to as an effect of *circular birefringence*. To evaluate the magnitude of the effect, *specific rotatory power* ρ is defined by the rotation of the polarisation plane per unit length of a crystal. For example rotatory power of quartz at 633 nm is $1.8 \times 10^3 \quad °/m$ which means that after passing 1mm distance in the crystal the polarization plane of a linearly polarized light is rotated by 1.8°. This rotation can be either left-handed or right-handed. When both optical activity and linear birefringence are present the solution of Maxwell's equations leads to two independent orthogonal waves. However, in crystals possessing the optical activity the two orthogonal eigenwaves are elliptically polarised (section 3.4). The presence of the optical activity in an electrooptic field sensor leads to a lower sensitivity of the sensor (section 4.2.1). The optical activity effect can be eliminated if a light beam passes through the crystal in opposite directions [7].

3.3.2 Faraday Rotation

Faraday rotation is a linear magnetooptic effect. An applied magnetic field along the light propagation direction rotates the plane of the polarisation of a linearly polarised light.The specific rotatory power ρ which express the rotation of the polarisation plane per unit length of the crystal can be written as

$$\rho = VB \tag{3.14}$$

where B is the magnetic flux density parallel to the light beam and V Verdet constant of a material. The Verdet constant characterises the magnitude of the Faraday effect in the materials. The optical activity and Faraday effect may seem to be very similar effects. However, it is not possible to eliminate the Faraday effect in the same way as the optical activity because the rotation of the polarisation plane

of a linearly polarised light in the reverse direction is added to the rotation of the forward beam. Thus when the light passes through a crystal and then is reversed and passes through the crystal in the opposite direction the effect of the optical activity is cancelled whereas the Faraday effect is doubled. Otherwise the Faraday rotation has the same effect on the light propagation as the optical activity and can be classified as an effect of circular birefringence.

3.3.3 Photoelastic Effect

When a crystal is exposed to external forces or there are strains in the crystal, optical properties of the crystal can be changed. Generally the effect is described by changes in the index ellipsoid. The strains and forces in a crystal can be expressed by the stress and strain tensors which are mutually connected by material constants called elastic compliances [7]. The deformation of the index ellipsoid can be expressed either in terms of the stress tensor (σ_{kl}) or in terms of the strain tensor (e_{kl}) as

$$\Delta\eta_{ij} = \pi_{ijkl}\sigma_{kl} \tag{3.15}$$

$$\Delta\eta_{ij} = p_{ijkl}e_{kl} \tag{3.16}$$

where $\Delta\eta_{ij}$ stands for a change in the impermeability tensor (3.10), π_{ijkl} and p_{ijkl} are the piezooptical and the elastooptical coefficients, respectively.

The photoelastic effect can be both beneficial and unwanted. For example, when a low frequency or DC electric field is applied to an electrooptic unclamped crystal, converse piezoelectric effect induces strains within the crystal and, therefore, the photoelastic effect. Thus the index ellipsoid is influenced not only by the electrooptic effect but by the photoelastic effect as well. In this case the electrooptic coefficients are denoted as r_{ij}^T. On the other hand, if the crystal is clamped or the applied electric field is of high frequency (the crystal is virtually clamped), there is no converse piezoelectricity and the photoelastic effect within the crystal. Then the electrooptic coefficients are denoted as r_{ij}^S and usually $r_{ij}^S < r_{ij}^T$. Thus at low frequencies of electric field the photoelastic effect is beneficial because it magnifies the electrooptic effect.

However, the following examples show that more often the photoelasticity is an unwanted effect. Any vibrations or forces applied to the electrooptic sensor influence the output signal due to the photoelastic effect. Therefore, it is important to avoid any unnecessary stresses or strains if possible. For example, in the sensor by Robertson [64], vibrations due to the rotation of the crystal were identified as the main source of noise, thus decreasing the sensitivity of the sensor.

Commercially manufactured crystals are never ideal crystals. Imperfections in crystal lattices cause local strains and therefore the photoelastic effect which is the reason why the extinction ratio of isotropic crystal placed between crossed polarizers is not zero. Such a built-in birefringence can be partially removed by annealing process.

3.3.4 Pyroelectric Effect

Certain crystals have the property of developing an electric polarization when their temperature is changed. If a spontaneous polarization already exists, it can be changed with temperature. This effect is called pyroelectricity and is restricted only to ten crystal classes [7]. The pyroelectricity is an unwanted effect in the electric field sensor applications because it induces the electric polarisation and thus indirectly the electrooptic effect. Therefore, it can cause a temperature instability of the sensor.

3.4 Wave propagation in crystals with linear and circular birefringence

3.4.1 Electromagnetic Theory

Both natural and induced linear birefringence in an electrooptic crystal can be accompanied by a circular birefringence in the form of Faraday rotation or in some non-centrosymmetrical classes in the form of optical activity. The permittivity tensor in crystals possessing only linear birefringence becomes generally complex and

hermitian (3.5). As in the case of a medium with a linear birefringence there are two solutions of the wave equation (3.6) termed eigenwaves [9] [75]. These eigenwaves are not linearly polarized waves but generally elliptically polarized waves. The eigenwaves are orthogonal to each other, i.e. the major axes of the polarization ellipses are perpendicular, with opposite sense of rotation of the electric field vector. The principal axes of the polarization ellipses are parallel to the polarization directions of the linearly polarized eigenwaves in the case of pure linear birefringence.

The two special cases of an elliptical polarization are linear and circular polarizations. These correspond to the electromagnetic wave propagation in purely linearly birefringent or purely circularly birefringent media. The mathematical model described in the section 3.5 is based on the mathematical description of the electromagnetic wave propagation in both linearly and circularly birefringent media.

3.4.2 Poincare Sphere

The Poincare sphere is a convenient geometric representation in which the state of polarization of a light beam can be denoted by a point on the sphere. The phenomena accompanying the propagation of the light through a medium exhibiting linear birefringence, optical activity or both can be determined by means of simple geometrical construction on the sphere [63] [38] [72] [2]. A short description of the Poincare sphere is given since the concept is used later to investigate the effect of optical activity in the electrooptic sensor.

A general point P on the Poincare sphere represents a general elliptic state of polarisation. The circle $HAVB$ (equator) in x_1x_3 plane (see Figure 3.3) represents all the possible linearly polarized states. It includes points H and V denoting horizontal and vertical plane polarisation. Points C_l and C_r represent left and right circular polarisation. The general point P stands for an elliptical vibrations. It is defined by its longitude 2λ and latitude 2ω. The major axis of the elliptic vibrations is at an angle λ to the horizontal axis and the ratio of the major to minor axes b/a is given by

$$\frac{b}{a} = \tan\omega \tag{3.17}$$

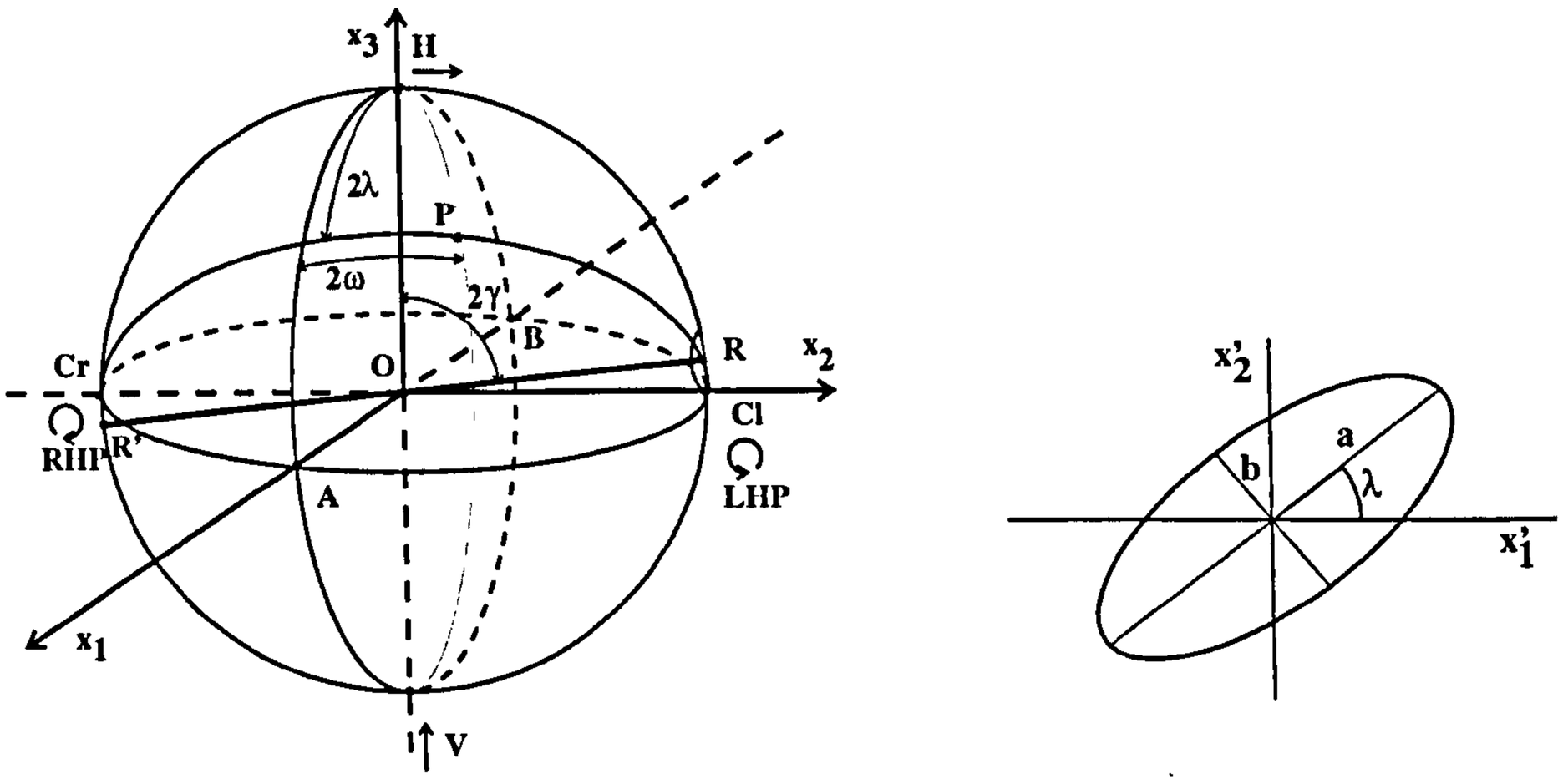

Figure 3.3: Poincare sphere, parameters of elliptically polarized light, and polarization ellipse (right).

(see Figure 3.3). The latitude 2ω is taken positive measured from the equator towards C_l and 2λ is taken to be positive for a counterclockwise rotation about C_l.

The Poincare sphere can be applied to the problem of propagation of polarized light in media with both linear and circular birefringence. The state of light polarisation after propagation in media possessing both linear and circular birefringence is obtained using the following construction [63]. Let H and V be the two principle eigenwaves in the medium without circular birefringence and δ the relative phase retardation per unit length introduced between them. Draw the line RR' in the plane x_2x_3 (HC_lVC_r) at an angle 2γ to HV where

$$\tan(2\gamma) = 2\,\frac{\rho}{\delta} \tag{3.18}$$

Then, if P is the state of polarisation of the incident light entering the crystal of thickness l, the polarisation state of the emerging light is obtained by rotating the sphere around the axis RR' by the angle

$$\Delta = \Delta_0 l \tag{3.19}$$

where

$$\Delta_0 = \sqrt{\delta^2 + 4\rho^2} \tag{3.20}$$

The angle Δ is called *composite phase difference*, δ is phase difference per unit length caused by linear birefringence and ρ is the rotatory power characterising a circular birefringence.

If a polarized light P on the Poincare sphere passes through a polarizer represented by a point Q, the light intensity behind the polarizer can be calculated as

$$I = \cos^2\left(\frac{\widehat{PQ}}{2}\right) = \frac{1}{2}(1 + \cos\widehat{PQ}) \tag{3.21}$$

where $\widehat{PQ}$ denotes the length of the great circular arc between P and Q.

The described construction follows from the electromagnetic theory of light but compared to it, the Poincare sphere can appreciably simplify the analytical treatment of the phenomena accompanying the passage through a medium exhibiting both linear and circular birefringence.

3.5 Summary

This chapter summarized the essential physics of electromagnetic wave propagation in crystalline media. The concept of index ellipsoid was described and propagation of light in an anisotropic media was discussed in terms of linearly polarized eigenwaves. The electrooptic effect and other effects in crystal which could influence the electrooptic sensor were explained. Finally, the description of the electromagnetic wave propagation was extended to media possessing both linear and circular birefringence, and the elliptically polarized eigenwaves were explained.

Chapter 4

Polarimetric Interferometric Sensor

This chapter addresses the first two main issues as they were identified in the aims and objectives of the project - material analysis and internal space charge effect. The structuring also reflects the progress of the project in time. The first two sections describe the principle of the electrooptic field sensor (4.1) and the mathematical model which was developed and used in simulations of different effects (4.2). The section on crystal selection 4.3 points out different criteria which should be applied to select an appropriate crystal for the DC and ELF application. Using these concepts, two most appropriate electrooptic crystals were selected. Their performance is discussed in separate sections for ELF field measurements (4.4) and DC field measurements (4.5). The last section of this chapter describe results of the investigations of the probe isotropy.

4.1 Principle of Electro-Optic Sensor

A schematic diagram of the electro-optic electric field sensor is shown in Figure 4.1. Light from a monochromatic source, a laser diode, is polarized using a polarizer. Using a quarter-wave plate it is then launched into the electrooptic crystal in such a way that it excites two propagation eigenmodes. In an ideal electrooptic crystal with no circular birefringence, these eigenmodes are linearly polarized waves with the

plane of polarization perpendicular to each other (section 3.1.2). They experience different refractive indices, the change of which depends on the electric field due to the electrooptic effect. The eigenwaves propagate with different phase velocities depending on the electric field intensity. The polarization of the light emerging

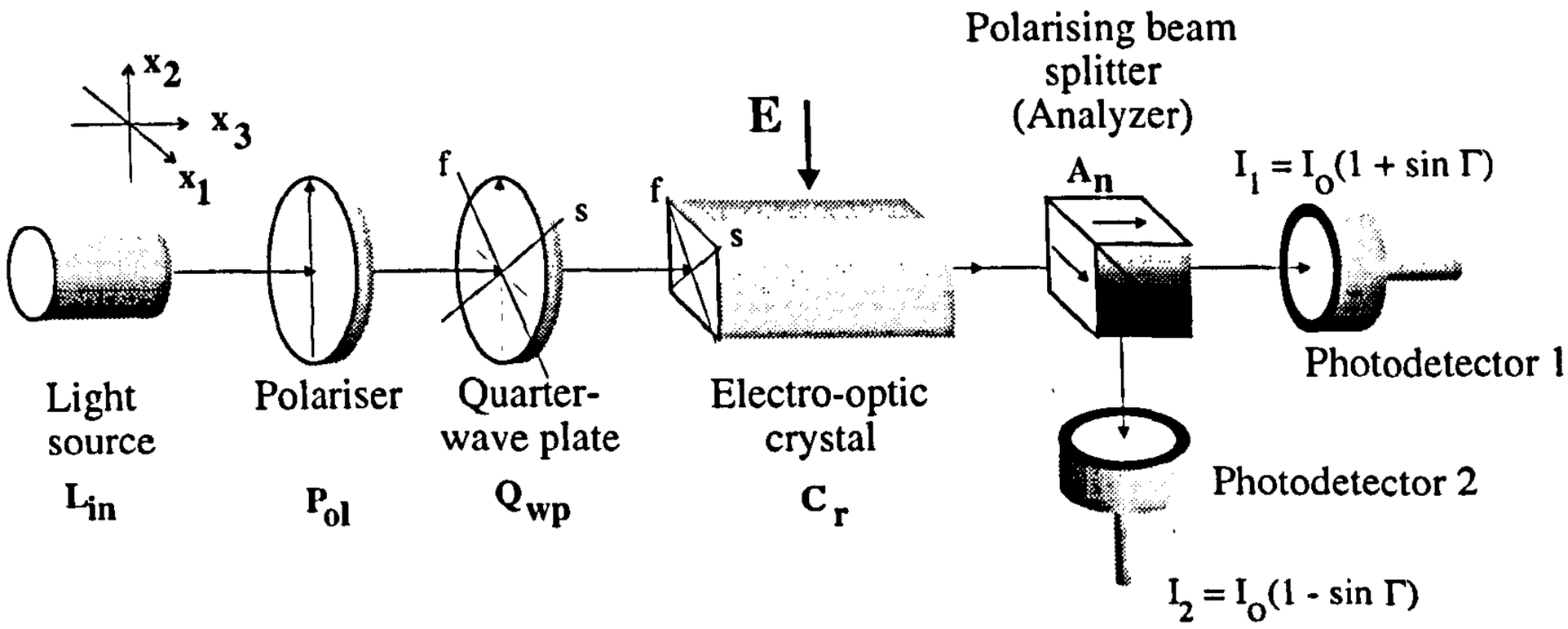

Figure 4.1: Schematic diagram of the electro-optic sensor.

from the crystal is, therefore, changed by the applied electric field. This change in polarization is then converted by the polarizing beamsplitter into a change in the light intensity and detected by the photodetectors. The quarter-wave plate inserted between the polarizer and the crystal produces an additional phase shift of $\pi/2$ radians between the eigenmodes, so that the sensor works well within the linear region of its transfer characteristic (Figure 4.2).

The placement of the wave plate in front of the crystal offers advantages compared to the position behind the crystal as it was used in the first sensors (section 2.1). In this case, induced fast and slow axes of the crystal do not have to be precisely aligned at 45° to the polarization plane of the linearly polarized light. The light behind the quarter-wave plate is circularly polarized and can, therefore, excite crystal eigenwaves of equal intensities for any orientation of crystal slow and fast axes. The wave plate also acts as an optical isolator not allowing the light reflected from crystal to be transmitted back to the laser which could influence the laser stability, causing power fluctuations and thus introducing additional noise. At first glance the quarter-wave plate may look as the means of eliminating the influence of

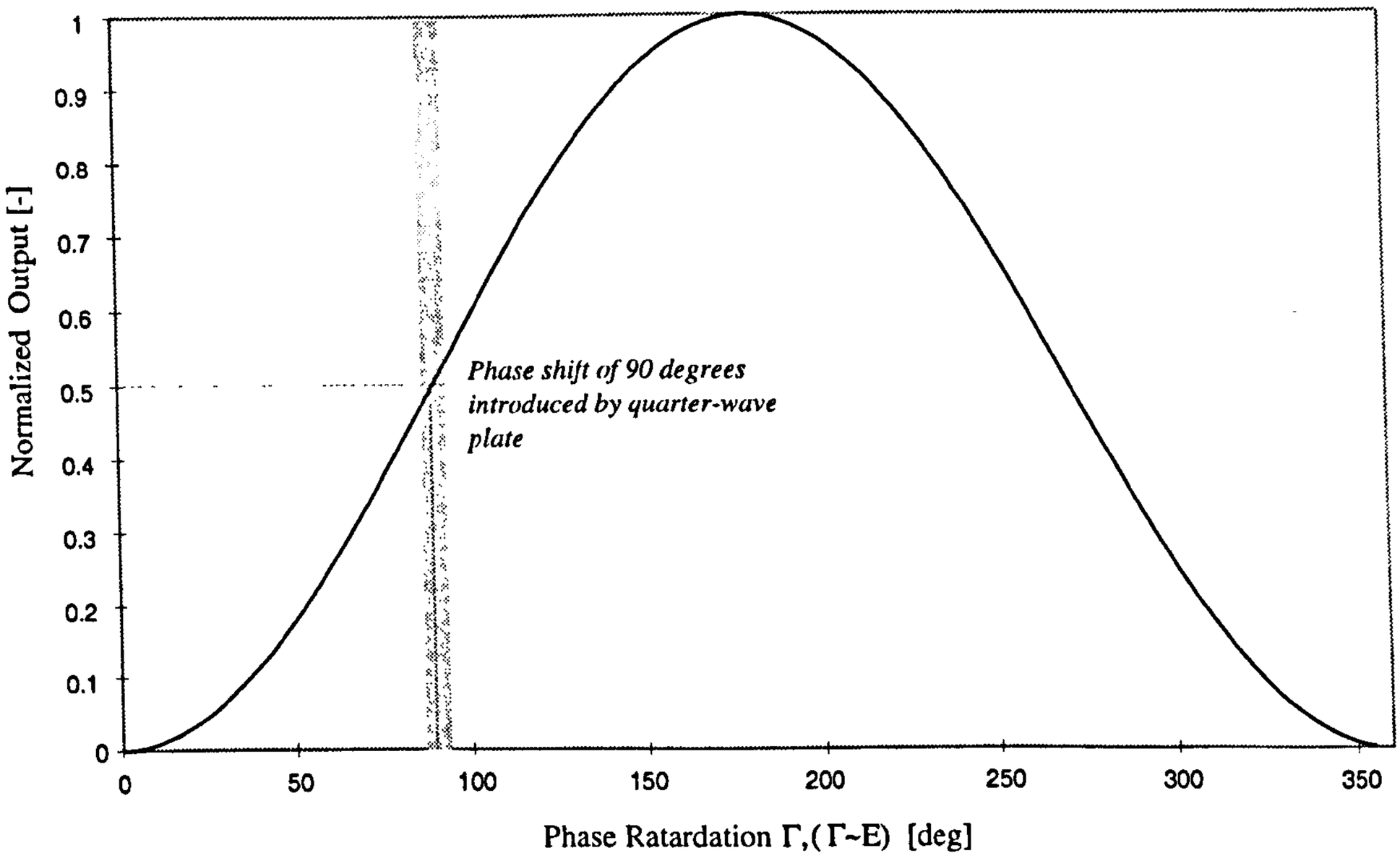

Figure 4.2: Transfer characteristic of the electro-optic sensor.

the circular birefringence of the crystal, since a circularly polarized light defined by the wave plate propagates through a circularly birefringent media without change in polarization. However, this is not the truth as it is shown in section 4.3.1 where the effect of a circular birefringence on the sensor is analyzed.

If the crystal is assumed to possess no natural and circular birefringence, the light intensities I_1 and I_2 at the photodetectors are found to be [9]

$$I_{1,2} = I_o(1 \pm \sin\Gamma(E)) \tag{4.1}$$

where I_o is the light intensity at the photodetectors without the measured field and Γ is the phase shift retardation between the eigenmodes of propagation induced by the measured electric field E. It is shown in [9](see equation 4.10) that Γ is directly proportional to the measured electric field E, and in most cases, the condition $\Gamma \ll 1$ is satisfied. The output can be then considered to be a linear function of the phase retardation Γ or the electric field intensity E:

$$I_{1,2} = I_o(1 \pm \Gamma(E)). \tag{4.2}$$

From the equation (4.2) it follows that the sensor is functional only with one output. The second output is complementary and using the detection scheme $I_1 - I_2$

it enables to increase the sensor sensitivity twice as $I_1 - I_2 = 2I_o\Gamma(E)$ and to decrease the effect of light power fluctuations as shown in section 6.5.

4.2 Mathematical and Computer Model of the Sensor

A mathematical model of the electro-optic sensor from Figure 4.1 was developed using Jones calculus. The model proved to be useful in investigations of different effects, e.g. effect of optical activity, disalignment of optical components, sensor isotropy and so on. It is coded in MAPLE software package.

The Jones calculus, invented in 1940 by R.C.Jones, is a powerful matrix method in which the state of polarization is represented by two-component vector, while each optical element is represented by 2x2 matrix [10]. The overall transfer matrix for the whole system is obtained by multiplying all the individual element matrices, and the polarization state of the transmitted light is computed by multiplying the vector representing the input beam by the overall matrix.

There are, however, several drawbacks in using Jones calculus. Firstly, it applies strictly to the description of perfectly polarized light. If the light in optical system is only partially polarized it might be necessary to use different means to describe the system (e.g. Mueller calculus [74]). For the purposes of this work Jones calculus is satisfactory. Secondly, usually it is tacitly assumed that there are no reflections of light from surfaces of individual components and the light is totally transmitted through where applicable. This shortage can be usually overcome by modifying the ideal Jones matrices (section 6.4).

If the light in the electrooptic sensor propagates along x_3 axis of the cartesian laboratory coordinate system $(x_1x_2x_3)$, Jones matrices of optical components apply to the x_1x_2 plane. Each optical component represented by a matrix M can be naturally rotated around x_3 axis, which gives different Jones matrix. However, all the rotations can be described by a unitary transformation (rotation around x_3 by angle α) and by so called standard Jones matrix of the component $\mathbf{M}^{st}$ (e.g. linear

polarizer aligned along x_1 axis, linear analyzer aligned along x_2 axis, quarter-wave plate with fast and slow axes along x_1 and x_2 etc.) in the following way:

$$\mathbf{M} = \mathbf{R}^{-1}(\alpha)\mathbf{M}^{st}\mathbf{R}(\alpha) \tag{4.3}$$

where $\mathbf{R}(\alpha)$ is the transformation matrix corresponding to the rotation around x_3 by an angle α and $\mathbf{R}^{-1}(\alpha)$ is the inverse matrix:

$$\mathbf{R}(\alpha) = \begin{pmatrix} \cos(\alpha) & -\sin(\alpha) \\ \sin(\alpha) & \cos(\alpha) \end{pmatrix} \tag{4.4}$$

$$\mathbf{R}^{-1}(\alpha) = \begin{pmatrix} \cos(\alpha) & \sin(\alpha) \\ -\sin(\alpha) & \cos(\alpha) \end{pmatrix} \tag{4.5}$$

The standard matrices for the polarizer (aligned along x_1), analyzer (aligned along x_2) and linear phase retarder (e.g. quarter-wave plate) with fast axis along x_1 and phase retardation $\Delta\varphi$ are:

$$\mathbf{P}_{ol}^{st} = \begin{pmatrix} a & 0 \\ 0 & b \end{pmatrix} \quad \mathbf{A}_{n}^{st} = \begin{pmatrix} c & 0 \\ 0 & d \end{pmatrix}, \quad 1 \geq a \gg b \geq 0, \quad 0 \leq c \ll d \leq 1 \tag{4.6}$$

$$\mathbf{Q}_{wp}^{st} = \begin{pmatrix} \exp i\frac{\Delta\varphi}{2} & 0 \\ 0 & \exp -i\frac{\Delta\varphi}{2} \end{pmatrix} \tag{4.7}$$

If the Jones vector of the incident polarized light is denoted as $\mathbf{L}_{in}$ then the vector of the light beam leaving the analyzer and impinging on the photodetector $\mathbf{L}_{out}$ can be expressed as

$$\mathbf{L}_{out} = \mathbf{A}_n \, \mathbf{C}_r \, \mathbf{Q}_{wp} \, \mathbf{P}_{ol} \, \mathbf{L}_{in} \tag{4.8}$$

where $\mathbf{C}_r$ is the Jones matrix of the electrooptic crystal. The Jones matrix of the crystal $\mathbf{C}_r$ has to be found using either index ellipsoid alone (linear birefringence only) or electromagnetic theory of the light propagation in doubly refractive media possessing both linear and circular birefringence. The schematic diagram of the evaluation process for $\mathbf{C}_r$ matrix is depicted in Figure 4.3. The light incident on the crystal ($\mathbf{Q}_{wp}\mathbf{P}_{ol}\mathbf{L}_{in}$) is expressed in the laboratory coordinate system (components

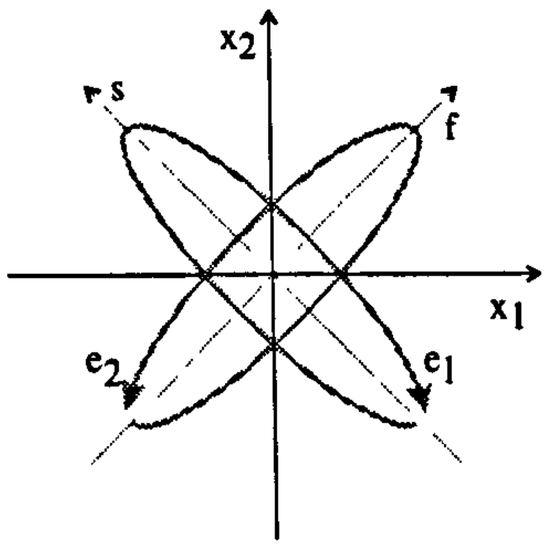

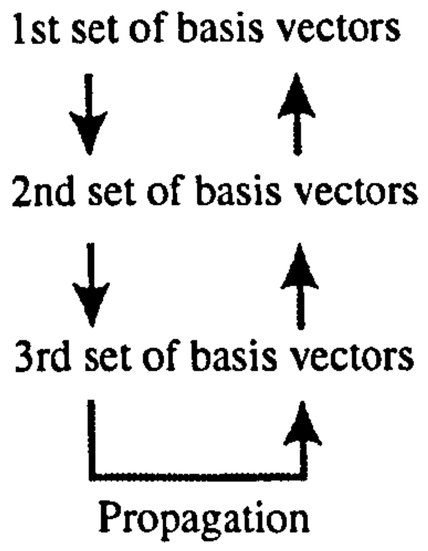

Linearly polarized waves (E_1, E_2)

Linearly polarized waves (E_f, E_s)

Elliptically polarized waves (e_1, e_2)

Phase shift between the elliptically polarized eigenmodes due to different refractive indices

Figure 4.3: Elliptically polarized eigenwaves and evaluation of $\mathbf{C}_r$ matrix.

E_1, E_2). To describe its propagation in both linearly and circularly birefringent media the vector needs to be decomposed in a new basis which corresponds to the two orthogonal elliptically polarized eigenwaves with opposite sense of rotation of the electric field vector. To do that, light is first transformed into the 2nd set of basis vectors corresponding to the eigenmodes in the presence of linear birefringence only. These eigenmodes are linearly polarized and mutually orthogonal waves. The orientation of their polarization planes and their refractive indices depend on the orientation of the crystal, applied electric field, and propagating light beam. It is readily found using the index ellipsoid. The polarization planes coincide with directions of major axes of elliptically polarized eigenwaves, which are the real eigenwaves in the case of crystals possessing both linear and circular birefringence. This fact is used in the 3rd transformation into the real eigenmodes basis. Once the incident light is expressed in the real eigenmodes basis, the different phase shifts due to different phase velocities of the eigenmodes can be applied in the form of a phase retardation matrix. Finally, the light vector is transformed back in to the (x_1, x_2) basis.

The photodetector detects the output light intensity which is found to be [9]

$$I = \mathbf{L}_{out}\, \mathbf{L}^*_{out} \tag{4.9}$$

where $\mathbf{L}^*_{out}$ is the complex conjugate of the vector $\mathbf{L}_{out}$.

The model incorporates crystals material constants and their temperature coefficients so that it can be used for evaluation of temperature effects as well, as long as the material constants are available.

4.3 Electrooptic Crystal Selection

The electrooptic crystal as the sensing element is the heart of the sensor and its properties influence final sensor characteristics. It must be, therefore, carefully chosen. There are several criteria which need to be taken into account. These are discussed in this section. First criterion is the magnitude of the electrooptic effect in the crystal which is required as high as possible to achieve a high sensitivity of the sensor. The magnitude of the effect is analyzed in the first subsection 4.3.1. It is shown how the magnitude depends on material constants of the electrooptic crystal and on the shape of the sensing element. The effect of a circular birefringence on sensor sensitivity is discussed in details. The second criterion which is discussed and found to be very important is crystal conductivity. A high conductivity of the electrooptic crystal causes an internal space charge effect which is described and analyzed in the subsection 4.3.2. This effect is found to be a dominant feature if the sensor is to be used for static and extra-low-frequency field measurement. The crystal is also required not to introduce unnecessary temperature instabilities. Based on this analysis two electrooptic crystals were identified as suitable for DC and ELF sensor applications.

4.3.1 Magnitude of Electro-Optic Effect

4.3.1.1 Pure Electrooptic Effect

The literature search revealed that optically isotropic cubic crystals are the most appropriate for sensor applications. The other two groups of crystals, uniaxial and biaxial crystals, inherently possess natural birefringence. The natural birefringence can cause the eigenwaves separation, in directions not parallel to the axes of the index ellipsoid (section 3.1.4). Even if this effect can be avoided by choosing a suitable direction of the laser beam in the crystal, the natural birefringence still introduces an additional phase shift between the eigenwaves which is strongly temperature dependent. Also, the natural birefringence can be so large (e.g.Lithium Niobate) that in some cases the light passing through the crystal gets partially depolarized which consequently degrades the sensor sensitivity. Theoretically, the natural birefringence

can be avoided in uniaxial crystals, if the light propagates along the optical axis of the crystal. In such a case, however, the alignment becomes critical and a small disalignment of the light from the optical axis may cause a strong temperature dependence due to the natural birefringence and pyroelectricity, if the latter is present (section 6.3). With regard to these problems the attention was primarily focused on cubic electrooptic crystals.

Cubic crystals are isotropic with no inherent natural birefringence and pyroelectricity. This makes this group of crystals attractive. Only two groups of cubic crystals, with 23 and $4\bar{3}m$ point group symmetries, exhibit linear electro-optic effect. Zinc Sulphide, Cadmium Telluride, etc., are crystals of $4\bar{3}m$ point group, which do not possess optical activity. The optical activity is present in the 23 point group crystals such as Bismuth Germanium Oxide (BGO) and Bismuth Silicon Oxide (BSO). In this section the sensitivity of both groups to the electric field is investigated, neglecting the effect of optical activity which is examined in details later in this section.

It follows from equations (4.2) that the sensitivity of the sensor is directly proportional to the light intensity I_o and to the relative phase retardation Γ produced by the electric field. This suggests that the phase retardation Γ, normalised to the crystal length and applied electric field, can be taken as a figure of merit representing crystals from the standpoint of the sensor sensitivity. In the following the evaluation of Γ is based on material constants, and systematic investigations have been carried out to compare different materials.

Theoretical analysis of the electro-optic effect in cubic crystals [58] shows that cubic crystals are suitable both for longitudinal (electric field parallel to incident light) and transverse (field perpendicular to the light) electro-optic modulation. The maximum phase retardation in both cases can be expressed as

$$\Gamma = \frac{2\pi}{\lambda} n^3 r E_m l \tag{4.10}$$

where λ is the wavelength of the light, n refractive index, r the electro-optic coefficient, l is the length of the crystal traversed by the light, and E_m is the macroscopic electric field intensity inside the crystal. In contrast to electro-optic modulators the

internal electric field is no longer uniform as the crystal is exposed to an electric field without electrodes. The internal electric field in a crystal of cylindrical or rectangular shape has a complicated spatial distribution. To estimate this internal field, the rectangular shape of the crystal is substituted by an ellipsoid of revolution. According to the electrostatic field theory [60] the internal field components E_m can be expressed in terms of depolarisation factors d_i, components of the external field E_i, and in terms of relative permittivity ϵ_r of the crystal, as

$$E_{mi} = \frac{E_i}{1 + \epsilon_r d_i - d_i}, \quad i = 1, 2, 3 \tag{4.11}$$

The depolarisation factor is a function only of crystal dimensions, more precisely of its axes ratio.

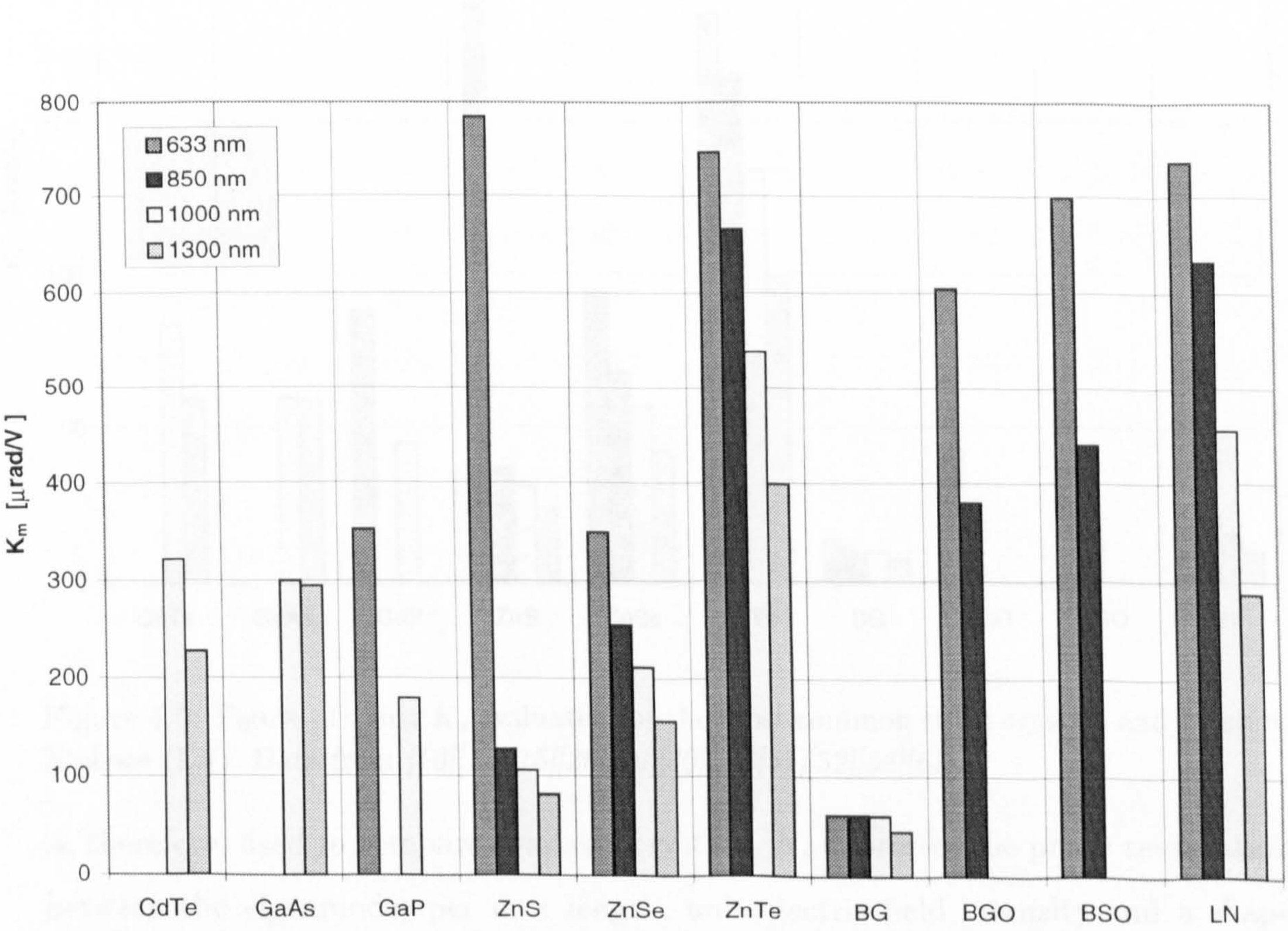

Figure 4.4: Figure of merit K_m for the most common cubic crystals and Lithium Niobate (LN). *Data taken from references [10][12][15][20][26][40][41][51][52][58][67]* .

The figure of merit K_m

$$K_m = \frac{2\pi}{\lambda} n^3 r \tag{4.12}$$

which has been used for optical modulators and is evaluated for the most common cubic crystals in Figure 4.4, is not appropriate for electro-optic sensors as it does not take into account the electric field attenuation inside the crystal discussed above. A new figure of merit

$$K_s = \frac{2\pi}{\lambda} \frac{n^3 r}{1 + \epsilon_{ri} d_i - d_i} \tag{4.13}$$

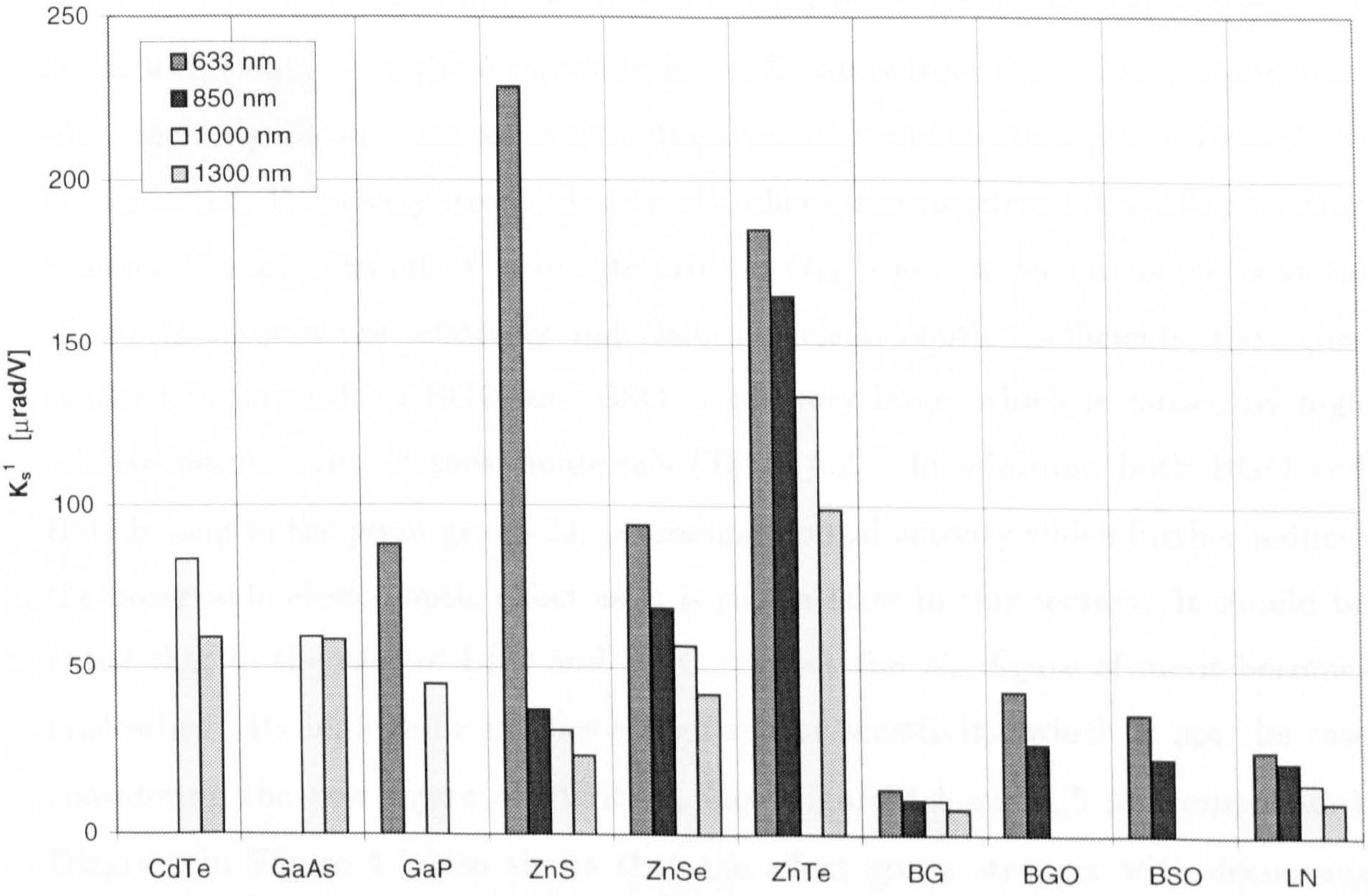

Figure 4.5: Figure of merit K_s evaluated for the most common cubic crystals and Lithium Niobate (LN). *Data from [10][12][15][20][26][40][41][51][52][58][67].*

is, therefore, used to compare available crystals. K_s expresses the phase retardation between the eigenmodes per unit length, unit electric field intensity and a shape characterized by the depolarization factor d. Since d depends exclusively on the ellipsoid axes ratio, it can be chosen arbitrarily to compare materials from the sensor sensitivity point of view. The results presented in Figure 4.5 refers to crystals of cubic shape with axes ratio equal to one and $d = 1/3$ for which (4.13) becomes

$$K_s^1 = \frac{2\pi}{\lambda} \frac{3n^3 r}{2 + \epsilon_r} \tag{4.14}$$

This figure of merit was calculated using available crystal data. Data for Cadmium Telluride (CdTe) and Gallium Arsenide (GaAs) are not available at 633 and 850 nm, because at these wavelengths a strong absorption occurs and the crystals are not transparent. It can be seen that crystals of Zinc Sulphide (ZnS) and Zinc Telluride (ZnTe) are the most sensitive. However, the electro-optic effect in ZnS becomes very small at higher wavelengths, whereas ZnTe is very sensitive even in the near infrared region. The significant difference between K_s^1 for Zinc Sulphide at 633nm and in the near infrared region is most likely caused by a discrepancy in the collected data since these wavelengths are far away from the intrinsic absorbtion edge where significant changes in the refractive index and electrooptic coefficient are not expected. Relatively strong electrooptic effect is encountered in CdTe and Zinc Selenide (ZnSe). Bismuth Germanate ($Bi_4Ge_3O_{12}$) shows a very weak electrooptic effect. In spite of the relatively high values of electro-optic coefficients, the figure of merit for crystals of BGO and BSO is not very large, which is caused by high relative permittivity of these materials (Table 4.2). In addition, both BGO and BSO belong to the point group 23, possessing optical activity which further reduces the observable electro-optic effect as it is shown later in this section. It should be noted that in the case of BSO and BGO crystals the K_m figure of merit becomes misleading. Its high value implies a high sensor sensitivity, which is not the case considering the new figure of merit K_s (see Figure 4.4 and 4.5 for comparison). Diagram in Figure 4.5 also shows that the effect grows stronger with decreasing wavelength of the light source which can be deduced from equation (4.13).

Conclusions. To compare different electrooptic materials a new figure of merit was derived which takes into account the attenuation of the electric field inside the crystal. This figure was evaluated using data available from literature. Zinc Telluride was found to be the most sensitive cubic crystal for sensor applications which can work both in the visible and near infrared region. The crystal of Bismuth Germanate offers the lowest sensitivity to the electric field from those considered.

4.3.1.2 Crystal Shape Considerations

In the analysis of the magnitude of the electrooptic effect the crystal was considered in the shape of an ellipsoid and the sensitivity was found to be a function of the depolarization factor d. This factor is a function of the ellipsoid axes ratios [60] and, therefore, the sensor sensitivity can be influenced by the shape of the crystal or that of the sensing head.

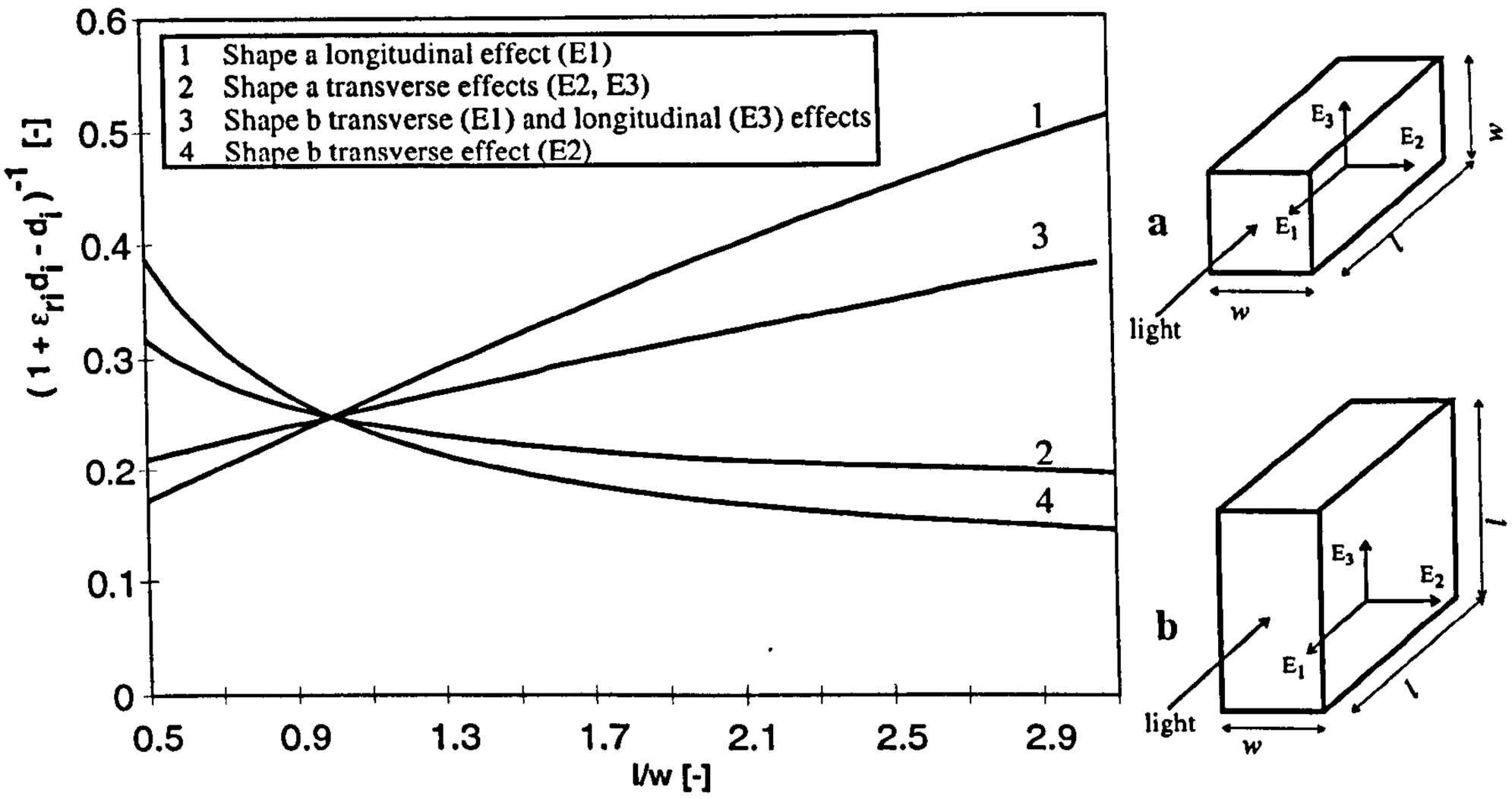

Figure 4.6: Quantity $(1+\epsilon_{ri}d_i-d_i)^{-1}$ versus l/w ratio for relative permittivity $\epsilon_r = 10$.

The effect of the crystal shape on the sensor sensitivity is demonstrated in Figure 4.6. Two crystal shapes are examined, both for perpendicular and longitudinal electro-optic effects. The shape a in Figure 4.6 was substituted by an ellipsoid of revolution with its major axis along the direction of E_1 and major to minor axes ratio equal to l/w. The quantity $1/(1+d_i\epsilon_r-d_i)$ expressing the attenuation of the external field, was calculated for different l/w ratios. The results are plotted in Figure 4.6. The graphs 1 and 2 shows that in a long crystal of shape a ($l/w > 1$) the transverse field (E_2, E_3) is attenuated more than the longitudinal field (E_1). For example, with the l/w ratio of 2.5, the attenuation of the transverse field is more than twice larger compared to the attenuation of the longitudinal field. Thus, when designing the sensor using longitudinal effect, crystal shape should be similar to shape a with the l/w ratio as high as possible to maximize sensor sensitivity. However, the shape

a is not the best choice for the transverse electrooptic effect. One can argue that the same attenuation of the transverse external field can be achieved with the l/w less than 1 (see graph 2). To get the same sensitivity as in the case of longitudinal effect (the same attenuation for the same length) crystal width becomes large. This implies a more expensive crystal, and a larger field perturbation. Therefore, for the transverse effect it is suggested to use shape **b** (graph 3 in Figure 4.6). Figure 4.6 shows that in this case the external transverse field E_3 is attenuated more than in the case of the longitudinal effect in shape **a**, but less than in the case of the transverse effect in shape **a**. Hence, for measurement of one component of the electric field the dimension of the crystal along the measured field should be much higher than the dimension perpendicular to it for the same optical path. The crystal shape **b** is suggested for use in electrooptic sensors based on the transverse electrooptic effect.

To examine the extent to which the ellipsoid approximation approaches the real situation, the electric field inside and around a rectangular piece of dielectric exposed to an uniform field was simulated using a finite element software package (ALGOR). The presented simulations were carried out in 2 dimensional space. Therefore, the simulated results correspond to an infinitely long crystal of a fixed cross-section exposed to a homogenous field perpendicular to the infinite dimension. The external field in simulations is generated by two parallel plates with symmetrical potentials $\pm V(= \pm 100V)$ separated by a distance $d \approx 8.5m$. The intensity of the generated electric field between the plates is $E_0 = 24V/m$. The crystal with relative permittivity $\epsilon_r = 10$ is placed in the middle of the air gap between the electrodes. Different crystal shapes were investigated: square, circle, rectangle, and rectangle immersed in a dielectric rod.

Analytical solution for an infinitely long crystal with the circle cross-section is known [60]. The internal electric field is homogenous and can be calculated from (4.11). The depolarisation factor for the discussed case is $d = 0.5$ and the internal electric field intensity E_m becomes:

$$E_m = \frac{3}{11} E_0 \tag{4.15}$$

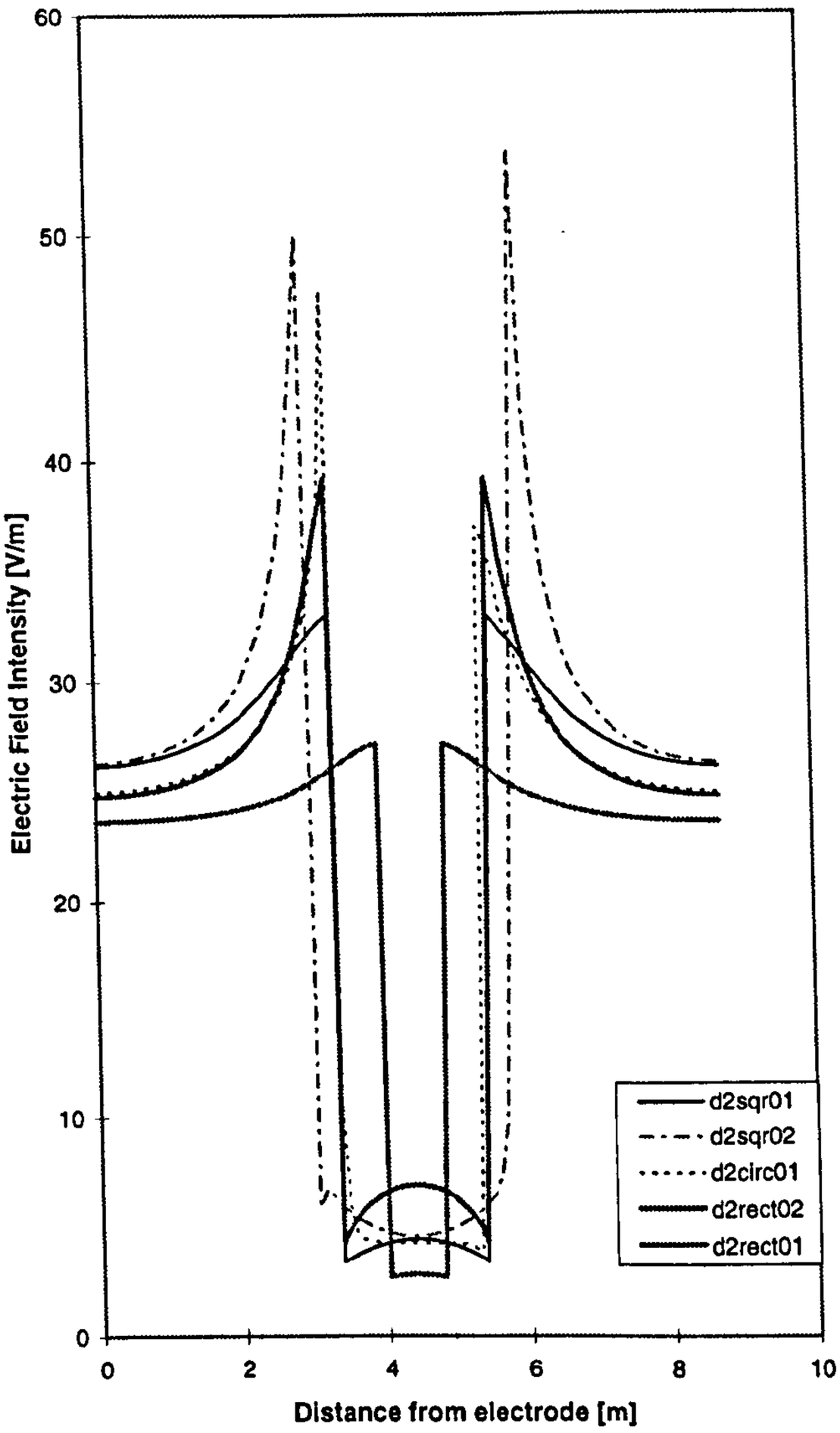

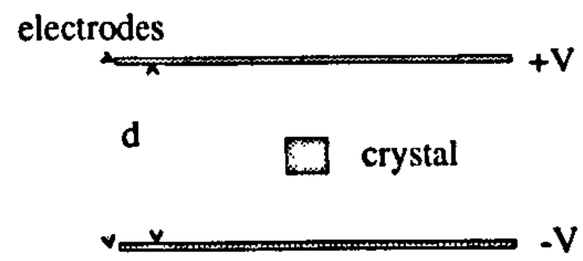

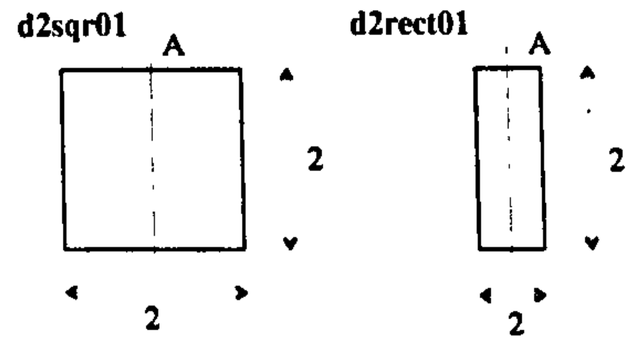

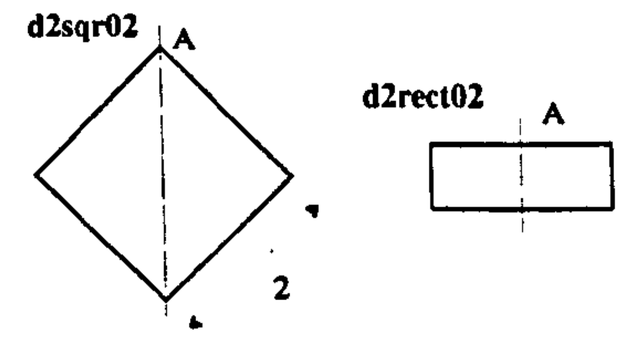

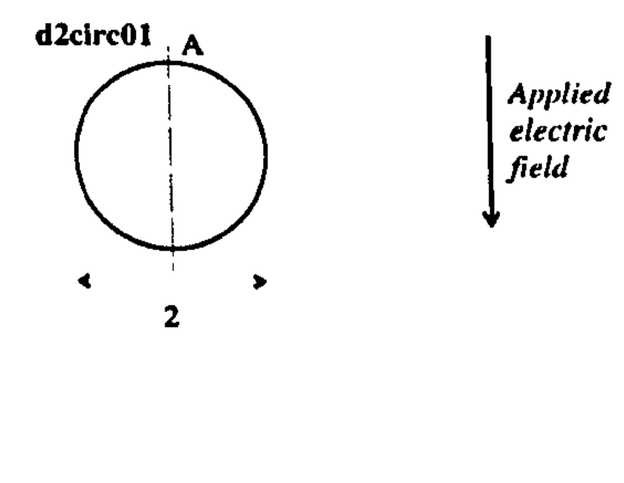

Figure 4.7: Effect of crystal shape on sensor sensitivity. *The crystal ($\epsilon_r = 10$) is placed in a uniform electric field generated by parallel electrodes.*

which gives the value $4.18V/m$. The simulation results of an infinitely long cylinder in a homogenous field are shown in Figure 4.7. The internal macroscopic field is constant across the cross-section A as it is expected, with a value of 4.3V/m which differs by 3% from the analytical solution. This is attributed to the quantisation error caused by the finite mesh. Slightly different results were obtained for a square shape cross-section (d2sqr01 in Figure 4.7). In this case the profile of the electric field intensity through the crystal looks like a concave curve with it maximum value of $4.46V/m$ in the middle of the crystal and minimum values near the crystal surfaces. The maximum value is approximately the same as in the case of circular cross-

section. When the crystal was rotated about 45 degrees the intensity profile became convex with its minimum value $4.6V/m$ in the centre of the crystal (d2sqr02). The results show that there is a slight difference between the circle and square profile. The internal field is not homogenous any more but the values of electric field intensity in the centre of the crystal do not differ more than 4%. More pronounced changes in the intensity profile are expected when the cross-section area is changed from square or circle to a rectangle. It can be seen that the field inside a crystal with a rectangular cross-section and the longer dimension along the electric field is approximately 2.4 times larger ($6.86V/m$) than the field inside the same crystal rotated by 90 degrees so that the short dimension is parallel to the electric field ($2.85V/m$, Figure 4.8). These results confirmed the general conclusion that to maximize sensor sensitivity the dimension along the measured field should be maximized with respect to the other two dimensions.

In a real situation the sensing element is enclosed in a dielectric tubing. Such a situation was simulated with crystals of a rectangular shape as depicted in Figure 4.8. The permittivity of the dielectric tubing was chosen to be 10 and that of the crystal 20. The results clearly show that even in this case the crystal shape still influences the macroscopic field inside the crystal. The effect in this case is not as pronounced as in the case without the tubing. However, the difference between the square profile and the rectangular one is about 18% which may not be negligible.

The results presented, based on the electrostatic field theory, may also be used for low frequency fields when the size of the sensing element is negligible compared to the wavelength of the electromagnetic wave. In such a case the spatial changes of the electric field, across the distance comparable with the sensor size, are negligible, and the electric field can be considered to be homogenous.

The simulations also shed some light on a problem of the measured field perturbation by the dielectric probe. Figures 4.7 and 4.8 show that the electric field changes rapidly in the vicinity of the dielectric object and at distances comparable to the size of the object, it retains the value close to the original field. The fact that the values of the electric field near the electrodes do not reach exactly the original value of 24V/m is caused by the small separation between the electrodes so that the

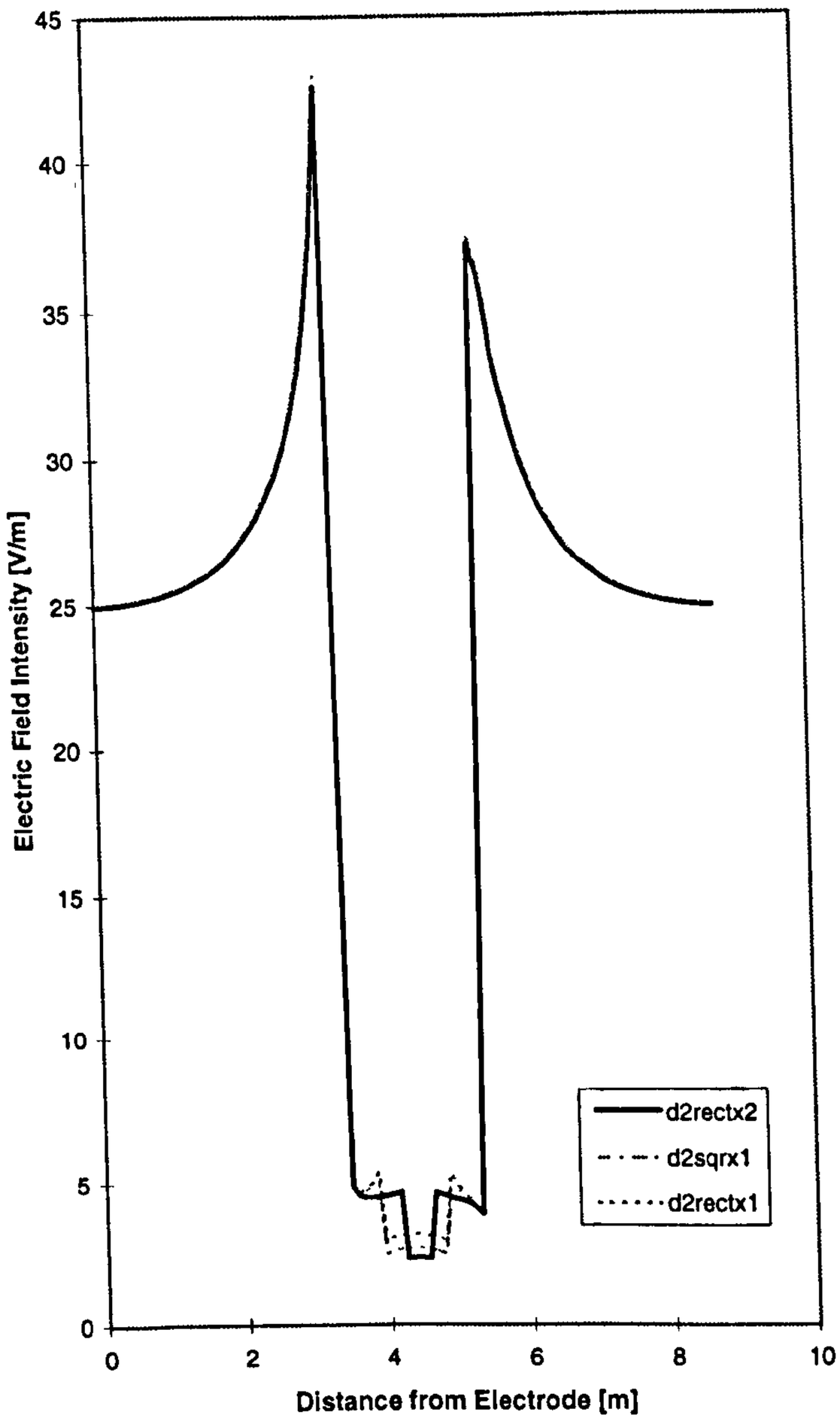

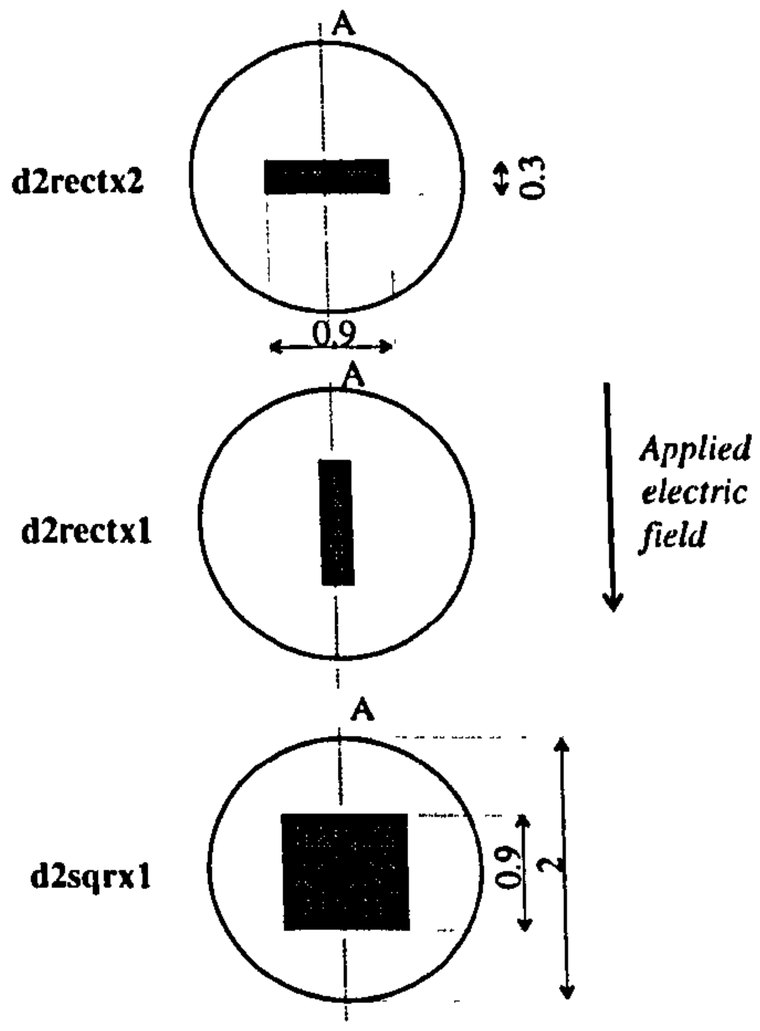

Figure 4.8: Effect of crystal shape on sensor sensitivity. *The crystal* ($\epsilon_r = 20$) *is placed in a dielectric enclosure of permittivity* $\epsilon_r = 10$.

disturbance of the field caused by the crystal extends to the area of the electrodes.

Conclusions. It has been demonstrated that the shape of the electrooptic crystal can influence sensor sensitivity. The effect of crystal shape was found to be not negligible even when a dielectric enclosure of the crystal was present. Using the outcome of this study, crystal shapes for the sensor based on both transverse and longitudinal electrooptic effect were suggested to optimize sensor sensitivity.

4.3.1.3 Effect of Optical Activity on Sensor Sensitivity

Cubic crystals were characterised by the figure of merit K_s which takes into account optical and dielectric properties of the electrooptic crystals. It was pointed out that the defined figure of merit does not account for the optical activity which may be present in some crystal classes. The effect of optical activity on sensor sensitivity and possibilities of minimizing this effect are presented in this section. A theoretical analysis, which uses the concept of Poincare sphere described in section 3.4.2, is supported by experimental results. This subsection thus completes the investigations of factors which influence the magnitude of the electrooptic effect.

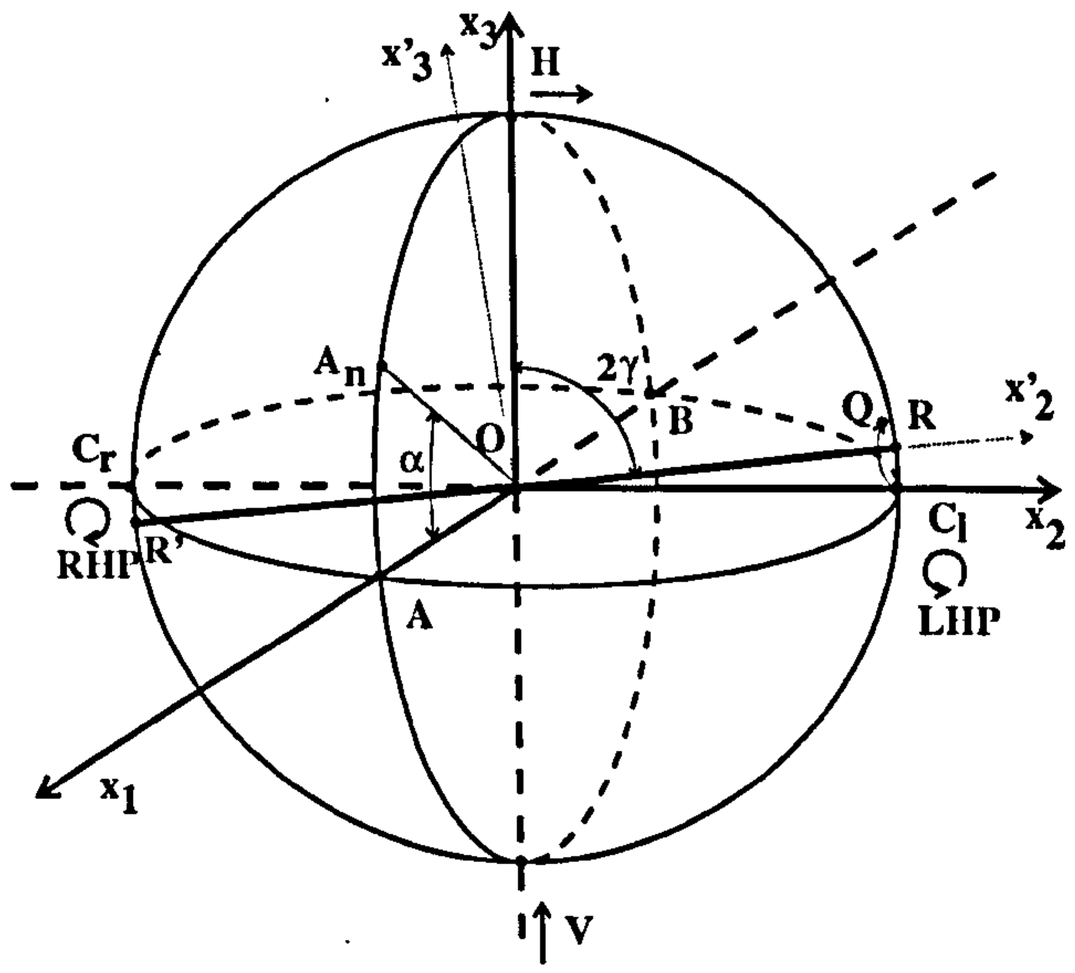

Figure 4.9: Poincare sphere.

Considering the sensor from Figure 4.1 the light incident on the electro-optic crystal is circularly polarized. It can be represented by the point C_l (or C_r) on Poincare sphere depending on the orientation of the quarter-wave plate (Figure 4.9). In the following analysis the left handed circularly polarized light is considered. In the case of pure linear electrooptic effect without optical activity this point rotates around the HV axis by an angle $\Delta = \Gamma l$. The result is the typical output characteristic of the electrooptic sensor (4.1). The optical activity changes the position of the axis of rotation, which according to (3.18) becomes dependent on the pure linear phase shift δ caused by the linear birefringence, and the rotatory power ρ. It should be

noticed that in real situations the values of Γ are of very small value for reasonable values of electric field (3MV/m is the breakdown limit for air). In the presence of a strong optical activity the composite phase difference Δ (3.19) becomes much larger and since $\rho \gg \Gamma$ the angle 2γ approaches 90° and the axis of rotation $\mathbf{RR'}$ gets very close to the $\mathbf{C}_l\mathbf{C}_r$ line. The consequence of the dominant optical activity is decreased sensitivity of the sensor because the point representing the polarisation of the light leaving the crystal moves in the vicinity of $\mathbf{C}_l$ and, therefore, is not causing large changes in intensity (3.21). It is possible to determine the sensor output light intensity expressing (3.21) as a function of δ, ρ and l. The task is tedious but straightforward. The left handed circularly polarized light is represented by point $\mathbf{C}_l = (0, 1, 0)$. The polarisation of the light leaving the crystal is found by rotation of $\mathbf{C}_l$ around the $\mathbf{RR'}$ axis by the angle of composite phase difference Δ. It is accomplished by transforming $\mathbf{C}_l$ into a new coordinate system $x_1'x_2'x_3'$ ($\mathbf{C}_l'$) in which $x_1 = x_1'$ and x_3' coincides with $\mathbf{RR'}$:

$$\mathbf{C}_l' = \begin{pmatrix} 1 & 0 & 0 \\ 0 & \cos 2\gamma & \sin 2\gamma \\ 0 & -\sin 2\gamma & \cos 2\gamma \end{pmatrix} \begin{pmatrix} 0 \\ 1 \\ 0 \end{pmatrix} \tag{4.16}$$

In the primed coordinates the rotation around $\mathbf{RR'}$ is simply achieved by applying rotation matrix around x_3'. The result is a point $\mathbf{Q'}$ representing polarization of the light behind the electrooptic crystal.

$$\mathbf{Q'} = \begin{pmatrix} \cos\Delta & -\sin\Delta & 0 \\ \sin\Delta & \cos\Delta & 0 \\ 0 & 0 & 1 \end{pmatrix} \mathbf{C}_l' \tag{4.17}$$

To obtain the representation of $\mathbf{Q'}$ in $x_1x_2x_3$ coordinates the inverse transformation is applied:

$$\mathbf{Q} = \begin{pmatrix} 1 & 0 & 0 \\ 0 & \cos 2\gamma & -\sin 2\gamma \\ 0 & \sin 2\gamma & \cos 2\gamma \end{pmatrix} \mathbf{Q'} \tag{4.18}$$

Finally, knowing the representation of the light beam behind the crystal and that of the analyzer (point $\mathbf{A}_n$ on Poincare sphere characterized by an angle α in Figure 4.9), the light intensity after the analyzer I can be expressed using (3.21) as:

$$I = \frac{1}{2}(1 - \sin\Delta\cos 2\gamma\cos\alpha + \cos\Delta\sin 2\gamma\cos 2\gamma\sin\alpha - \sin 2\gamma\cos 2\gamma\sin\alpha) \quad (4.19)$$

Taking the sensor sensitivity sns as the slope of the transfer characteristic for electric field intensity $E = 0$, it can be written as

$$sns = \left.\frac{\partial I}{\partial E}\right|_{E=0} = \left.\frac{\partial I}{\partial \Gamma}\frac{\partial \Gamma}{\partial E}\right|_{E=0} \quad (4.20)$$

where the term $(\partial\Gamma/\partial E)|_{E=0}$ is a constant for a given material and orientation, and characterises the sensitivity of the sensor without optical activity. For the purpose of this work it is sufficient to define the relative sensitivity RS as sensor sensitivity normalized to the sensitivity without optical activity:

$$RS = \left.\frac{\partial I}{\partial \Gamma}\right|_{\Gamma=0} = \left.\frac{1}{l}\frac{\partial I}{\partial \delta}\right|_{\delta=0} = \frac{\sin(2\rho l - \alpha) + \sin\alpha}{2\rho l} \quad (4.21)$$

The relative sensitivity RS is a function of rotatory power ρ, crystal length l and angle α which characterises the position of the analyzer. Therefore, one can find the angle of the analyzer α_{optim} for which RS is maximized:

$$\alpha_{optim} = \frac{\rho}{2}l + j\frac{\pi}{2}, \quad j = 0, 1, 2, \ldots \quad (4.22)$$

The angle α_{optim} is measured from the axis which is at 45 degrees to the induced fast and slow axis of the crystal. It should be noticed that the real angle of the analyzer rotation is twice the angle α. Substituting (4.22) into (4.21), the maximum relative sensitivity for a given crystal length is found to be:

$$RS = \frac{\sin(\rho l)}{\rho l} \quad (4.23)$$

The equation (4.23) shows that the presence of the optical activity always decreases sensor sensitivity since the function $\sin x/x \leq 1$. It is apparent that the sensitivity may also be maximized with respect to crystal length. The calculated optimal length l_{optim} can be expressed as:

$$l_{optim} = \frac{\pi}{2\rho} + k\frac{\pi}{\rho}, \quad k = 0, 1, 2, \ldots \quad (4.24)$$

Simulation results

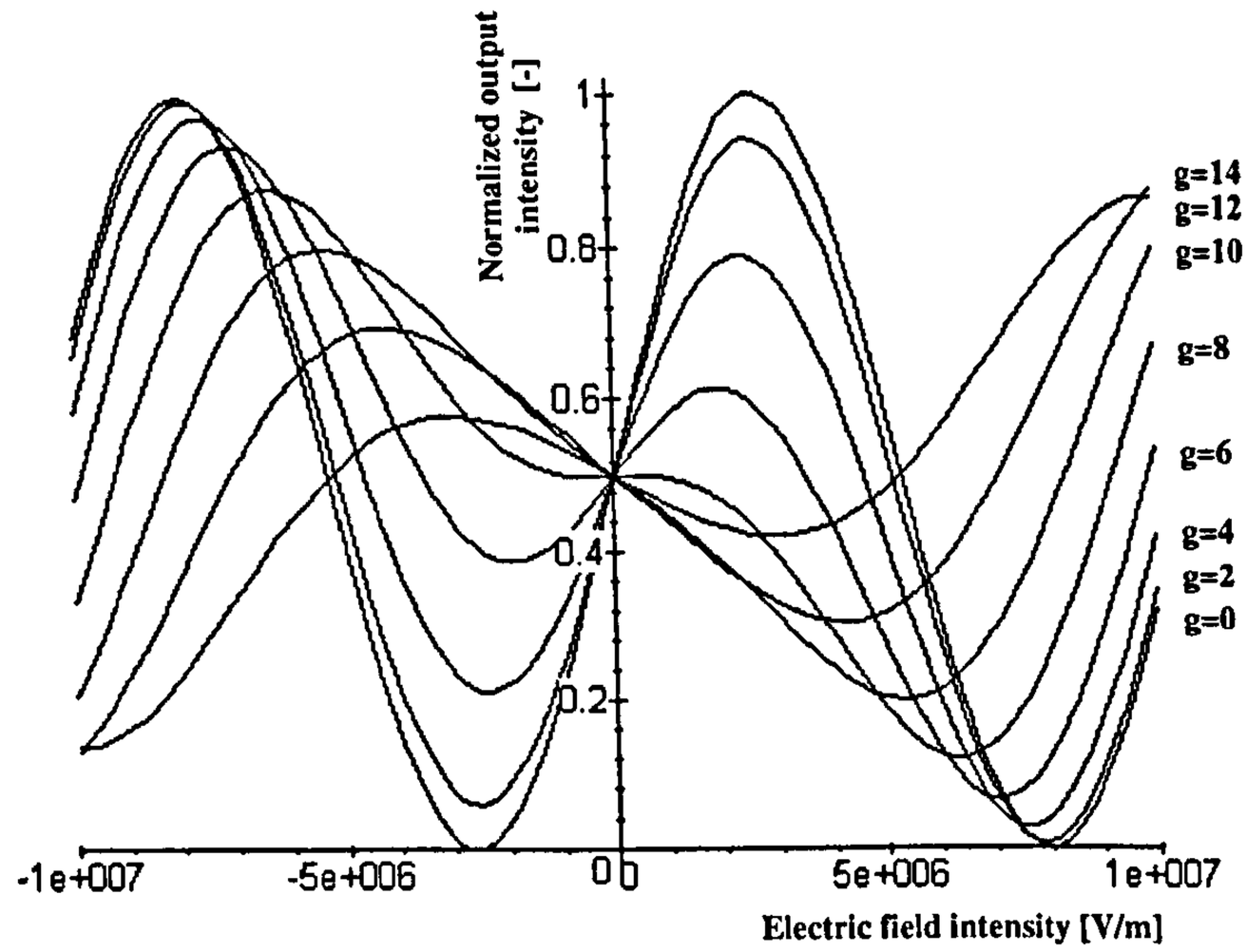

Figure 4.10: Transfer characteristics of the electro-optic sensor for different values of the gyration factor g.

The obtained theoretical results were verified by numerical simulations using the mathematical model described in section 4.2. The calculations were carried out using data for a 10x10x5mm crystal of Bismuth Germanium Oxide ($Bi_{12}GeO_{20}$, 23 point group) at $\lambda = 633nm$. The optical activity in the model was characterized by a gyration factor g [9] which is related to the rotatory power as $g = \rho\lambda n/\pi$ where n is the refractive index and λ the optical wavelength.

The effect of the optical activity was studied by changing the gyration factor g and observing the sensor output. The results in Figure 4.10 clearly show that the optical activity have a pronounced effect on sensor transfer characteristic. Figure 4.11 shows simulated relative sensitivity RS of the sensor as a function of gyration factor. The graph (a) corresponds to the situation when the position of the analyzer and the length of the crystal are fixed. It is apparent that by increasing g the sensor sensitivity periodically becomes zero with a generally decreasing tendency. The graph corresponds to equation (4.21) for a position of the analyzer characterized by angle $\alpha = 0$. Graph (b) shows the relative sensitivity RS for the optimized position of the analyzer, when $\alpha = \alpha_{optim}$. The curve is in agreement with equation (4.23).

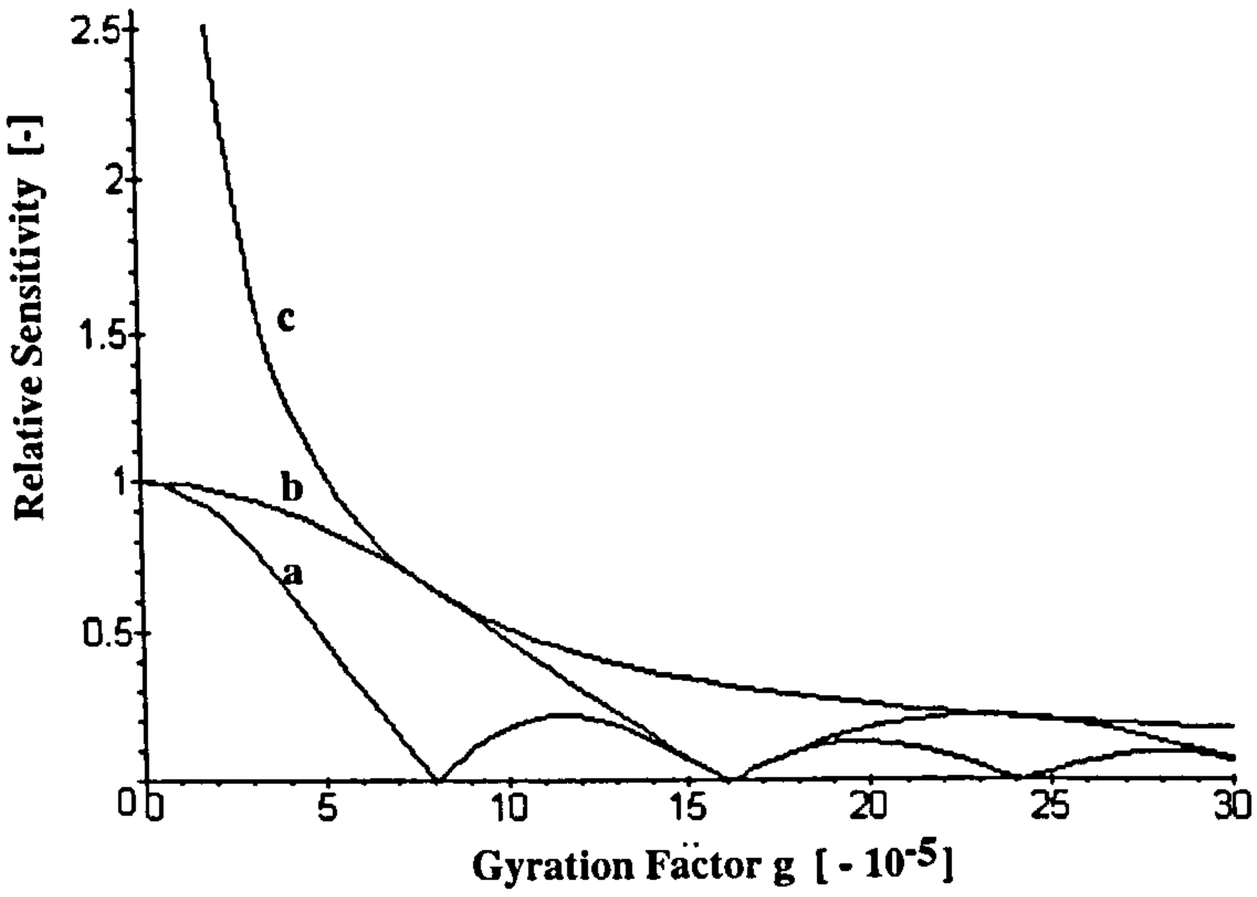

Figure 4.11: Relative sensitivity as a function of gyration factor g. *a - fixed crystal length and analyzer, b - fixed crystal length, analyzer position optimized, c - sensor sensitivity for the optimal length and optimal position of the analyzer, normalized to the sensitivity of 10mm long BGO crystal without optical activity.*

Figure 4.12 shows the sensor sensitivity as a function of the crystal length. In this simulation the analyzer was set according to equation (4.22) to maximize sensor response. The sensitivity is clearly a periodic function of crystal length and again in agreement with the theoretical result given by (4.24). Finally, the graph (c) in Figure 4.11 depicts the situation when both the length of the electrooptic crystal and the position of the analyzer are optimized. The feasibility of the crystal length optimization depends on the required size of the probe and the magnitude of the rotatory power. It may not be always possible to optimize the length of a crystal, as the crystal may become impractically long. The relative sensitivity RS for the optimal length l_{optim}, the RS is equal to $2/\pi \approx 0.64$, which corresponds to the first intersection of graphs (b) and (c).

Measurements

The theoretical predictions were verified by experiments carried out with Bismuth Germanium Oxide crystal (23 point group). The figure of merit K_m (4.12) of 16.24mm long crystal of BGO was measured at three different wavelengths. The

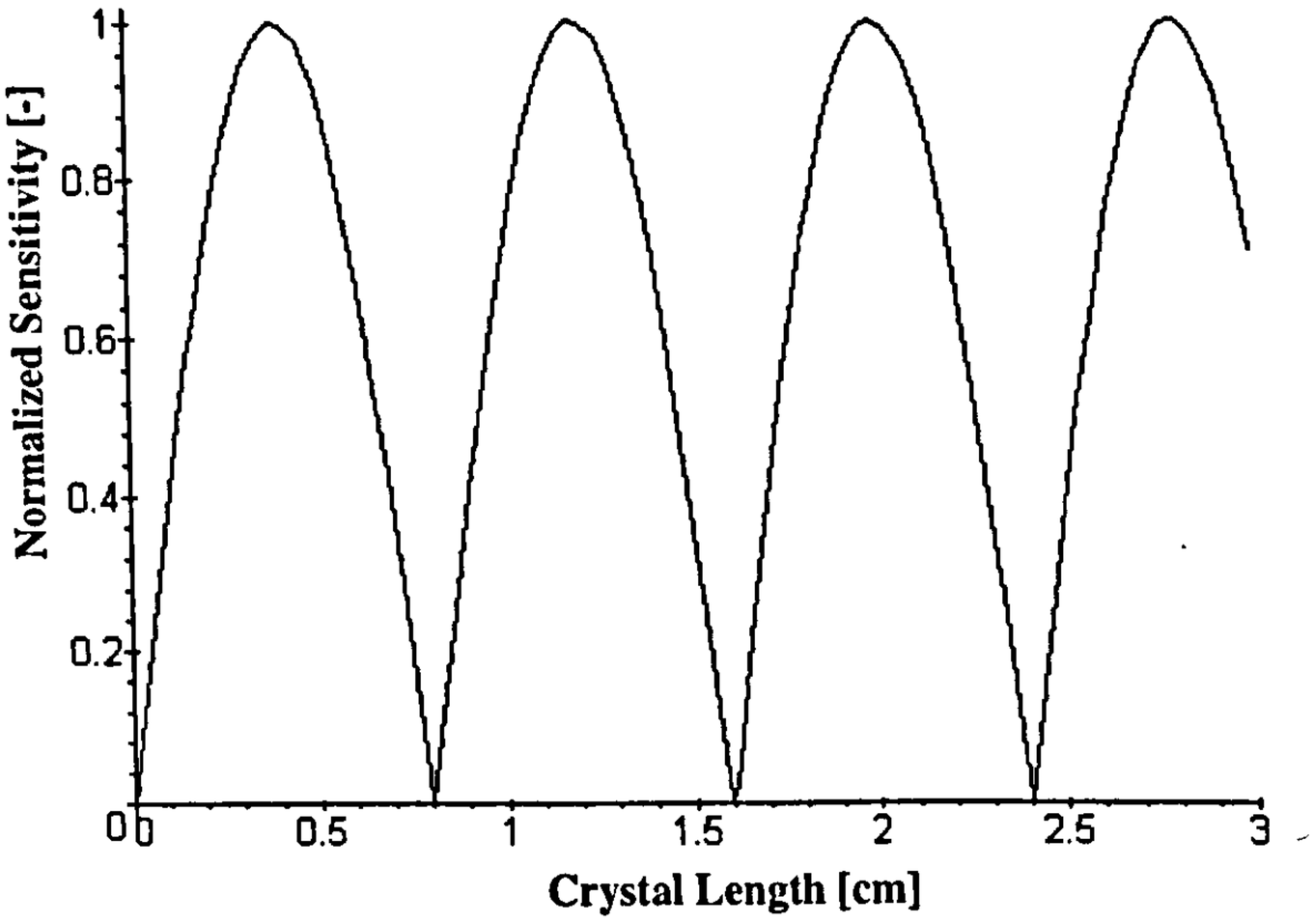

Figure 4.12: Normalized sensitivity versus crystal length.

results displayed in Table 4.1 also contain measured values of the rotatory power and calculated relative sensitivity. As the measurements of the rotatory power were ambiguous due to the large crystal length, the results were compared with those in reference [50] to determine the true values of ρ.

The measured absolute values of K_m are much smaller than one would expect for one of the suitable crystal cuts [58], even after corrections for optical activity. This was attributed to the crystallographic orientation of the sample that was not known. However, it is possible to compare relative values. The figure of merit K_m is highest at 1296nm, very small at 854 and rising again at 689nm. Without the optical activity, K_m should decrease with wavelength according to equation (4.12). This evidently does not happen as the figure of merit does not account for the effect of optical activity. The measured values can be explained on the basis of the results

Table 4.1: Measured Figure of Merit K_m, rotatory power ρ and calculated relative sensitivity RS.

BGO	Wavelength		
	689nm	854	1296
$K_M[\mu rad/V]$	5.8	0.3	14.8
$\rho[rad/mm]$	0.2899	0.2118	0.1237
$RS[-]$	0.212	0.085	0.4508

obtained. The calculated relative sensitivity RS shows that the optical activity should have the strongest influence on the sensor at 854nm and the smallest at 1296nm which is in agreement with the measured K_m. The ratios of K_m at different wavelength are also in reasonable agreement with ratios for relative sensitivity RS.

Conclusions. The optical activity present in 23 point group cubic crystals was found to have a strong influence on the sensor sensitivity. It was shown that in the presence of a circular birefringence, the sensitivity of the sensor is decreased by the factor of $\sin(\rho l)/(\rho l)$. The effect can be minimized by choosing optimal length of the crystal and by aligning the analyzer to maximal response. The theoretical results obtained using the concept of Poincare sphere are in agreement with the simulations based on electromagnetic theory as well as the results reported in [21] and [45]. The results of measurements of figure of merit K_m in Bismuth Germanium Oxide ($Bi_{12}GeO_{20}$) electro-optic modulator at three different wavelengths were also found in agreement with the theoretical results obtained.

4.3.2 Internal Space Charge Effect

In this section the effect of a finite resistivity of the electrooptic crystals on the ELF and DC field sensor is presented. It is shown that the most important criterion for building a DC field sensor is the requirement of a high resistivity of the electrooptic crystal and an elimination of the photoconductivity effect in the crystal. Based on the analysis carried out, suitable crystals are selected for the DC and ELF electric field sensor.

When a crystal of a finite resistivity is exposed to a static electric field, the free charge carriers start drifting along the electric field lines and accumulate on crystal boundaries. The accumulated space charge generates an electric field with orientation opposite to the original internal field. Therefore, the resultant field, which is a superposition of the original field and the field of accumulated space charge, continuously decreases. The speed of this process depends on the density of free charge carriers which is proportional to crystal conductivity. A detailed analysis shows (appendix A) that the internal macroscopic field $E_m(t)$ in a crystal exposed

to a static external field, decays exponentially as

$$E_m(t) = E_{m0}e^{-\frac{t}{\tau}} = E_{m0}e^{-\frac{\sigma}{t\epsilon_r\epsilon_0}} \tag{4.25}$$

where ϵ_r, ϵ_0 are the crystal relative permittivity and permittivity of vacuum, respectively, σ is the crystal specific conductivity, and

$$\tau = \frac{\epsilon_r\epsilon_0}{\sigma} \tag{4.26}$$

is the *charge relaxation time constant*. Since the electrooptic effect is caused by the internal electric field, the sensor output does not correspond to the measured static field but to the decaying internal field. It is evident that if the crystal is not to be rotated, the conductivity of the electrooptic crystal needs to be considered in the first place. Its low value can make the crystal unsuitable for low frequency and DC field sensing.

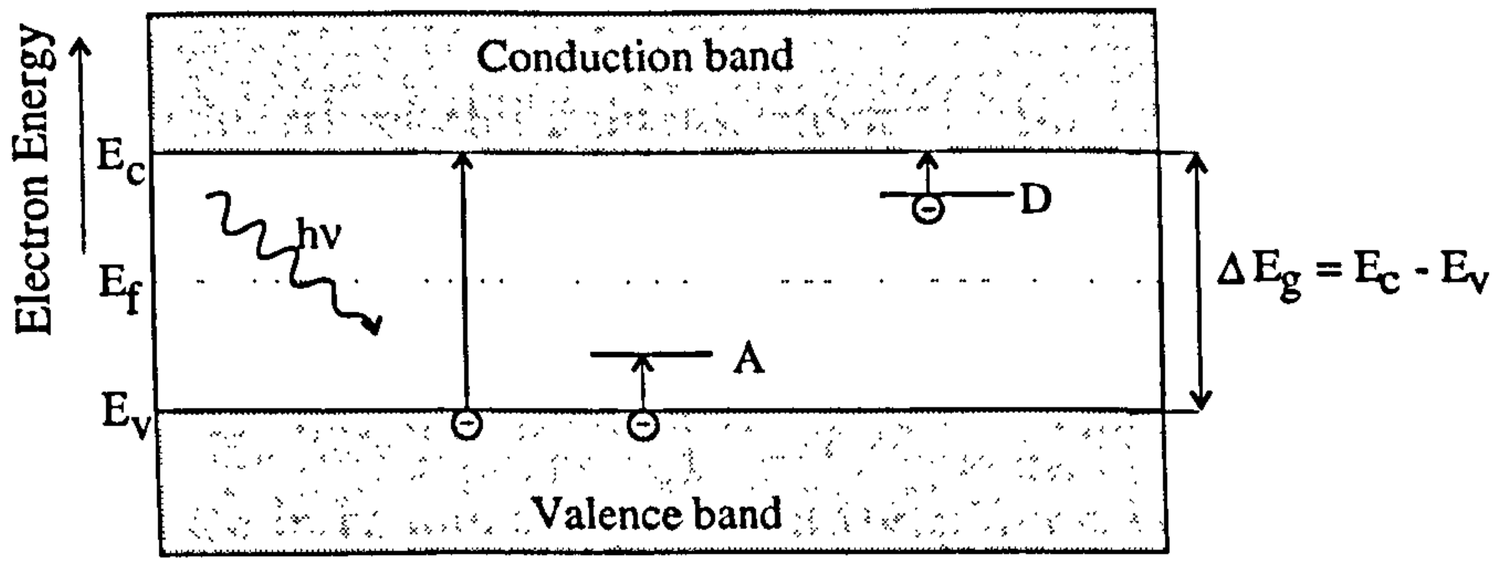

Figure 4.13: Energy band structure of insulators and semiconductors. *Optical excitation (photons with energy $h\nu$) of the electrons from the valence band to conduction band or acceptor levels (A) and excitation of the electron from donor levels (D) to the conduction band is the source of the charge carriers in photoconductivity. E_c, E_v, E_f are energies of the bottom of conduction band, top of valence band and Fermi energy, respectively. The bandgap of the material is defined as $\Delta E_g = E_c - E_v$.*

Most of the electrooptic crystals are dielectrics. It means either semiconductors or insulators. According to the energy band theory of solids [4], the conductivity of these materials is caused by a thermal excitation of free charge carriers. It depends on the temperature, concentration of lattice defects, and the bandgap of the material. The lowest conductivity of a crystal is the conductivity in the absence of lattice

defects (e.g. impurities and dislocations), so called intrinsic conductivity, when the charge carriers are generated by a thermal excitation of electrons from the valence band to the conduction band (Figure 4.13). The larger the bandgap of the material the higher its resistivity. The conductivity of the crystal is strongly influenced by impurities and other defects. They cause the appearance of allowed energy levels in the forbidden band (energy levels A,D in Figure 4.13) which decreases the activation energy of free carriers generation and therefore increases the conductivity. To maximize the charge relaxation time constant so that it is possible to measure DC field, the electrooptic crystals must be of highest quality, free of impurities and other lattice defects, preferably with a wide bandgap.

Another source of free charge carriers inside crystals can be the photoconductivity effect. In this case the excitation energy necessary to generate the carriers is supplied by a flux of photons with energies $h\nu$, where ν stands for frequency of light and h for the Plank constant. In intrinsic materials, the photon energy must be enough to excite electrons from valence band to the conduction band, i.e. $h\nu \geq \Delta E_g$. The wavelength of the light at which the photon energy is equal to the bandgap energy defines intrinsic absorption edge and is shown in table 4.2 as a critical wavelength λ_c for selected electrooptic crystals. At wavelengths $\lambda < \lambda_c$ the laser radiation is strongly absorbed in the crystal. This strong absorption is accompanied by increase in conductivity due to the photoconductivity effect. The critical wavelength represent a limit for the wavelength of optical sources used in the sensor and, therefore, a limit for the sensor sensitivity since the figure of merit K_s (see equation 4.13) is indirectly proportional to λ_c. It is evident that the critical wavelength represents not only limitation for the DC field sensor due to the photoconductivity effect but also for AC field sensors due to the strong absorption of the light beam. The critical wavelengths λ_c in table 4.2 were calculated using available data on bandgaps of the selected crystals.

Real electrooptic crystals are often far from perfect and contain defects such as impurities and dislocations. These defects are demonstrated as discrete energy levels or even thin bands in the band gap (Figure 4.13). The electrons can be excited into and from these energy levels by photons with energies less than the

band gap. Therefore, in imperfect crystals the free charge carriers can be generated by the photoconductivity effect at wavelengths $\lambda > \lambda_c$ depending on the density of the defects and the position of the defect levels in the bandgap. In this case the photoconductivity effect present the limitation to the DC field sensor but not for the AC field sensor as the light absorption is not very strong. An example of this effect is shown in Figure 4.14. The frequency response of the electrooptic sensor with Zinc Sellenide as shown in Figure 4.1, was measured in the frequency range 0.2-100Hz. The electric field was generated by parallel plane electrodes connected to an AC voltage source. The frequency response at the wavelengths of 660 and 685nm is clearly influenced by the photoconductivity effect. The effect is most pronounced at the wavelength of 660nm and is fully eliminated in the same frequency range using the wavelength of 1310nm.

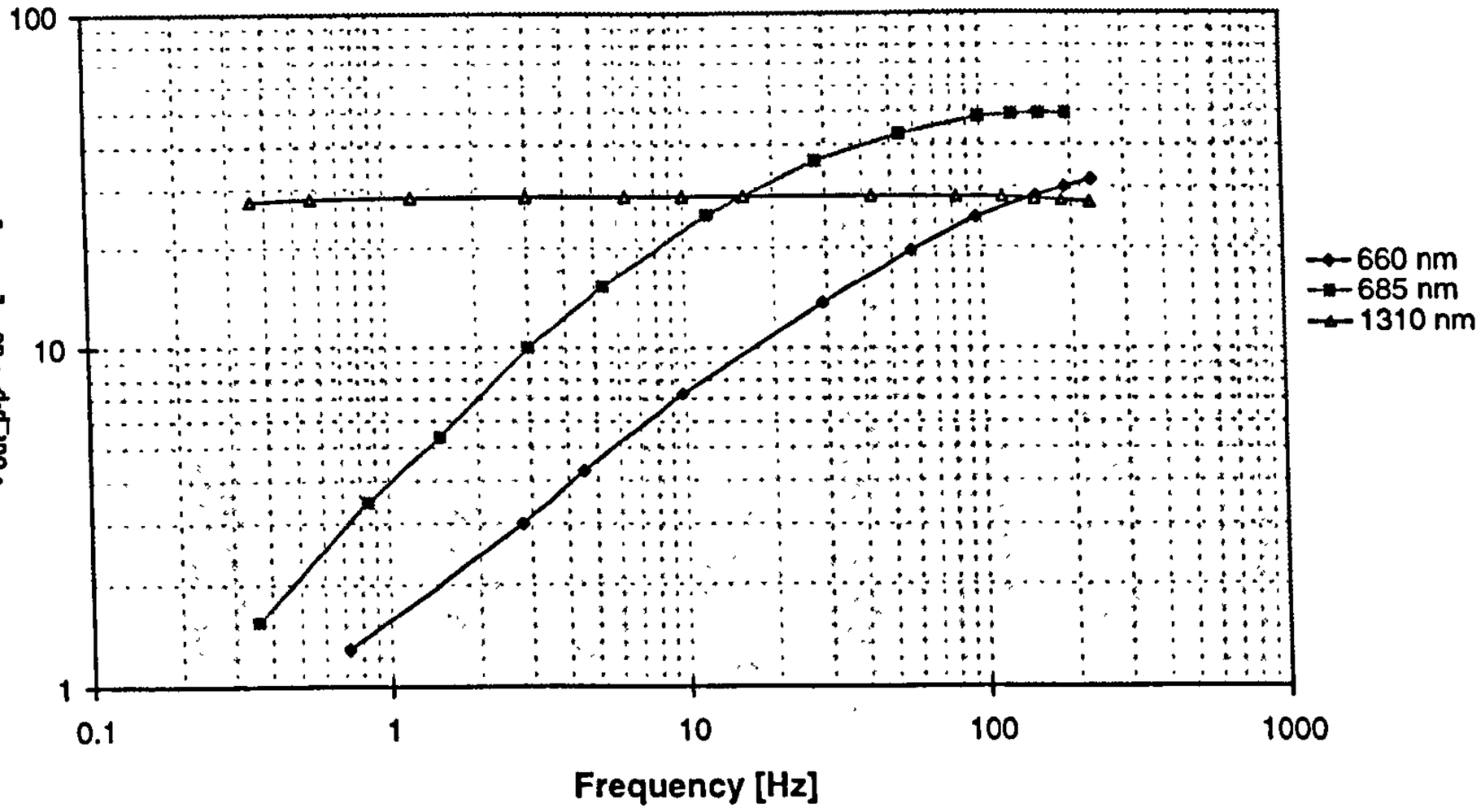

Figure 4.14: Frequency responce of the sensor with Zinc Selenide. $V_{out.p-p}$ *is the peak-to-peak output voltage and* V_{dc} *is the DC output voltage. The applied electric field is* $E_{rms} = 47.4kV/m$. *The photoconductivity effect is eliminated at the wavelength of 1310nm in the measured frequency range.*

The relaxation time constant τ (4.26), sometimes called Maxwellian relaxation time constant, was used to estimate the effect of crystal conductivity on an electrooptic sensor at DC and low frequencies. Application of the Laplace transformation on a system characterized by time constant τ as in (4.25) gives a limit frequency of $f_{3dB} = 1/(2\pi\tau)$, at which the sensor response is decreased by 3dB. Cadmium Tel-

Table 4.2: Point group symmetry, critical wavelength λ_c, specific conductivity σ, relative permittivity ϵ_r, and charge relaxation time constant τ in selected cubic crystals and Lithium Niobate (LN).

	CdTe	*GaAs*	*GaP*	*ZnS*	*ZnSe*	*ZnTe*	*BG*	*BSO*	*BGO*	*LN*
symmetry	$\bar{4}3m$	$\bar{4}3m$	$\bar{4}3m$	$\bar{4}3m$	$\bar{4}3m$	$\bar{4}3m$	$\bar{4}3m$	23	23	3m
$\lambda_c[nm]$	862	920	552	345	480	549	-	394	394	350
$\sigma[S/m]$	10^{-8}	10^{-5}	-	10^{-8}	10^{-6}	10^{-7}	10^{-13}	10^{-9}	2.10^{-12}	10^{-16}
$\epsilon_r[-]$	9.6	13.2	10	8.3	9.1	10.1	16	40	56	85
$f_{3dB}[Hz]$	20	14469	-	11	198	18	10^{-4}	0.56	6.10^{-4}	2.10^{-8}
$\tau[s]$	0.08	10^{-5}	-	0.01	8.10^{-4}	0.009	1380	0.28	248	7.10^{6}

luride (CdTe), for example, with its conductivity $10^{-8}S/m$, has the estimated limit frequency of 20Hz, and at frequencies below this value, the internal electric field intensity decreases rapidly due to the crystal conductivity.

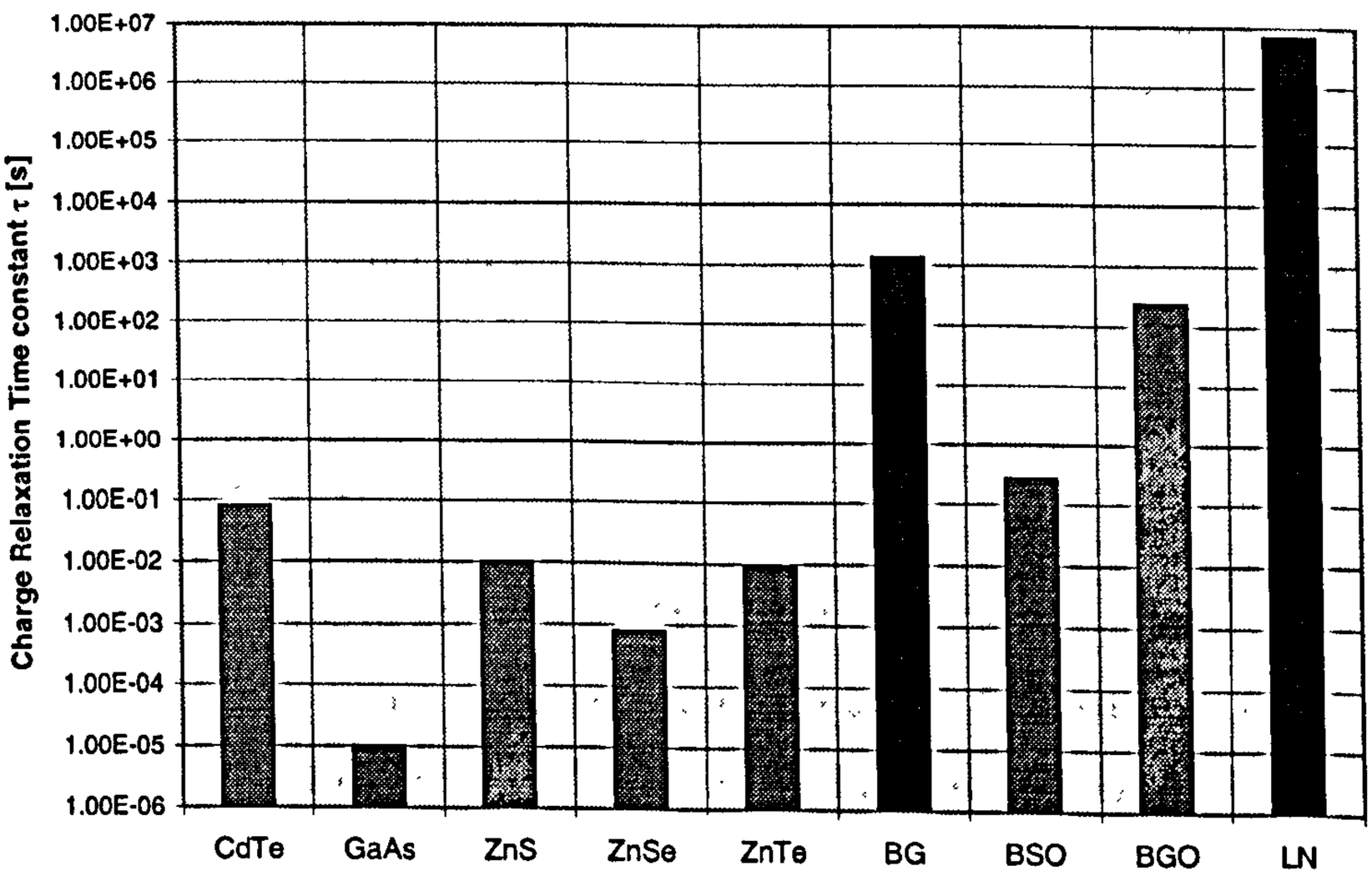

Figure 4.15: Charge relaxation time constant τ of selected cubic crystals and Lithium Niobate (LN).

Table 4.2 shows conductivity of selected electrooptic crystals together with their relative permittivities, and calculated limit frequencies and charge relaxation time constants which are also plotted separately in Figure 4.15. The low values of time constants imply that crystals like gallium arsenide ($GaAs$), gallium phosphide (GaP) and zinc selenide ($ZnSe$) are theoretically not suitable for DC and low frequency applications. ZnS, $ZnTe$ and $CdTe$ have relatively high resistivity but they

are still unsuitable for DC applications. They can be used for ELF applications because of their relatively low limit frequencies but the decay of the DC internal electric field due to the conductivity effect is still very fast.

Conclusions. From the beginning the process of crystal selection was mainly concentrated on cubic crystals because of their excellent features such as low permittivity and the absence of the natural birefringence, pyroelectricity and optical activity (only $\bar{4}3m$ group symmetry). The analysis of the conductivity effect, however, showed that the semiconductor cubic crystals have relatively small resistivity values. Only Bismuth Germanate which is an insulator seemed to have sufficiently low conductivity for DC field measurements. From other crystal classes only $LiNbO_3$ has been identified as a crystal with high enough resistivity suitable for DC and ELF measurements. Since the conductivity effect influences the functionality of the electrooptic sensor and because the problem of both internal and external space charge should be solved without a physical rotation of the crystal, Lithium Niobate ($LiNbO_3$) and Bismuth Germanate ($Bi_4Ge_3O_{12}$) were selected as suitable crystals for the DC and ELF electrooptic field sensor.

4.3.3 Summary

This section was focused on the selection of an electrooptic crystal suitable for both DC and ELF field measurements. A new figure of merit was defined and used to compare selected electrooptic crystals. Zinc Telluride, Zinc Sulphide and Zinc Sellenide were found to be the most sensitive to the applied electric field. It was also found that the shape of the electrooptic crystal and its enclosure can influence the sensitivity of the sensor. The investigation of the effect of crystal geometry showed that different crystal shapes should be used for transversal and longitudinal electrooptic effect in order to maximize the sensor sensitivity. As a part of the analysis of the sensor sensitivity , the effect of the optical activity on the sensitivity of the sensor was also investigated. Theoretically, it has been shown that the optical activity, which is present in cubic crystals of 23 point group, always decreases the sensitivity of the sensor. Applying the concept of Poincare sphere to the problem

of light propagation in the electrooptic sensor, the conditions for maximum sensor sensitivity were derived, i.e. optimal length of the crystal and the optimal position of the analyzer. These findings were verified experimentally using an optically active crystal of Bismuth Germanium Oxide.

Apart from analysing the sensitivity of different cubic crystals to the electric field, the effect of crystal conductivity and photoconductivity effect were also investigated. The conductivity effect was characterised by a charge relaxation time constant. This time constant was evaluated for the available cubic electrooptic crystals. Most of the cubic crystals were found to have a high conductivity and, therefore, the associated charge relaxation time constant was too low for the crystals to be successfully used in an electrooptic field sensor, without the necessity to rotate the sensing element. Theoretically, only Bismuth Germanate, which has a very weak electrooptic effect, showed relatively high time constant (20 minutes). Since the time constant was found to be the most important criterion in a DC field sensor, the attention was turned to other electrooptic crystals trying to identify the most suitable crystal, with high enough time constant for DC field measurements. Finally, it was found that the cubic crystal of Bismuth Germanate and non-cubic crystal of Lithium Niobate are the most appropriate crystals to be used as a sensing element for DC field measurements.

4.4 ELF and DC Electric Field Sensor

In the previous section the crystals of Bismuth Germanate and Lithium Niobate were selected as suitable materials for DC and ELF electrooptic sensor. The following section starts with a basic analysis of the electrooptic effect in $LiNbO_3$ and $Bi_4Ge_3O_{12}$ crystals. Appropriate directions of the laser beam propagation and of the measured electric field are determined with respect to the crystallographic orientation of the crystals (section 4.4.1). Sections 4.4.2 and 4.4.3 reports on experimental results obtained with both electrooptic crystals in measurements of extra low frequency electric fields and in DC field measurements.

4.4.1 Electrooptic Effect in Bismuth Germanate and Lithium Niobate

Bismuth germanate is an isomorph of the naturally occurring mineral eulite $Bi_4Si_3O_{12}$. It is a cubic crystal with $\bar{4}3m$ point group symmetry. The crystal has no natural birefringence, no pyroelectricity or optical activity. It is transparent throughout the visible and the near infrared regions.

The theoretical analysis of the electrooptic effect in cubic crystals, carried out by Namba in 1961 [58], showed that the cubic crystals are suitable both for a longitudinal (electric field parallel to the light beam) and for a transversal (field perpendicular to the light beam) electrooptic effect. Table 4.3 shows the induced phase retardation Γ for suitable directions of the electric field in terms of the crystal length l in the direction of the light beam, applied electric field E, and the figure of merit K_s defined by (4.13).

Table 4.3: Phase retardation between two eigenwaves Γ for different orientations of electric field and laser beam in cubic crystals as a function of sensor figure of merit K_s, crystal length l in the direction of the light beam, and applied electric field E. *The directions of the applied electric field and beam propagation are described by Miller indices in the subscripts ([4], Figure 4.52).*

$E_{<001>}$ case1	$E_{<001>}$ case2	$E_{<110>}$ case3	$E_{<111>}$ case4
$\Gamma_{<001>} = lK_sE$	$\Gamma_{<110>} = \frac{1}{2}lK_sE$	$\Gamma_{<\bar{1}10>} = lK_sE$	$\Gamma_{(111)} = \frac{\sqrt{3}}{2}lK_sE$
longitudinal effect	transversal effect	transversal effect	transversal effect

It can be seen that for cubic crystals the largest phase retardation and thus the sensitivity is achieved for an electric field in <001> direction in the longitudinal effect, and for an electric field in <110> direction in the transverse effect. The transverse effect was chosen for practical reasons, such as easy manipulation during experiments and electric field generation.

Lithium Niobate is an optically anisotropic ferroelectric crystal of $3m$ point group [7] transparent from 0.4 to $5\mu m$. Its Curie temperature is between 1070 and $1190°C$ depending on the method of crystal preparation [16]. It is an optically uniaxial crystal (its index ellipsoid is a rotational ellipsoid) and possesses a strong natural

Table 4.4: Electrooptic properties of $LiNbO_3$ (class $3m$). *The r_{51}^2 terms have been deleted from the expressions since they appear as higher order effects. l is the crystal length along the direction of the light beam, d is the thickness in field direction, $V = Ed$ is the applied voltage, n_o the ordinary index of refraction, n_e the extraordinary index of refraction (taken from [5]).*

Induced Retardation Γ	$E\|\|x_1$	$E\|\|x_2$	$E\|\|x_3$
$light\|\|x_1$		$\Gamma = \frac{\pi l_1 V_2 n_o^3 r_{22}}{\lambda_0 d_2}$	$\Gamma = \frac{\pi l_1 V_3}{\lambda_0 d_3}(n_o^3 r_{33} - n_o^3 r_{22})$
$light\|\|x_2$		$\Gamma = \frac{\pi V_2 n_o^3 r_{22}}{\lambda_0}$	$\Gamma = \frac{\pi l_2 V_3}{\lambda_0 d_3}(n_o^3 r_{33} - n_o^3 r_{22})$
$light\|\|x_3$	$\Gamma = \frac{2\pi l_3 V_1 n_o^3 r_{22}}{\lambda_0 d_1}$	$\Gamma = \frac{2\pi l_3 V_2 n_o^3 r_{22}}{\lambda_0 d_2}$	$\Gamma = 0$

birefringence and pyroelectricity which can cause a strong temperature instability of the sensor (section 6.3).

The analysis of electrooptic effect in $3m$ point group crystals was summarised by Lenzo et al. in [50] and can be found in table 4.4. The inspection of the table shows that both the longitudinal and transverse electrooptic effects are possible. However, only for the laser beam along the x_3 axis it is possible to avoid the natural birefringence. In all other directions of the beam the crystal shows the natural birefringence which causes a strong output dependence on the temperature (section 6.3). The sensor based on such an orientation of the crystal would act rather as a temperature sensor than electric field sensor.

If the laser beam is directed along the optical axis x_3, the crystal of Lithium Niobate behaves ideally as an isotropic media with no natural birefringence. According to the table only the transverse electrooptic effect is possible for this beam orientation because the field applied along x_3 does not induce any phase retardation. This transverse effect orientation has another advantage. Due to the pyroelectric effect (section 3.3.4.) in $3m$ cubic crystals, temperature variations cause changes in the polarization vector in the direction of the optical axis x_3. This effect is very strong. In Lithium Niobate crystal, a temperature change of $1°C$ induces a change in polarization of magnitude $40\mu Cm^{-2}$, which corresponds to a change in internal electric field intensity of $\approx 160kV/m$ [8]. Ideally, the induced electric field is oriented exactly in the direction of the x_3 axis and does not induce any phase shift between the two eigenwaves propagating in the same direction and, therefore, has

no influence on the output of the sensor. Thus the effect of the pyroelectricity on sensor output can be theoretically eliminated. The transverse electrooptic effect with laser beam along the x_3 axis was chosen for the electrooptic sensor based on Lithium Niobate.

Conclusions. It was shown that both longitudinal and transverse electrooptic effect can be used in a sensor with Lithium Niobate and Bismuth Germanate. The maximum magnitude of the effects in the crystal of Bismuth Germanate is the same for both orientations of the electric field. For practical reasons, it was decided to use the transverse electrooptic effect for sensor constructed using Bismuth Germanate. The transverse effect was also chosen for sensor constructed with Lithium Niobate to avoid spurious effects of crystal natural birefringence and pyroelectricity.

4.4.2 Extra-low-frequency Field Measurements

The performance of the chosen electrooptic crystals was first investigated for extra-low-frequency electric field measurements. The measured frequency characteristics of the sensor from Figure 4.1, with crystals of LN and BG, are depicted in Figures 4.16 and 4.17. The electric field in the experiments was generated by parallel plate electrodes connected to an AC voltage source. Both characteristics are flat in the frequency range from 0.3 to 200 Hz. There is no observable effect of the conductivity

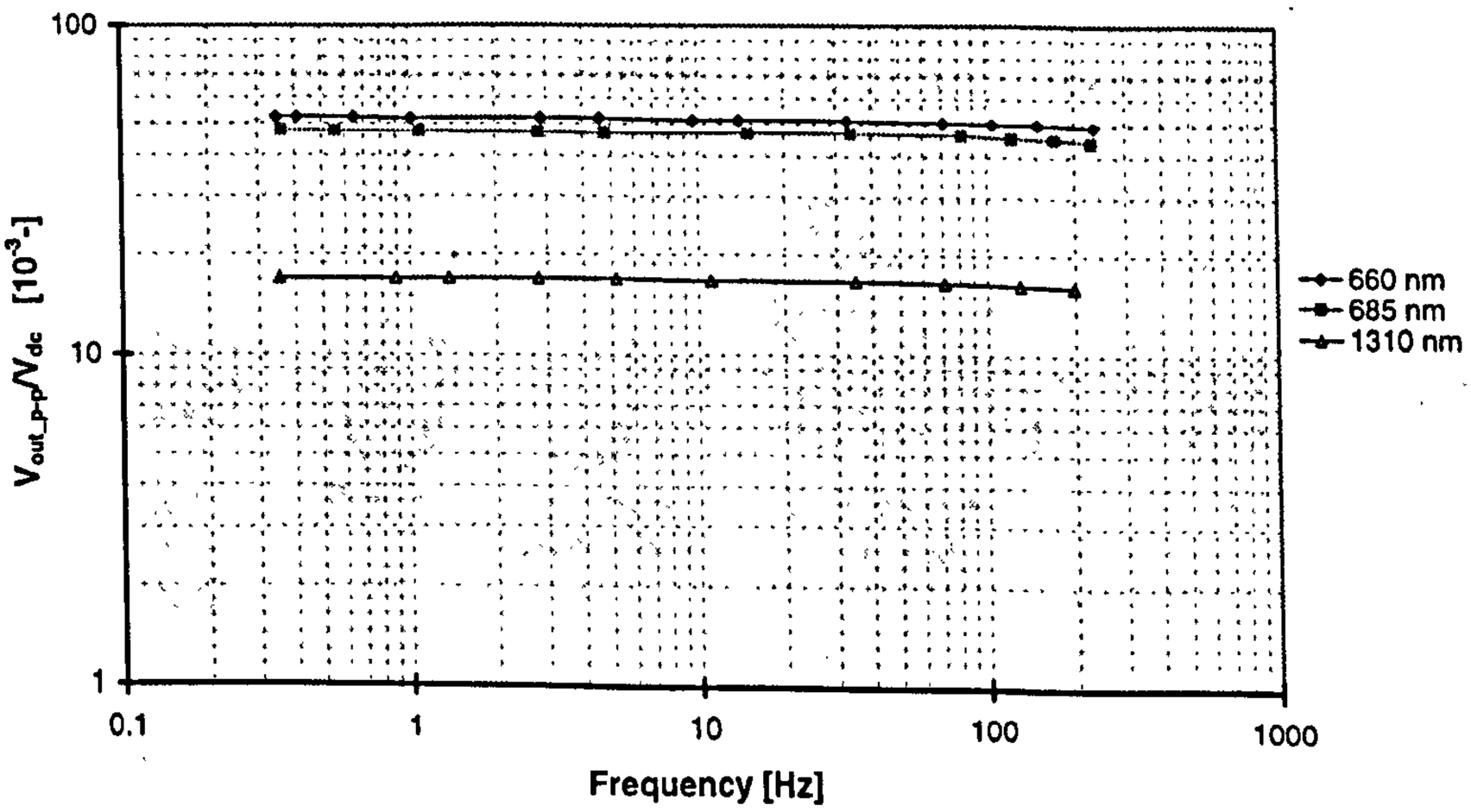

Figure 4.16: Frequency response of the sensor with Lithium Niobate. $V_{out.p-p}$ *is the peak-to-peak output voltage and* V_{dc} *is the DC output voltage. The applied electric field is* $E_{rms} = 47.4kV/m$.

or photoconductivity at wavelengths ranging from 660nm up to 1310nm as it was expected. Sensor sensitivity decreases with increasing wavelength as explained in section 4.3.1.1 (see equation 4.13).

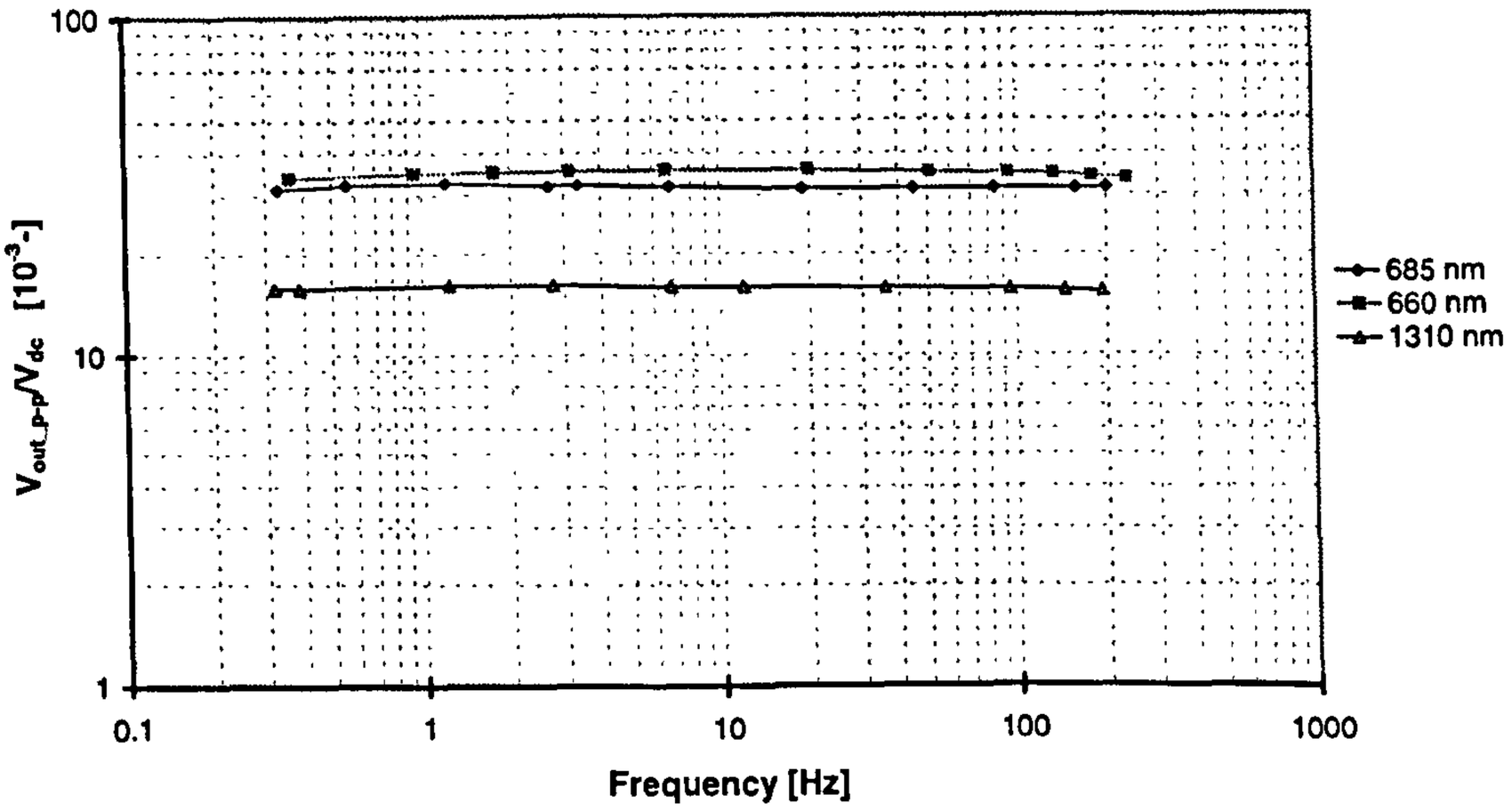

Figure 4.17: Frequency response of the sensor with Bismuth Germanate. $V_{out.p-p}$ *is the peak-to-peak output voltage and* V_{dc} *is the DC output voltage. The applied electric field is* $E_{rms} = 47.4kV/m$.

Transfer characteristics of ELF field sensor were measured in experimental arrangement according to Figure 4.18. One output of the polarimetric electrooptic sensor operating at the wavelength of 1296nm was connected to the input of the lock-in amplifier. The amplifier is locked to the measured frequency using its internal oscillator. The output was monitored by a D/A convertor connected to a computer. The sensor was calibrated for frequencies ranging from 50Hz down to

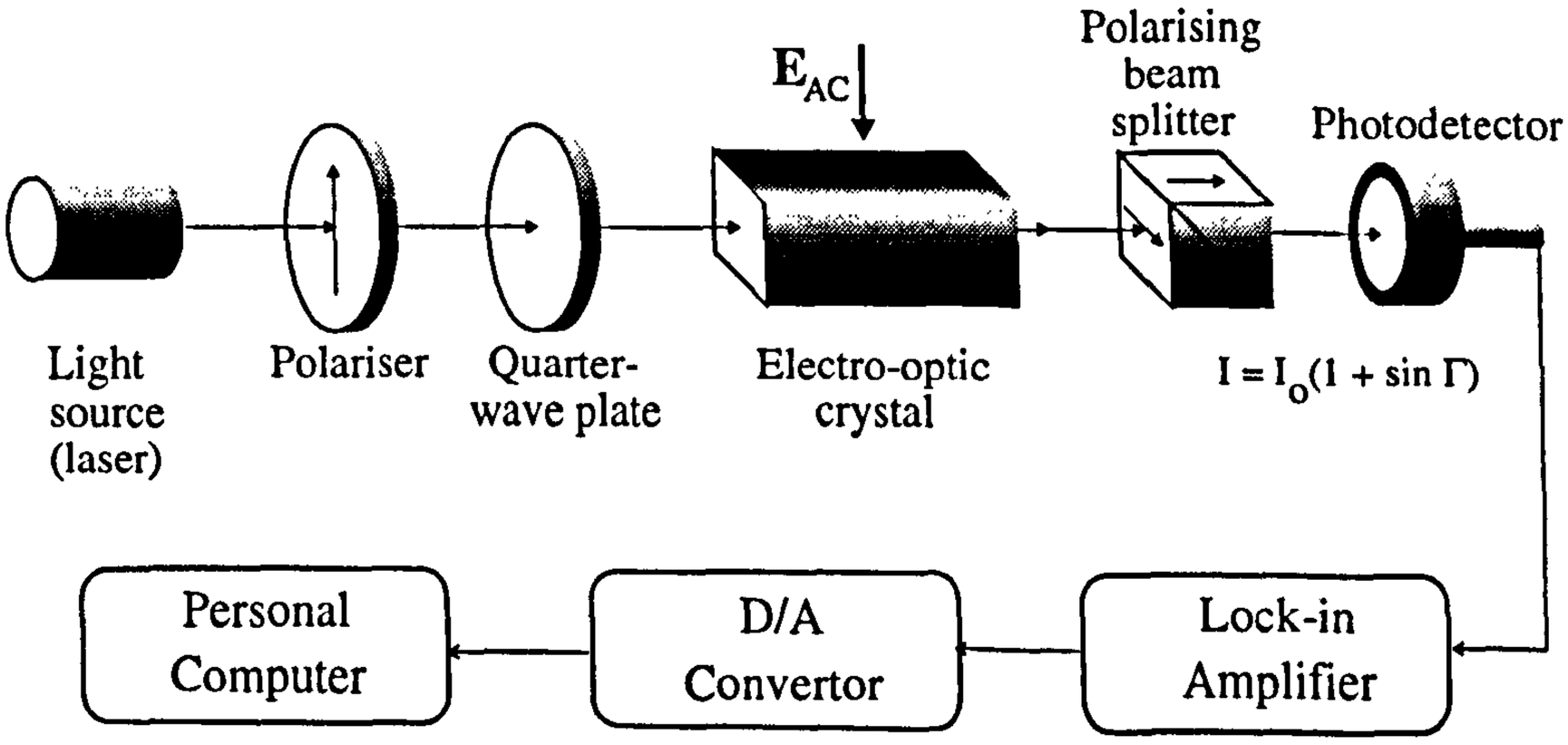

Figure 4.18: ELF sensor with Bismuth Germanate and Lithium Niobate. *The lock-in amplifier is locked to the frequency of measured field using the internal oscillator.*

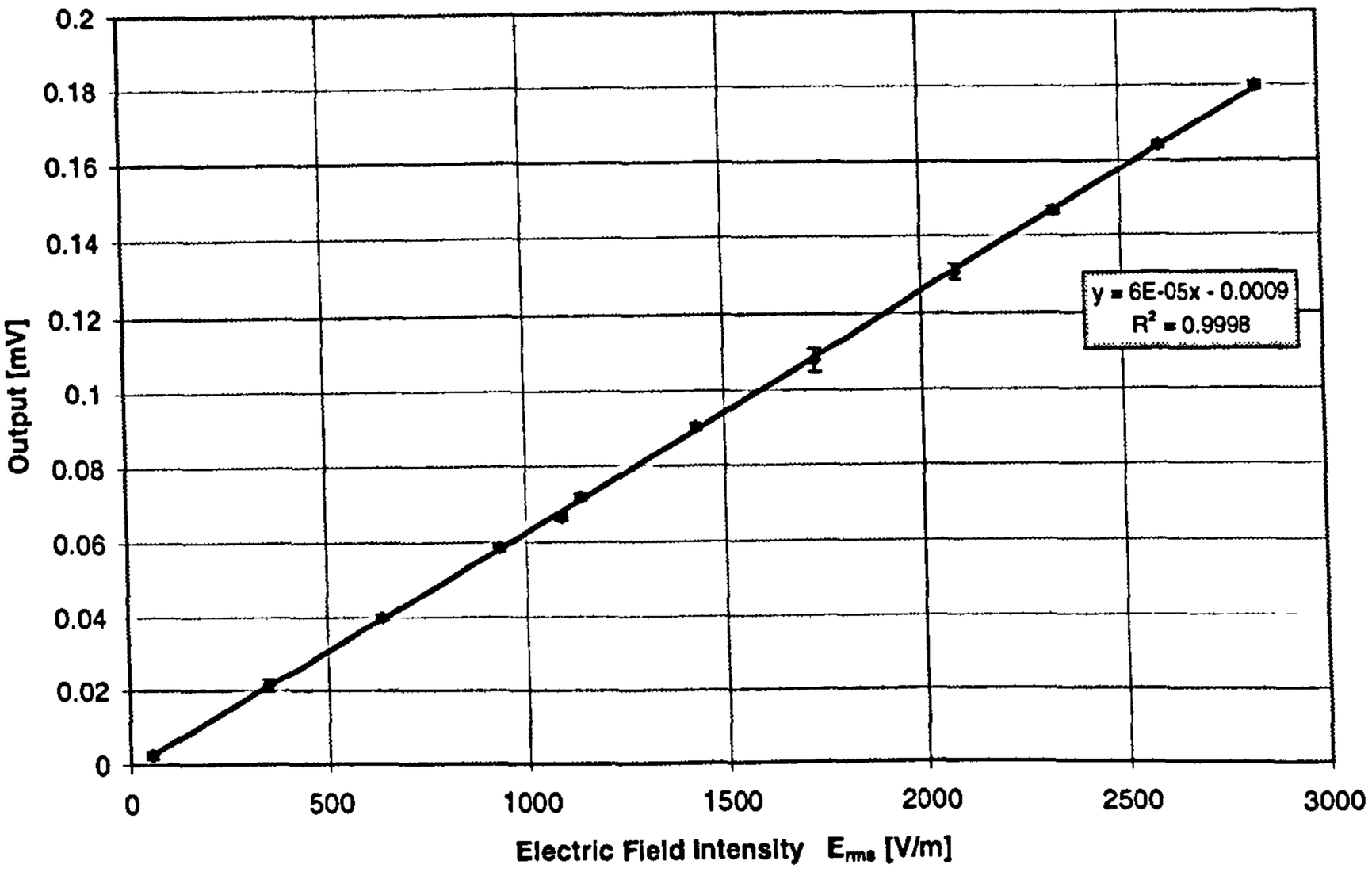

Figure 4.19: Transfer characteristic of ELF sensor with Lithium Niobate at 1296nm. *Measurements were done with ELF field at 50Hz in the range 0-3kV/m. The minimum measured value of the electric field is 50V/m and the resolution 30V/m, with S/N=1.*

2Hz. The measured minimum detection levels and resolutions were different for different settings of the lock-in amplifier. Figures 4.19 and 4.20 show transfer characteristics for two different ranges of electric field. The minimum measured value of the electric field intensity was 1V/m with resolution of 1V/m in the range 0-180V/m and with the output signal to noise ratio $S/N = 0dB$ (Figure 4.20, BG sensor). For example in the range 0-3kV/m the minimum measurable value of electric field was 50V/m and the resolution 32V/m (Figure 4.19). These values were approximately the same for both LN and BG sensors.

The sensor sensitivity can be further improved in several ways. The sensitivity to the electric field can be increased twice by subtracting signals from two outputs of the sensor in Figure 4.1 (section 4.1). Employing a shorter wavelength will also positively influence the sensitivity which follows from (4.13) and can be observed on the graphs of frequency response of the sensor (Figures 4.16 and 4.17). Another possibility is to use more sensitive electrooptic crystal as for example Zinc Telluride depending on the frequency range which is to be measured.

Conclusions. It was demonstrated that both selected crystals (Lithium Niobate and Bismuth Germanate) perform well in measurements of extra-low-frequency

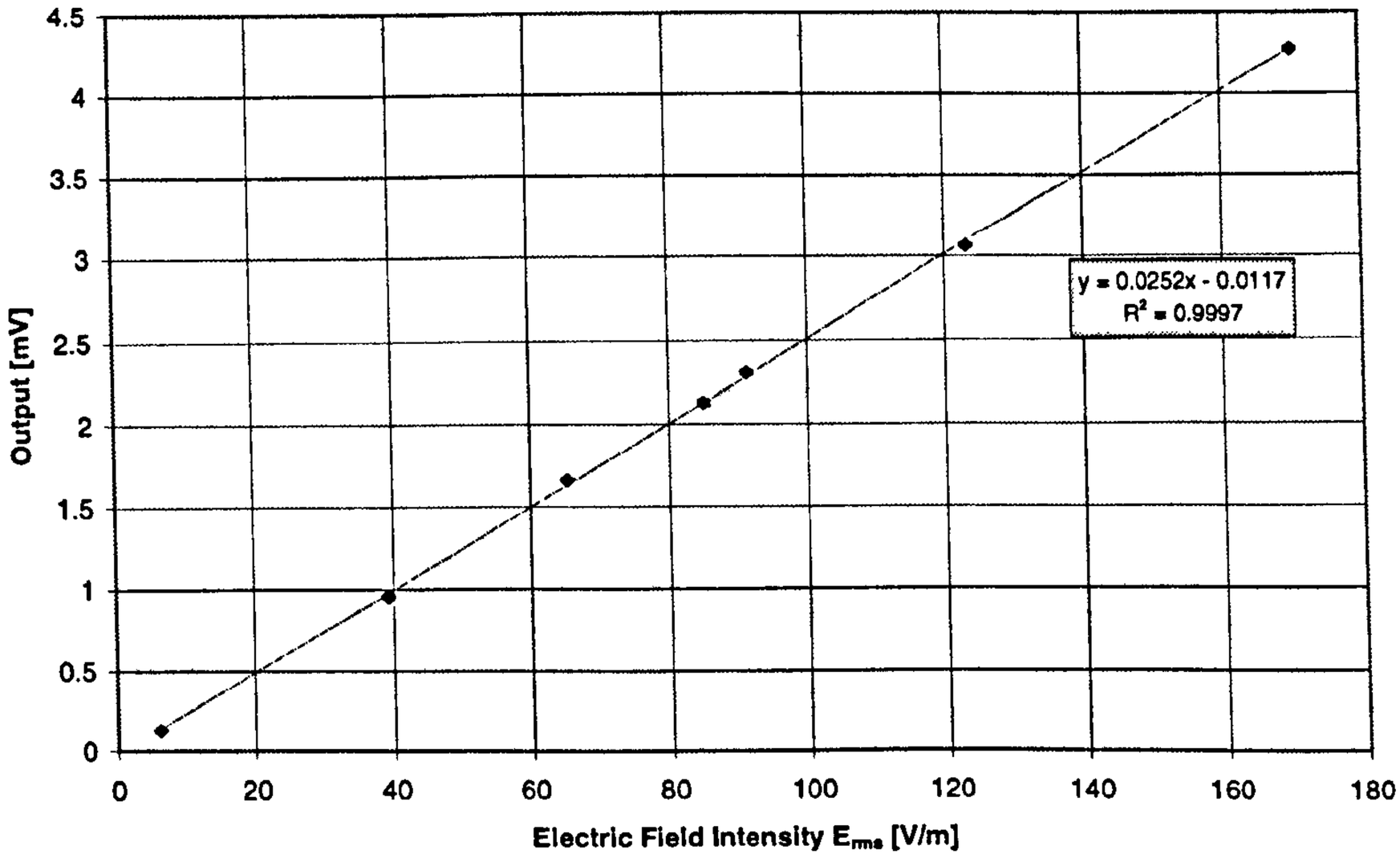

Figure 4.20: Transfer characteristic of ELF sensor with Bismuth Germanate at 1296nm. *Measurements were done with ELF field at 2Hz in the range 0-180V/m. The minimum measured value of the electric field and the resolution are 1V/m, with S/N=1.*

electric field, achieving approximately the same sensitivity to the electric field. The measured frequency characteristics of the sensor were flat in the measured frequency range from 0.3Hz up to 200 Hz. In conjunction with a lock-in amplifier in the detection scheme, locked to the measured frequency, it was possible to achieve a minimum detectable level of the electric field of 1V/m, with a signal to noise ratio equal to 0dB and a resolution of 1V/m.

4.4.3 DC Field Measurements

The performance of the sensor at frequencies lower than 1Hz and DC field measurements were investigated observing the response of the sensor to a step function electric field. Such a response exhibits an exponential decay with time due to the finite resistivity of electrooptic crystal. The time constant of this decay was used to characterize the crystal performance.

At the wavelength of 685nm the time constant of both LN and BG is insufficient for DC field measurement (table 4.5). An improvement was observed at 1310nm, where the time constant of LN reached very high value (>2hrs). The time constant of BG increased about 4 times, yet inadequate for DC measurements. The

Table 4.5: Time constant τ of Bismuth Germanate (BG) and two crystals of Lithium Niobate (LN1, LN2) at 685 and 1310nm.

	wavelength [nm]	LN1	LN2	BG
τ[s]	685	50	225	1.2
τ[s]	1310	>2hrs	>2hrs	8

difference in the measured time constants at 685nm and 1310nm was attributed to the photoconductivity effect which was eliminated in the case of LN at 1310nm. The measurements with BG were also carried out at 1569nm without an apparent improvement. The low value of its time constant was attributed to the high conductivity of the crystal. This was estimated to be $2.10^{-11} S/m$. It is more than one order of magnitude higher than the value measured in [40](table 4.2) and makes the crystal of Bismuth Germanate unsuitable for static field measurements as it was originally intended.

It was demonstrated that out of the selected electrooptic crystals only Lithium Niobate has conductivity low enough to be used in the DC field sensor. However, difficulties were encountered with Lithium Niobate with respect to long term stability of the charge relaxation time constant. Temperature experiments were performed on the highly resistive samples of Lithium Niobate by heating up to $70°C$. The samples used in these experiments became highly conductive, showing a charge relaxation time constant of 10s for a long time after cooling (several months). This was not expected and it is believed that some internal damage may have taken place during the heat treatment, which may account for this unexpected behaviour. New samples were bought and tested. Even the new crystals exhibited very low time constant.

According to equation (4.26), this sudden and large change in the charge relaxation time constant could be caused either by a change in the permittivity or a change in the crystal conductivity. The temperature dependence of the relative permittivity of Lithium Niobate was studied [66] in the temperature range from 0 to $100°C$ and no anomaly of the permittivity was reported. The only dielectric anomaly observed was a sharp rise of the dielectric constant along the optical axis

near the Curie temperature which is about 1200°C [16]. Since this anomaly is far from the temperatures used in the experimental study presented, the change in the permittivity was ruled out as the possible reason for the change in the measured charge relaxation time constant. Values of the time constant, obtained from measurements at wavelengths 850, 1269 and 1569nm with the power of the laser beam varied from 0.05 to 5mW, were very similar, approximately 10s. This confirmed that the low values of the time constant were not caused by the photoconductivity effect but by the bulk conductivity of the samples which changed by about 3 orders in magnitude compared to its original state. This change was attributed to the effect of thermally stimulated conductivity which was reported for some wide band gap materials including Lithium Niobate [22] [23] [13]. Exposing these crystals to an elevated temperature in the presence of a DC electric field, the crystals acquire a state of high conductivity. The stimulated conductivity was reported to be several orders of magnitude higher than that of prior to the heat treatment. It was also reported that a state of low conductivity can be achieved by heating the material to a higher temperature (400°C).

The samples of Lithium Niobate were, therefore, subjected to a thermal treatment. The old samples (LN1, LN2) were heated directly to 400°C, whereas the new samples (LN3, LN4) were heated in stages to temperatures of 100, 200, 300 and 400°C. During the heat treatment, the temperature was gradually increased to the required value (30 minutes), then kept constant for half an hour, and finally the crystals were slowly cooled down. The charge relaxation time constants of the samples, measured between the heat treatments, are shown in table 4.6. An improvement in

Table 4.6: Approximate values of charge relaxation time constant τ of Lithium Niobate crystals (LN1-LN4) after each heat treatment.

Treatment	100°C	200°C	300°C	425°C
LN1	-	-	-	>2hrs
LN2	-	-	-	>2hrs
LN3	10s	600s	1hr	>2.7hrs
LN4	-	30s	27min	>1.2hrs

the time constant was observed after heating to $200°C$. To obtain crystals with high values of time constant, the heat treatment at $400°C$ was necessary. The samples required several days after the treatment at $300°C$ and $425°C$ to attain the state of high resistivity. Whether the low resistivity state of LN was really caused by thermally stimulated conductivity exposing the crystal to temperatures of $\approx 70°C$ where its resistivity exhibits a local minimum [22] was not investigated. Using the described method it was possible to obtain crystals with time constants more than 3 hours.

Another major problem, when measuring DC electric field, was encountered in stabilizing the output signal of the DC sensor. The DC field measurements were done using the experimental setup shown in Figure 4.18 with the exception of the lock-in amplifier and another photodetector used to measure the second output from the polarizing beamsplitter. The outputs of the photodetectors were monitored directly by a data acquisition board connected to a computer. Compared to the ELF measurements the DC measurements were influenced to a great extent by a long term drift of the sensor output. The sources of the drift were both photodetectors and optical components, mainly the crystal of Lithium Niobate. An uncorrelated drift of the photodetectors which was about 0.1% of the photodetector output in 20 minutes and the temperature instability of Lithium Niobate crystal (section 6.3) limited the static field measurements to pulses with duration no longer that 200s, if the output uncertainty was to be acceptable. Due to the uncorrelated drift of the photodetectors, it was impossible to employ the subtraction detection scheme to suppress the output voltage fluctuations (section 6.5). In the described experimental setup the achieved minimal detectable level of the electric field intensity was 2.4kV/m, over a period of 200s.

Conclusions. DC field measurements were found possible only with crystal of Lithium Niobate since the intrinsic resistivity of the Bismuth Germanate was not sufficiently high. It was demonstrated that even though Lithium Niobate has sufficiently high relaxation time constant for DC field measurement, it may suffer from long term instability caused by the effect of thermally stimulated conductivity. Consequently, this finding limits the usage of the crystal in DC field sensor applications.

4.4.4 Summary

The theoretical findings for crystals of Lithium Niobate and Bismuth Germanate were investigated experimentally. The transverse electrooptic effect was chosen to be used in sensor with both Lithium Niobate and Bismuth Germanate. The selected crystals performed well at extra-low-frequencies having approximately the same sensitivity to the electric field. The measured frequency characteristics of the sensor with both crystals were flat in the measured frequency range from 0.3Hz up to 200 Hz. The minimum measurable value of electric field intensity at extra low frequencies was 1V/m with signal to noise ratio of 0dB.

The performance of the selected crystals at frequencies lower than 1Hz and the measurement of static fields were investigated by measuring the charge relaxation time constant. This was found to be too low for static field measurements in the case of Bismuth Germanate which was attributed to a low conductivity of the sample. The time constant of Lithium Niobate was found to be very high exhibiting the potential for DC field measurements. Difficulties were encountered with respect to long term stability of the time constant of Lithium Niobate which was attributed to the effect of thermally stimulated conductivity. High resistivity samples suitable for DC field measurements were prepared by heating the crystal of Lithium Niobate at $400°C$. Due to the long term drift of the sensor output, caused by both photodetectors and the crystal, the static field measurements were limited to measurements of pulses with a duration of 200s. The minimum detectable level of the electric field intensity was 2.4kV/m.

4.5 Directivity of the sensor

In the previous sections it was always assumed that the crystal was exposed to the applied electric field in a way appropriate to the chosen transverse electrooptic effect (section 4.4.1). In practice the orientation of the measured electric field may not be known. It is, therefore, important to know how the sensor responses to the electric field with orientation different from that for which it was designed. The influence of all three components of the field on the electrooptic sensor is investigated in

this section separately for Lithium Niobate and Bismuth Germanate. First, the electrooptic effect is described in details. The results are then used to show that in both cases the sensor is sensitive only to one component of the electric field for which it was designed. The theoretical findings are then supported by experimental results.

4.5.1 Directivity of the LN sensor

The orientation of the measured field with respect to the crystallographic axes of the crystal and the direction of the laser beam in the crystal of Lithium Niobate were specified in section 4.4.1. The light propagates along the optical axis x_3 and the electric field is applied along either x_1 or x_2 axes (table 4.4, Figure 4.21). It will be shown that the E_3 component of the electric field, parallel to the laser beam, does not influence the sensor output and that the sensor measures only one component of the electric field in the plane perpendicular to the optical axis. It is also shown that the orientation of the measured component depends on the position of the analyzer.

Using the electrooptic coefficients r_{ij} for $3m$ symmetry group crystals [9], the index ellipsoid (3.13) can be written:

$$\left(\frac{1}{n_0^2} - r_{22}E_2 + r_{13}E_3\right) x_1^2 + \left(\frac{1}{n_0^2} + r_{22}E_2 + r_{13}E_3\right) x_2^2$$
$$+ \left(\frac{1}{n_e^2} + r_{33}E_3\right) x_3^2 + 2x_2x_3r_{51}E_2 + 2x_1x_3r_{51}E_1 - 2x_1x_2r_{22}E_1 \;=\; 1 \qquad (4.27)$$

where n_0, n_e are the ordinary and extraordinary refractive indices, respectively. The equation (4.27) describes the optical properties of the electrooptic crystal under the influence of an electric field and is used to find the eigenmodes of the propagating light beam as well as the corresponding refractive indices (chapter 3). Letting x_3 in (4.27) equal to zero we obtain the equation of an ellipse which completely characterises the light propagation:

$$\left(\frac{1}{n_0^2} - r_{22}E_2 + r_{13}E_3\right) x_1^2 + \left(\frac{1}{n_0^2} + r_{22}E_2 + r_{13}E_3\right) x_2^2$$
$$-2x_1x_2r_{22}E_1 \;=\; 1 \qquad (4.28)$$

The orientation of the polarisation planes of the linearly polarized eigenwaves coincides with the eigenaxes of the ellipse (4.28) and their refractive indices are equal to the lengths of its major and minor axes. To find the eigenaxes the equation is transformed into a new coordinate system (x'_1, x'_2) as shown in Figure 4.21:

$$\begin{pmatrix} x'_1 \\ x'_2 \end{pmatrix} = \begin{pmatrix} \cos\theta & \sin\theta \\ -\sin\theta & \cos\theta \end{pmatrix} \begin{pmatrix} x_1 \\ x_2 \end{pmatrix} \tag{4.29}$$

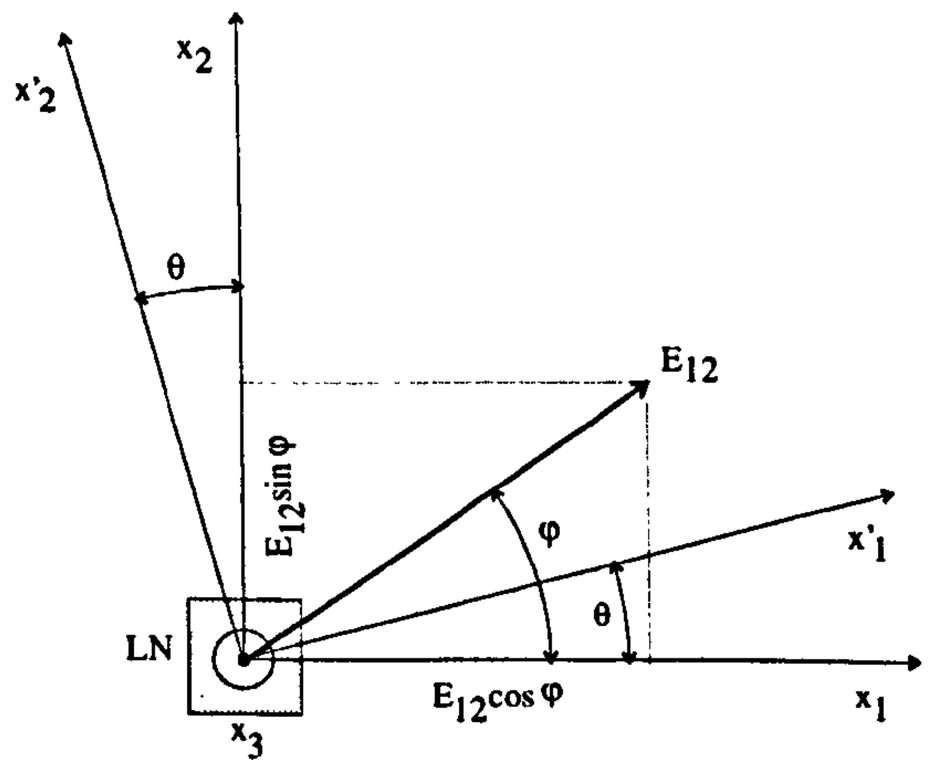

Figure 4.21: Crystallographic axes of Lithium Niobate (mirror plane perpendicular to x_1) and the rotation of the coordinate system around the optical axis x_3.

In the new prime coordinates the equation (4.28) becomes:

$$\begin{aligned} &\left(\frac{1}{n_0^2} - r_{22}E_2 + r_{13}E_3\right)\left(x_1'^2\cos^2\theta + x_2'^2\sin^2\theta - 2x'_1x'_2\cos\theta\sin\theta\right) \\ &+\left(\frac{1}{n_0^2} + r_{22}E_2 + r_{13}E_3\right)\left(x_1'^2\sin^2\theta + x_2'^2\cos^2\theta + 2x'_1x'_2\cos\theta\sin\theta\right) \\ &-2r_{22}E_1\left(x_1'^2\cos\theta\sin\theta + x'_1x'_2\cos^2\theta - x'_1x'_2\sin^2\theta - x_2'^2\sin\theta\cos\theta\right) \\ &= 1 \end{aligned} \tag{4.30}$$

The prime coordinates x'_1,x'_2 coincide with the sought eigenaxes when the mixed terms in (4.30) vanish. This condition leads to the following equation:

$$\frac{E_2}{E_1} = \tan\varphi = \frac{1}{\tan(2\theta)} \tag{4.31}$$

where φ defines the orientation of the electric field vector $\mathbf{E_{12}} = \mathbf{E_1} + \mathbf{E_2}$ in the plane perpendicular to the optical axis x_3, and θ defines the orientation of the

optical eigenaxes. Using trigonometric identities one can relate the orientation of the induced eigenaxes to the orientation of the electric field:

$$\theta = \frac{\pi/2 - \varphi}{2} \tag{4.32}$$

According to the equation (4.32) the rotation of the electric field in (x_1x_2) plane causes the optical eigenaxes to rotate in the opposite direction to that of the electric field vector and twice as slower. For example, when the electric field has only the $\mathbf{E}_1$ component the eigenaxes are at 45° to x_1 and x_2 axes. When the electric field is along the x_2 axis the eigenaxes coincide with x_1 and x_2.

If the refractive indices of the eigenmodes are denoted n_1 and n_2 the quantities $1/n_1^2$ and $1/n_2^2$ are given by the $x_1'^2$ and $x_2'^2$ terms in (4.30), respectively (section 3.1.3):

$$\frac{1}{n_1^2} = \frac{1}{n_0^2} + r_{13}E_3 - r_{22}E_2\cos(2\theta) - r_{22}E_1\sin(2\theta) \tag{4.33}$$

$$\frac{1}{n_2^2} = \frac{1}{n_0^2} + r_{13}E_3 + r_{22}E_2\cos(2\theta) + r_{22}E_1\sin(2\theta) \tag{4.34}$$

Using (4.32) and noticing that the $\mathbf{E}_1$ and $\mathbf{E}_2$ components of the electric field vector in the (x_1x_2) plane $\mathbf{E}_{12}$ can be written as $E_1 = E_{12}\cos\varphi$ and $E_2 = E_{12}\sin\varphi$ we finally arrived at

$$n_1 = n_0 - \frac{n_0^3}{2}(r_{13}E_3 - r_{22}E_{12}) \tag{4.35}$$

$$n_2 = n_0 - \frac{n_0^3}{2}(r_{13}E_3 + r_{22}E_{12}) \tag{4.36}$$

This last step also employed the result of differential calculus $\mathrm{d}n = -(n^3/2)\mathrm{d}(1/n^2)$ which is justified by the fact that changes in refractive indices are very small compared to n_0 [9].

Using (4.36), the induced birefringence Δn is readily found:

$$\Delta n = n_2 - n_1 = n_0^3 r_{22}E_{12} \tag{4.37}$$

Although the refractive indices n_1, n_2 depend on the E_3 component of the electric field, the induced birefringence was found to be independent of E_3. The sensor

output is a function of the induced phase retardation Γ :

$$\Gamma = \frac{2\pi}{\lambda}\Delta n l \tag{4.38}$$

where λ is the optical wavelength and l is the length of the crystal. The sensor output is not influenced by the E_3 component of the electric field. It is also evident from (4.37) that the transverse electro-optic effect in a crystal of 3m point group symmetry with light beam along optical axis has rotational symmetry along this axis. There is no privileged direction of the electric field in the (x_1x_2) plane for which the electrooptic effect would have its maximum. The field vector can have an arbitrary orientation in this plane to achieve the same phase retardation. Changes in orientation of the electric field cause only changes in orientation of the optical axes but not of the birefringence.

In the electrooptic crystal the light passes the polarizer and the quarter-wave plate before entering the crystal. These two components ensure that the incident light is circularly polarized. As such it is composed of two linearly polarized waves with polarization planes perpendicular to each other and with the mutual phase shift of $\pi/2$. The orientation of their polarisation planes can be arbitrary as long as the planes are perpendicular. For the sake of simplicity of calculations the polarization vector of these waves were chosen parallel to the cartesian laboratory coordinate axes x_1, x_2 (Figure 4.21). Then light entering the crystal is then described by Jones matrix:

$$\mathbf{L}_q = \frac{1}{\sqrt{2}} \begin{pmatrix} 1 \\ i \end{pmatrix} \tag{4.39}$$

To obtain the Jones representation of the light behind the crystal $\mathbf{L}_c$, the circularly polarized light (4.39) is transformed first into the coordinates (x_1', x_2') which coincide with the crystal optical eigenaxes. Then the phase retardation is applied by multiplying the transformed light matrix by the retardation matrix (4.7) with the phase retardation Γ (4.38), and finally the inverse transformation back to (x_1, x_2) system is achieved:

$$\mathbf{L}_c = \frac{1}{\sqrt{2}} \begin{pmatrix} \cos\theta & -\sin\theta \\ \sin\theta & \cos\theta \end{pmatrix} \begin{pmatrix} e^{i\frac{\Gamma}{2}} & 0 \\ 0 & e^{-i\frac{\Gamma}{2}} \end{pmatrix} \begin{pmatrix} \cos\theta & \sin\theta \\ -\sin\theta & \cos\theta \end{pmatrix} \begin{pmatrix} 1 \\ i \end{pmatrix} \tag{4.40}$$

In the electro-optic sensor the analyzer is firmly fixed with respect to the crystal, the quarter-wave plate and the polarizer, and the orientation of the electric field varies. As it was derived above, the $\mathbf{E}_3$ component of the measured electric field does not influence the sensor output. The sensor can be influenced only by an electric field with the orientation perpendicular to the optical axis. In the following the analyzer is considered to be fixed with the orientation along the x_1 axis. The output light $\mathbf{L}_a$ of the sensor is found by multiplying the Jones matrix of the analyzer by the Jones representation of the light behind the crystal $\mathbf{L}_c$:

$$\mathbf{L}_a = \begin{pmatrix} 1 & 0 \\ 0 & 0 \end{pmatrix} \mathbf{L}_c =$$

$$\frac{1}{\sqrt{2}} e^{i\frac{\Gamma}{2}} \begin{pmatrix} (\cos^2\theta + i\sin\theta\cos\theta) - e^{i\Gamma}(i\sin\theta\cos\theta - \sin^2\theta) \\ 0 \end{pmatrix} \tag{4.41}$$

The light intensity I_{out} is found as the product of the $\mathbf{L}_a$ and its complex conjugate $\mathbf{L}_a^*$ (section 4.2.1):

$$I_{out} = \mathbf{L}_a \mathbf{L}_a^* = \frac{1}{2}(1 + \sin\Gamma\sin\theta) \tag{4.42}$$

Substituting (4.32) into (4.42), the output intensity of the sensor can be written as a function of the induced phase retardation Γ and the angle φ characterizing orientation of the electric field in the (x_1, x_2) plane:

$$I_{out} = \frac{1}{2}(1 - \Gamma\cos\varphi) \tag{4.43}$$

Since the phase retardation Γ (4.38) is proportional to the induced birefringence, the output of the sensor is directly proportional to the $E_{12}\cos\varphi$ which is the $\mathbf{E}_1$ component of the electric field:

$$I_{out} = \frac{1}{2}\left(1 - \frac{2\pi}{\lambda} n^3 r E_1\right) \tag{4.44}$$

The result obtained can be generalized, and it can be said that the studied electrooptic sensor with Lithium Niobate measures always only one component of the electric field, which is perpendicular to the optical axis. The orientation of this component depends on the orientation of the analyzer. It can be obtained from the

equation (4.32) considering the induced eigenaxes, characterized by the angle θ, to be at 45° to the analyzer. The conclusion is based on the fact that the induced birefringence does not depend on the orientation of the electric field in the plane perpendicular to the optical axis, and the orientation of the optical axes changes according to the orientation of the electric field. All directions of the electric field are, therefore, equally suitable and the sensor response can be maximized for any orientation of the electric field $\mathbf{E_{12}}$ by aligning the analyzer.

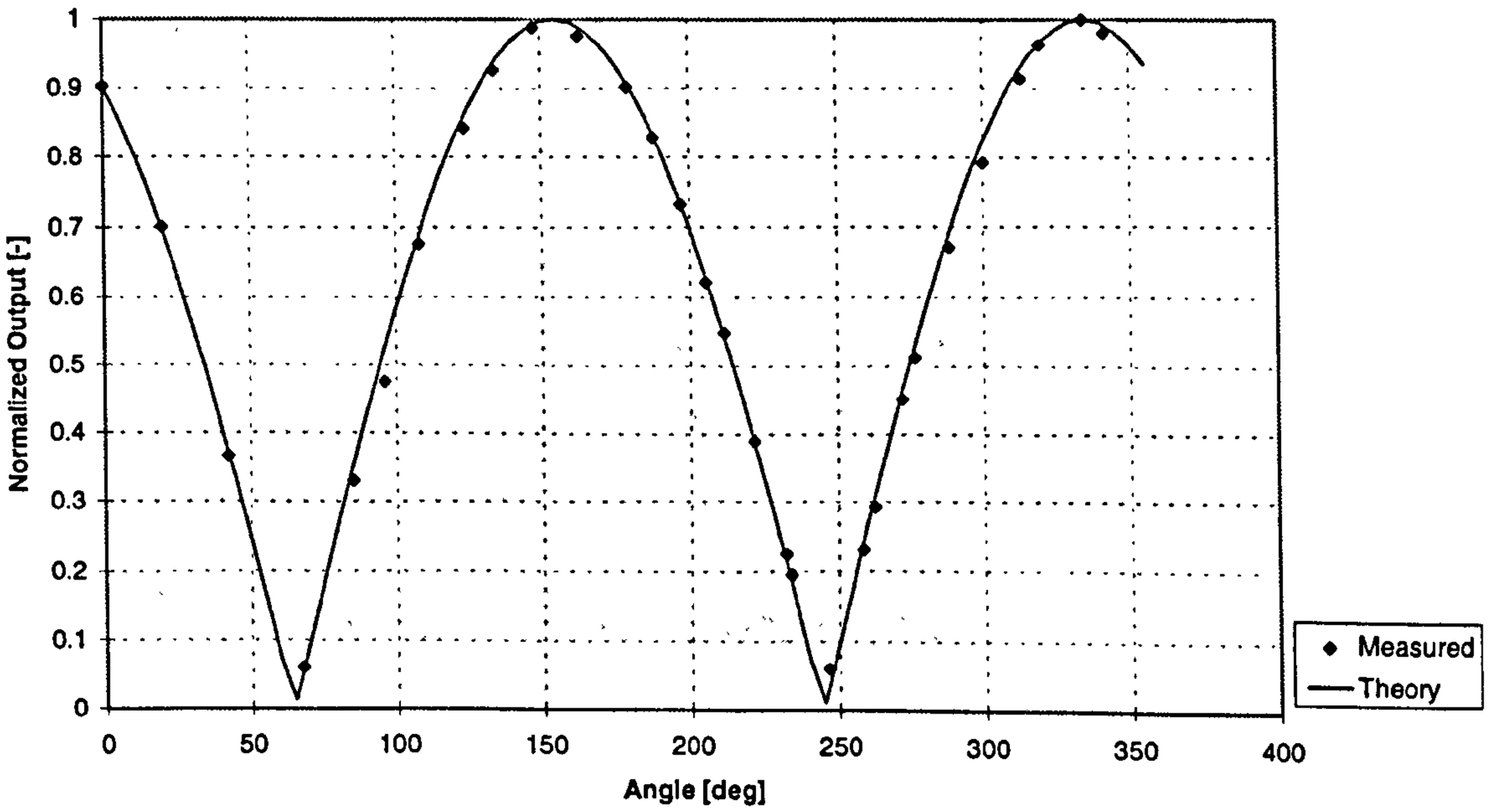

Figure 4.22: Normalized output of the electrooptic sensor with Lithium Niobate as a function of the orientation of the electric field. *The orientation of electric field vector in the plane perpendicular to the laser beam is characterised by an rotational angle in the range 0..360° (relative values).*

The theoretical results were verified experimentally. The electric field was generated by two parallel electrodes held in a cylindrical base which could be rotated. The crystal was suspended between the electrodes. The experiments were done with a constant AC electric field at the frequency of 50Hz. According to (4.43) the output of the sensor is expected to be in the form of $|\cos(\varphi + \alpha_0)|$ where α_0 is a constant depending on the position of the analyzer. The measurements results, depicted in Figure 4.22, confirmed the theoretical predictions. No influence of the electric field along the optical axis was observed.

Conclusions. The electrooptic sensor using Lithium Niobate was found to be

sensitive only to one component of the electric field in the plane perpendicular to the optical axis. The orientation of this field can be chosen arbitrarily by aligning the analyzer to a maximum response of the sensor.

4.5.2 Directivity of the BG sensor

The electrooptic effect and the isotropy of the sensor were also investigated for a sensor based on a crystal of Bismuth Germanate. As in section 4.7.1, the transverse electrooptic effect is investigated thoroughly and the results are used to predict the isotropy of the sensor with Bismuth germanate. The analytical results are supported by numerical simulations and experiments.

The crystal cut used in the sensor was selected in section 4.4.1. The physical shape of the crystal and the orientation of the crystallographic axes are shown in Figure 4.23. In the crystallographic coordinates (x_1, x_2, x_3) the index ellipsoid (3.13) can be written as ([9]):

$$\frac{x_1^2 + x_2^2 + x_3^2}{n^2} + 2r_{41}E_3x_1x_2 + 2r_{41}E_2x_1x_3 + 2r_{41}E_1x_2x_3 = 1 \tag{4.45}$$

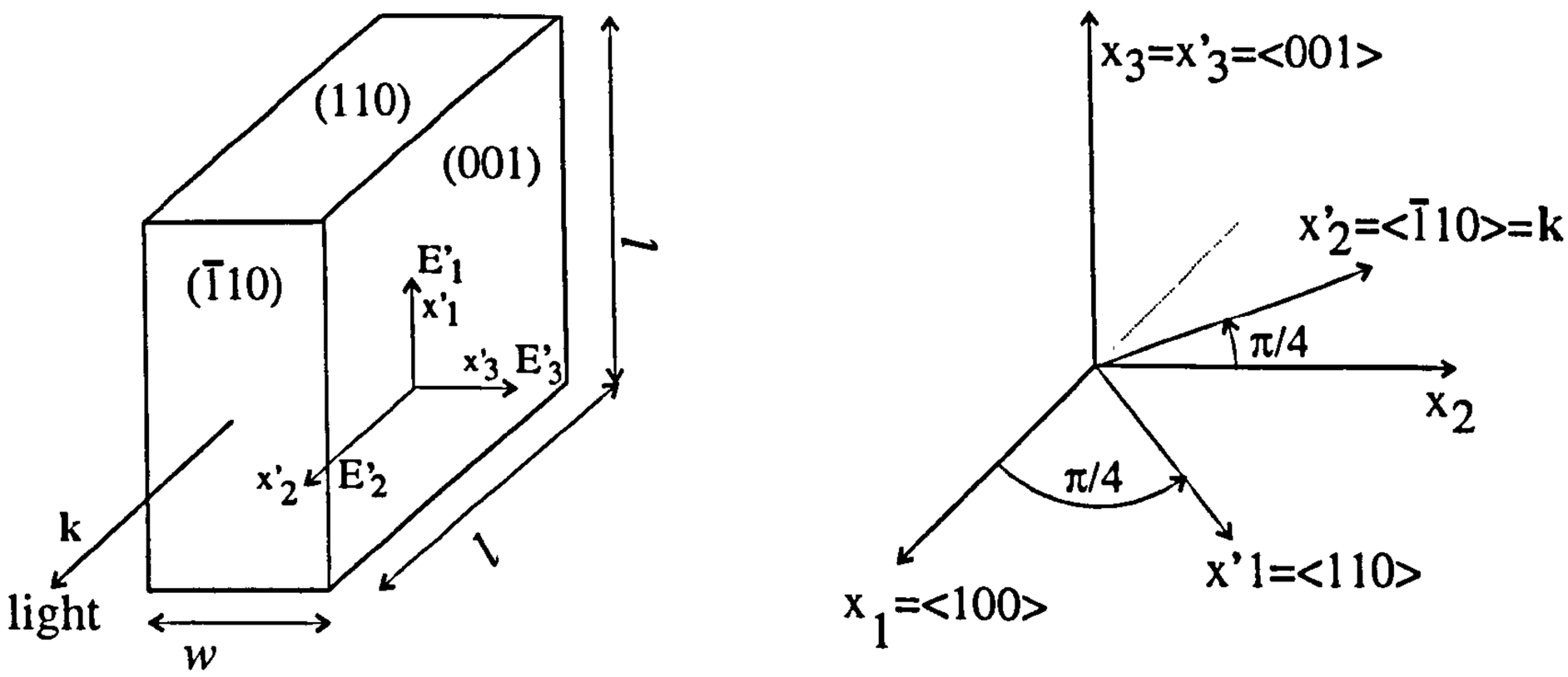

Figure 4.23: Crystallographic coordinate system (x_1, x_2, x_3) and its relation to the laboratory system (x'_1, x'_2, x'_3) and the shape of the crystal. *The directions are also expressed using Miler indices [4].*

It is more convenient to work in the laboratory coordinate system (x'_1, x'_2, x'_3), which is easily identified physically (see Figure 4.23), applying the following transforma-

tion:

$$\begin{pmatrix} x'_1 \\ x'_2 \\ x'_3 \end{pmatrix} = \begin{pmatrix} \cos\frac{\pi}{4} & \sin\frac{\pi}{4} & 0 \\ -\sin\frac{\pi}{4} & \cos\frac{\pi}{4} & 0 \\ 0 & 0 & 1 \end{pmatrix} \begin{pmatrix} x_1 \\ x_2 \\ x_3 \end{pmatrix} \tag{4.46}$$

The procedure of finding the eigenmodes of propagation and the refractive indices is similar to the case of Lithium Niobate, discussed in section 4.5.1. Once the equation (4.45) is expressed in the new prime coordinates, the sought cross-section of the ellipsoid with the plane perpendicular to the light beam is obtained by putting x'_2 equal to zero:

$$x_1'^2(\frac{1}{n^2} + r_{41}E'_3) + x_3'^2\frac{1}{n^2} + 2r_{41}E'_1x'_1x'_3 = 1 \tag{4.47}$$

The major and minor axes of the ellipse (4.47) determine both the orientation of the polarization planes of the eigenwaves and the corresponding refractive indices (chapter 3). Similar to the case of Lithium Niobate the eigenaxes are found using another transformation (Figure 4.23) :

$$\begin{pmatrix} x''_1 \\ x''_3 \end{pmatrix} = \begin{pmatrix} \cos\zeta & \sin\zeta \\ -\sin\zeta & \cos\zeta \end{pmatrix} \begin{pmatrix} x'_1 \\ x'_3 \end{pmatrix} \tag{4.48}$$

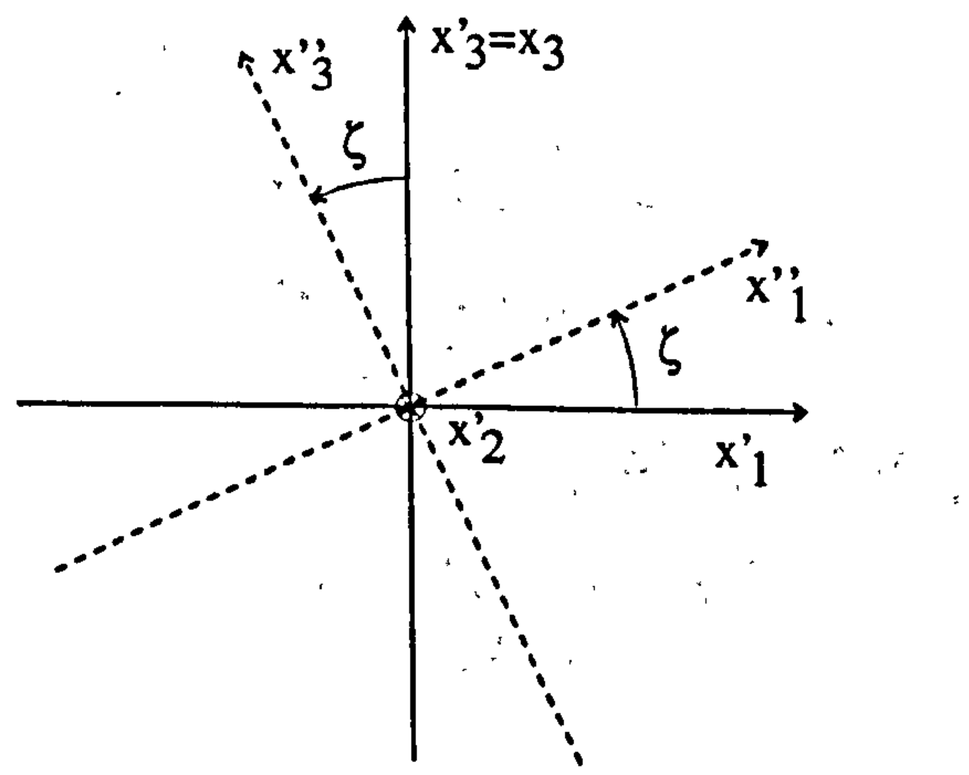

Figure 4.24: Transformation of (x'_2, x'_3) to (x''_2, x''_3) used to find the eigenaxes.

Thus transforming the equation (4.47) in the double prime coordinates

$$\begin{aligned} & x_3''^2\left[\frac{1}{n^2} + r_{41}E'_3\sin^2\zeta + r_{41}E'_1\sin(2\zeta)\right] + \\ & +x_1''^2\left[\frac{1}{n^2} + r_{41}E'_3\cos^2\zeta - r_{41}E'_1\sin(2\zeta)\right] + \\ & +x''_3x''_1\left[(\sin(2\zeta)r_{41}E'_3 + 2\cos(2\zeta)r_{41}E'_1\right] = 0 \end{aligned} \tag{4.49}$$

and forcing the mixed terms to zero leads to the following condition for the angle ζ:

$$\tan 2\zeta = \frac{2E'_1}{E'_3} \tag{4.50}$$

The angle ζ from the equation (4.50) defines the orientation of the induced eigenaxes which coincide with x''_3, x''_1 axes. The x''^2_3 and x''^2_1 terms in (4.49) give the refractive indices n_1, n_2 experienced by the eigenwaves in the crystal:

$$\begin{aligned} n_1 &= n_0 - \frac{n_0^3}{2}(-\cos^2\zeta r_{41}E'_3 - r_{41}E'_1 \sin 2\zeta) \\ n_2 &= n_0 - \frac{n_0^3}{2}(-\sin^2\zeta r_{41}E'_3 + r_{41}E'_1 \sin 2\zeta) \end{aligned} \tag{4.51}$$

The natural birefringence in the direction of beam propagation is readily found using (4.51):

$$\Delta n = n_2 - n_1 = \frac{r_{41}n^3}{2}\left(E'_3 \cos(2\zeta) - 2E'_1 \sin(2\zeta)\right) \tag{4.52}$$

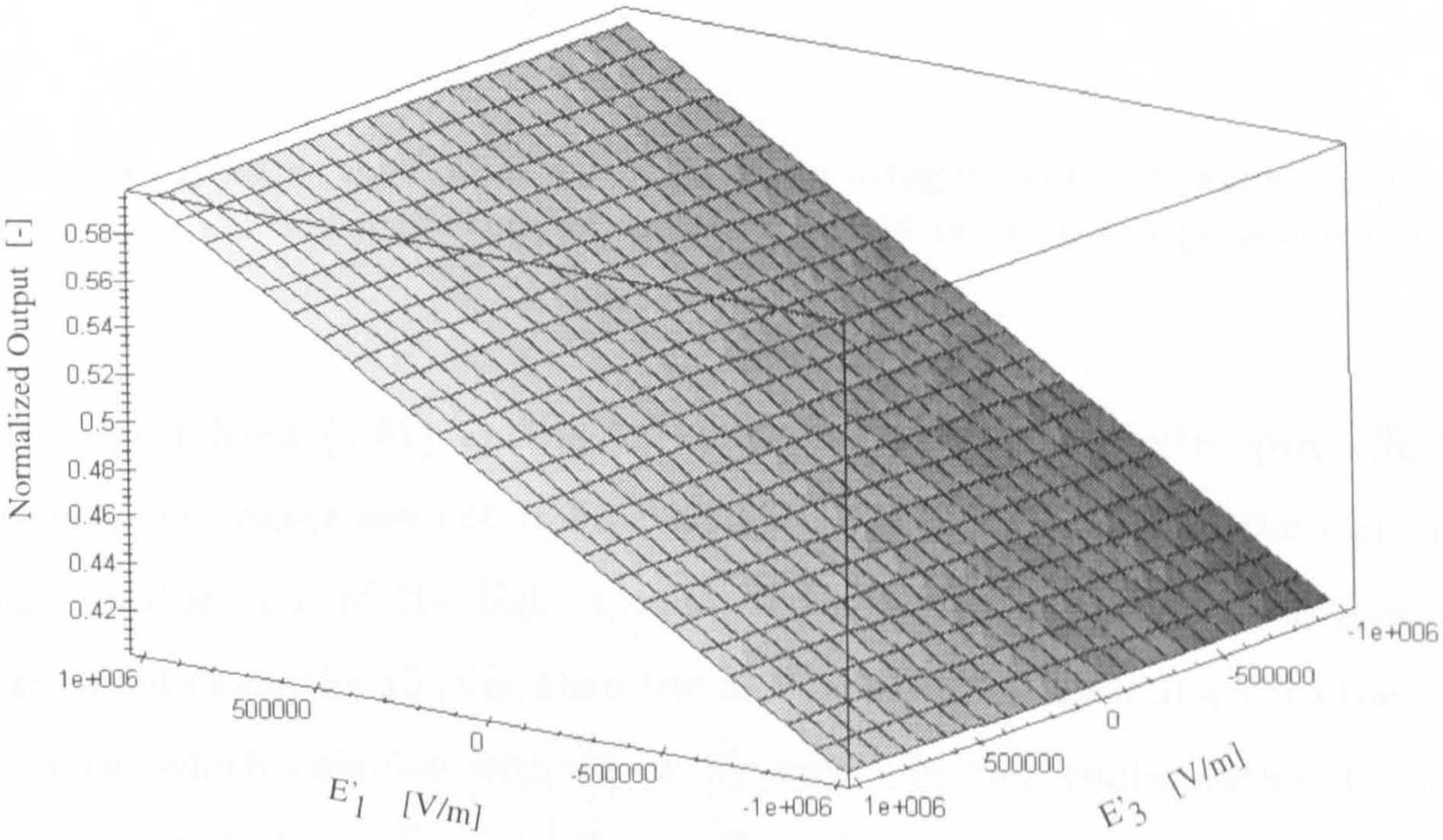

Figure 4.25: Simulated transfer characteristic of the electrooptic sensor based on the crystal of Bismuth Germanate.

If the E'_3 component of the electric field is equal to zero the eigenaxes are orientated at 45° to the x'_3 axis and the induced birefringence is $r_{41}n^3E'_1$, whereas if the E'_1 component is zero, the eigenaxes coincide with x'_3 and x'_1 and the induced birefringence is decreased two times ($r_{41}n^3E'_3/2$). It is evident that the transverse

electrooptic effect depends on the direction of the field in the plane perpendicular to the light beam, and the magnitude of the effect has its maximum for the electric field along x_1' axis, which was not the case of Lithium Niobate.

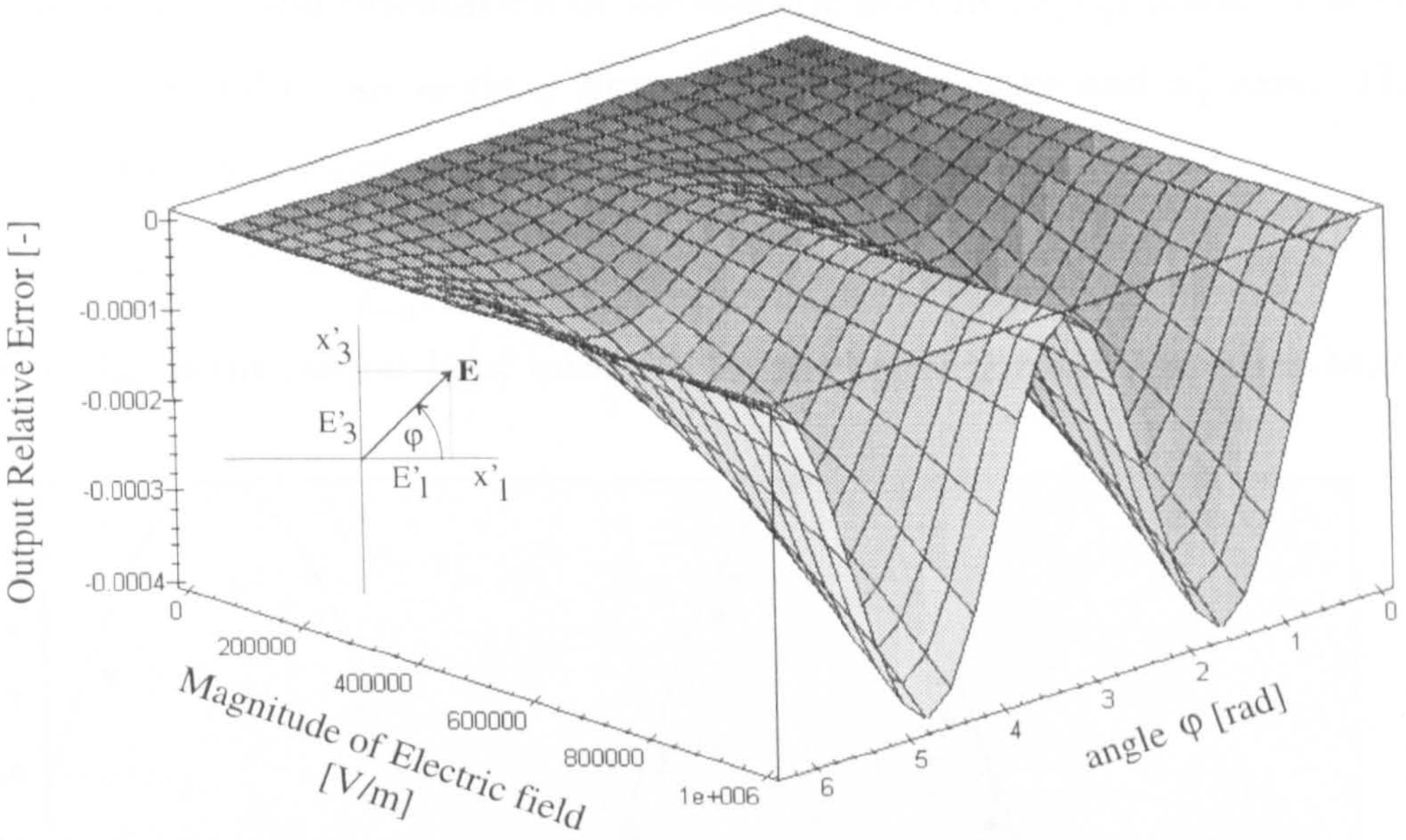

Figure 4.26: Relative error of the output in sensor using Bismuth Germanate as a function of the orientation and magnitude of the electric field in the plane perpendicular to the light beam.

It follows from (4.51) and (4.52) that the transverse electrooptic effect and, therefore, the sensor are not influenced by the E_2' component of the electric field along the direction of the light beam. If the sensor is designed to measure an electric field along the x_1' axis, than the analyzer is orientated at 45° to the induced eigenaxes, which coincide with x_1' or x_3' axes. In this configuration the electric field orientated along x_3' axis will not effect the output of the sensor since in this particular case the induced eigenaxes are at 45° to x_3' and x_1'. Therefore, the analyzer completely blocks one eigenwave and is transparent to the other one, not allowing to detect changes in the light polarization behind the crystal. However, the response of the sensor to an electric field having both E_1' and E_3' components in the plane perpendicular to the light beam is not so straightforward and the situation was analyzed using the developed computer model. Figure 4.25 shows the output of the

sensor as a function of the electric field components E'_1 and E'_3. It can be seen that the sensor responds linearly to the E'_1 component and is seemingly independent of E'_3. Further investigation showed a small influence of E'_3 component on the sensor output. The graph in Figure 4.26 shows a relative error of the output as a function of the magnitude and orientation of the electric field in $(x'_1x'_3)$ plane. The orientation is characterized by an angle φ between the field vector and x'_1 axis. The relative error of the sensor output is defined as:

$$\Delta = \frac{I_{out}(E'_1, E'_2, E'_3) - I_{out}(E'_1, 0, 0)}{I_{out}(E'_1, 0, 0)} \tag{4.53}$$

where I_{out} is the output light intensity for the field orientation given in brackets. The

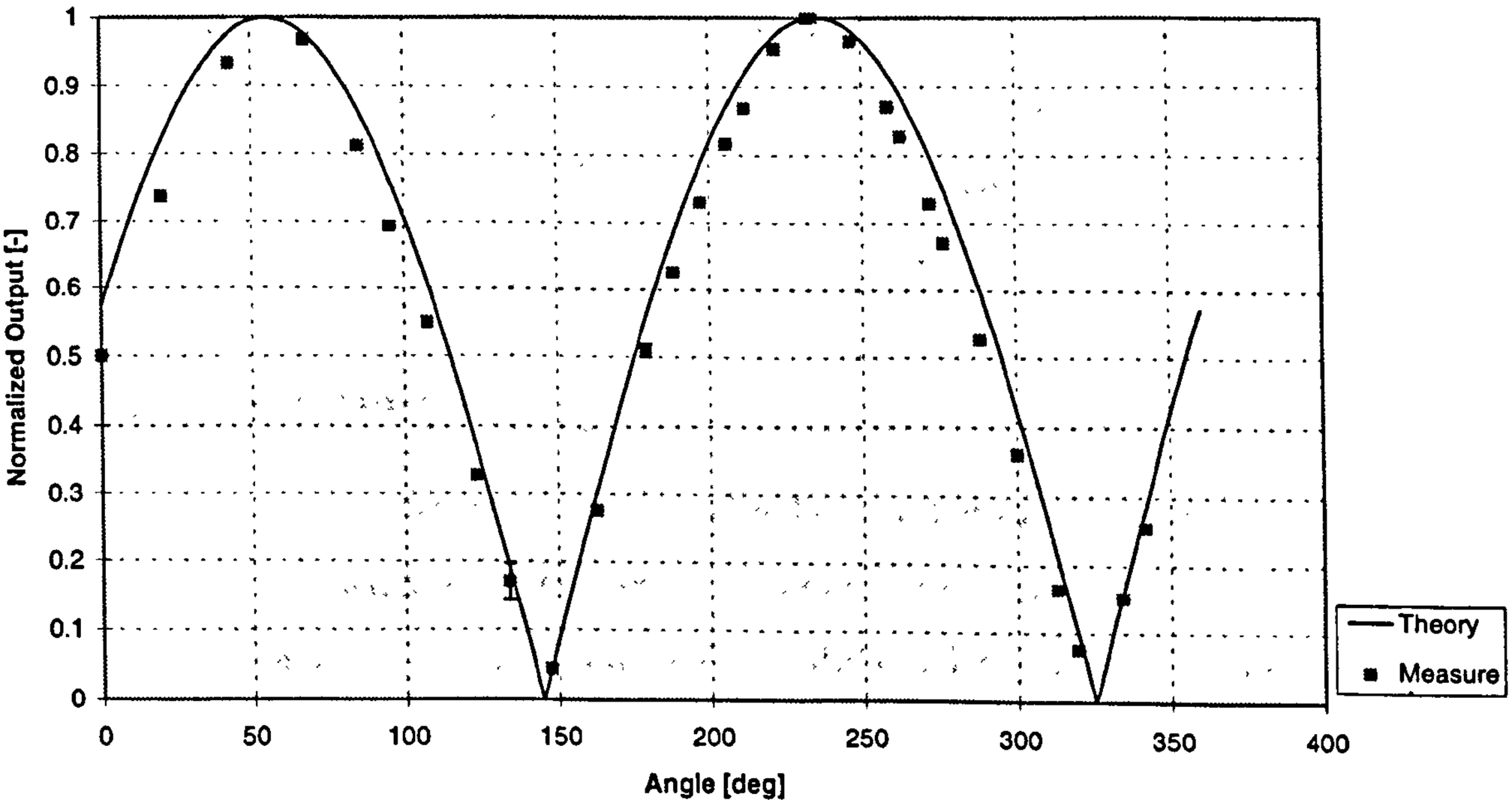

Figure 4.27: Normalized output of the electrooptic sensor with Bismuth Germanate as a function of the orientation of the electric field. *The orientation of electric field vector in the plane perpendicular to the laser beam is characterised by an rotational angle in the range 0..360° (relative values).*

relative error Δ expresses a normalized deviation of the output from its expected value (only E'_1 component is measured). The graph shows that the relative error has its maximum for electric field orientation at 45° to x'_1 and x'_3 axes. The investigated error does not exceed 0.04% even for high intensity fields of 1MV/m and can be, therefore, neglected.

The theoretical results were verified experimentally. The electric field was generated by two parallel electrodes held in a cylindrical base which could be rotated.

The crystal was suspended between the electrodes. The experiments were carried out with a constant AC electric field at the frequency of 50Hz. The output of the sensor is expected to be in the form of $|\cos(\varphi+\alpha_0)|$, where φ characterizes the orientation of the measured electric field and α_0 is a constant depending on the position of measuring scale. The measurements results, shown in Figure 4.27, confirmed the theoretical predictions. No influence of the electric field along the optical axis was observed.

Conclusions. The analysis of the transverse electrooptic effect in Bismuth Germanate shows that the orientation of the eigenaxes and the refractive indices are independent of the electric field component along the light beam propagation. The induced birefringence was found to depend on the orientation of the electric field in the plane perpendicular to the beam propagation, with its maximum value for electric fields along x_1' axis. The sensor based on Bismuth Germanate crystal was found to measure only one component of the electric field.

4.5.3 Summary

Isotropy of the electrooptic sensor with both Lithium Niobate and Bismuth Germanate was investigated theoretically and experimentally. It was found that a sensor using transversal electrooptic effect in crystals of Bismuth Germanate and Lithium Niobate is not isotropic. The sensor measures only one component of the electric field. The other two perpendicular components do not influence the output of the sensor. These conclusions were confirmed by experiments.

Chapter 5

External Space Charge Effect

This chapter addresses one of the main objectives of the project - investigations of the external space charge effect and the possibility of its elimination using an artificial extension of the sensing element. The presented discussion is limited not only to the electrooptic sensor; the results are also valid for any dielectric sensor sensitive to the electric field, exposed to a space charge environment.

The effect of the external space charge on the sensor is first explained in the introduction section 5.1. The problem of a charge, deposited on the surface of an electric field probe in a space charge environment, is then formulated as an electrostatic problem, and a mathematical model is developed by solving the Laplace equation for appropriate boundary conditions (section 5.2). The developed model is used in discussions of a dielectric probe, exposed to an electric field in bipolar and unipolar space charge environments, and to calculate the effect of the charge deposited on the surface of a dielectric probe (sections 5.3 and 5.4). The obtained theoretical results are verified in the experimental part 5.5 which also addresses the efficiency of the virtual extension of the sensing element to eliminate the effect of a space charge.

5.1 Introduction

When a dielectric probe is placed in a uniform electric field, the probe becomes polarised and the electric field around the probe is distorted as a consequence of

the difference between the relative permittivity of the probe and the air. Figure 5.1 shows equipotential and electric field lines around a dielectric probe in the shape of a ball, immersed in a homogeneous electric field in the air. The field is clearly distorted in the vicinity of the probe. If the measured environment is characterised by the presence of charged particles (*space charge environment*), the positively charged particles will drift in the electric field along the field lines, in the direction of the electric field intensity. Particles with negative charge will move in the opposite direction. Inevitably, some of the drifting charged particles will hit the surface of the probe as some of the electric field lines enter the surface of the dielectric probe. Assuming a very low surface conductivity of the dielectric probe, the charged particles will stay attached to the surface. This is a common assumption in most charging theories [3]. The process of charge deposition continues until an equilibrium is reached. This happens when the attractive force acting on a charged particle in the vicinity of the surface, caused by the original field, is equal to the repulsive force due to the deposited charge. The charge, deposited on the surface of an electric field probe, causes a change in the electric field intensity inside the probe, in this case in the electrooptic crystal. Thus the probe gives different readings according to whether the environment is with or without a space charge. In the presented work the described effect of the charge deposition is referred to as the *external space charge effect.*

In 1982 Hidaka [33] and in 1985 Robertson [64] et al. used electrooptic probes to measure the electric field intensity in a space charge environment of corona discharges. They solved the problem of the sensor output offset due to the charge deposition by rotating the sensing head. With the rotation, the charge deposition on the surface of the probe was uniform, and its contribution to the measured field was negligible. The accumulated charge only increased the perturbation of the measured field. However, rotating the electrooptic crystal was a source of optical disalignment, and as a consequence, a high level of noise was generated. Therefore, the aim of the presented work was to avoid the physical rotation of any sensor element in order to decrease the generated noise and to increase the sensor sensitivity to the measured electric field. The possibilities of dealing with the external space

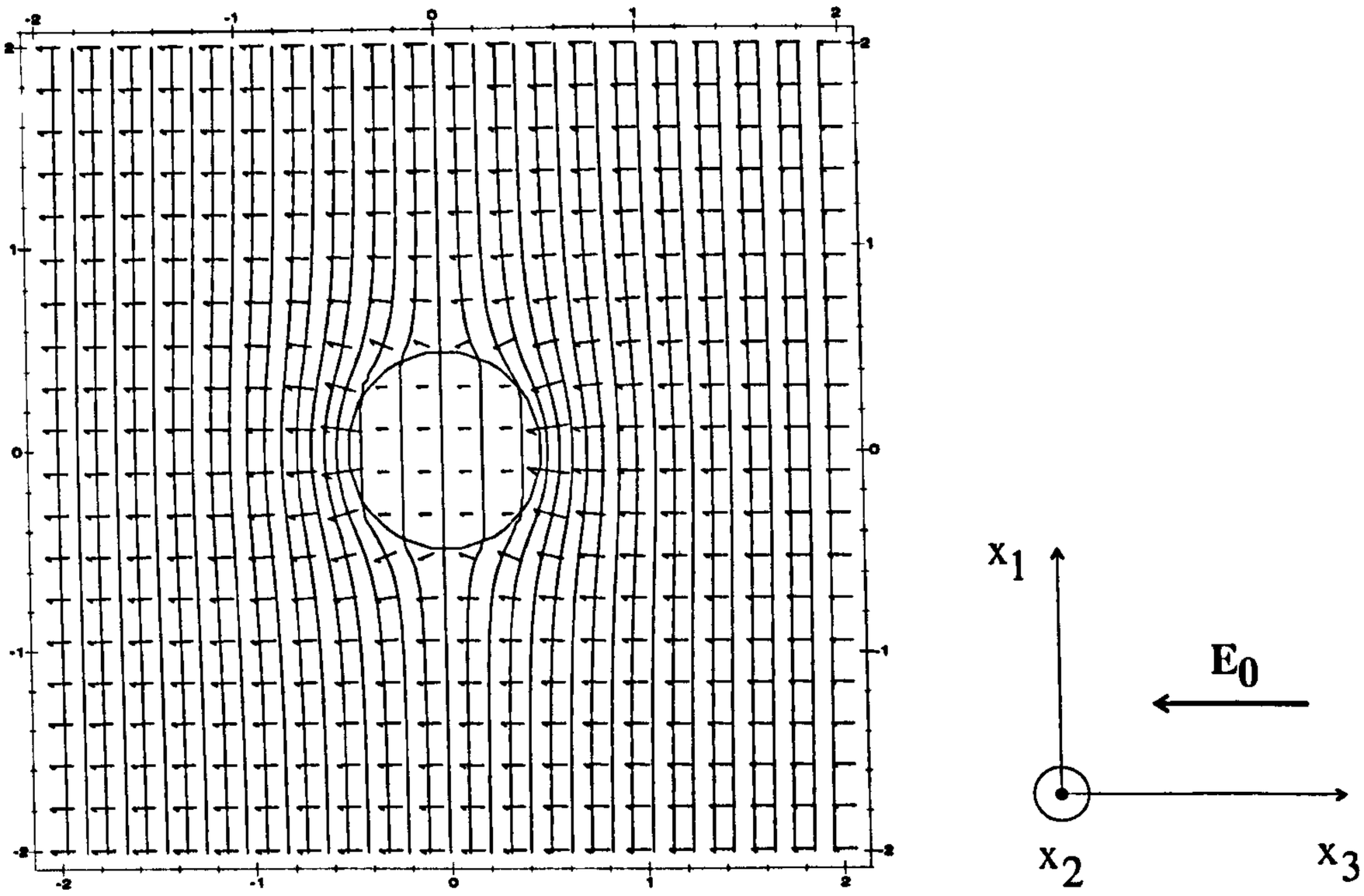

Figure 5.1: Equipotential lines and electric field intensity (arrows) for the dielectric ball of permittivity $\epsilon_r = 4$ immersed in a uniform electric field.

charge effect without using a physical rotation of any part of the sensor are discussed in the following sections.

5.2 Dielectric Ball Probe with a Known Surface Charge Density in Uniform Electric Field

This section describes a mathematical model which was created in order to investigate the effect of the space charge deposition on the probe surface and factors by which this effect can be influenced. The model was used in theoretical analysis and numerical simulations of the external space charge effect, in both unipolar and bipolar environment (sections 5.3 and 5.4), and in discussion on the efficiency of the artificial extension of the sensing element (section 5.5).

If the space charge densities of positive and negative ions are assumed to be small, so that the ions move in the environment independently and their contribution to the electric field is negligible, the problem of the external space charge deposition can be defined as an electrostatic problem of finding the potential and electric field

intensity generated by the original electric field, the polarization surface charge and the charge deposited on the surface of the probe. This assumption is justified as it was satisfied in all space charge experiments described in section 5.5. Considering the space charge contribution to the electric field to be negligible, the potential of the electric field V around a charged dielectric probe can be calculated using the Laplace equation:

$$\triangle V = 0 \tag{5.1}$$

where $\triangle$ is the Laplace operator.

To simplify the calculations of the potential V, the probe is considered as an isotropic dielectric ball of the diameter a and relative permittivity ϵ_r immersed in a homogeneous electric field (Figures 5.1 and 5.2). This approximation enables an analytical solution of the Laplace equation. The orientation of the electric field and the coordinate system are defined in Figure 5.2. Because of the geometrical symmetry of the dielectric probe, the space charge is deposited on the surface of the probe with a distribution which is symmetrical around the x_3 axis. It is suitable to use the polar coordinate system (Figure 5.2) because the E_ϕ component of the electric field in polar coordinates, as well as the derivative $\partial V/\partial\phi$, are equal to zero. Thus the original 3-dimensional problem of solving (5.1) is reduced to 2 dimensions and the 2-dimensional Laplace equation is readily solved using the method of separation of variables (e.g.[6], a short description is also in appendix B):

$$V = \sum_{n=0}^{\infty} A_n r^n P_n(\cos\theta) + \sum_{n=0}^{\infty} B_n r^{-(n+1)} P_n(\cos\theta) \tag{5.2}$$

where A_n and B_n are coefficients satisfying boundary conditions and $P_n(cos(\theta))$ are Legendre's polynomials of n-th order with argument $\cos(\theta)$ ([1]). The equation (5.2) is a general solution of the Laplace equation which is valid for both inside and outside the dielectric ball but not on its surface where we assume a layer of a deposited charge. The problem of finding the electric field potential in the case of a probe with a charge deposited on its surface, immersed in a uniform field, can be solved by imposing the following boundary conditions:

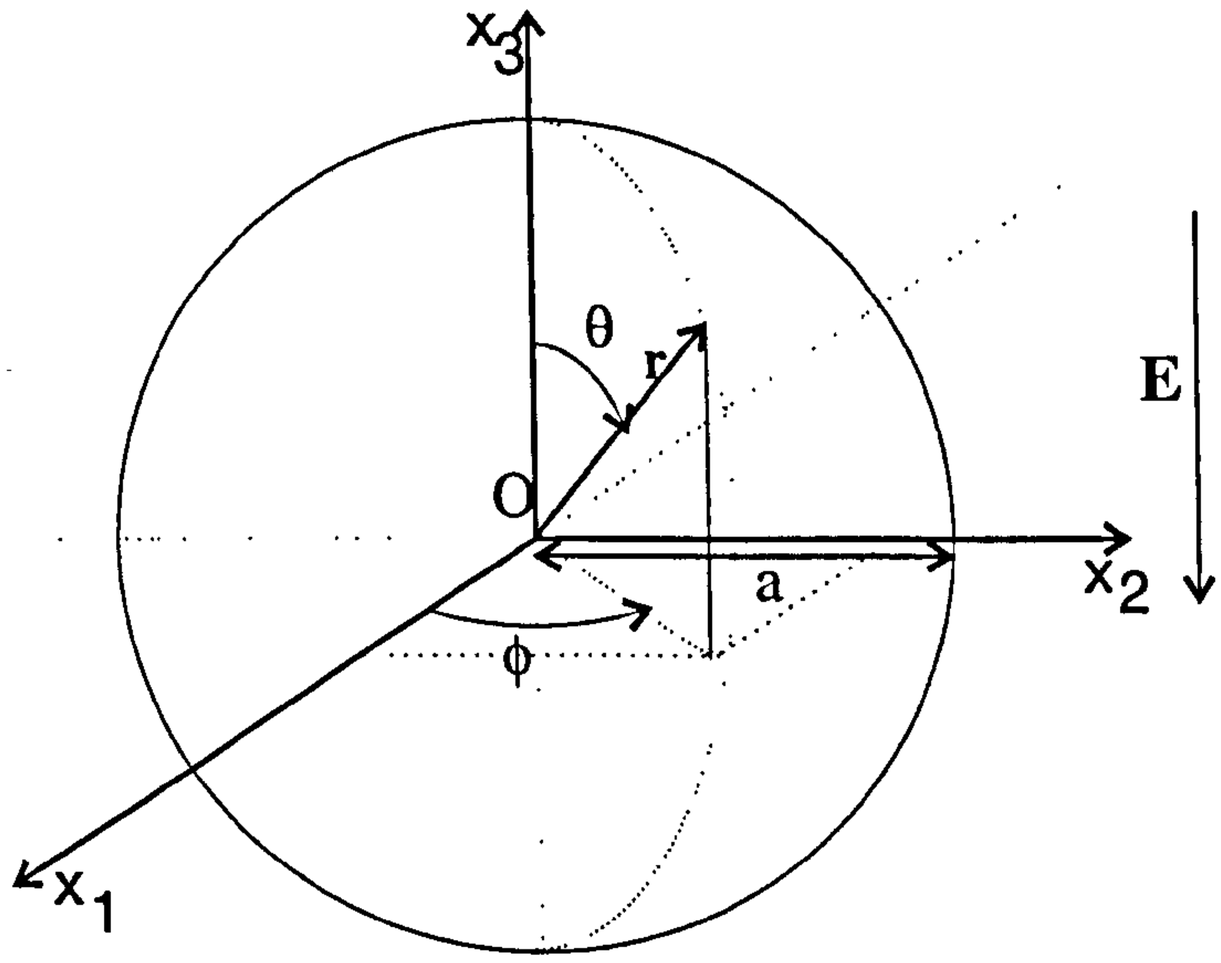

Figure 5.2: Polar coordinate system (r, ϕ, θ). *The dielectric probe was modeled as an isotropic ball of dielectric permittivity* ϵ_r *exposed to a uniform electric field* **E**.

1. The electric field is uniform in the absence of the sphere:

   $V \to -\infty$ for $x_3 \to -\infty$

   $V \to +\infty$ for $x_3 \to +\infty$

2. Potential V is continuous across the boundary ([6])

3. the normal components D_{n1}, D_{n2} of the electrical displacement vector **D** are not continuous any more and satisfy ([6])

   $D_{n1} - D_{n2} = \sigma;$ for $r = a$

   where σ is a surface charge density, a is the probe diameter.

The surface charge density acquires the same axial symmetry as the electric field and can be, therefore, expressed as a function of only one variable *0*. Since the Legendre's polynomials form a complete set, the surface charge density σ can be expressed in the form of Legendre's expansion:

$$\sigma = \sum_{n=0}^{\infty} \sigma_n P_n(cos(\theta)) \tag{5.3}$$

where $\theta \in \langle 0..\pi \rangle$ (Figure 5.2) and σ_n are the coefficients of the Legendre's expansion. The coefficients A_n and B_n are then found using (5.2),(5.3) and the boundary conditions. The potential outside the probe V_{out} and the potential inside the probe

V_{in} can be finally expressed as

$$V_{out} = \frac{\sigma_0 a^2}{r} - E_0 r\cos\theta + \frac{[\sigma_1 + E_0(\epsilon_r - 1)]a^3}{r^2(\epsilon_r + 2)}\cos\theta + \ldots$$
$$+\frac{\sigma_n a^{n+2}}{(\epsilon_r + 1)n + 1}\frac{1}{r^{n+1}}P_n(\cos\theta) + \ldots \qquad n = 2,3,4\ldots \tag{5.4}$$

$$V_{in} = \sigma_0 a + \frac{\sigma_1 - 3E_0}{2 + \epsilon_r} r\cos\theta + \frac{\sigma_2}{a[2(1+\epsilon_r)+1]} r^2 P_2(\cos\theta) + \ldots$$
$$+\frac{\sigma_n a^{1-n}}{(\epsilon_r + 1)n + 1} r^n P_n(\cos\theta) + \ldots \qquad n = 2,3,4\ldots \tag{5.5}$$

where E_0 is the measured electric field intensity. Since the potential is defined as a negative gradient of the electric field intensity

$$\mathbf{E} = -\nabla V \tag{5.6}$$

the components of the electric field intensity in polar coordinates inside ($E_{rin}, E_{\theta in}$) and outside ($E_{rout}, E_{\theta out}$) the dielectric probe are easily obtained:

$$E_{rout} = \frac{\sigma_0 a^2}{r^2} + E_0\cos\theta + 2\frac{[\sigma_1 + E_0(\epsilon_r - 1)]a^3}{r^3(\epsilon_r + 2)}\cos\theta$$
$$+(1+n)\frac{\sigma_n a^{n+2}}{(\epsilon_r + 1)n + 1}\frac{1}{r^{n+2}}P_n(\cos\theta) + \ldots \quad n = 2,3,4\ldots \tag{5.7}$$

$$E_{\theta out} = -E_0\sin\theta - \frac{[\sigma_1 + E_0(\epsilon_r - 1)]a^3}{\epsilon_r + 2}\frac{1}{r^3}\frac{\partial P_1}{\partial\theta}$$
$$-\frac{\sigma_n a^{n+2}}{(\epsilon_r + 1)n + 1}\frac{1}{r^{n+2}}\frac{\partial P_n(\cos\theta)}{\partial\theta} - \ldots \qquad n = 2,3,4\ldots \tag{5.8}$$

$$E_{rin} = -\frac{\sigma_1 - 3E_0}{2 + \epsilon_r}\cos\theta - \frac{\sigma_2}{a[2(1+\epsilon_r)+1]} r P_2(\cos\theta) - \ldots$$
$$-\frac{\sigma_n a^{1-n}}{(\epsilon_r + 1)n + 1} r^{n-1} P_n(\cos\theta) - \ldots \qquad n = 3,4,5\ldots \tag{5.9}$$

$$E_{\theta in} = \frac{\sigma_1 - 3E_0}{2 + \epsilon_r}\sin\theta - \frac{\sigma_2}{a[2(1+\epsilon_r)+1]} r\frac{\partial P_2(\cos\theta)}{\partial\theta} - \ldots$$
$$-\frac{\sigma_n a^{1-n}}{(\epsilon_r + 1)n + 1} r^{n-1}\frac{\partial P_n(\cos\theta)}{\partial\theta} - \ldots \qquad n = 3,4,5\ldots \tag{5.10}$$

The derived equations express the electric field inside and outside the probe as a function of the probe diameter, the permittivity and the known surface charge density. A detailed derivation can be found in appendix B.

Conclusions. Assuming small densities of the charged particles in a space charge environment, the problem of the space charge effect was defined as an electrostatic problem. The dielectric probe was approximated by a dielectric ball, and by solving the Laplace equation the external and internal electric field intensities were calculated for a known surface charge distribution.

5.3 Dielectric Probe in a Bipolar Environment

The mathematical model described in the previous section is applied to the problem of a dielectric probe in a bipolar environment, in order to evaluate the effect of the space charge deposition on the measured field and on the output of the sensor. A bipolar environment contains both positive and negative ions which drift in opposite directions along the field lines, due to the presence of an electric field. It is assumed that once the ion hits the surface of the probe it will stay attached to it so that there is no migration of the charges on the surface. This mechanism of charging is known as field charging or Pauthenier charging. However, the analysis of Pauthenier charging, as presented in [3], assumes that the dielectric ball is exposed to the electric field in such a way that the resultant charge density on the surface is uniform (a particle of diameter a rotates randomly in the field). In the presented case, the probe is assumed to be fixed with respect to the electric field orientation, and the problem is approached in a slightly different way.

The densities of positive and negative ions and their mobilities are first assumed to be the same. Once the charge starts accumulating on the probe the perturbation of the field will change, as will the force acting on the ions in the vicinity of the probe surface (see the electric field lines in the vicinity of the probe surface in Figure 5.1, 5.3 and 5.4). In the situation depicted in Figure 5.1 the left hemisphere will collect negative ions whereas the right hemisphere collects the positive ions. Due to the axial symmetry, the electric field force in the vicinity of the surface **F** will

have only two components: $\mathbf{F}_r, \mathbf{F}_\theta$. The force $\mathbf{F}_r$ is pushing the ions away from the surface when positive (orientation away from the surface) or pulling them towards the surface when negative, whereas $\mathbf{F}_\theta$ tries to move them along the surface. The charging process will cease, once the radial force acting on the ions in the vicinity of the surface is equal to zero. In this case the electric field lines will not enter the dielectric probe, and ions will drift past the probe without further deposition (Figure 5.4). Thus the equilibrium condition can be expressed in the form:

$$\mathbf{F}_r = 0 \tag{5.11}$$

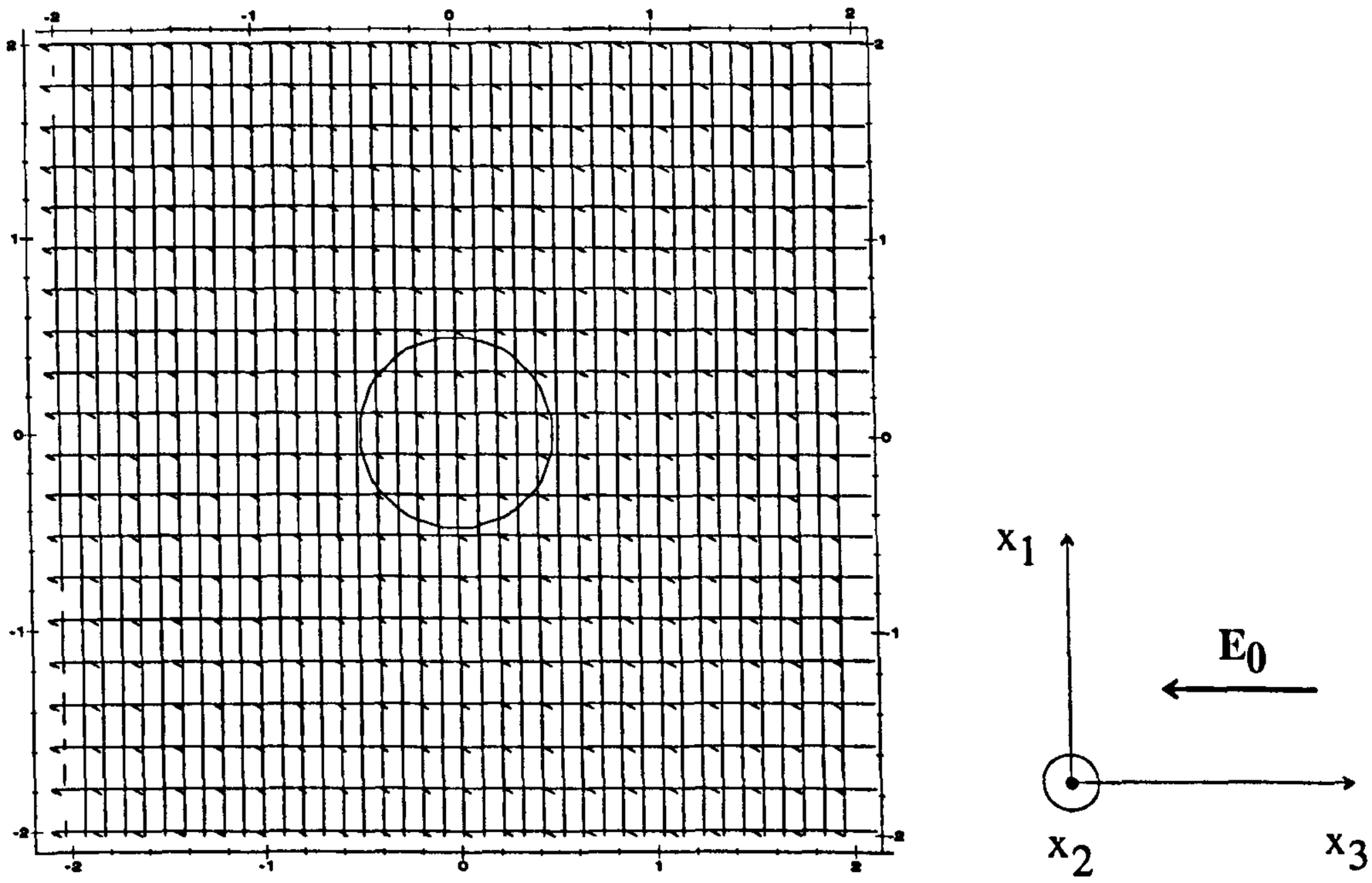

Figure 5.3: Equipotential lines (vertical lines) and electric field intensity (arrows) for the dielectric ball of permittivity $\epsilon_r = 4$ immersed in a uniform electric field with surface charge density $\sigma = \sigma_0 cos(\theta)$ where $\sigma_0 = -3\epsilon_0$.

Since in a bipolar environment charges of both polarities are available the charge deposition will be over the whole surface of the probe and, therefore, the equilibrium state will be reached when the condition (5.11) applies to the whole surface of the probe. As in the case of the surface charge density σ, the radial component of the electric field intensity on the surface of the dielectric probe can be written in the form of Legendre's expansion, and the equilibrium condition (5.11) can be written

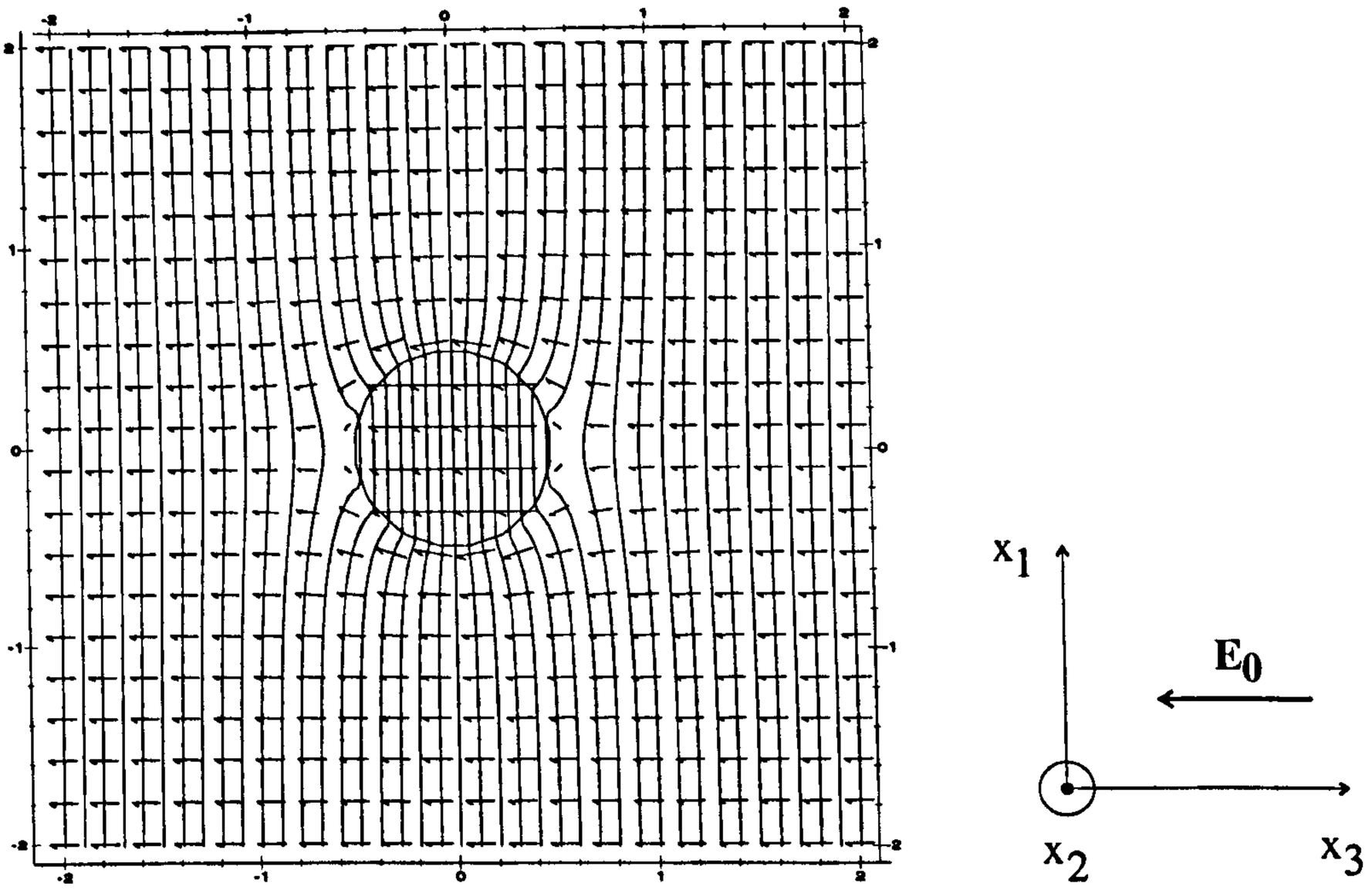

Figure 5.4: Equipotential lines (vertical lines) and electric field intensity (arrows) for the dielectric ball of permittivity $\epsilon_r = 4$ immersed in a uniform electric field with surface charge density $\sigma = \sigma_0 cos(\theta)$ where $\sigma_0 = -6\epsilon_0$.

as:

$$E_r = \sum_{n=0}^{\infty} e_{rn} P_n(\cos\theta) = 0 \tag{5.12}$$

where e_{rn} is the n-th coefficient of the Legendre's expansion and $P_n(\cos\theta)$ is the n-th Legendre's polynomial with argument $\cos\theta$. The coefficients σ_n can be found using the orthogonal properties of Legendre's polynomials [1]:

$$\int_{-1}^{1} P_n(cos\theta) P_m(cos\theta) d(\cos\theta) = \frac{2\delta_{mn}}{2n+1}, \quad m, n = 0, 1, 2, \ldots \tag{5.13}$$

where δ_{mn} is the Kronecker delta [1]. Substituting $r = a$ (surface of the dielectric ball) in (5.7) one obtains the expansion (5.12). By multiplication of both sides of (5.12) by $sin(\theta)P_n(cos\theta)$ and finally integrating over the interval $(0, \pi)$, the σ_n coefficients are found to be:

$$\sigma_n = 0, \quad n \neq 1 \tag{5.14}$$

$$\sigma_1 = -\frac{3}{2} E_0 \epsilon_r \epsilon_0 \tag{5.15}$$

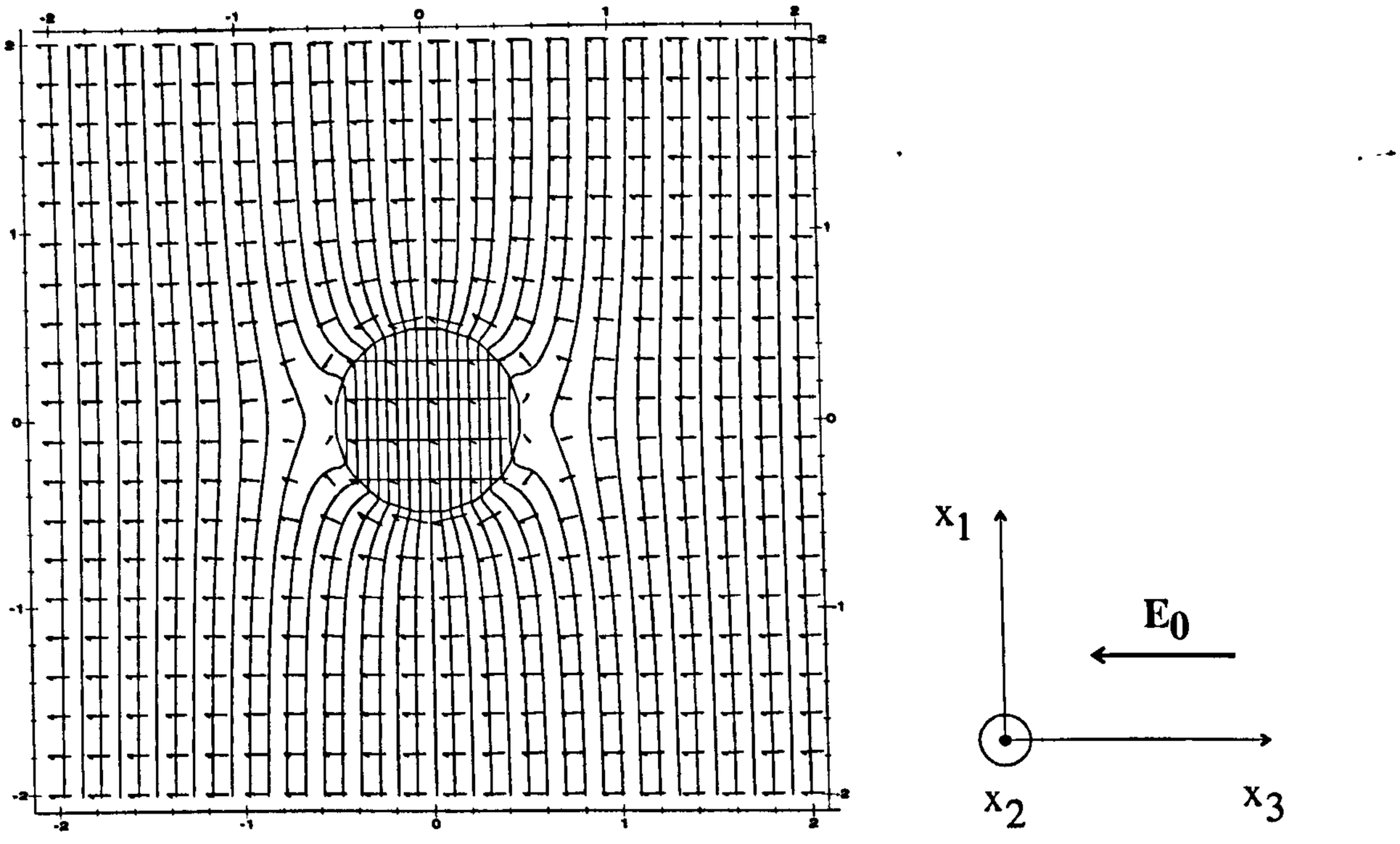

Figure 5.5: Equipotential lines (vertical lines) and electric field intensity (arrows) for the dielectric ball of permittivity $\epsilon_r = 4$ immersed in a uniform electric field with an excessive surface charge density $\sigma = \sigma_0 cos(\theta)$ where $\sigma_0 = -8\epsilon_0$. *The repulsive force acting on the ions in the vicinity of the surface can be seen at the poles of the probe.*

The equilibrium surface charge density in a bipolar environment can be finally written as

$$\sigma(\theta) = -\frac{3}{2} E_0 \epsilon_r \epsilon_0 cos\theta \tag{5.16}$$

The corresponding internal field in the probe is obtained by substituting the calculated surface charge density (5.16) into (5.9) and (5.10), and transforming it back to the cartesian coordinates:

$$\mathbf{E}_{in} = \frac{3}{2}\mathbf{E}_0 \tag{5.17}$$

The derived equation (5.17) shows that the field inside the dielectric ball is uniform with an orientation in the direction of the original field $\mathbf{E}_0$. The internal field is found to be independent of the permittivity of the probe and directly proportional to the external field. Moreover, it is 1.5 times higher than the external field. Thus theoretically in the bipolar environment the electrooptic probe should measure the field with higher sensitivity. For example, if the dielectric probe has the relative permittivity of 85 (Lithium Niobate) the internal field in an environment without a

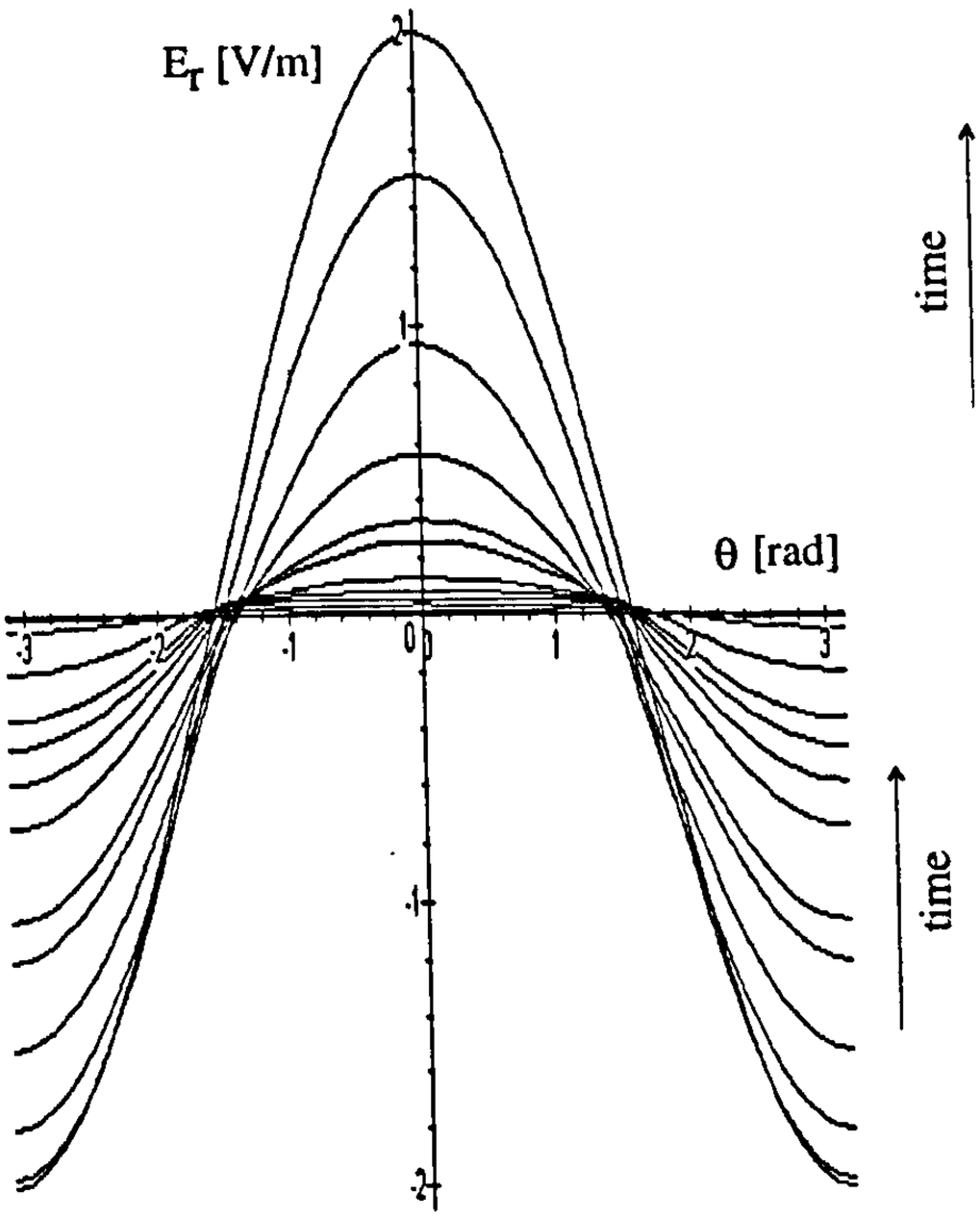

Figure 5.6: Time development of the radial component of the electric field intensity and the surface charge density on the surface of the probe in bipolar environment. *The surface charge density approaches the function* $\sigma = \sigma_1 \cos\theta$ *and the radial component of the electric field in the vicinity of the probe surface tends to zero.*

space charge would be $0.3E_0$ (4.11), whereas in the bipolar environment the field is $1.5E_0$. The internal field is 5 times higher in the presence of the ions, theoretically increasing the sensitivity by 5 times.

Figures 5.3, 5.4 and 5.5 show the electric field and potential lines for the dielectric probe of relative permittivity 4 with a surface charge density $\sigma = \sigma_1 \cos\theta$ immersed in a uniform electric field for different values of σ_1. Another interpretation of these figures could be the development of the electric field and potential in time, when a charge is deposited on the surface of the dielectric probe proportionally to $E_r(\theta)$. Such an interpretation refers to the situation when concentrations and mobilities of both positive and negative ions are the same. One can observe the deviation of the electric field lines from the surface, which is complete in Figure 5.4 which depicts

the equilibrium state, when ions are expected to flow around the probe without a deposition. The field lines are wrapped around the ball and do not enter or come out of the surface. Figure 5.5 shows the situation when an excessive amount of the space charge is deposited on the dielectric surface. Clearly, there are pronounced areas where the drifting charge is repelled or the already deposited charge is pulled out of the surface. In a more real situation, whether or not this pulling force would be successful would depend on the forces bounding ions and other charged particles (if present) to the surface.

In reality the mobility of the charged particles can differ greatly and their concentrations can also be different. In such a case the charge deposition will be faster from one side of the probe depending on the ion mobilities and concentrations. Figure 5.6 shows the simulated development of the surface charge density and the radial component of the electric field on the probe surface in an environment where the deposition of the positive charges is 3 times slower than the deposition of the negative charges. The radial component of the electric field in the vicinity of the probe surface is decreasing faster in the area of the positive E_r, due to the faster deposition of negative ions. After a while, when the surface charge density is approaching its equilibrium value, the deposition of negative ions slows down and becomes slower than the deposition of positive ions. It can be noticed that the deposition area for positively charged particles (area with $E_r < 0$) is enhanced at the beginning of the charging process. As the charge deposition continues, the radial component of the field on the surface tends to zero and the charge distribution comes to the saturation value which is defined by (5.16).

As in the analysis of Pauthenier charging in reference [3], it must be said that a finite time is needed for the equilibrium to develop. This transition time will depend on the concentration and mobility of ions in the environment and on the probe permittivity.

Conclusion. Based on the model developed in the previous section the surface charge distribution and internal field were analytically calculated for the case of a bipolar environment. The electric field in the probe was found to be uniform, linearly dependent only on the external measured field.

5.4 Dielectric Probe in a Unipolar Environment

The equilibrium state described in section 5.3 for a bipolar environment will be different in a unipolar environment with charged particles of only one polarity. In this case the charge deposition is limited only to one hemisphere of the probe and, therefore, the final charge distribution on the surface will differ from the previous case. Based on the results derived for bipolar environment and using the same assumptions, the internal electric field along the x_3 axis (Figure 5.2) is assumed to be directly proportional to the external measured field so that it can be written as

$$E_{in3}(\theta, r) = C(\theta, r)E_0 \tag{5.18}$$

where E_{in3} is the electric field component inside the probe, C is a constant for a given position (θ, r) and E_0 is the measured external field. The factor C depends on coordinates since the field inside the probe will be proved to be no more homogeneous and uniform. This hypothesis is investigated theoretically in this section and experimentally in section 5.5.

The constant C can be obtained from the mathematical model once the deposited charge distribution σ is known. This was not found analytically but it was estimated by simulating the deposition of the ions in a unipolar environment. Generally, the equilibrium condition (5.11) is not valid over the whole surface of the probe. It must be substituted by a condition $\mathbf{F}_r \geq 0$, where the equality sign applies to the charge collecting area. It is not necessarily over the whole hemisphere as the simulations showed.

The process of charge deposition was simulated for a negative unipolar environment using the developed mathematical model. By adding step by step layers of the negative charge, the simulation approached the equilibrium state. In each iteration the charge was deposited only in areas with a positive electric field intensity, where the ions are attracted to the surface. The deposited charge density was proportional to the radial component of the electric field on the surface of the probe. This means that the highest deposition rate is in those places where E_r is negative and its absolute value has a maximum. There is no charge deposition allowed if $E_r \leq 0$. The graphs of the radial component of the electric field and the deposited surface charge

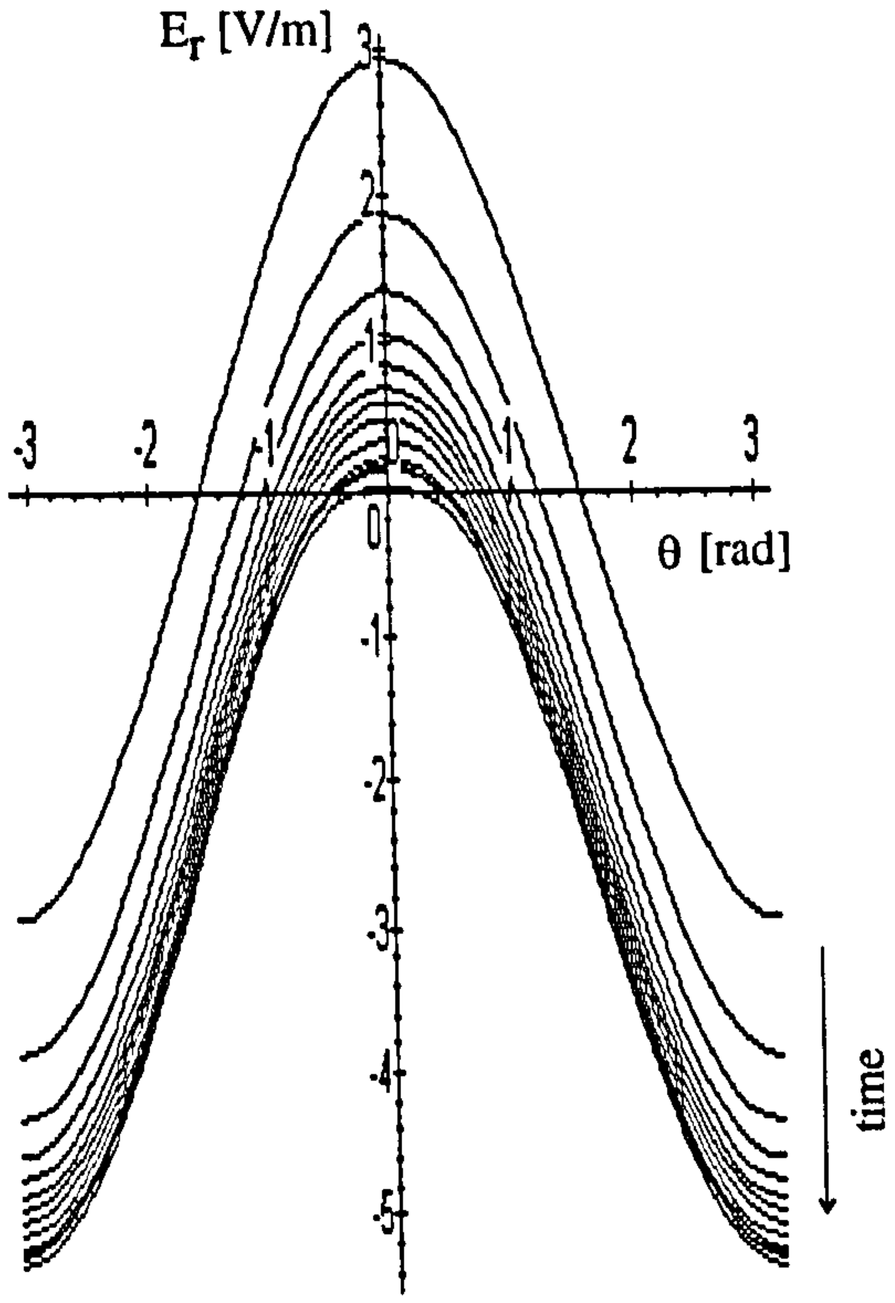

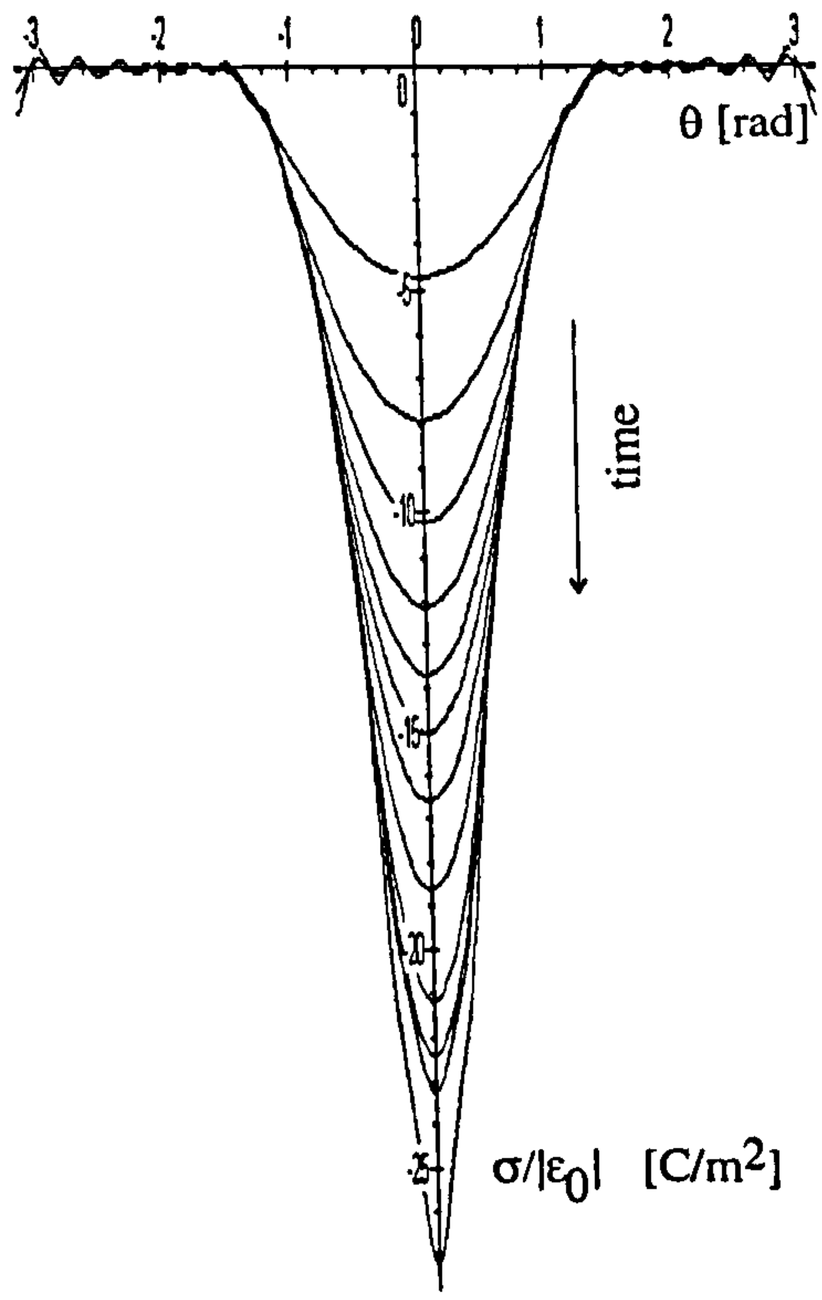

Figure 5.7: The development of the radial component of the electric field intensity and the surface charge density on the surface of the probe ($\epsilon_r = 85$) in unipolar environment. *The charge exposed to the positive radial force was not allowed to leave the surface.*

density, on the probe with relative permittivity of 85, are shown in Figure 5.7. It can be seen that during the process of charge deposition, the area collecting the charges is getting smaller. In some parts of the probe surface, the already deposited charge is exposed to a force which is trying to pull this charge away from the surface. Whether this force successfully detaches the already deposited charge will depend on the way of bonding of the ions to the surface [76].

Figure 5.8 shows the development of the radial component of the electric field and the surface charge density, on the surface of the probe with relative permittivity $\epsilon_r = 4$. In this simulation the already deposited charge was allowed to leave the surface if exposed to a positive force $\mathbf{F}_r$, which pulls it away from the surface. The rate of the charge detachment was taken to be proportional to the radial component of the electric field E_r. It can be seen that the region of the deposited charge

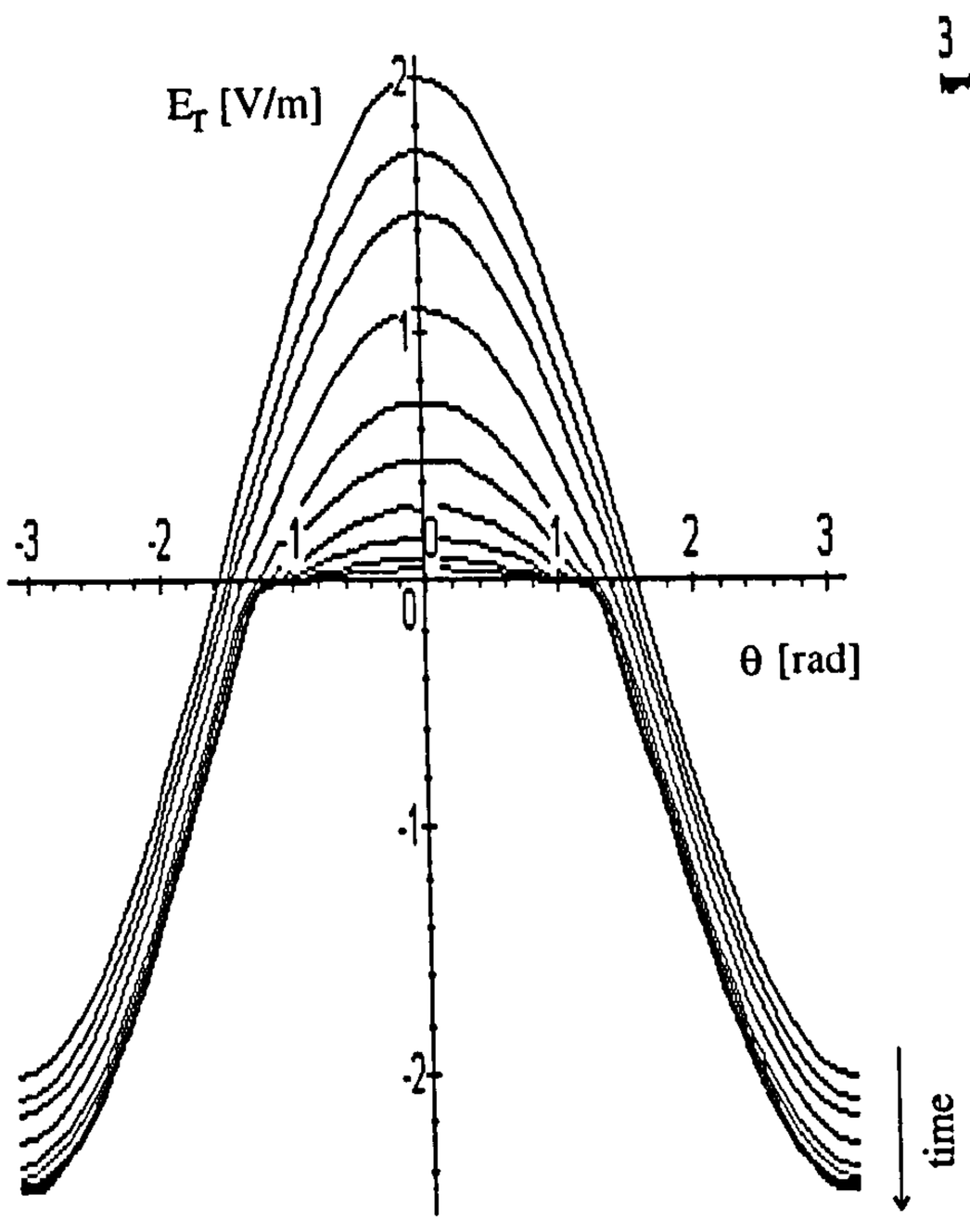

Figure 5.8: The development of the radial component of the electric field intensity and the surface charge density on the surface of the probe ($\epsilon_r = 4$) in unipolar environment. *The charge exposed to the positive radial force was allowed to leave the surface.*

does not span the whole hemisphere as in Figure 5.7, and the condition for the equilibrium $\mathbf{F}_r = 0$ does not necessarily hold on the whole hemisphere, as it has been already pointed out. The oscillations in the obtained σ function are due to the limited number of terms used in the Legendre's expansion of this function. These simulations were run using twenty terms in the expansion and usually about 500 iterations. Figure 5.9 shows the electric field in the probe and its vicinity for the surface charge distribution corresponding to the equilibrium state in Figure 5.8. The field in the probe is clearly non-uniform. Its E_{in3} component along the external field varies from the value of $1.1E_0$ near the deposition surface to $0.7E_0$ on the opposite side.

Table 5.1 shows the values of the E_{in3} component of the electric field in the middle of the probe exposed to a uniform field of 1V/m. The electric field intensity

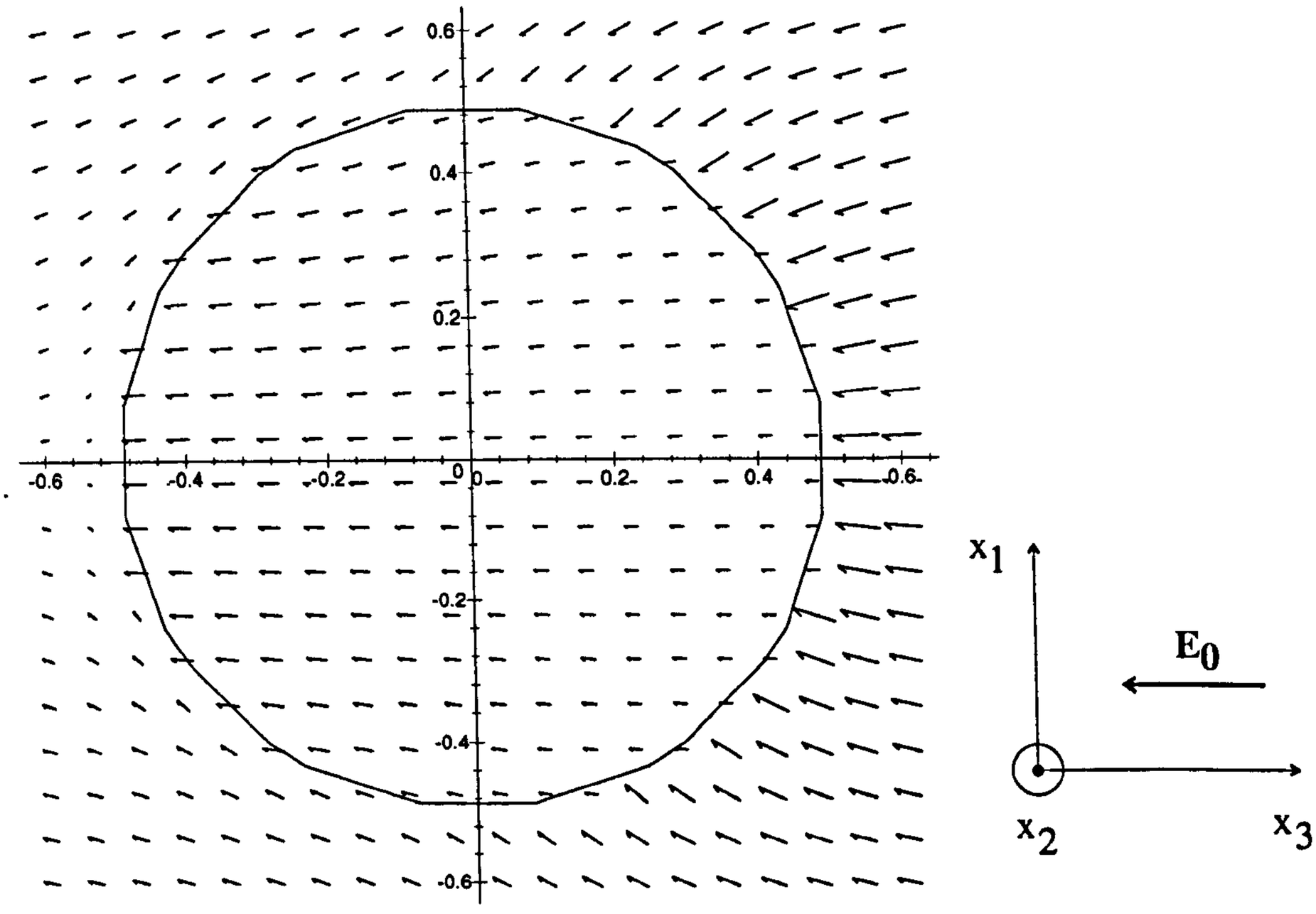

Figure 5.9: The electric field intensity in the dielectric probe immersed in a unipolar space charge environment with a uniform electric field.

E_{in3} was calculated for two different permittivities of the probe, as explained above. The values of E_{in3} in an environment without a space charge and in a bipolar environment are shown for comparism. Method 1 refers to the simulations in which the already deposited charge is not allowed to leave the surface of the probe (Figure 5.7), whereas method 2 allows the charge detachement (Figure 5.8). Both methods gave very similar results showing that the constant $C(r, \theta)$ is a function of the relative permittivity ϵ_r, in contrast to the bipolar environment where it depends only on the external electric field.

Conclusions. The surface charge density was derived considering two different mechanisms of charging: one with the possibility for the deposited charges to be detached from the surface of the probe; and the other without this possibility. The results obtained by both methods are very close and confirmed the prediction that the internal field in a unipolar environment depends on the permittivity of the material. The proportionality constant $C(0,0)$ was found for probes with dielectric permittivities $\epsilon_r = 85$ and $\epsilon_r = 4$. However, proof that this constant is independent

Table 5.1: The calculated values of the internal electric field $E(0,0)$ in the centre of the dielectric probe exposed to a uniform electric field of 1V/m. *Method 1 enables the already deposited charge to be detached, in contrast to method 2 which does not allow it.* E_{in0} *is the internal electric field without any space charge,* E_{bi} *is the internal electric field in a bipolar environment.*

ϵ_r	$E(0,0)$ [V/m] method 1	$E(0,0)$ [V/m] method 2	E_{in0} [V/m] no deposition	E_{bi}/E_{in0} [-]
4	0.81	-	0.5	3
85	0.106	0.101	0.034	44

of the external electric field intensity was left to experiments.

5.5 Results of Space Charge Experiments

The experimental work was focused on the investigation of the possibilities of using the sensor for electric field measurements in a space charge environment. This section presents the experimental setup used to investigate the effect of the space charge environment on the electrooptic probe, and a discussion on the validity of the theoretical assumptions of the previous sections. The results of experiments with Lithium Niobate crystal are then compared with the theoretical predictions. Finally the efficiency of the artificial extension of the sensing head, as a means of eliminating the space charge effect, is discussed.

5.5.1 Experimental Setup

The experimental setup was arranged as shown in Figure 5.10. Since the electrooptic scheme was already discussed in section 4.1, the main focus is on the electric field and space charge generators.

The crystal was exposed to the electric field generated by two parallel plates. The plates had dimensions 0.3x0.3m and were 0.16m apart from each other. The positive ions were generated by a sharp needle maintained at a positive potential, placed in the middle of the aperture of the grounded electrode. The negative ions were generated by the negative corona discharge at a needle placed in the middle of

the aperture of the negative high voltage electrode. In experiments with a unipolar environment, a plain metallic plate was used as the negative bottom electrode.

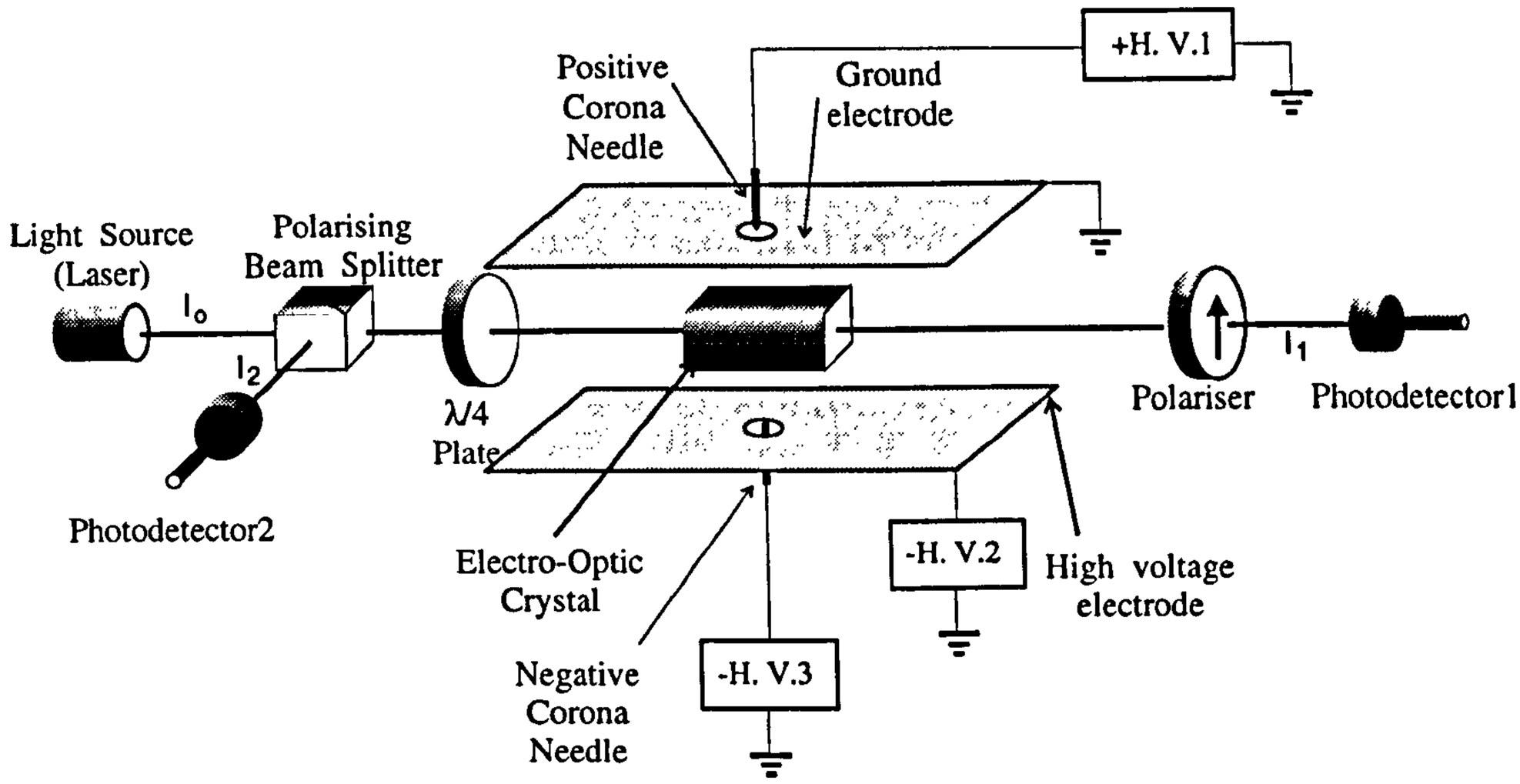

Figure 5.10: The experimental setup for measurements in space charge environment.

The electric field was considered to be generated only by the plate electrodes and the electric field contribution due to the high potential needles was considered to be negligible. This assumption was based on the simulation results obtained using electrostatic finite element software package (ALGOR). In these simulations the positive needle with potential 4kV (corona onset votage was > 2.2kV) was found to influence the electric field between the plates by 2.8%. This value is based on the electrostatic modeling which does not take into account the effect of the generated space charge. In the case of the corona generation, the electric field can depend on the generated space charge density. The onset of the space charge effect can be estimated by comparing the number of field lines from the electrodes with that from the space charge in the volume between the electrodes [11]. For the values of the corona current and the current between the electrodes, it can be shown that the space charge will effect the field between the needle electrode and the nearest plate electrode but its influence on the field between the plate electrodes can be neglected. Therefore, the assumptions made in the theoretical analysis were considered to be a reasonable approximation. The effect of the needle potential was also verified experimentally. Within the limits of the measurement error there was no difference

observed in the sensor output when the positive needle potential was zero and 1kV (below corona onset). The generated electric field could be varied from 0 to 93kV/m.

The designed space charge generator may not be considered as an ideal source of a uniformly distributed space charge. It is assumed that the generated ions will be flowing as 'water from the shower hub' and the ion flow covers the whole area of the crystal. The space charge density is assumed to be proportional to the current between the electrodes which can be regulated by the needle potential. The corona onset was experimentally established to be about 2.2kV depending on the position of the needle and its polarity. It was possible to change the space charge current between the electrodes from 0 to $0.4\mu A$ by changing the needle potential up to 4kV. The overall corona current at the potential of 4kV reached about $14\mu A$. Thus only a very small part of the generated charge was flowing between the electrodes.

One of the main problems experienced during the measurements was a drift of the zero output level. The drift was caused mostly by an uncorrelated long term drift of the photodetectors, and to a lesser extent, by laser power fluctuations and crystal of Lithium Niobate. It was, therefore, necessary to define the zero level before each measurement. In the case of the space charge measurements, the zero level was defined always after neutralizing the sensing element by an AC corona discharge and waiting until the output was stable. The measurements were performed by switching on the electric field and afterwards the ion (charge) source. The response of the sensor was monitored every 500ms for approximately 20s and the output value was obtained by averaging the acquired data. If not stated otherwise, the error bars in the graphs refer to the standard deviation of the data acquired in the 20s interval and, therefore, this error indicates the fluctuations of the output due to the DC drifts of the whole sensor.

5.5.2 Experiments with Lithium Niobate Crystal.

Figure 5.11 shows the typical response of the sensor in a unipolar environment. The first step in output corresponds to an applied DC field of about 38kV/m, whereas the second step at time 1508s occurred when the positive ion source was switched

on. The equilibrium state was established almost immediately after the activation of the charge generator for any voltage above the corona onset. The electric field and the ion source were switched off at time 1539s. The sensor output, however, did not return to the same value as before the beginning of the measurement. The charge deposited on the surface of the probe stays partially attached to the surface, and it is, therefore, necessary to neutralize the sensing head after each measurement if a correct reading is to be obtained. The neutralization by an AC corona discharge was done in the time span from 1552s to approximately 1570s.

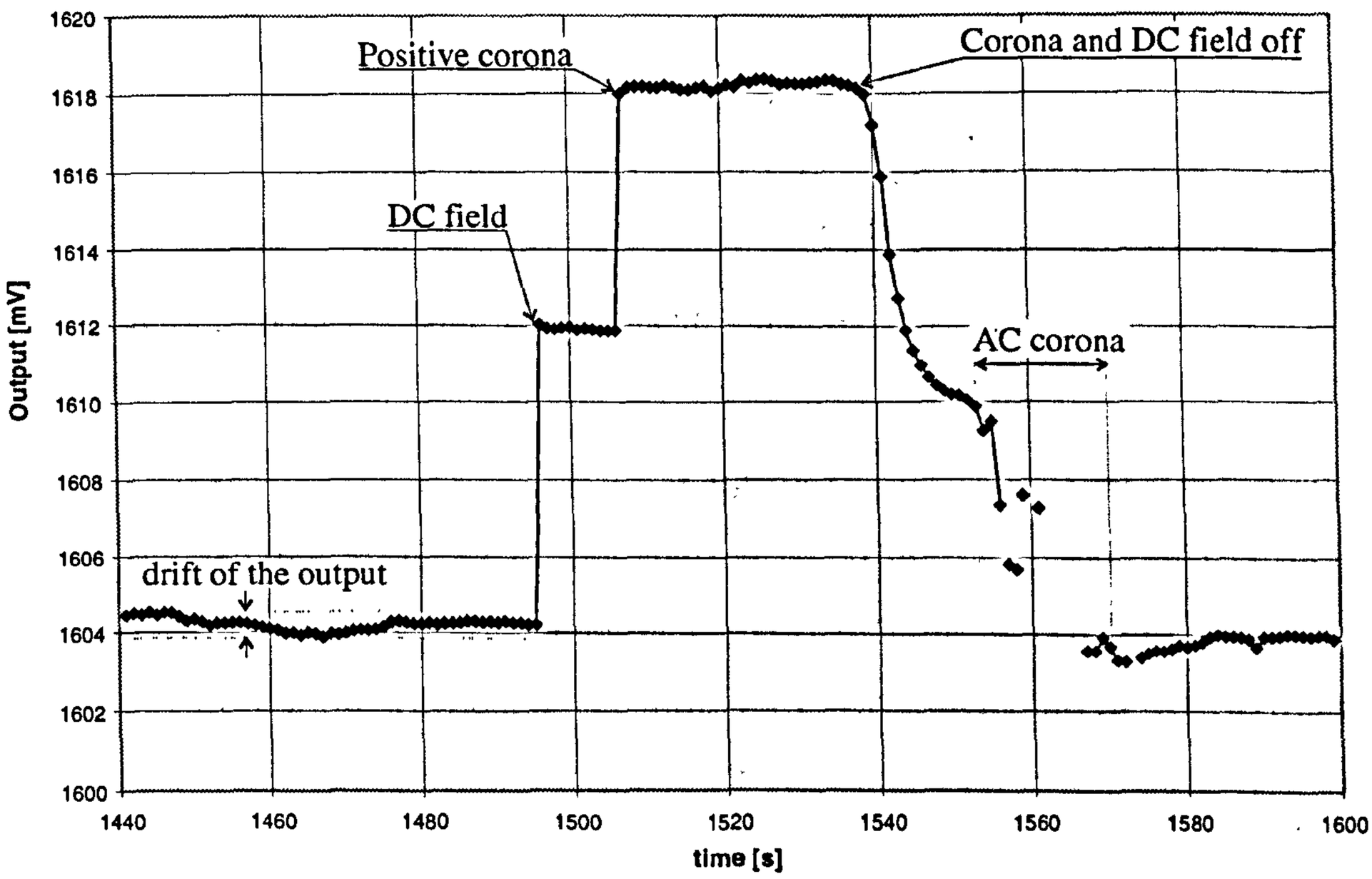

Figure 5.11: Response of the sensor to a uniform electric field (37.5kV/m) in the unipolar environment.

Changing the applied electric field and the corona generating voltage, the sensor transfer characteristic was measured. Figure 5.12 depicts the normalized output as a function of the applied electric field in both the unipolar environment and the environment without space charge. The sensor output is found to be a linear function of the applied electric field which verifies the hypothesis of the internal electric field being proportional to the applied external electric field. The output of the sensor was linear even without the neutralisation, as long as the electric field was increased. However, when decreasing the field without neutralization after each

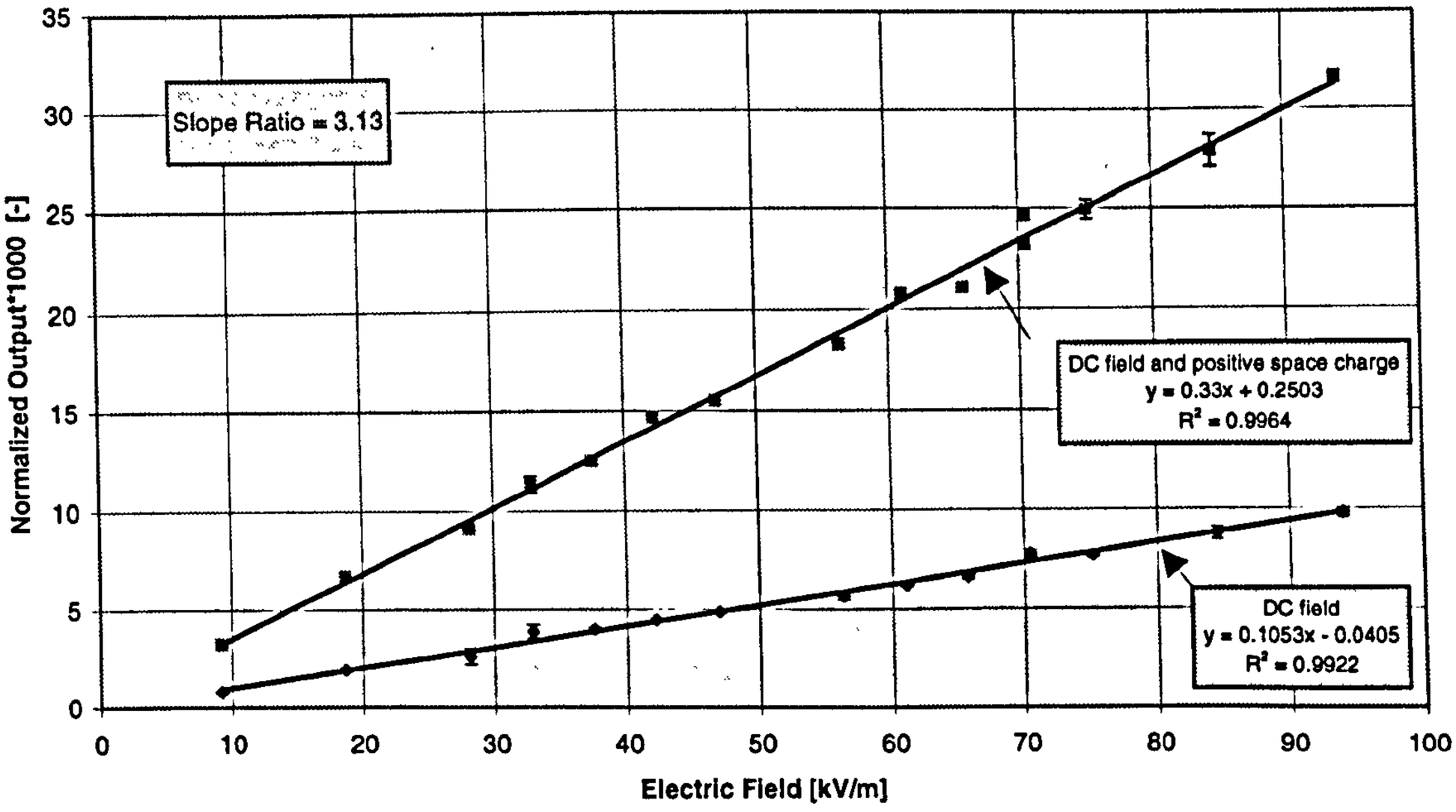

Figure 5.12: Normalized output change $(V_{out}-V_0)/V_0$ as a function of applied electric field for the DC sensor with Lithium Niobate crystal without any enclosure in both unipolar space charge environment and environment without space charge. *V_{out} is sensor output, V_0 is the output voltage without electric field; humidity 37%, T=21.9°C.*

measurement the sensor response did not follow the transfer characteristic, due to the excessive charge attached to the surface. The measurements in the unipolar environment were in a remarkable agreement with the theoretical prediction. The ratio of the internal electric field in the unipolar environment and in the environment without a space charge was estimated to be 3.11 (table 5.1), and the measured value is 3.13 (Figure 5.12). Table 5.2 shows slopes of the transfer characteristics for different corona currents. The space charge density is assumed to be proportional to the current between the electrodes, the value of which is estimated in table 5.2 as I_{SPCest}. The slopes are found to be equal within the experimental error. This leads to the conclusion that in the performed experiments the sensor response was not influenced by the space charge density, as had been suggested in the theoretical part.

Difficulties were experienced when measuring high electric field intensities ($\approx$ 70 kV/m). The output of the sensor still showed a step response to the switching on of the ion generator as before; however, it did not stay constant (Figure 5.13). After a while, depending on the applied field intensity, the output started rising. The

Table 5.2: Measured slopes of sensor transfer characteristics for different corona currents I_c. I_{SPCest} *is the estimated value of the current between the electrodes caused by the drifting space charge. The current* I_{SPCest} *is proportional to the space charge density.*

$I_c[\mu A]$	2	4	8	14
$I_{SPCest}[\mu A]$	0.23	0.3	0.34	0.43
$Slope[m/kV]$	0.338	0.314	0.352	0.33

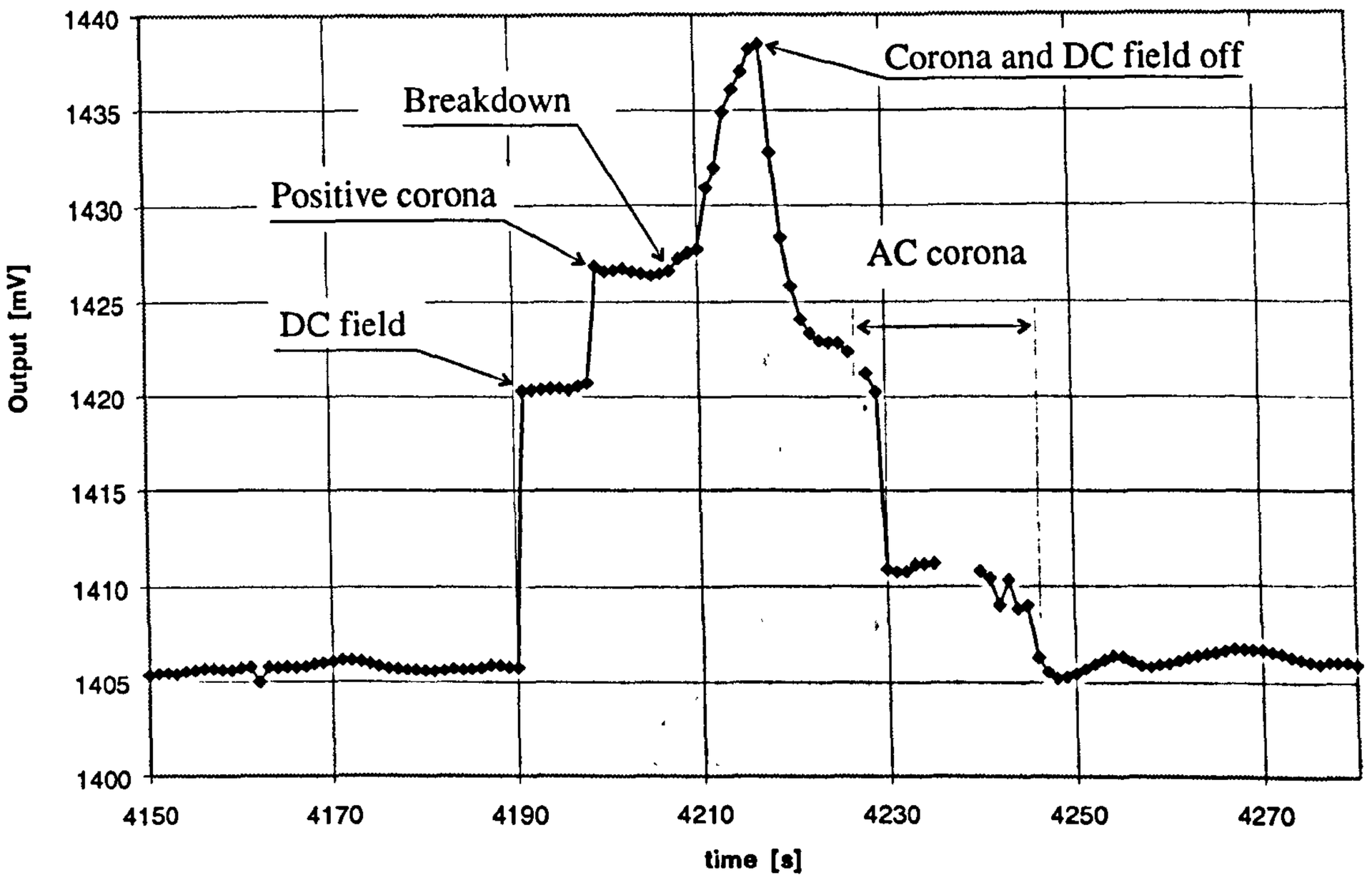

Figure 5.13: Response of the sensor to a uniform electric field (75kV/m) in the unipolar environment - breakdown due to ionisation.

process of 'breakdown' was more pronounced at higher field intensities. The effect was attributed to a change in the surface charge distribution since the neutralization after the measurement caused the output to attain the original value before the beginning of the measurement. This breakdown was attributed to a generation of the ions of opposite polarity, possibly due to the primary ionization of the air in the gap or due to a secondary ionization at the electrodes [11]. Since this breakdown effect did not occur in the case of the bipolar environment, the ionization of the probe surface was excluded.

The experiments in the bipolar environment were done by switching on the DC

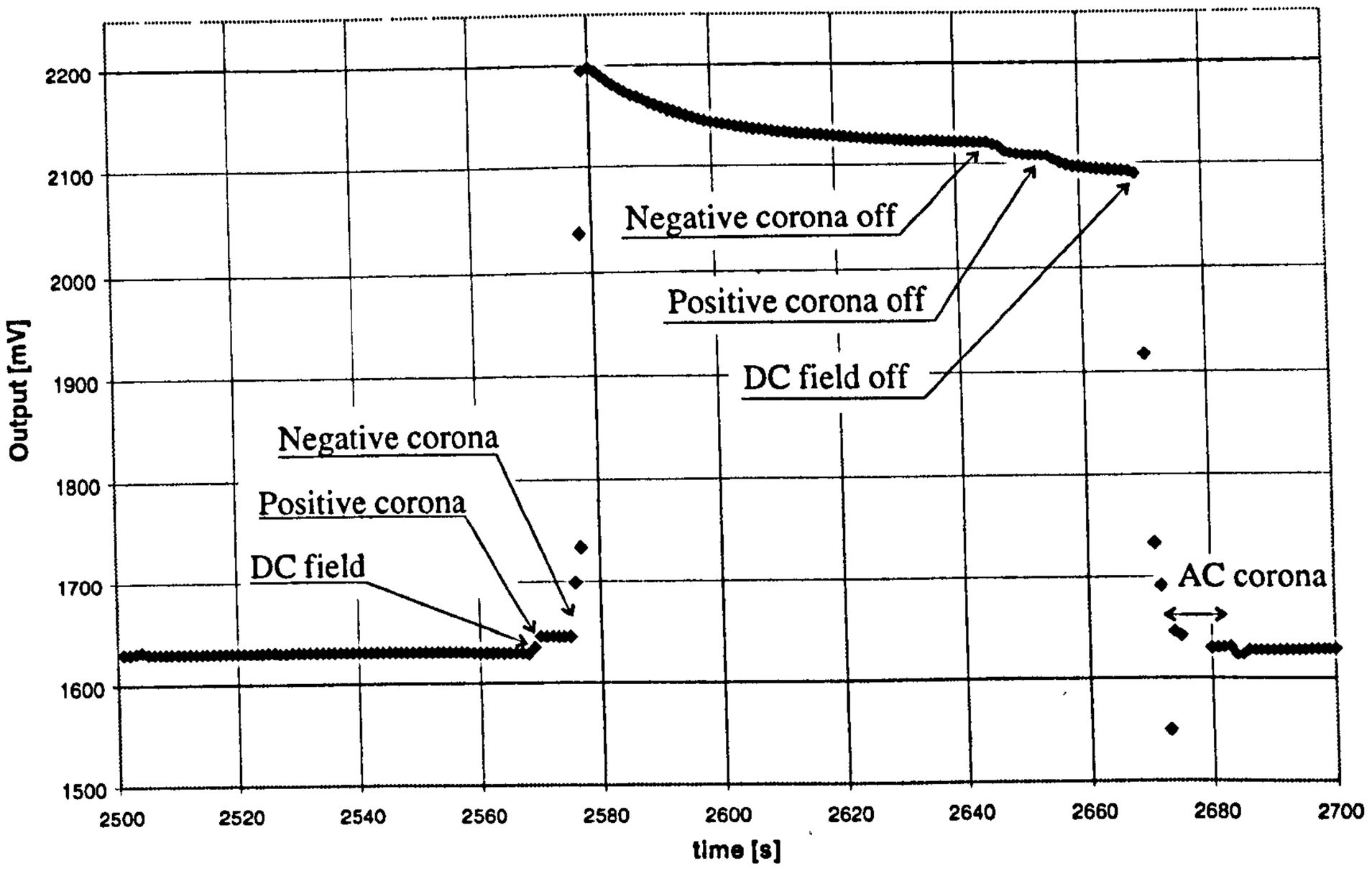

Figure 5.14: Response of the sensor to a uniform electric field (75kV/m) in the bipolar environment.

field, then the positive ions generator, and finally the negative ions generator. The sensor response is shown in Figure 5.14. The first step, due to the applied DC field without any space charge, is hardly visible, while the second step after activating the positive ions source is already visible, followed by the final jump at 2575s when the negative ion source was activated. The response of the sensor is not stable. The output voltage decreases approaching a stable value (2645s). At times 2645s and 2655s the negative and positive ions generators are switched off. Finally the measured field is switched off at time 2670s and the probe is neutralized. The observed decrease of the sensor output does not correspond to the prediction from section 5.3, where the output of the sensor was expected to rise till it reached the equilibrium value and then to stay constant. The observed 'decay' effect was attributed to the rectangular shape of the sensing element used in the experiments. It is assumed that due to the geometrical shape of the crystal, the equilibrium surface charge density in the unipolar environment in some areas exceeds the equilibrium surface charge density in the bipolar environment. Since the experiments were done in such a way that the bipolar charging was preceded by a unipolar charging, the observed decay of

the sensor output can be attributed to the release of this excessive charge deposited in the first stage of unipolar charging. The duration of this process depends on the surface properties of the sensing head and on environmental characteristics, such as temperature, humidity, pressure, chemical composition. Since the positive and negative ions have generally different mobilities and concentrations the described process can hardly be eliminated even if the probe is exposed directly to the bipolar environment.

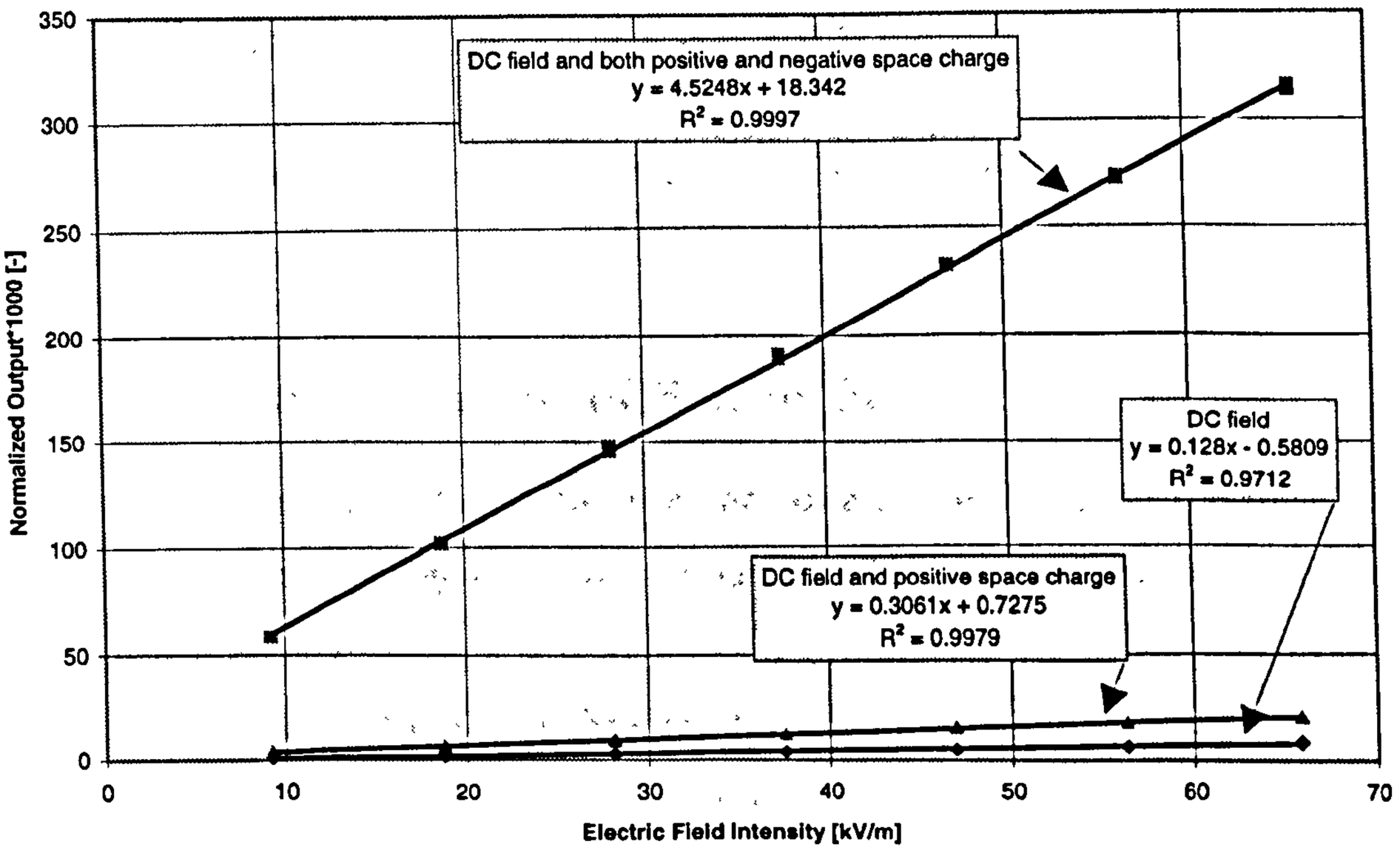

Figure 5.15: Normalized output change of the sensor $(V_{out} - V_0)/V_0$ as a function of applied electric field for the DC sensor with Lithium Niobate crystal without any enclosure in bipolar space charge environment, unipolar space charge environment and environment without space charge. *V_{out} is sensor output, V_0 is the output voltage without electric field; humidity 37%, T=21.9°C.*

The transfer characteristic of the sensor in the bipolar environment in Figure 5.15 was obtained using the maximum values of the response (as in Figure 5.14 at time 2580s). The measured ratio of the internal electric field in the bipolar environment to that in the environment without the space charge is 38. Since this value was obtained considering the output maximum, the real value will be even smaller. The difference between the measured and calculated ratio (table 5.1) is attributed to the shape of the sensing head. Similar results were obtained when the generators were switched on in the reverse order.

Conclusion. The experiments with the Lithium Niobate in a unipolar space charge environment confirmed the validity of the theoretical hypothesis. The response of the sensor was found to be a linear function of the applied electric field intensity, independent of the space charge density in the measured environment. It is, therefore, possible to measure the electric field in the unipolar environment once the probe is calibrated and the space charge density is low enough not to influence the measured field. The case of high space charge densities, when the space charge effect on the field cannot be neglected, was not examined. The measurements in a bipolar environment were found theoretically possible; however precise practical measurements were not successful due to an unstable sensor output in such an environment.

5.5.3 Artificial Extension of Sensor Head

The previous sections showed that the presence of a space charge in the measured environment can cause a large offset of the output. The slope of the transfer characteristic in such an environment was found to be many times higher than the slope of the transfer characteristic in the absence of a space charge.

The first idea of measurements in a space charge environment was to eliminate the effect of the deposited space charge by separating the deposited charges, using an artificial extension of the sensing head. The idea was based on the fact that two separate sheets of surface charge densities $\pm\sigma$, separated by a gap as depicted in Figure 5.16, generate an electric field $\mathbf{E}$ at the origin (appendix C):

$$E = E_3 = \frac{\sigma}{\epsilon_0}\left(1 - \frac{d}{\sqrt{d^2 + 4a^2}}\right) \tag{5.19}$$

This field is decreased with increasing distance between the plates according to the graph in Figure 5.16, which shows the factor $1 - d/\sqrt{d^2 + 4a^2}$ versus the ratio $d/2a$. For example, when considering the increase in the $d/2a$ ratio from 1 to 3, the electric field at the origin is decreased more than ten times. Similar results were obtained from 3 dimensional simulations of the sensing heads, according to Figure 5.17, with a constant positive charge distributed uniformly on the top of each enclosure. The results of these simulations are shown in table 5.3. The value of the deposited charge

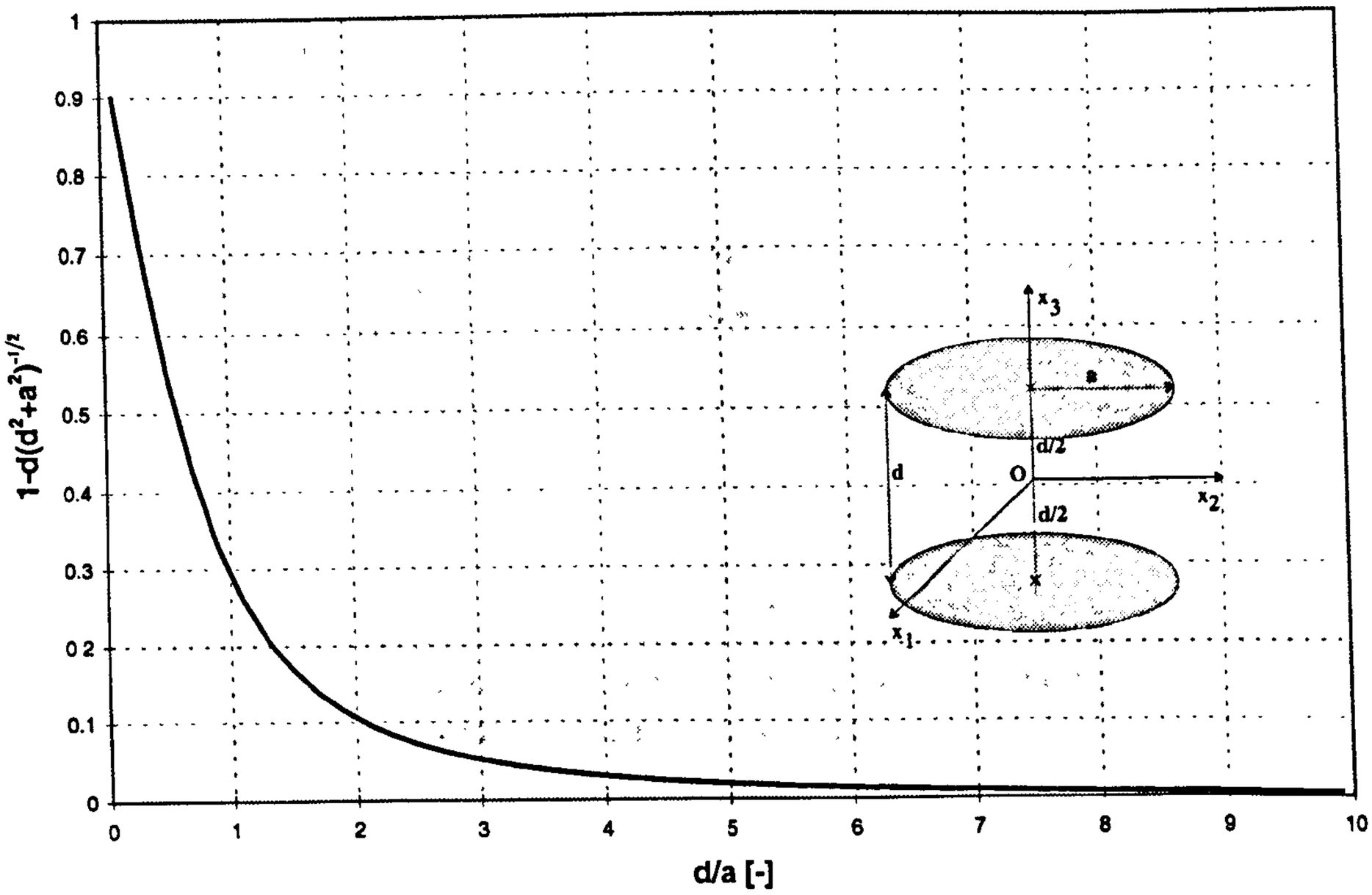

Figure 5.16: Factor $1 - d(d^2 + 4a^2)^{-1/2}$ versus ratio $d/2a$.

was chosen to give realistic results (see equation 5.16). The presented results show that extending the sensing head by the same material as that of the crystal in the shape of the long enclosure, could reduce the effect of the deposited charge 5 times. This is about twice less than in the case of the air gap. Compared to the short extension, the long extension would reduce the effect of the deposited charge by the factor of approximately 1.5. This reduction is the same in the case of the enclosure made of the same material as the crystal and in the case of PTFE enclosures.

Experimental investigations were done with Lithium Niobate crystal of dimensions 10x10x10mm, which was artificially extended using a PTFE enclosures as shown in Figure 5.17. The measured transfer characteristics for the sensing head with 'long' and 'short' enclosures, for both the unipolar environment and the en-

Table 5.3: The electric field intensity E in the middle of the sensing heads of dimensions as in Figure 5.17. *Xtl corresponds to the crystal alone, Xtl-short and Xtl-long to the short and long enclosures made out of the crystal material and Xtl-PTFE- to the enclosures out of PTFE. The charge of* $7.10^{-14}C$ *is uniformly distributed across the top of each enclosure. Simulations were done using MAFIA software.*

Sensing head	Xtl	Xtl-short	Xtl-long	Xtl-PTFE-short	Xtl-PTFE-long
E [V/m]	17.5	5.1	3.3	0.32	0.19

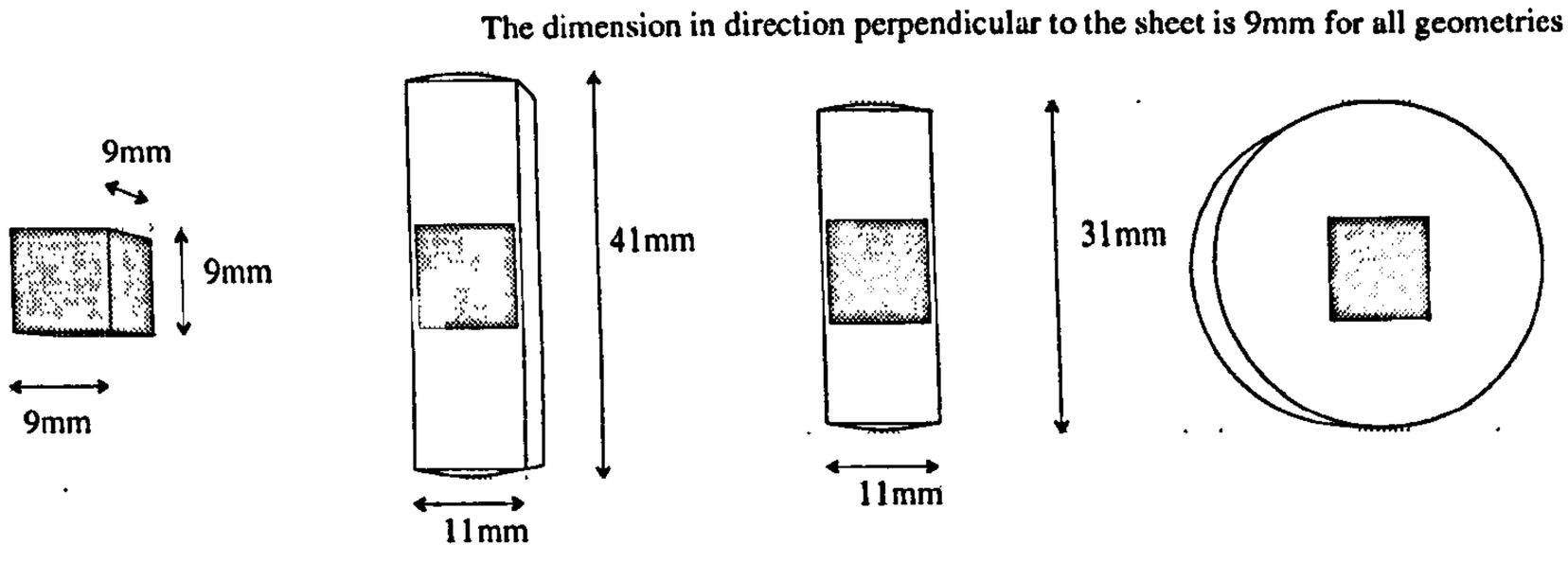

Figure 5.17: Geometry and dimensions of the Lithium Niobate crystal (sample LN2) and PTFE enclosures used in the space charge experiments.

vironment without a space charge, are shown in Figures 5.18 and 5.19, together with the ratio of their slopes. Clearly all the characteristics are linear with a very small difference in the slopes in the case of the short and the long enclosures. On the whole, compared to the experiments with Lithium Niobate crystal without any enclosure (Figures 5.12, 5.15), the effect of the space charge is suppressed. The slope ratio improved approximately twice from 3.13 in the case without any enclosure to 1.56 in the case of long enclosure. Ideally the slope ratio would be equal to one. However, the difference between the short and long enclosures is minimal and within the uncertainty of the measurements which shows that the effect of the extension is not as large as it was expected. The ratio of the transfer characteristics slopes in the environments with and without the space charge for the circular extension was measured 1.7.

The measured slope ratios of the sensor with short, long and circular enclosures were found to be very close. According to the simplified analysis of the separate charged sheets the difference should have been more pronounced. Taking the ratio for the long enclosure to be 1.56, the ratio for the short enclosure is expected to be about 1.87, which differs greatly from the actual measurement 1.64. These results suggest that the shape of the probe does not play as important role as was expected and that the used model is oversimplified. A close inspection of the equation (5.16) shows that the surface charge density in a bipolar environment is proportional to the

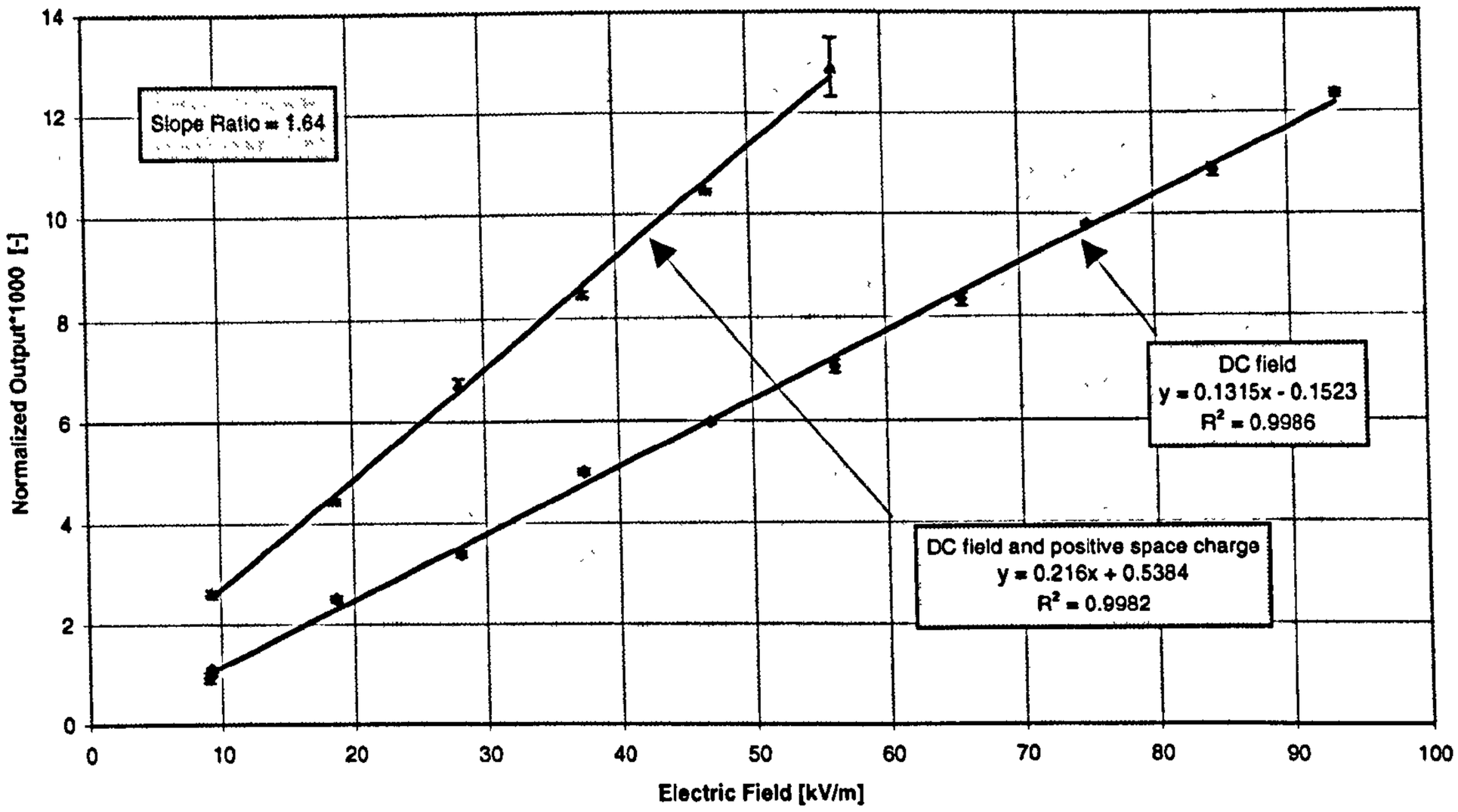

Figure 5.18: Normalized output of the DC sensor with Lithium Niobate crystal with short enclosure for both unipolar space charge environment and environment without space charge. *humidity 37%*, T=21.9°C.

relative permittivity of the probe , and independent of the size of the probe. If this result is generalized for a unipolar environment and different shapes of the probe, one can say that once the probe is enclosed by a dielectric of different permittivity the surface charge density will differ, as will the effect of the space charge on the transfer characteristic. Since the PTFE enclosure has a low relative permittivity of 2.2 compared to Lithium Niobate which has 85, the surface charge density will be much smaller than in the case without any enclosure, and the space charge effect will be suppressed. Thus taking into the account these facts, one is led to a conclusion that the improvement using the long extension is caused to a greater extent by the very low permittivity of the PTFE material rather than by the length of the enclosure. This conclusion is also supported by the results of simulations from table 5.1. Here the calculated slope ratio in a unipolar environment for a spherical probe with permittivity of 4 is 1.62 is close enough to measured values of 1.56, 1.64 and 1.7 for long, short and circular enclosure, respectively.

Conclusions. The experiments with the artificial extensions of the sensing head confirmed that the transfer characteristic of the sensor in a unipolar environment is a linear function of the applied field, depending on the shape of the probe. The idea

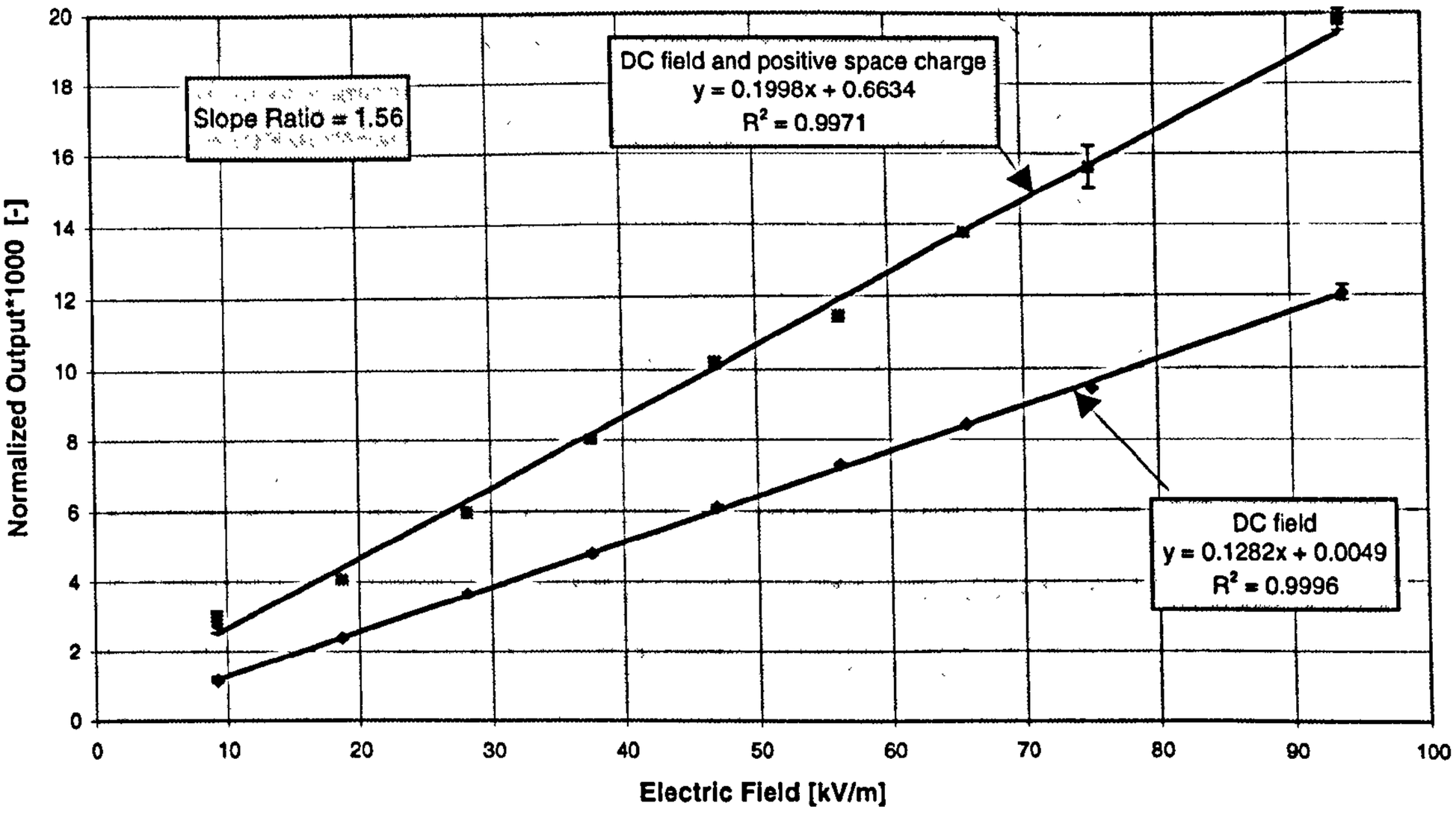

Figure 5.19: Normalized output of the DC sensor with Lithium Niobate crystal with long enclosure for both unipolar space charge environment and environment without space charge. *humidity 37%*, T=21.9°C.

of suppressing the space charge effect using the artificial extension was found to be not sufficiently efficient for practical use. The improvement in the sensor response in a space charge environment was found to be caused mainly by the low permittivity of the enclosure rather than its length.

5.6 Summary

In order to assess the effect of the external space charge deposition on the crystal surface, a mathematical model was developed for calculations of electric field intensity for a known surface charge distribution. The problem of charge deposition in a bipolar environment was formulated and successfully solved analytically. For the surface charge distribution in a unipolar environment, the analytical solution could not be found due to problem complexity and, therefore, a numerical method was used instead. Both analytical and numerical solutions were experimentally verified to a good agreement. Results obtained indicated that the linear response of the probe could be maintained regardless of the presence of the space charge. The results also indicated that the presence of the external space charge significantly

increases the sensitivity of the probe, and that this is independent of the space charge density. The sensitivity is, however, different for unipolar and bipolar space charge environments. These findings suggest that the probe could be used in the presence of an external space charge, but it has to be neutralized (discharged) after each measurement. Moreover, the presence of the space charge could be beneficially utilized to increase the sensitivity of the probe.

In the case of a bipolar space charge environment, the output of the probe shows a transient behaviour caused by an excessive charge deposition on the surface of the probe. This effect, in conjunction with other offsets (photodetector, light source, etc.), makes the probe practically unsuitable (high measurement uncertainty) for measurement of DC fields in bipolar environments.

In a unipolar environment, the probe could be used to measure fields from 2kV/m up to 60kV/m. The upper limit of 60kV/m was caused by the onset of ionization in the measured environment which changed the environment from unipolar to bipolar and hence the probe could not be used for the same reasons mentioned above.

After completing the investigations of the space charge effect on the probe, the concept of the virtual extension of the sensing crystal was explored, with a view of eliminating the space charge effect. The electrooptic crystal was extended in the direction of the measured field using various shapes and sizes of PTFE enclosures. Although, the effect of the space charge was suppressed due to the presence of virtual extension, it was not sufficient enough for use in practical applications. It was found that the improvement was mainly due to the low dielectric constant of the enclosures rather than due to its geometric shape and dimensions, as was expected.

Chapter 6

Temperature Stability of the Electro-Optic Sensor

The sensor is to be able to measure electric field with desired precision and minimal disturbance of the measured field. On the other hand it has to be relatively insensitive to the environmental changes like temperature, pressure, humidity. The following sections are concerned with an analysis of the temperature stability of the sensor. The temperature effects of the quarter-wave plate, polarizers and electrooptic crystals on the DC field sensor stability are discussed and compared. The analysis starts with a temperature analysis of cubic crystal and polarizers which are the less sensitive components (section 6.1). It is then focused on the quarter-wave plate whose characteristics are shown to be strongly influenced by temperature variations (section 6.2). A method of its temperature compensation based on an optimal positioning of optical components is proposed and analyzed using the Jones calculus. The temperature analysis is then extended in section 6.3, to a sensor with crystal of Lithium Niobate which is an anisotropic material. The effects of its natural birefringence and pyroelectricity on the sensor temperature stability are investigated. The last two sections deals with the effect of multiple reflections in the electrooptic crystal (section 6.4) and with a possible elimination of the spurious effect of light intensity fluctuations on the sensor output (section 6.5).

6.1 Cubic $\bar{4}3m$ Electro-Optic Crystals and Polarizers

The transfer characteristic of the sensor (4.1), introduced in section 4.1, is expressed in terms of the phase retardation Γ and the light intensity on the photodetector without applied electric field I_0. In the following discussion the crystal is assumed not to cause any temperature variations in I_0 and only the temperature variations of Γ are investigated. The effect of fluctuations in laser power I_0 is then discussed in section 6.5.

Changes in the output intensity of the sensor caused by temperature variations can be characterized by a temperature coefficient α_T defined as

$$\alpha_T = \frac{1}{I_0}\frac{\partial I}{\partial T} \approx \frac{\partial \Gamma}{\partial T} \tag{6.1}$$

where it is assumed that the induced phase retardation $\Gamma \ll 1$ (section 4.3.1). The temperature coefficient α_T expresses a normalized change in the sensor output with temperature. Substituting the phase retardation (4.10) in (6.1) α_T becomes:

$$\alpha_T \approx \frac{2\pi}{\lambda} n^3 r \frac{E_0 l}{1 + d\epsilon - d}\left(\frac{3}{n}\frac{dn}{dT} + \frac{1}{r}\frac{dr}{dT} + \frac{1}{l}\frac{dl}{dT} - \frac{1}{\lambda}\frac{d\lambda}{dT} - \frac{d}{1 + d\epsilon_r - d}\frac{d\epsilon_r}{dT}\right) \tag{6.2}$$

where λ is the wavelength of the light, n refractive index, r the electro-optic coefficient, l is the length of the crystal traversed by the light, d is the depolarisation factor, and E_0 is the measured electric field intensity.

Considering a 10mm long Bismuth Germanate crystal at a wavelength of 633nm in the presence of an the electric field of 1kV/m and data available from literature, the equation (6.2) gives $\alpha_T \approx 5.10^{-9}$. The temperature dependence of the electro-optic coefficient r was neglected in this estimate as, to the best of the author's knowledge, this has not been reported. Results of the same order of magnitude were obtained for cubic crystal of Cadmium Telluride (10^{-9}) and for Lithium Niobate (3.10^{-9}) using transverse electrooptic effect with light beam along the optical axis. The estimated normalized change in the output intensity of the sensor with BG due to an electric field of 1kV/m is $\approx 10^{-4}$. These values show that the crystal material alone introduces negligible temperature dependence of the sensor output.

The estimated values show that the precision of the sensor with Bismuth Germanate could be $\approx 1\%$ in the temperature range from 0 to $100°C$. This conclusion applies for most cubic crystals since the material constants are similar. In the case of Lithium Niobate the estimate of α_T was done for the crystal orientation in which the light does not experience natural birefringence and pyroelectricity. Practically it is very difficult to avoid these effects and the conclusions of high temperature stability, therefore, do not apply for anisotropic materials.

The effect of polarizers on the temperature stability can be characterized by α_T as well. However, no temperature effects of the polarizer have been reported. The measurements in our laboratory in the temperature range from 20 to $42°C$ confirmed that the Glan-Thompson polarizers do not influence the sensor output.

Conclusions. The effect of the temperature dependence of the induced phase shift on sensor stability was found to be very small, suggesting achievable precision of 1% of a sensor based on a cubic crystal in the temperature range $0 - 100°C$. The effect of polarizers on sensor temperature stability was found negligible.

6.2 Quarter-Wave Plate and Polarizers

A birefringent quarter-wave plate uses the natural birefringence of a suitable material (e.g.quartz or mica) to introduce a desired phase shift between two eigenmodes of propagation. This implies that there is a relatively strong temperature dependence of its phase retardation. The best temperature stability of phase retardation is achieved with zero-order quartz quarter-wave plates with a typical value of $\partial\gamma/\partial T = 2.2 \quad 10^{-4}$rad/K [27], where γ is the phase retardation of the quarter-wave plate (ideally $\pi/2$). This change in the phase retardation with temperature is several orders of magnitude higher than the temperature induced phase retardation in the crystal $\partial\Gamma/\partial T$, and is comparable with the phase retardation caused by the measured electric field. Therefore, the quarter-wave plate can, as it is shown later, cause a strong temperature instability of the sensor output if it is not compensated.

A method of minimizing the temperature effect of the quarter-wave plate was developed. It relies on a proper alignment of the electro-optic crystal and the analyzer

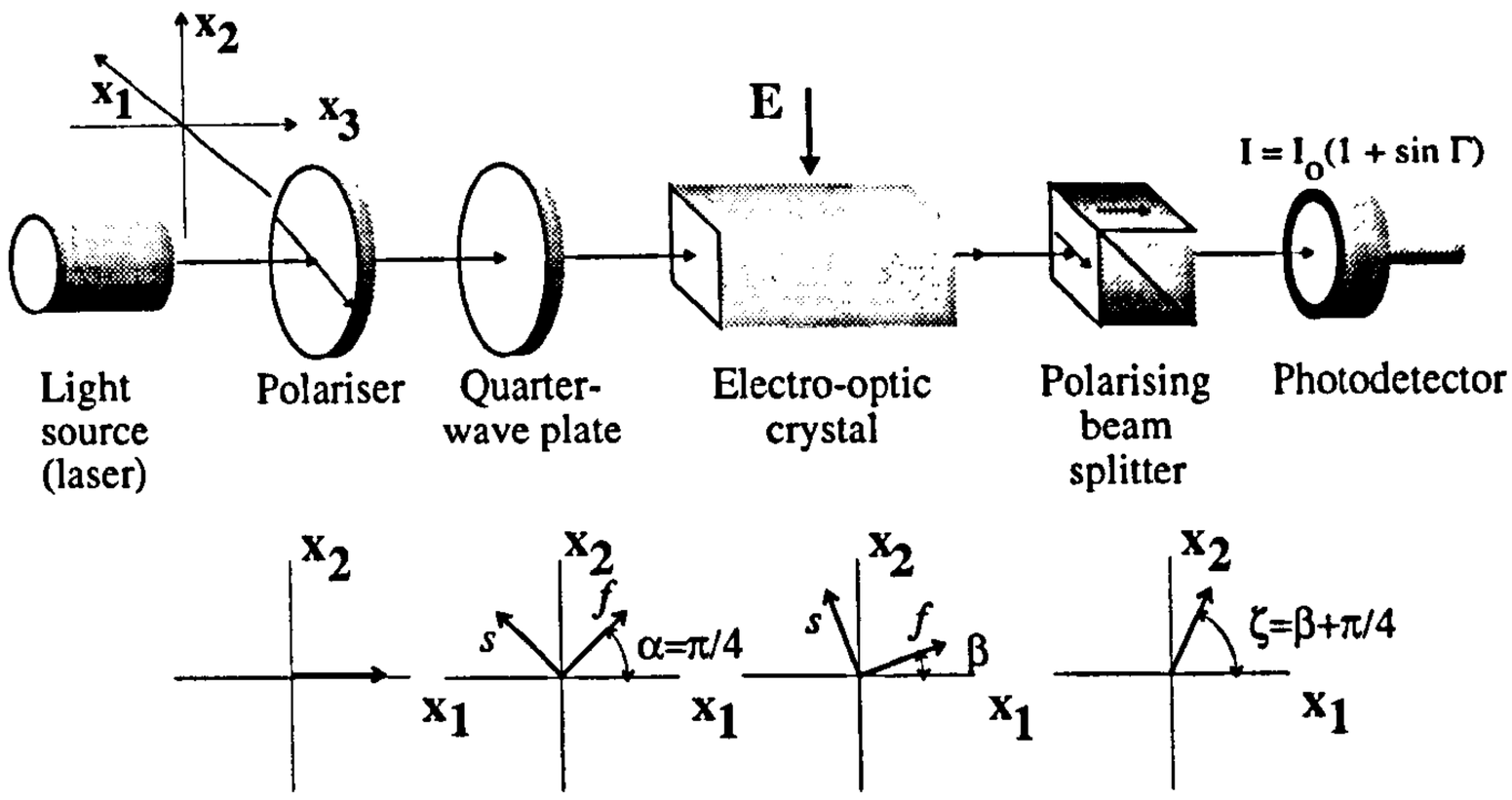

Figure 6.1: Schematic diagram of the electro-optic sensor. Definitions of the coordinate system and rotation angles of quarter-wave plate (α), crystal (β) and analyzer (ζ).

with respect to the fast and slow axes of the quarter-wave plate. In the sensor given in Figure 6.1 the quarter-wave plate ideally produces a circularly polarized light. Since the circularly polarized wave can be always described by means of two orthogonal but otherwise arbitrarily oriented linearly polarized waves, the position of the unit containing the electro-optic crystal and the analyzer can be arbitrary with respect to the polarizer and the quarter-wave plate. When mutually aligned crystal and analyzer are rotated together so that one of the wave plate eigenaxes is aligned with the analyzer, the influence of its temperature instability can be suppressed.

In the following analysis, based on Jones calculus, two cases are considered; i) the analyzer is at 45 degrees to the wave plate eigenaxes, and ii) the analyzer and one of the wave plate eigenaxes are parallel. The first one corresponds to the *worst case*. In the latter case the temperature effect of the quarter-wave plate is suppressed. If the Jones matrices of the analyzer, crystal and quarter-wave plate are denoted as $\mathbf{A}_n$, $\mathbf{C}_r$ and $\mathbf{Q}_{wp}$, respectively, the Jones vector of the light at the photodetector $\mathbf{L}_{out}$ is calculated as:

$$\mathbf{L}_{out} = \mathbf{A}_n \, \mathbf{C}_r \, \mathbf{Q}_{wp} \, \mathbf{L}_p \tag{6.3}$$

where $\mathbf{L}_p$ is the Jones representation of the input light after the polarizer given by

$$\mathbf{L}_p = \begin{pmatrix} 1 \\ 0 \end{pmatrix} \tag{6.4}$$

The Jones representation of the quarter-wave plate with its fast optical axis along x_1 is given by:

$$\mathbf{Q}_{wp} = \begin{pmatrix} \exp(i\frac{\gamma}{2}) & 0 \\ 0 & \exp(-i\frac{\gamma}{2}) \end{pmatrix} \tag{6.5}$$

with the phase retardation $\gamma = \pi/2$. Similarly, the representation of the crystal with its fast axis along x_1 is

$$\mathbf{C}_r = \begin{pmatrix} \exp(i\frac{\Gamma}{2}) & 0 \\ 0 & \exp(-i\frac{\Gamma}{2}) \end{pmatrix} \tag{6.6}$$

with phase retardation Γ given by (4.10). The Jones matrix of an analyzer with the principle direction along x_1 axis is:

$$\mathbf{A}_n = \begin{pmatrix} 1 & 0 \\ 0 & 0 \end{pmatrix} \tag{6.7}$$

The rotation of the components is accounted for by applying axes transformation matrix $\mathbf{R}$ (see section 4.2, equation (4.4)) as

$$\mathbf{L}_{out} = \mathbf{R}(\zeta)\, \mathbf{A}_n\, \mathbf{R}(-\zeta)\, \mathbf{R}(\beta)\, \mathbf{C}_r\, \mathbf{R}(-\beta)\, \mathbf{R}(\alpha)\, \mathbf{Q}_{wp}\, \mathbf{R}(-\alpha)\, \mathbf{L}_p \tag{6.8}$$

where α, β, ζ are the rotation angles of quarter-wave plate, crystal and analyzer, respectively, shown in Figure 6.1.

For the case with the analyzer aligned at 45° to the quarter-wave plate eigenaxes, i.e. $\alpha = \pi/4$, $\beta = \pi/4$ and $\zeta = \pi/2$, the equation (6.8) becomes:

$$\mathbf{L}_{out} = \begin{pmatrix} \cos\left(\frac{\gamma+\Gamma}{2}\right) \\ 0 \end{pmatrix} \tag{6.9}$$

The intensity of the light at the photodetectors, calculated as $\mathbf{L}_{out}\mathbf{L}^*_{out}$ where (*) denotes the complex conjugate, is found from (6.9) as

$$I = \cos^2\left(\frac{\gamma+\Gamma}{2}\right) \tag{6.10}$$

Finally using the definition (6.1), $\alpha_T$is found to be:

$$\alpha_T = \sin(\gamma+\Gamma)\left(\frac{\partial\gamma}{\partial T} + \frac{\partial\Gamma}{\partial T}\right) \approx \frac{\partial\gamma}{\partial T} \tag{6.11}$$

In equation (6.11) it was assumed that $\Gamma \ll 1$, $\gamma \approx \pi/2$ and $\partial\Gamma/\partial T \ll \partial\gamma/\partial T$. It becomes evident that the temperature stability is dominated by the temperature dependence of the quarter-wave plate phase retardation $\partial\gamma/\partial T$.

The temperature effects of the quarter-wave plate can be minimized by positioning the plate and the analyzer. If the analyzer is aligned along the fast axis of the quarter-wave plate, when $\alpha = \pi/4$, $\beta = \pi/2$ and $\zeta = \pi/4$, equations (6.3), (6.10) and (6.11) become:

$$\mathbf{L}_{out} = \frac{1}{2}\begin{pmatrix} \cos\left(\frac{\gamma-\Gamma}{2}\right) + \imath \sin\left(\frac{\gamma+\Gamma}{2}\right) \\ -\cos\left(\frac{\gamma-\Gamma}{2}\right) - \imath \sin\left(\frac{\gamma+\Gamma}{2}\right) \end{pmatrix} \tag{6.12}$$

$$I = \frac{1}{2}\cos^2\left(\frac{\gamma-\Gamma}{2}\right) + \frac{1}{2}\sin^2\left(\frac{\gamma+\Gamma}{2}\right) \tag{6.13}$$

$$\alpha_T = \frac{1}{2}\frac{\partial\gamma}{\partial T}(\sin(\gamma+\Gamma)-\sin(\gamma+\Gamma)) + \frac{1}{2}\frac{\partial\Gamma}{\partial T}(\sin(\gamma+\Gamma)+\sin(\gamma-\Gamma)) \approx \frac{\partial\Gamma}{\partial T} \tag{6.14}$$

In this case the temperature dependence of the sensor is given by the temperature dependence of the phase retardation in the crystal which is much smaller than that of the quarter-wave plate (section 6.1).

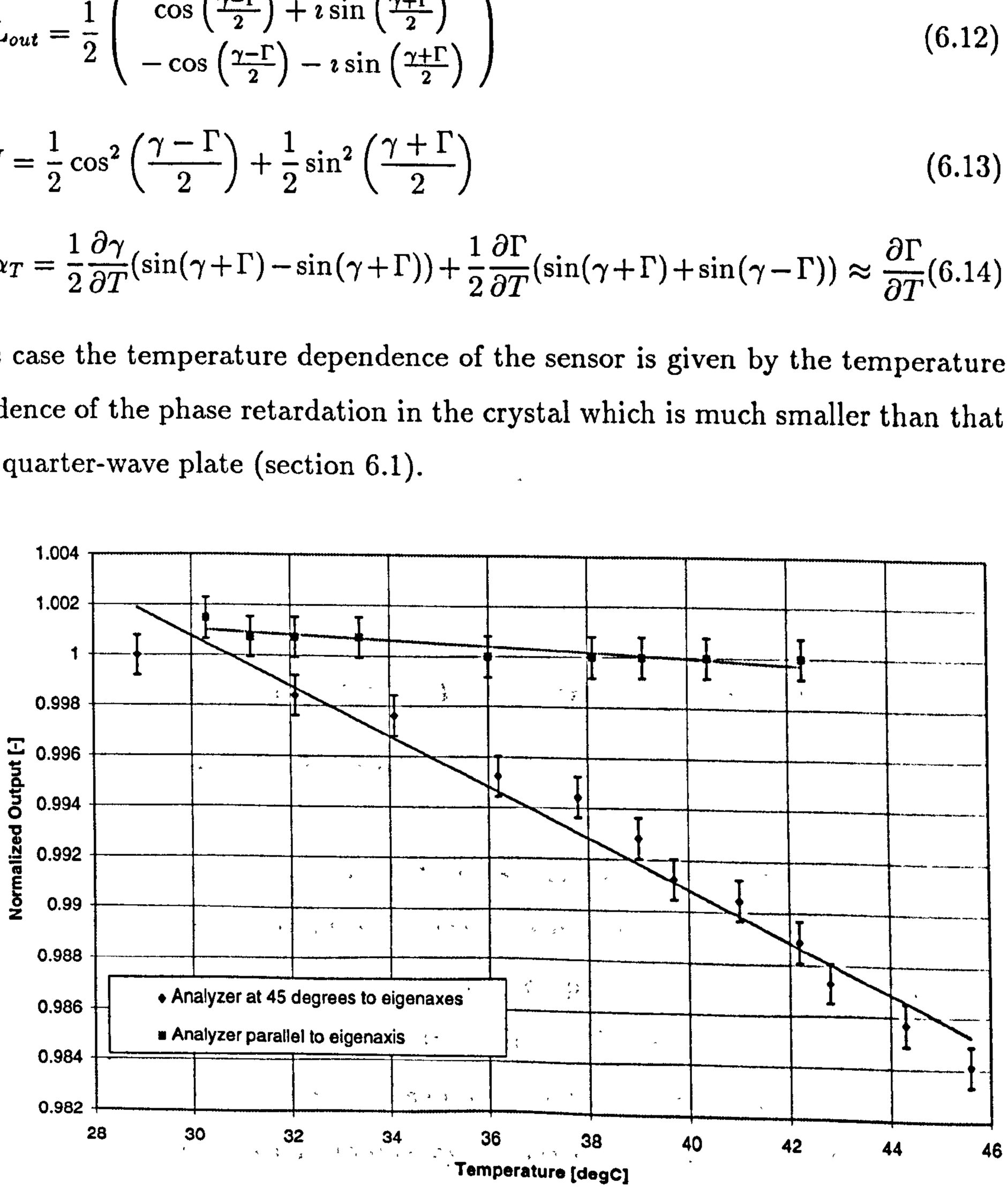

Figure 6.2: Temperature stability of the low-order quarter-wave plate at 850nm. *Normalized output of the sensor without the electro-optic crystal as a function of temperature.*

Figure 6.2 shows the temperature effect of the quarter-wave plate on the sensor output. A low order quarter-wave plate at the wavelength of 850nm was used in these experiments. The experimental setup was similar to Figure 6.1 with the exception that the electro-optic crystal was not used. Only the quarter-wave plate was exposed to the temperature variations.

A strong temperature dependence of the output was observed when the analyzer was aligned at 45° to the quarter-wave plate eigenaxes. The measured temperature coefficient α_T of the sensor output is 10^{-3}. The estimated temperature coefficient of the quarter-wave plate $\partial\gamma/\partial T$, according to the equation (6.11) is $\approx 10^{-3}$rad/K. With the analyzer aligned parallel to the quarter-wave plate eigenaxes, the temperature stability has been improved by a factor > 10. The small variations of the output with temperature are within the range of the measurement error.

Conclusions. It has been shown that the temperature dependence of the quarter-wave plate phase retardation can introduce a large error in measurements since the temperature induced phase retardation is larger than the retardation due to the electric field. A method of quarter-wave plate temperature compensation, based on an optimal optical alignment of the crystal and the analyzer with respect to the quarter-wave plate, has been described and experimentally verified.

6.3 Natural Birefringence and Pyroelectricity in Lithium Niobate

In section 6.1 it has been shown that the sensor with cubic crystals can achieve an excellent temperature stability. However, when a naturally anisotropic crystal is used as a sensing element, problems with temperature stability arise due to the natural birefringence and pyroelectricity. Lithium Niobate which was identified as a suitable crystal for DC applications is of 3m point symmetry group and possesses a strong natural birefringence as well as pyroelectricity. In section 4.4.1 it was shown that theoretically, if the light beam is perfectly aligned along the optical axis, the crystal does not exhibit the natural birefringence and even the pyroelectric effect

can be eliminated. This section analyzes the case of a small disalignment of the beam from the optical axis and consequent effects of both natural birefringence and pyroelectricity.

In a real situation the disalignment has to be expected to some extent. It can be due to a bad parallelism of the quarter-wave plate and the crystal or due to the finite precision of the crystal cut in case of optical components connected together or simply by limitations of the aligning process. The parallelism of commercially available optical components is commonly guaranteed to be about 1'($\approx 0.016°$). On special requests the minimum of 5"($\approx 0.001°$) can be achieved. The accuracy of the optical axis orientation is less than 5". Therefore, the disalignment was investigated in the range from 0 to 0.1°.

A small disalignment of the laser beam from the optical axis causes the crystal of Lithium Niobate to exhibit a natural birefringence. This causes a change in the light polarization by introducing a phase shift between the eigenwaves. As a result, the sensor transfer characteristic is changed. In the simplest case when the eigenaxes of both quarter-wave plate and crystal are parallel, the working point on the transfer characteristics is simply shifted away from the quadrature point (Figure 4.2). This is tolerable as long as the sensor works in the linear region for assumed range of electric field intensities. The problem, however, arises with temperature variations in the measured environment.

It follows from the discussion in section 4.5 on sensor isotropy that the sensor response is maximized when the analyzer is at 45° to the induced fast and slow optical axes of the electrooptic crystal. This result also applies to the situation when a natural birefringence is induced by a disalignment of the crystal. The temperature effects of natural birefringence will be, therefore, maximized when the optical eigenaxes are at 45° to the analyzer. It can also be said that in the case of eigenaxes parallel to the analyzer, the output of the sensor is not influenced. This is based on the same principle as the compensation method developed for the Quarter-wave plate, and theoretically, it can be used to suppress the temperature instability due to the natural birefringence. The worst case of optical eigenaxes at 45° to the principal direction of the analyzer is considered in the following analysis.

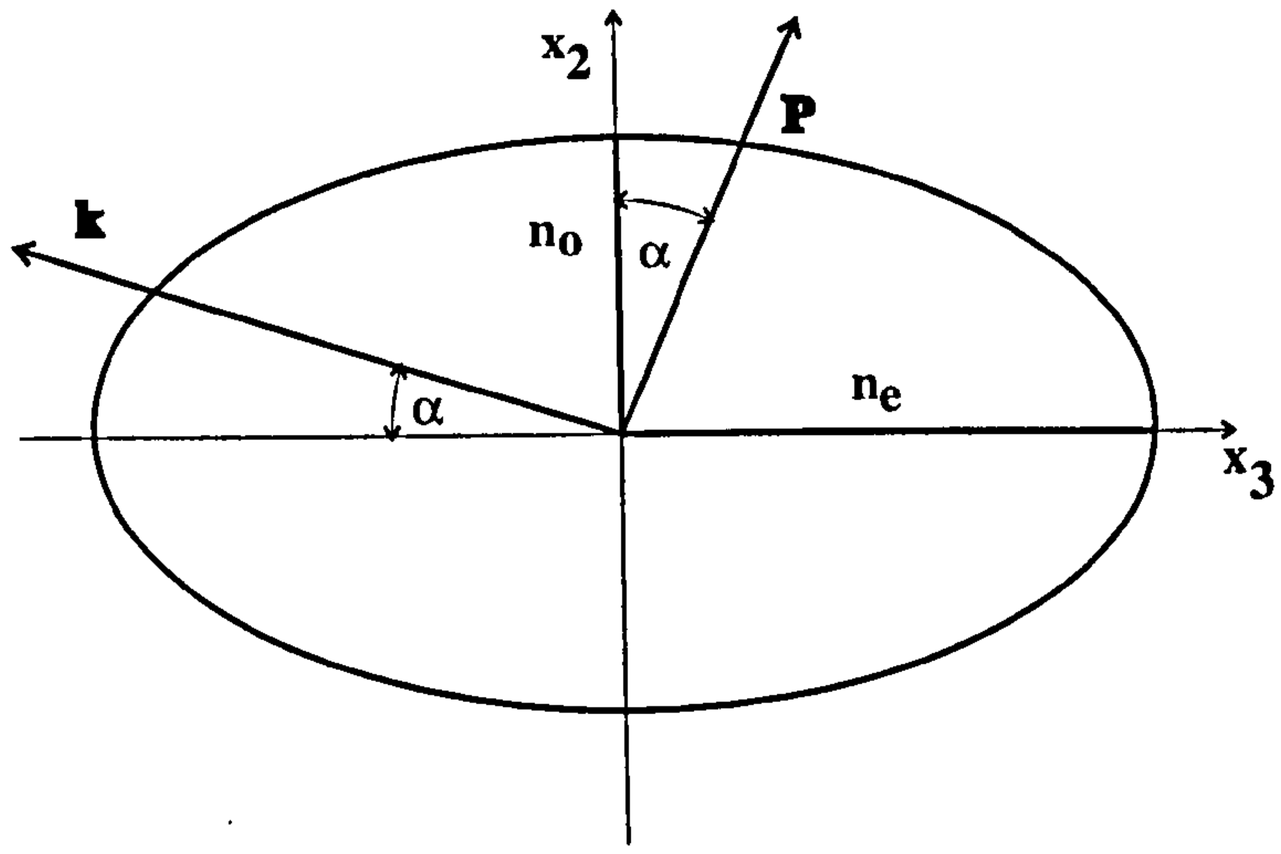

Figure 6.3: Cross-section of the index ellipsoid showing the optical disalignment from the optical axis by an angle α. n_0, n_e *are the ordinary and extraordinary refractive indices,* $\mathbf{k}$ *is the wave vector and* $\mathbf{P}$ *shows the polarization direction of the extraordinary eigenwave (the ordinary wave polarization is perpendicular to the sheet).*

From the geometry of the index ellipsoid it follows that when the light wave vector $\mathbf{k}$ is at angle α with the optical axis, the extraordinary eigenaxis is lying in the plane defined by $\mathbf{k}$ and the optical axis. The extraordinary refractive index can be, therefore, calculated using the cross-section of the index ellipsoid with the $(\mathbf{k}, z)$ plane as in (Figure 6.3) and the natural birefringence can be expressed as:

$$\Delta n = \frac{n_o n_e}{\sqrt{n_e^2 \cos^2(\alpha) + n_o^2 \sin^2(\alpha)}} - n_o \tag{6.15}$$

where n_e, n_o are the extraordinary and ordinary refractive indices, respectively. Under the assumed circumstances (crystal eigenaxes at 45 degrees to the analyzer) the output intensity without an applied field becomes [5]:

$$I = I_0(1 + \sin \Gamma_{nb}) = I_0 \left(1 + \sin\left(\frac{l\Delta n}{\lambda} 2\pi\right)\right) \tag{6.16}$$

where Γ_{nb} is the phase retardation due to the natural birefringence, l is the crystal length along the light beam, Δn natural birefringence and λ wavelength of the light wave in vacuum. Figure 6.4 shows the relative change of the sensor output as a function of the disalignment angle α. The graph shows that a relatively small disalignment of the optical beam from the optical axis causes large changes in the output of the sensor. The deviation of 0.9 degree at 850nm or 1.1 degree at 1310nm shifts the working point on the transfer characteristic to its minimum in the nonlinear

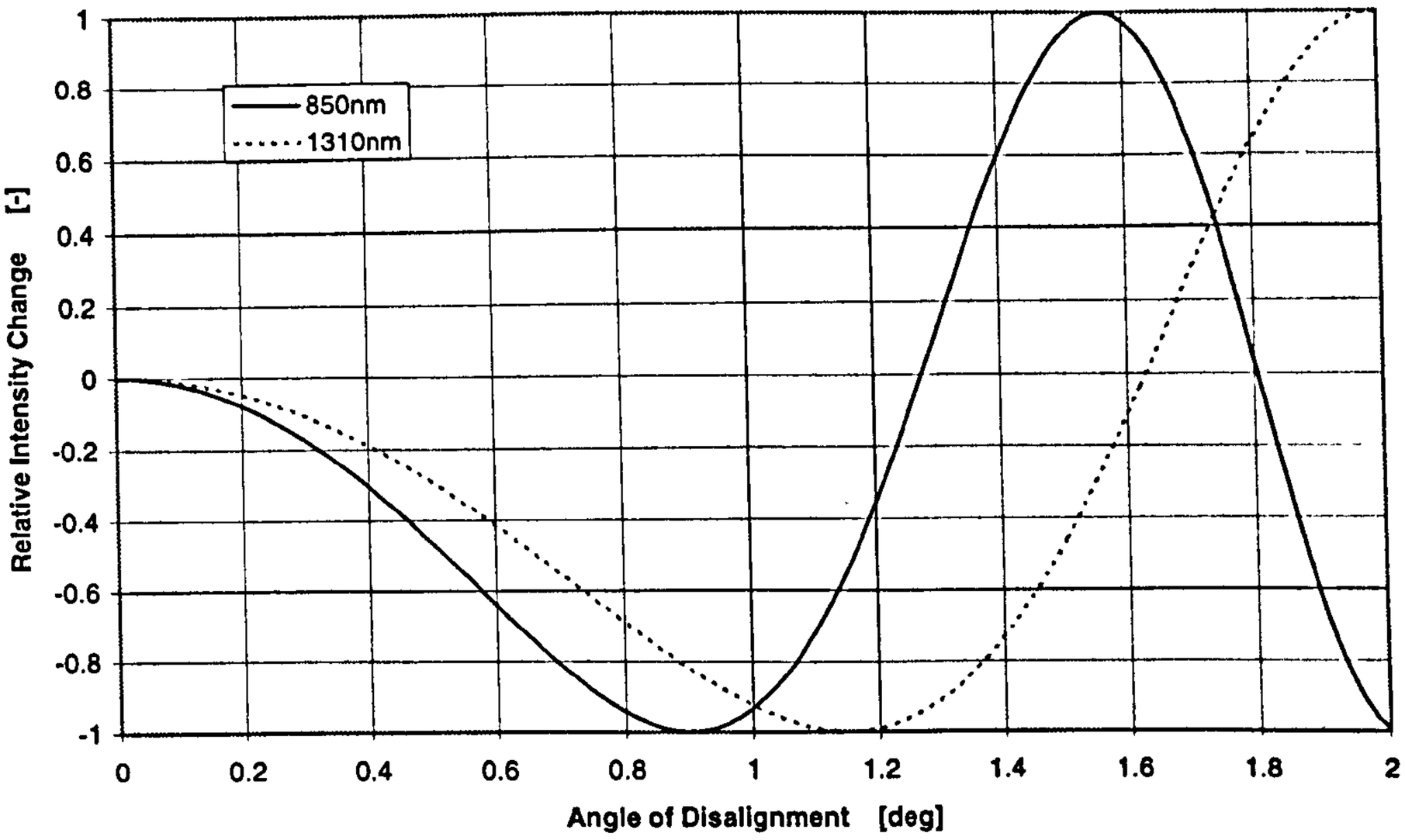

Figure 6.4: Normalized change of the output of the electrooptic sensor with Lithium Niobate $(I - I_0)/I_0$ versus the angle of disalignment α.

region, which coincides with the induced phase shift of $-\pi/2$ (Figure 4.2). However, the most important effect of the natural birefringence is the temperature dependence of the phase retardation Γ_{nb}. Knowing the output intensity in terms of natural birefringence, the temperature coefficient α_{T-nb} of the sensor output due to the natural birefringence is found using (6.1):

$$\alpha_{T-nb} = \frac{2\pi}{\lambda}\left(\Delta n\frac{dl}{dT} + l\frac{d\Delta n}{dT}\right)\cos\left(\frac{l\Delta n}{\lambda}2\pi\right) \approx \frac{2\pi}{\lambda}\left(\Delta n\frac{dl}{dT} + l\frac{d\Delta n}{dT}\right) \quad (6.17)$$

where l is the crystal length along the light beam, Δn is the natural birefringence and λ is wavelength of the light wave in vacuum. Figure 6.5 shows the dependence of α_T on the disalignment angle α for the wavelengths of 850 and 1310nm. It is evident that α_T decreases with increasing wavelength. The graph also depicts the levels which correspond to the phase retardation caused by an applied electric field of intensities 1, 10 and 100V/m. It is immediately evident that the natural birefringence can cause a strong temperature dependence of the sensor output. This happens when the temperature coefficient α_{T-nb} becomes comparable to the phase retardation induced by the electric field.

Table 6.1 summarizes the temperature effects of the quarter-wave plate, the

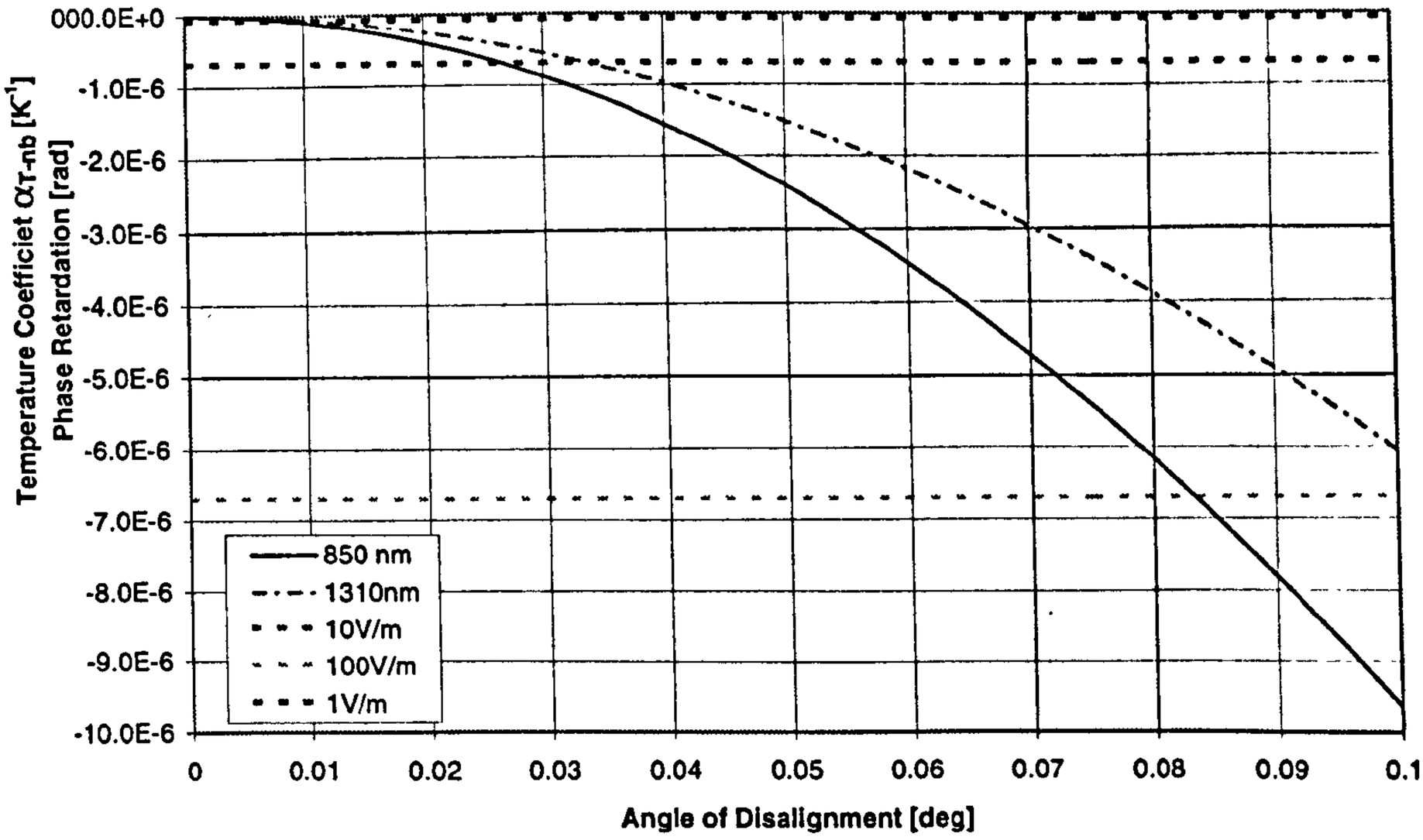

Figure 6.5: Temperature coefficient α_{T-nb} as the function of the disalignment angle α. *The levels corresponding to the induced phase retardation by electric field of 1, 10, 100V/m are depicted by the horizontal lines.*

electrooptic effect and the natural birefringence. The phase retardation Γ induced by the electric field of 10 V/m is shown for the comparison. It can be seen that the temperature instability of the sensor is mainly due to the temperature effects of the quarter-wave plate and the natural birefringence in the crystal. To avoid the effect of natural birefringence the crystal has to be aligned along the optical axis with precision better than 0.01°.

Lithium Niobate is also a pyroelectric crystal. Therefore, variations in the crystal

Table 6.1: Temperature coefficients of the sensor α_T due to the quarter-wave plate, natural birefringence of $LiNbO_3$ and electrooptic effect compared to the phase retardation Γ induced in $LiNbO_3$ by field of 10V/m.

	Quarter-wave plate	Crystal natural birefringence (disalignment)		Electro-optic effect
	Quartz	0.1deg	0.01deg	10V/m
Γ	-	-	-	$0.7\text{x}10^{-6}$rad
α_T	$5\text{x}10^{-4}$ rad/K	10^{-5} rad/K	10^{-7} rad/K	$3.6\Gamma\text{x}10^{-4}$ rad/(V/m)

temperature will affect the magnitude of spontaneous polarization in the form of the pyroelectric effect. A change of $1°C$ can induce an internal electric field of magnitude 10^5V/m in the direction of optical axis [8]. The spontaneous polarization charges are compensated by free electric charges through the conduction process in the same way as it was described in the section 4.3.2. Due to the extremely low bulk conductivity of the crystal at room temperature, the charge relaxation process is very slow so that even crystal temperature variation as low as 10^{-1} $°Ch^{-1}$ may set up a pronounced electric field [8]. Hence, because of the high charge relaxation time constant and random temperature fluctuations, the crystal of Lithium Niobate is virtually always in a non-equilibrium state which is characterised by a finite value of the internal electric field. The internal electric fields of the order of 10^7V/m were reported [8].

It was shown in section 4.5 on the sensor isotropy, that an internal electric field in the direction of the optical axis should not give rise to the transverse electrooptic effect, and, ideally, the sensor should not be influenced by the crystal pyroelectricity. Nevertheless, an appearance of the internal electric field components perpendicular to the optical axis was reported [8]. It is supposed that these electric field components were caused by a non-uniformity of the pyroelectric field as a result of a structural inhomogeneity in the crystal. The component of the pyroelectric field E_{12}, perpendicular to the optical axis, was determined experimentally to be $E_{12} = \alpha E_3$, where α characterizes the inhomogeneity of the crystal ($\approx 10^{-3}$) and E_3 is the internal electric field along the optical axis [8]. The value of E_{12} field of 10^4V/m were confirmed experimentally.

Comparing the values of the pyroelectric field with the expected range of the measured field (0-3.10^6V/m) it is obvious that the pyroelectric effect may be a serious issue for temperature stability of the electrooptic sensor. This conclusion was confirmed experimentally. Figure 6.6 shows typical response of the sensor to temperature changes. In these experiments the crystal was placed on a metallic holder enclosed in a box with openings for the laser beam to enter and exit the sensing crystal. Two high power resistors placed in the box were used as heating elements. To ensure that output variations are not due to the laser power fluctuations, the light intensity in front of the quarter-wave plate was monitored using a beamsplitter

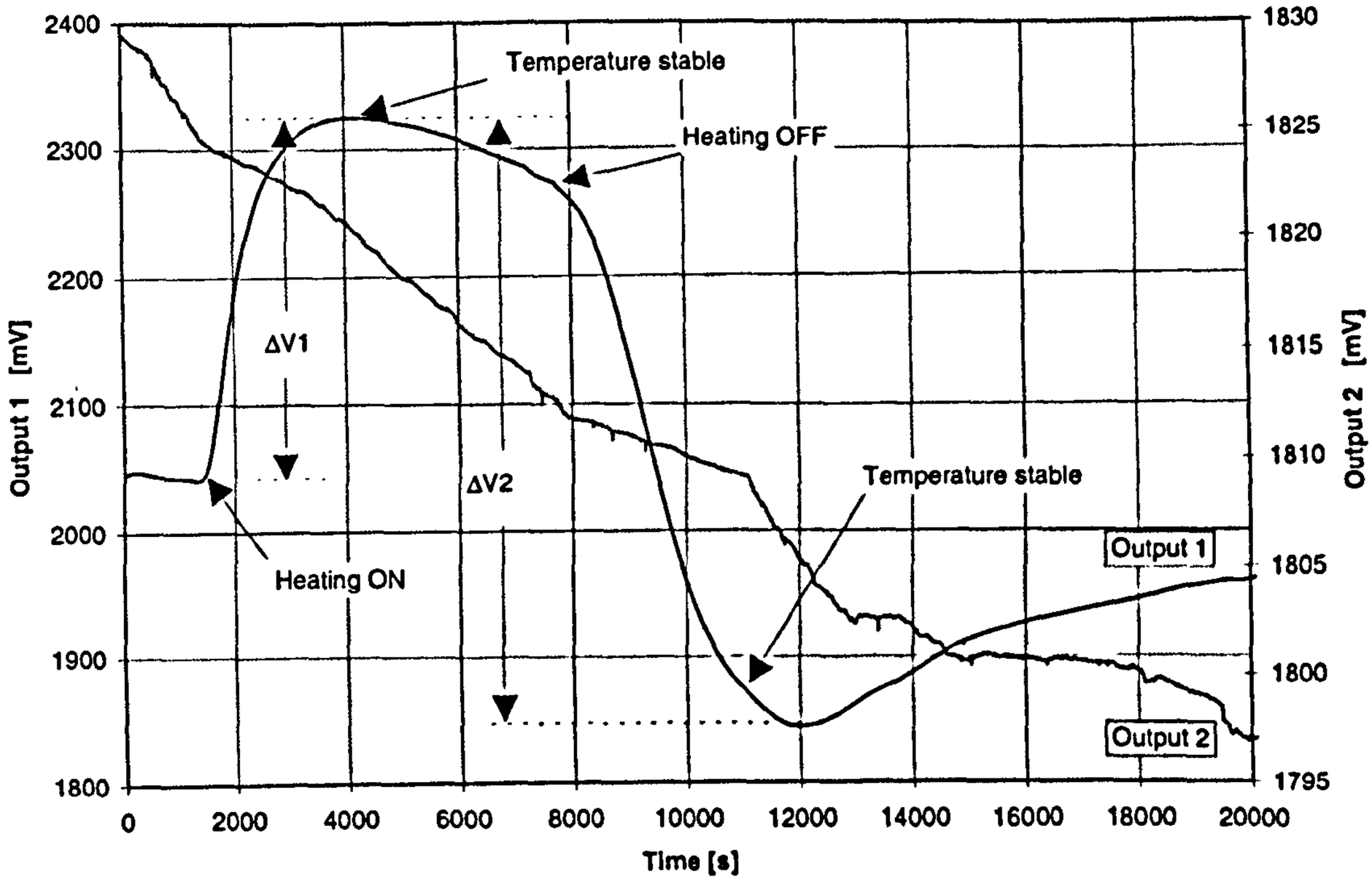

Figure 6.6: Temperature experiment with Lithium Niobate. *The crystal was heated from 21 to 29° and then allowed to cool down.*

(output 2 in Figure 6.6). The used optical scheme was the same as in the space charge experiments (Figure 5.10). The graph clearly shows a relaxation of the sensor output, with an estimated time constant of 20000s (5.5 hours). It supports the conclusion that the temperature stability is caused to a great extent by the pyroelectric effect, since the natural birefringence is not expected to cause any relaxation of the output. Instead of attaining a stable value after having reached the thermal equilibrium, the output reaches its maximum and then decreases. This decrease was attributed to the relaxation of the pyroelectric internal field due to the non-zero bulk conductivity. After switching off the heating the temperature decreases and the pyroelectric field changes the orientation and the redistribution of free charges continues this time in the opposite direction.

If the pyroelectric field is assumed to be induced in a fixed direction changing only the magnitude with temperature and the natural birefringence can be neglected, there is a possibility of suppressing the effect of the pyroelectric field. In section 4.5.1 it was shown that the sensor with Lithium Niobate is sensitive only to one component of the electric field in the plane perpendicular to the optical axis. The orientation

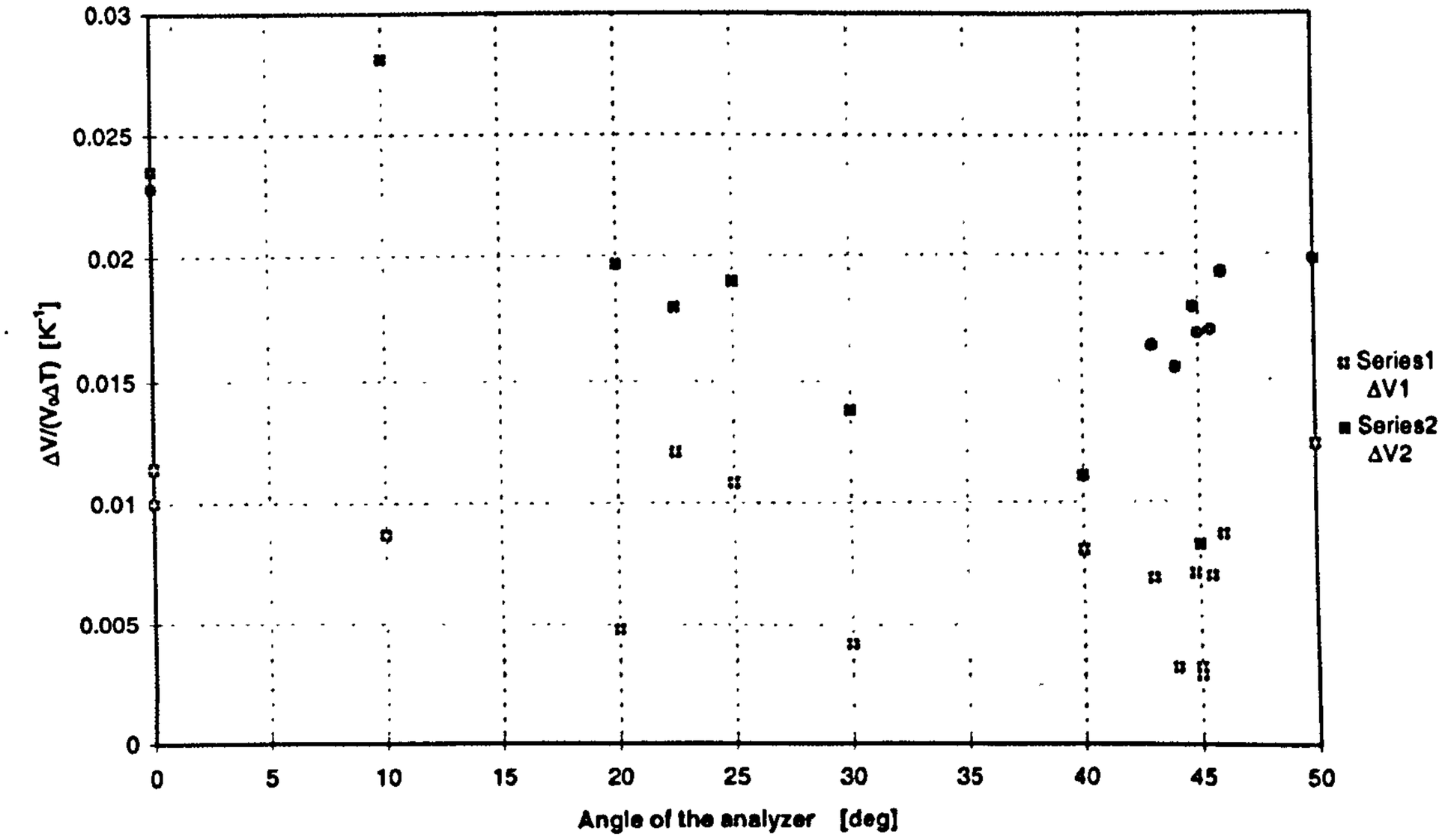

Figure 6.7: Relative change of the sensor output normalized to the temperature change; *V_0 is the output of the sensor at room temperature, ΔV is the change of the output during the temperature experiment and ΔT is change in temperature. ΔV in series 1 is the maximum change during the heating (ΔV_1 in Figure 6.6), whereas in series 2 it is the maximum change during the whole experiment (ΔV_2 in Figure 6.6).*

of this component is given by the orientation of the analyzer. Theoretically it is, therefore, possible to adjust the analyzer in such a way that the pyroelectric field component, perpendicular to the optical axis, does not influence the output of the sensor. The measured field is then perpendicular to this suppressed component of the pyroelectric field. Figure 6.7 shows the relative change of the sensor output normalized to the change in temperature as a function of analyzer orientation. If the method described above worked, there would be a visible improvement in the temperature stability when rotating the analyzer from a fixed position by an angle up to 45 degrees. In this range of angles, the analyzer should become parallel with one of the eigenaxes which would suppressed the effect of the pyroelectric field. However, the graph 6.7 does not show any strong improvement. It was, therefore, concluded that the pyroelectric field changes the direction with temperature changes or the effect of both natural birefringence and pyroelectricity together causes the optical eigenaxes to rotate which makes it impossible to employ the suggested compensation method.

Conclusions. The natural birefringence and the pyroelectric effect in the crystal of Lithium Niobate were found to be a source of a strong temperature instability of the electrooptic sensor. Theoretically, both effects could be suppressed by aligning the light beam along the crystal optical axis. It was found that in order to suppress the effect of the natural birefringence sufficiently the alignment has to be better than 0.01°. However, experimentally it was impossible to achieve a reasonable good temperature stability of the sensor for practical measurements.

6.4 Multiple reflections in Electrooptic Crystal

If the coherence length of the light source is long with respect to the thickness of the crystal, multiple reflections within the crystal can cause a significant change in the induced optical birefringence and thus in the sensor output characteristic. Moreover, the induced birefringence has a strong temperature dependence as it is shown in this section.

The coherence time of a semiconductor laser diode is typically $\tau_c \approx 10^{-8}$s [77] which corresponds to the coherence length of 30m. This length is much larger than the length of the used electrooptic crystal which enables the interference of the reflected waves up to 3000 reflections. In the case of the gas lasers like He-Ne the coherence time is even higher reaching 10^{-4}s due to the narrow laser linewidth [77].

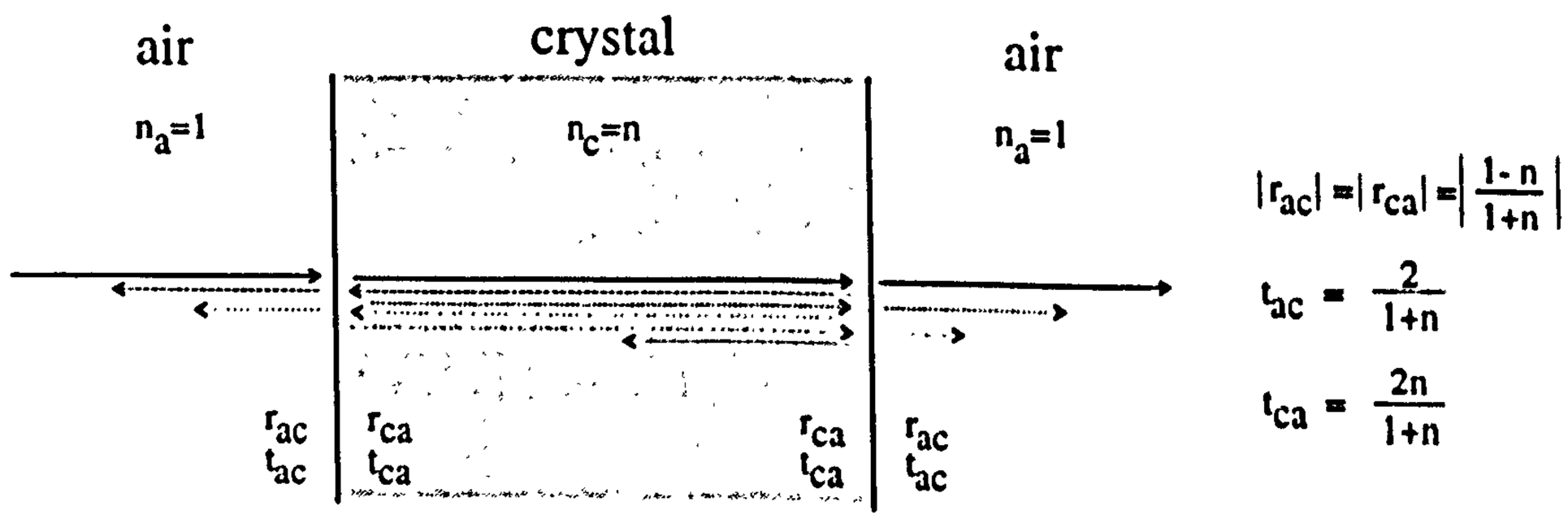

Figure 6.8: Multiple reflections of the light wave in the electrooptic crystal.

The reflections happen at the air-crystal and crystal-air interfaces as shown in

Figure 6.8. The electromagnetic wave behind the crystal is a superposition of the wave transmitted without reflection and the waves which underwent multiple reflections at the polished facets of the crystal. Using the amplitude transmittance and reflectance coefficients $t_{ac}, t_{ca}, r_{ac}, r_{ca}$ (Figure 6.8) the electric field intensity vector for the ordinary eigenwave behind the crystal E_{1out} can be written as [5]:

$$E_{1out} = E_{1in} t_{ac} t_{ca} e^{-ik_1 l} e^{-\alpha l} \left(1 + r_{ca}^2 e^{-2k_1 l} e^{-2\alpha l} + r_{ca}^4 e^{-4k_1 l} e^{-4\alpha l} + \ldots\right) \qquad (6.18)$$

where E_{1in} is the electric field intensity of the incident light, k_1 is the propagation constant of the first eigenwave linearly polarized along the eigenaxis x_1, α is the absorption coefficient and l is crystal length. Recognizing the quantity in brackets in equation (6.18) as a geometric progression, finding its sum and simplifying it, the electric field intensity E_{1out} can be written as:

$$E_{1out} = E_{1in} \frac{t_{ac} t_{ca} e^{-\alpha l}}{e^{ik_1 l} - r_{ca}^2 e^{-2\alpha l} e^{-i2k_1 l}} = E_{1in} A_1 e^{-i\Phi_1} \qquad (6.19)$$

A similar equation can be written for the second eigenwave. Using these results the Jones matrix of the electrooptic crystal becomes:

$$\mathrm{C}_r = \begin{pmatrix} A_1 e^{-i\Phi_1} & 0 \\ 0 & A_2 e^{-i\Phi_2} \end{pmatrix} \qquad (6.20)$$

Generally, the matrix (6.20) describes any optical linear retarder, i.e. also the quarter-wave plate. Considering multiple reflections only in the electrooptic crystal and using the derived Jones matrix (6.20) for the electrooptic crystal, Day and Lee [27] derived the output intensity of the sensor from Figure 4.1 in terms of reflectivity $R = r_{ac}^2 = r_{ca}^2$ and transmissivity $T = 1 - R$. In their report the absorption in the crystal was not considered. Using (6.19) and (6.20) the output intensity can be easily corrected to account for the effect of the absorption and is found to be:

$$I = \frac{T'^2}{2} \frac{1 - \sin\Gamma - 2R' \cos(2\beta l)\cos\Gamma}{1 - 4R' \cos\Gamma \cos(2\beta l)} \qquad (6.21)$$

where

$$\beta = \frac{1}{2}\left(\frac{2\pi n_1}{\lambda} + \frac{2\pi n_2}{\lambda}\right) \qquad (6.22)$$

is half of the sum of propagation constant of the eigenwaves, $R' = Re^{-2\alpha l}$ and $T' = Te^{-\alpha l}$ are the corrected reflectivity and transmissivity, n_1, n_2 are the refractive

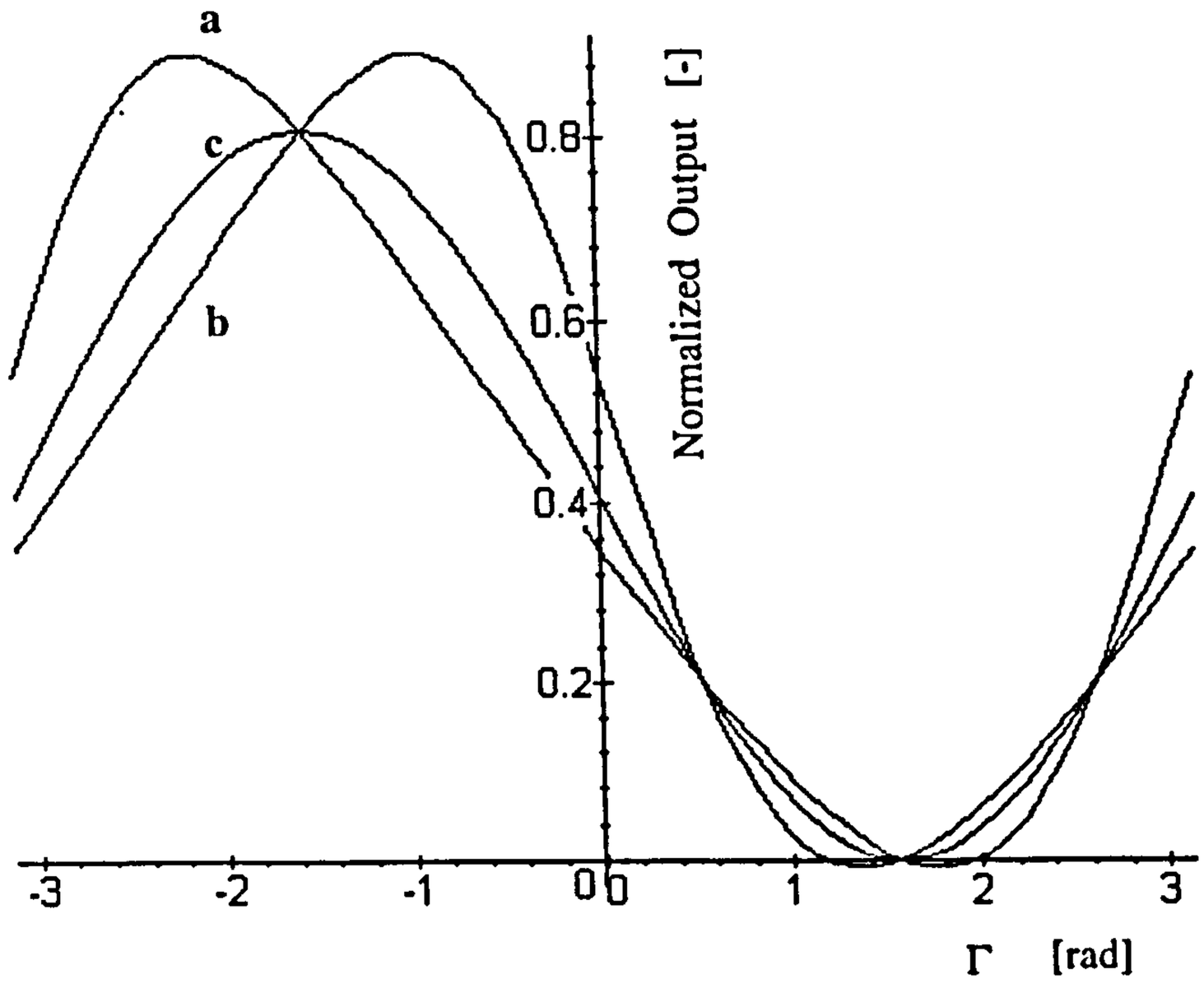

Figure 6.9: Sensor transfer characteristics considering multiple reflections of the light wave in the electrooptic crystal with reflectivity $R = 0.1$. *graph (a)* - $2\beta l = (2n + 1)\pi$, *graph (b)* - $2\beta l = 2n\pi$, *graph (c)* - $2\beta l = \pi/2$.

indices and λ is the light wavelength. The relative sensitivity (4.21) defined in section 4.3.1 becomes:

$$RS = \left.\frac{\partial I}{\partial \Gamma}\right|_{\Gamma=0} = \frac{I_0 T'^2}{2} \frac{-1}{1 - 4R' \cos(2\beta l)} \tag{6.23}$$

From (6.23) it can be easily found that the relative sensitivity has its maximum and minimum when the quantity $(2\beta l) = 2n\pi$ and $(2\beta l) = (2n + 1)\pi$, respectively. Figure 6.9 shows the plots of the transfer characteristics for $R = 0.1$ corresponding to the minimum and maximum sensitivities. The usual squared sinusoid response function is distorted in both amplitude and shape. More important, the sensor response becomes significantly dependent on the quantity $2\beta l$. Temperature changes influence both the length and the refractive index of the crystal. For Bismuth Germanate, with the temperature coefficient of the refractive index and thermal expansion $\alpha_{kn} = 3.9\,10^{-5}$ and $\alpha_{kl} = 5\,10^{-6}$, a change in temperature of $0.1°C$ causes a change of 2.9π radians in the quantity $2\beta l$. It becomes evident that the small temperature deviations can cause a strong instabilities of the sensor output. When the temperature is gradually decreased or increased, the transfer characteristic of

the sensor changes periodically between the characteristics (a) and (b) in Figure 6.9, with a period of $\approx 0.12\,°C$. The relative sensitivity oscillates between the maximum and minimum values :

$$RS_{min,max} = \frac{I_0 T'^2}{2} \frac{1}{1 \pm 4R'} \tag{6.24}$$

so that the relative imprecision RI defined in [27] as the largest RS minus the smallest RS divided by their sum can be written:

$$RI = \frac{RS_{max} - RS_{min}}{RS_{max} + RS_{min}} = 4R' \tag{6.25}$$

This result shows that even a sensor with a high quality coating ($R = 0.001$) suffers the relative imprecision of $\pm 0.4\%$. The relative sensitivity and the relative imprecision are suitable to characterise an AC sensor. However, in a DC sensor also the changes of the output intensity without applied electric field (not only a change in the slope of the transfer characteristic) must be taken into account as it cannot be distinguished between slow changes due to temperature variations and slow changes in measured field. With decreasing or increasing temperature the output intensity without an applied field oscillates between the maximum and minimum values I_{max}, I_{min}:

$$I_{max,min} = \frac{I_0 T'^2}{2} \frac{1 \pm 2R'}{1 \pm 4R'} \tag{6.26}$$

The changes in the DC output can be described by a relative uncertainty of the output $\Delta_{out-rel}$ calculated as a maximum change of the output normalized to the quantity $I_0 T^2/2$ which is an average DC power incident on the photodetector:

$$\Delta_{out-rel} = \frac{I_{max} - I_{min}}{I_0 T'^2/2} = \frac{4R'}{1 - 16R'^2} \approx 4R' \tag{6.27}$$

The best quality coatings offer the reflection coefficient of 0.002, typically 0.001. For these small values the relative uncertainty of the output is 4.10^{-3}. Compared to the temperature coefficients of quarter-wave plate and crystal in table 6.1, it can be seen that the effect of multiple reflections in optical components can be a critical issue in the electrooptic sensor even for the best quality coating. The effect of the multiple reflections was not observed experimentally since the uncertainty introduced by a

DC drift of the photodetectors exceeded the expected output changes due to the discussed effect.

Conclusions. The effect of the multiple reflections in the electrooptic crystal was found to introduce not negligible changes in the transfer characteristic of the sensor. Moreover, the calculated temperature instability due to the effect was found large, exceeding that of quarter-wave plate. The effect can be suppressed sufficiently in the case of AC measurements at extra low frequencies of measured field. It becomes critical in the case of DC measurements, without a physical rotation of the sensing element. It is suggested that the best antireflection coatings should be used in the electrooptic sensor.

6.5 Laser Power Fluctuations

Semiconductor laser diodes are known for their temperature dependent output characteristics. To operate them at constant power requires not only a precise current controller but a temperature control as well. This is not always available. Furthermore, power fluctuations can be caused by mode coupling and losses in optical fibres, coupling between laser and optical fibre, collimators alignment which can be temperature dependent. However, most of these temperature induced changes can be considered as light power fluctuations. One of the ways how to suppress these light power fluctuations due to the temperature changes, is to use a differential detection scheme which is described in this section.

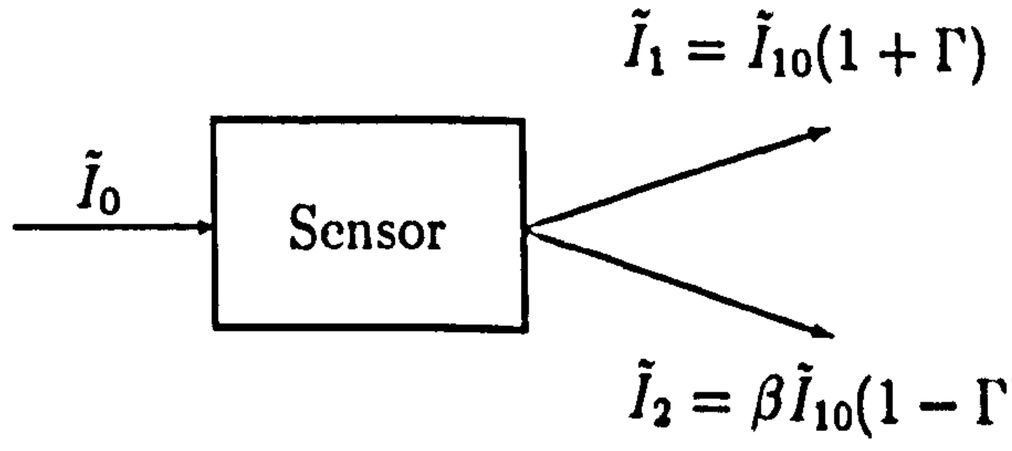

Figure 6.10: Electrooptic Sensor. Light intensity distribution.

A schematic diagram of electro-optic sensor in terms of light intensities incident

on the crystal $\tilde{I}_0$ and on the photodetectors $\tilde{I}_1$,$\tilde{I}_2$ is shown in Figure 6.10. As it was explained in section 4.1 the output intensities are changed with an applied electric field as:

$$\tilde{I}_1 = \tilde{I}_{10}(1 + \Gamma) \tag{6.28}$$

$$\tilde{I}_2 = \tilde{I}_{20}(1 - \Gamma) \tag{6.29}$$

where Γ is the phase retardation induced by the electric field intensity. The optical intensity fluctuations (ΔI) can be expressed using time dependent intensity fluctuation factor $\alpha(t)$:

$$\tilde{I}_0 = I_0 + \Delta I = I_0(1 + \alpha(t)) \tag{6.30}$$

where I_0 is a DC value of the incident light intensity which is constant in time. In practical situation the two output are not exactly symmetrical for example due to different coupling efficiencies of photodetectors, which can be described introducing asymmetry factor β in the following way:

$$\tilde{I}_{10} = \beta \tilde{I}_{20} \tag{6.31}$$

In an ideal case without optical losses the total output intensity is equal to the input intensity:

$$\tilde{I}_0 = \tilde{I}_{20} + \tilde{I}_{10} = \tilde{I}_{20}(1 + \beta) \tag{6.32}$$

The absorption and reflection losses can be accounted for using additional constant in the expression. However, this does not influence the final result and for simplicity reasons the ideal case is described. Using (6.28)-(6.32) the output intensities $\tilde{I}_1$ and $\tilde{I}_2$ in the presence of the electro-optic effect and power fluctuations can be written:

$$\tilde{I}_1 = \frac{\beta I_0(1 + \alpha(t))}{1 + \beta}(1 + \Gamma) \tag{6.33}$$

$$\tilde{I}_2 = \frac{I_0(1 + \alpha(t))}{1 + \beta}(1 - \Gamma) \tag{6.34}$$

Three detection schemes are considered : i) single output ($\tilde{I}_{10}$) ii) differential output ($\tilde{I}_1 - \tilde{I}_2$) iii) normalized differential output $(\tilde{I}_1 - \tilde{I}_2)/(\tilde{I}_1 + \tilde{I}_2)$. The different

schemes are characterized by a ratio Δ_{rel} of changes of the output due to the light intensity fluctuations ΔOut_α and due to the electric field ΔOut_Γ as follows:

$$\Delta_{rel} = \frac{\Delta I_\Gamma}{\Delta I_\alpha} \tag{6.35}$$

- In the case of single output $Out = \tilde{I}_2$ the ratio Δ_{rel} is found to be

$$\Delta_{rel} = \frac{\alpha}{\Gamma} \tag{6.36}$$

Typical values of Γ are of the order 10^{-5} (section 4.3.1) and α of the order 10^{-3} (laser driver precision 0.1%). It gives $\Delta_{rel} = 10^2$ which means that the output of the sensor is influenced about 100 times more by laser power fluctuations than by changes in the measured electric field.

- Differential scheme $\tilde{I}_1 - \tilde{I}_2$ can be used to avoid this strong influence of laser power fluctuations on the sensor output. Using (6.33) and (6.34) the output can be written:

$$Out = \tilde{I}_1 - \tilde{I}_2 = -\frac{I_0(1+\alpha)(1-\beta)}{1+\beta} + \Gamma I_0(1+\alpha) \tag{6.37}$$

and

$$\Delta_{rel} = \frac{\alpha}{\Gamma}\frac{\beta-1}{1+\beta} \tag{6.38}$$

When the output intensities $\tilde{I}_{10}, \tilde{I}_{20}$ are equal ($\beta = 1$), the ratio Δ_{rel} becomes zero and the effect of laser intensity fluctuations is eliminated. If the intensities differ ($\beta \neq 1$) the output is influenced by the intensity fluctuations depending on the asymmetry factor β. For example for $\beta = 0.8$ and the values of α and Γ used above, the ratio Δ_{rel} becomes 10. The output is then 10 times less sensitive to the light intensity fluctuations compared to the case of single output $\tilde{I}_2$. In most cases this kind of detection is sufficient to suppress light intensity fluctuations.

- Similarly for the detection scheme $(\tilde{I}_1 - \tilde{I}_2)/(\tilde{I}_1 + \tilde{I}_2)$ one can derive:

$$Out = \frac{\tilde{I}_1 - \tilde{I}_2}{\tilde{I}_1 + \tilde{I}_2} = \frac{-1+\beta+\Gamma(1+\beta)}{1+\beta-\Gamma(1-\beta)} \tag{6.39}$$

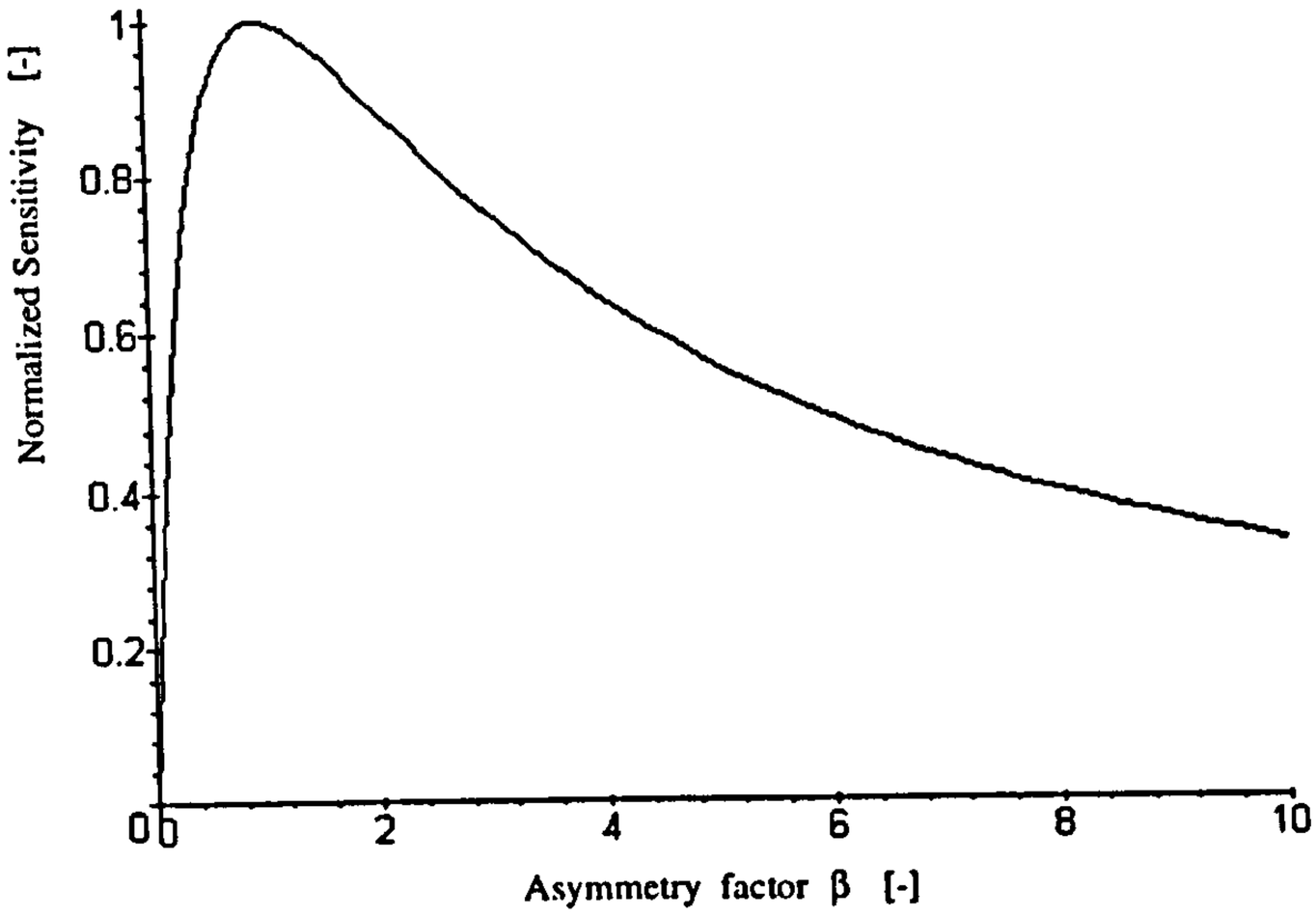

Figure 6.11: Normalized sensitivity versus the asymmetry factor β.

It can be seen that the second differential scheme does not depend on the fluctuation factor α which means that $\Delta_{rel} = 0$ and the light intensity fluctuations theoretically do not influence the sensor output. The asymmetry factor β can change the sensor sensitivity, defined as the slope of the transfer characteristic at the origin (section 4.3.1, equation 4.20). Figure 6.11 shows the normalized sensor sensitivity with respect to the asymmetry factor β. It can be seen that the maximum sensitivity of the described detection scheme is achieved for symmetrical outputs ($\tilde{I}_{10} = \tilde{I}_{20}$). If the output intensities $\tilde{I}_{10}, \tilde{I}_{20}$ differ ($\beta \neq 1$), the sensitivity of the sensor decreases according to Figure 6.11.

Conclusion Three different detection schemes were discussed. It was shown that the light intensity fluctuations which occur before the light beam enters the sensing head can be suppressed by employing one of the discussed differential detection schemes. These fluctuations in light intensity can be caused by a temperature dependence of the laser diode or its driver. Also any other changes in the light intensity transmitted to the sensing head (i.e. incident on the polarizer) such as optical fibre losses due to temperature variations and bending, temperature dependent coupling losses from laser to fiber and from fibre to collimator, can be suppressed using the described differential schemes. However, any fluctuations in intensity which occur

behind the analyzer will not be eliminated by using the differential optical scheme, since the signal variations due to these fluctuations will not be correlated. This method could not be successfully used in the performed experiments because of an uncorrelated drift of the photodetectors.

6.6 Summary

Although, experimentally it has been successfully demonstrated that Lithium Niobate can be used as a sensing element in DC field sensor, the temperature stability of such a sensor was found to be poor. Lithium Niobate is optically anisotropic and exhibits pyroelectric effect. The theoretical analysis showed that the temperature dependence of the sensor output is strongly influenced by the quarter-wave plate and Lithium Niobate. This was confirmed experimentally. It was found that the polarizer and the analyzer do not contribute to the temperature instability. A new method was developed to compensate for the temperature effect caused by the quarter-wave plate. The method is based on a suitable orientation of the quarter-wave plate with respect to other optical components. By aligning the principal direction of the analyzer along the optical eigenaxis of the quarter-wave plate the temperature effect of the plate on the output is suppressed. Using this compensation technique the temperature stability was improved by a factor of 10.

The temperature instability of Lithium Niobate is more dominant than that of the quarter-wave plate. The experimental results confirmed that the temperature instability of the sensor output was caused by the combined effect of natural birefringence and pyroelectric effect. A change in temperature of $8°C$ caused an output change of 24%, whereas the output change due to an electric field of 10kV/m is about 0.17%. Though, it is theoretically possible to suppress these effects by aligning the light beam along the optical axis, in practice it was difficult to achieve. This is attributed mainly to a component of the pyroelectric field which is perpendicular to the optical axis. The origin of such a field may be due to optical inhomogeneities as it was reported. A compensation scheme similar to that for the quarter-wave plate was tested, however, the attempt was not successful.

Theoretical investigation of the multiple reflections in the electrooptic crystal also showed that a high quality antireflection coating on optical components is necessary to reduce the effect of multiple reflections on the temperature stability of the sensor. It was also shown that the laser power fluctuations can be suppressed using one of the differential detection schemes presented in section 6.5.

From these findings it is clearly evident that Lithium Niobate can not be used as a sensing element in DC field measurements due to its low temperature stability.

Chapter 7

Conclusions

7.1 General Conclusions

Available cubic electrooptic crystals were compared from the sensor sensitivity point of view. A new figure of merit was used, taking into account the attenuation of the electric field in the dielectric crystal and its shape. The effect of optical activity in 23 cubic crystals was found to decrease the magnitude of the pure electrooptic effect; conditions for optimal crystal length and analyzer orientation were derived. The cubic crystals were further characterised for the charge relaxation time constant to estimate their performance in DC field measurements. Cubic crystal of Bismuth Germanate and non-cubic crystal of Lithium Niobate were identified as suitable electrooptic materials for the DC field sensor.

The selected crystals were found suitable at extra-low-frequencies. DC field measurements were impossible with Bismuth Germanate because of its low charge relaxation time constant, which is approximately 10s. The time constant of Lithium Niobate, which is about three hours, was sufficient for static field measurements. It was, however, found that the conductivity and the time constant of Lithium Niobate crystal are influenced to a great extent by temperature changes and the thermal history of the sample. A long term change in the time constant of three orders of magnitude was experienced. This change, which made the crystal unsuitable for DC field measurements, was attributed to the effect of stimulated conductivity. It was

demonstrated that high resistivity of crystals can be achieved by heat treatment at 400°C. After such heat treatment, Lithium Niobate could be used as a sensing element for DC field measurements.

Investigations of temperature stability of the DC field sensor showed that the main sources of the temperature instability are the quarter-wave plate and the crystal of Lithium Niobate. A new method of temperature compensation of the quarter-wave plate is proposed. By aligning the principal direction of the analyzer along the optical eigenaxes of the quarter-wave plate, the effect of quarter-wave plate temperature instability on sensor output is suppressed. Experimentally, the temperature stability of the plate was improved by a factor of 10. The temperature instability of Lithium Niobate was mainly attributed to the pyroelectric effect and natural birefringence. The temperature instability makes the sensor difficult to use in practical applications. No suitable temperature compensation method could be found.

Theoretical and experimental investigation of the external space charge effect showed that the sensor sensitivity is significantly influenced by this effect. The proposed method of its elimination, using an artificial extension of the sensing element, did not reduce the space charge effect adequately so that it could be used in a practical environment. The response of the sensor, with and without the extension, in both unipolar and bipolar environment, was found to be linear. A surface charge neutralisation of the probe was necessary before each measurement. The measured linear transfer characteristic was found to be independent of the space charge density. This enabled the measurement static fields in a unipolar environment. The direct field measurements in the bipolar environment suffered from a drift. This was attributed to a surface charge redistribution, which is intolerable in practical measurements.

The achieved minimum detection level of the sensor in the frequency range from 1 to 200Hz, was 1V/m with a signal to noise ratio equal to 0dB and a resolution of 1V/m. Due to a long term drift of photodetectors, the static field measurements were limited to the measurements of pulses with the duration of 200s. The achieved minimum detection level was 2.4kV/m.

7.2 Originality of the Presented Work

To the best of the author's knowledge, the following parts of the work presented in this thesis are original contributions in the area of electric field sensors in general, and in particular in the area of electro-optics:

- Comparison of cubic electrooptic crystals from the standpoint of sensor sensitivity using a new figure of merit. This figure of merit takes into account not only the refractive index and the electrooptic coefficients, but also the dielectric property and the shape of the crystal (section 4.3.1).

- Analysis of the effect of optical activity on sensor sensitivity using the concept of the Poincare sphere. The presented approach is an alternative to the commonly used method of Jones calculus (section 4.3.1).

- Comparison of selected cubic crystals from the standpoint of suitability for DC field measurements, based on the evaluation of their charge relaxation time constant (section 4.3.2).

- Use of selected electrooptic crystals of Lithium Niobate and Bismuth Germanate for electric field measurements at extra low frequencies in the range from 1Hz to 100Hz, with minimum detection level of 1V/m and resolution 1V/m without a physical rotation of the sensor (section 4.4.2).

- Use of the sensing crystal of Lithium Niobate for DC electric field measurements without attached electrodes and without the necessity of physical rotation of the crystal, under controlled conditions (section 4.4.3).

- Both theoretical and experimental analysis of the isotropy of the electrooptic sensor based on the crystals of Lithium Niobate and Bismuth Germanate (section 4.5).

- Theoretical and experimental analysis of the external space charge effect. Demonstration of possible measurements in unipolar space charge environment without the necessity of physical rotation of the sensing head (chapter 5).

- Theoretical and experimental analysis of the temperature stability of DC field electrooptic sensor using a sensing crystal of Lithium Niobate (section 6.3).

- Method of temperature compensation of the quarter-wave plate in the DC electrooptic field sensor (section 6.2).

In the duration of the project three conference papers were published [19] [78] [79], three presentations were given, two papers were accepted for conference presentations [80] [81], and one journal paper is in preparation [82].

7.3 Further Work

Although it was demonstrated that a DC electric field can be measured without a physical rotation of the probe, the temperature stability of such a sensor was found to be low, thus not allowing use of the probe in practical applications. The temperature stability of the sensor may be improved by developing a temperature compensation method for the crystal of Lithium Niobate or by finding a new, highly resistive cubic electrooptic crystal. The temperature compensation of Lithium Niobate is a real challenge and if successfully solved could most probably be utilised in other areas of electrooptics since there are a lot of devices based on this crystal. The material research was extensive and at present Lithium Niobate was identified as the only commercially available electrooptic material with high enough resistivity. However, in the near future other suitable materials may become available. If such a crystal is isotropic and without optical activity the problem of the temperature stability of the sensor can be addressed.

The detection system needs to be improved to avoid the strong drift experienced in the experiments. An improvement might be achieved by using the laser light intensity modulation, for example using optical chopper or direct modulation of the laser diode current, and the subtraction scheme in conjunction with a lock-in amplifier.

In order to use the sensor for measurements in a space charge environment, without physical rotation of the crystal, further research needs to be done on the

effect of the humidity on the sensor response to electric field. Further investigations are also necessary into the sensor performance in an environment with high space charge density, and into the possibility of elimination of the output drift in the bipolar environment by choosing a suitable geometry of the probe. However, due to complications such as the neutralisation of the probe after each measurement and the necessity of knowing the type of environment before measurements, it is suggested that one should focus on the development of an electrooptic probe using rotating sensing head. This solution should eliminate the problems of the DC drift of the sensor output caused by the photodetectors. Also one would expect the temperature stability to be improved since the output signal would be modulated by the rotation of the sensing head at frequencies higher than the temperature fluctuations of the environment. The main problem in designing and building such a sensor will be the optical alignment of the components in the probe and the coupling of the light into the output optical fibres. This is due to the possible disalignment caused by the rotation. The minimum value of the electric field intensity measured with such a probe is expected to be several V/m. The probe could be used for continuous monitoring of an electric field and could also be used in the space charge areas without the necessity of using another calibration.

This alternative method is currently being investigated, and a probe which uses a rotating sensing head is being developed.

Appendix A

Electric field in the crystal with conductivity σ and permittivity ϵ exposed to a static field

When a crystal of a finite resistivity is exposed to a static electric field, the free charge carriers start drifting along the electric field lines and accumulate on crystal boundaries. The accumulated space charge generates an electric field with orientation opposite to the original internal field. Therefore, the resultant field, which is a superposition of the original field and the field of accumulated space charge, continuously decreases. The first Maxwell equation (Gauss Law) can be written in the form:

$$div\mathbf{E} = \frac{\rho}{\epsilon} \tag{A.1}$$

where $\mathbf{E}$ is the electric field vector, ρ is the space charge density and ϵ is the permittivity of the crystal. If the electric field and its changes are assumed to be in x direction than the equation (A.1) becomes:

$$\frac{dE_x}{dx} = \frac{\rho}{\epsilon} \tag{A.2}$$

where E_x is the component of the electric field along x axis. This equation can be rewritten as

$$dE_x = \frac{\rho dx}{\epsilon} = \frac{dQ}{\epsilon} \tag{A.3}$$

where dQ is a variation of the space charge density. A space charge field establishes itself in the crystal due to the drift of free charge carriers in the external field and the accumulation of the space charge on the boundaries of the crystal. Space charge density variations dQ in time dt are determined by the density of current flowing per unit area inside the crystal in the time dt and (A.3) is found to be

$$dE_x = \frac{J(t)dt}{\epsilon} = \frac{\sigma(E_{x0} - E_x)dt}{\epsilon} \tag{A.4}$$

where $J(t)$ is the current density, σ is the specific conductivity of the crystal and E_{x0} is the original static field. The current density $J(t)$ is determined by the conduction current in the resultant field $E_{x0} - E_x$. Thus the final differential equation is obtained:

$$\frac{dE_x}{dt} + \frac{\sigma}{\epsilon}E_x - \frac{\sigma}{\epsilon}E_{x0} = 0 \tag{A.5}$$

This is a linear first-order ordinary differential equation whose solution is

$$E_x(t) = E_{x0}(1 - e^{-\frac{t}{\tau}}) \tag{A.6}$$

where

$$\tau = \frac{\epsilon}{\sigma} \tag{A.7}$$

is so called charge relaxation constant. The resultant internal field $E_m(t)$ is a superposition of the original field E_{x0} and the built-up field E_x, which have opposite orientations, and was found to be:

$$E_m(t) = E_{x0}e^{-\frac{t}{\tau}} \tag{A.8}$$

The field inside a dielectric crystal of a non-zero conductivity σ exposed to a static field decreases exponentially with time constant τ.

Appendix B

Dielectric Ball with a Surface Charge Density Distribution in Uniform Electric Field

Problem: to find electric field intensity inside and outside an isotropic dielectric ball with a symmetrical surface charge density exposed to a uniform electric field.

Solution: To solve the problem one has to solve the Laplace equation:

$$\Delta V = 0 \tag{B.1}$$

where V is the potential of the electric field. The equation (B.1) can be written in spherical coordinates as [1]:

$$\Delta V = \frac{1}{r^2}\frac{\partial}{\partial r}\left(r^2\frac{\partial V}{\partial r}\right) + \frac{1}{r^2\sin\theta}\frac{\partial}{\partial\theta}\left(\sin\theta\,\frac{\partial V}{\partial\theta}\right) + \frac{1}{r^2\sin^2\theta}\frac{\partial^2 V}{\partial\varphi^2} = 0 \tag{B.2}$$

The orientation of the electric field and the coordinate system are defined in Figure B.1. Because of a geometrical symmetry of the dielectric probe the space charge is deposited on the surface of the probe with a distribution which is symmetrical around the x_3 axis. It is suitable to use polar coordinate system shown in Figure 5.2, because the E_ϕ component of the electric field in polar coordinates as well as the derivative $\partial V/\partial\phi$ are equal to zero. Thus the Laplace equation (B.2) becomes

$$\Delta V = \frac{\partial}{\partial r}\left(r^2\frac{\partial V}{\partial r}\right) + \frac{1}{\sin\theta}\frac{\partial}{\partial\theta}\left(\sin\theta\,\frac{\partial V}{\partial\theta}\right) = 0 \tag{B.3}$$

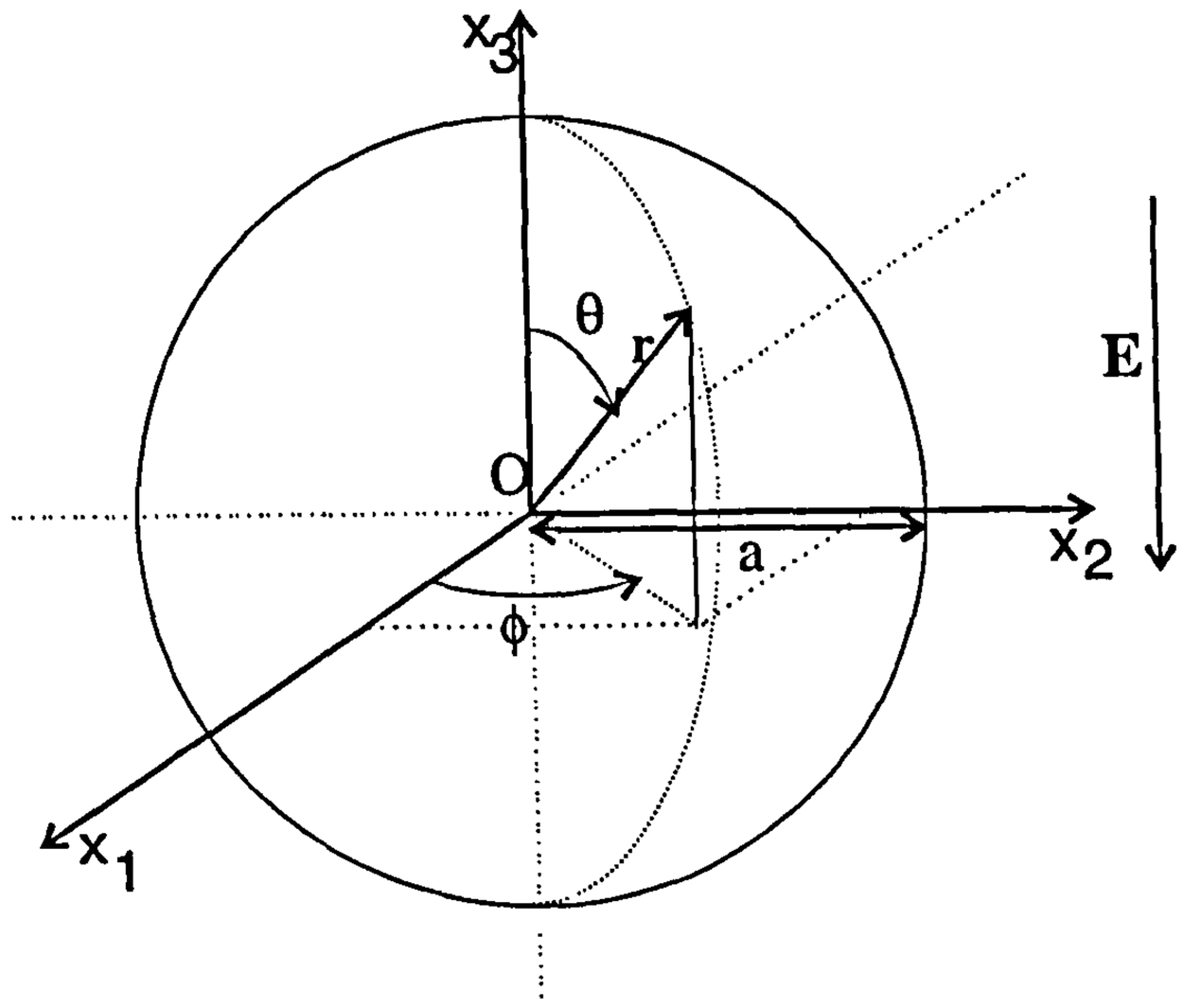

Figure B.1: The dielectric probe modeled as an isotropic ball of dielectric permittivity ϵ_r exposed to a uniform electric field **E**. *Calculations are simplified using polar coordinate system* (r, ϕ, θ).

and originally 3-dimensional problem becomes 2-dimensional. The solution of the equation (B.3) can be found using the method of separation of variables in the form $V(r,\theta) = R(r)\Theta(\theta)$ which leads to two equations:

$$\frac{1}{R}\frac{d}{dr}\left(r^2\frac{dR}{dr}\right) = k \tag{B.4}$$

and

$$\frac{1}{\Theta\sin\theta}\frac{d}{d\theta}\left(\sin\theta\,\frac{d\Theta}{d\theta}\right) = -k. \tag{B.5}$$

where k is a constant. The general solution of (B.3) is found by solving the equations (B.4) and (B.5) (e.g. [6]):

$$V = \sum_{n=0}^{\infty} A_n r^n P_n(\cos\theta) + \sum_{n=0}^{\infty} B_n r^{-(n+1)} P_n(\cos\theta) \tag{B.6}$$

where A_n and B_n are coefficients satisfying boundary conditions and $P_n(cos(\theta))$ are Legendre's polynomials of n-th order with argument $\cos(\theta)$ ([1]). The equation (5.2) is a general solution of the Laplace equation which is valid both inside and outside the dielectric ball but not on its surface, where we assume a layer of a deposited charge. The problem of finding the electric field potential in the case of a probe with a charge deposited on its surface, immersed in a uniform field, can be solved imposing the following boundary conditions:

1. The electric field is uniform in the absence of the sphere:

   $V \to -\infty$ for $x_3 \to -\infty$

   $V \to +\infty$ for $x_3 \to +\infty$

2. Potential V is continuous across the boundary ([6])

3. the normal components D_{n1}, D_{n2} of the electrical displacement vector $\mathbf{D}$ are not continuous any more and satisfy ([6])

   $D_{n1} - D_{n2} = \sigma;$ for $r = a$

   where σ is a surface charge density, a is the probe diameter. In spherical coordinates this condition becomes:

$$-\epsilon_0 \frac{\partial V_{out}}{\partial r} + \epsilon_0 \epsilon_r \frac{\partial V_{in}}{\partial r} = \sigma$$

   for $r = a$.

The surface charge density acquire the same axial symmetry as the electric field and can be, therefore, expressed as a function of only one variable θ. Since the Legendre's polynomial form a complete set, the surface charge density function σ function can be expressed in the form of Legendre's expansion:

$$\sigma = \sum_{n=0}^{\infty} \sigma_n P_n(cos(\theta)) \tag{B.7}$$

where $\theta \in \langle 0..\pi \rangle$ (Figure 5.2) and σ_n are the coefficients of the Legendre's expansion. The coefficients A_n and B_n are then found using (B.6),(B.7) and the boundary conditions.

Outside the sphere the solution must have $-E_0 r \cos\theta$ term according to the first boundary condition. Furthermore, this is the only harmonic with positive power of r that can be permitted. Otherwise the boundary condition 1. would be violated. Therefore, the potential outside the sphere can be written as:

$$V_{out} = -E_0 r \cos\theta + \sum_{n=0}^{\infty} B_n r^{-(n+1)} P_n(\cos\theta). \tag{B.8}$$

When considering potential distribution inside the dielectric ball, the terms with negative powers of r are not permissible since such terms would produce infinite

electric field in the ball. This is clearly impossible because the charges creating the field are the induced and deposited charges on the surface of the dielectric and no volume charge distribution is assumed. Thus the field potential inside the dielectric ball is found to be:

$$V_{in} = \sum_{n=0}^{\infty} A_n r^n P_n(\cos\theta) \tag{B.9}$$

The boundary condition 2. and 3. can be written as:

$$-E_0 a\cos\theta + \sum_{n=0}^{\infty} B_n a^{-(n+1)} P_n(\cos\theta) = \sum_{n=0}^{\infty} A_n a^n P_n(\cos\theta) \tag{B.10}$$

$$\begin{aligned} &E_0 P_1 + \frac{B_0}{a^2}P_0 + \frac{2B_1}{a^3}P_1 + \frac{3B_2}{a^4}P_3 + \ldots + \\ &+\epsilon_r\left[A_1 P_1 + 2A_2 r P_2 + 3A_3 r^2 P_3 + \ldots\right] = \sigma \end{aligned} \tag{B.11}$$

Using (B.7),(B.10) and (B.11) the coefficients A_n and B_n are found to be:

$$A_0 = \sigma_0 a \tag{B.12}$$

$$A_1 = \frac{\sigma_1 - 3E_0}{2+\epsilon_r} \tag{B.13}$$

$$A_n = \frac{\sigma_n a^{1-n}}{(\epsilon_r+1)n+1} \qquad n = 3,4,5\ldots \tag{B.14}$$

$$B_0 = \sigma_0 a^2 \tag{B.15}$$

$$B_1 = \frac{[\sigma_1 + E_0(\epsilon_r - 1)]a^3}{\epsilon_r + 2} \tag{B.16}$$

$$B_n = \frac{\sigma_n a^{n+2}}{(\epsilon_r+1)n+1} \qquad n = 3,4,5\ldots \tag{B.17}$$

Finally the potential outside and inside the ball (V_{out}, V_{in}) can be expressed

$$\begin{aligned} V_{out} \;=\; & \frac{\sigma_0 a^2}{r} - E_0 r\cos\theta + \frac{[\sigma_1 + E_0(\epsilon_r-1)]a^3}{r^2(\epsilon_r+2)}\cos\theta \\ & + \frac{\sigma_n a^{n+2}}{(\epsilon_r+1)n+1}\frac{1}{r^{n+1}}P_n(\cos\theta) + \ldots \end{aligned} \tag{B.18}$$

$$V_{in} = \sigma_0 a + \frac{\sigma_1 - 3E_0}{2+\epsilon_r} r\cos\theta + \frac{\sigma_2}{a[2(1+\epsilon_r)+1]} r^2 P_2(\cos\theta) + \ldots + \frac{\sigma_n a^{1-n}}{(\epsilon_r+1)n+1} r^n P_n(\cos\theta) + \ldots \quad \text{(B.19)}$$

The electric field intensity can be calculated as negative gradient of the field potential V. The components E_r and E_θ of the electric field in spherical coordinates can be found as

$$E_r = -\frac{\partial V}{\partial r} \quad \text{(B.20)}$$

$$E_\theta = -\frac{1}{r}\frac{\partial V}{\partial \theta}. \quad \text{(B.21)}$$

Using the derived equations for the field potential inside and outside the dielectric ball the internal and external field intensities (E_{in}, E_{out}) are finally found:

$$E_{rout} = \frac{\sigma_0 a^2}{r^2} + E_0\cos\theta + 2\frac{[\sigma_1 + E_0(\epsilon_r - 1)]a^3}{r^3(\epsilon_r+2)}\cos\theta + (1+n)\frac{\sigma_n a^{n+2}}{(\epsilon_r+1)n+1}\frac{1}{r^{n+2}}P_n(\cos\theta) + \ldots \quad n = 2,3,4\ldots \quad \text{(B.22)}$$

$$E_{\theta out} = -E_0\sin\theta - \frac{[\sigma_1 + E_0(\epsilon_r-1)]a^3}{\epsilon_r+2}\frac{1}{r^3}\frac{\partial P_1}{\partial\theta} - \frac{\sigma_n a^{n+2}}{(\epsilon_r+1)n+1}\frac{1}{r^{n+2}}\frac{\partial P_n(\cos\theta)}{\partial\theta} - \ldots \quad n = 2,3,4\ldots \quad \text{(B.23)}$$

$$E_{rin} = -\frac{\sigma_1 - 3E_0}{2+\epsilon_r}\cos\theta - \frac{\sigma_2}{a[2(1+\epsilon_r)+1]} r P_2(\cos\theta) - \ldots - \frac{\sigma_n a^{1-n}}{(\epsilon_r+1)n+1} r^{n-1} P_n(\cos\theta) - \ldots \quad n = 3,4,5\ldots \quad \text{(B.24)}$$

$$E_{\theta in} = \frac{\sigma_1 - 3E_0}{2+\epsilon_r}\sin\theta - \frac{\sigma_2}{a[2(1+\epsilon_r)+1]} r\frac{\partial P_2(\cos\theta)}{\partial\theta} - \ldots - \frac{\sigma_n a^{1-n}}{(\epsilon_r+1)n+1} r^{n-1}\frac{\partial P_n(\cos\theta)}{\partial\theta} - \ldots \quad n = 3,4,5\ldots \quad \text{(B.25)}$$

The derived set of equations was used to model sensor in the uniform electric field with space charge density not violating the assumption for use of Laplace equation.

Appendix C

The electric field between circular plates with uniform surface charge density

Problem: to find the electric field intensity in the origin O between circular plates with uniform surface charge density of opposite polarities, as depicted in Figure C.1.

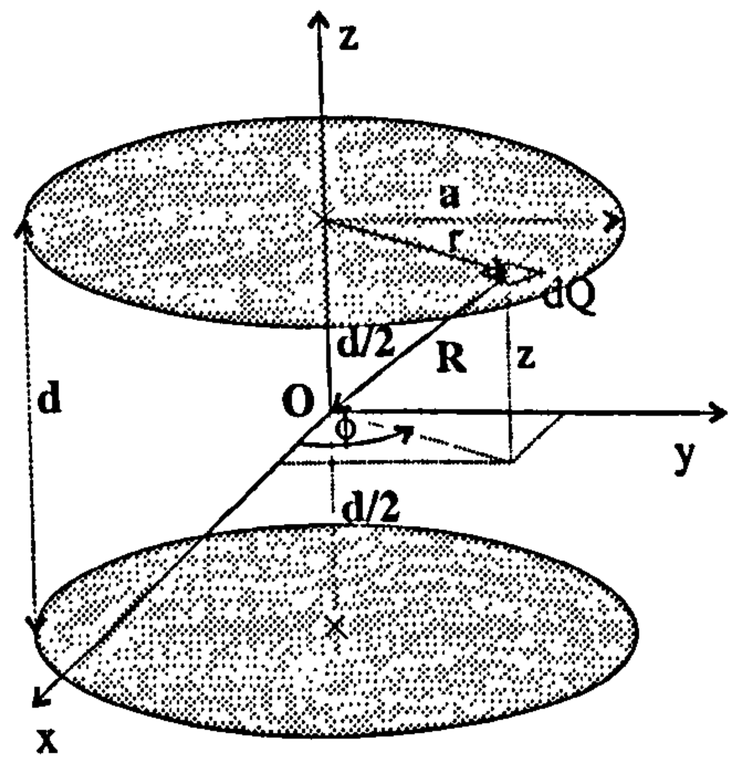

Figure C.1: Two circular plates of opposite uniform surface charge densities.

Solution: If the surface charge density of the upper electrode is denoted σ the electric field intensity in the origin $d\mathbf{E}$ which originates from an infinitesimal charge

$dQ = \sigma dS$ can be found using Coulomb's law:

$$d\mathbf{E} = \frac{1}{4\pi\epsilon_0}\frac{dQ}{R^2}\frac{\mathbf{R}}{R} \tag{C.1}$$

where $\mathbf{R}$ is the vector from the point of the infinitesimal charge dQ to the origin and R is its absolute value. The expression (C.1) can be written in cylindrical coordinates (r, ϕ, z) as

$$d\mathbf{E} = \frac{\sigma r dr d\phi}{4\pi\epsilon_0(r^2+z^2)}\frac{-r\mathbf{e_r} + z\mathbf{e_z}}{\sqrt{r^2+z^2}} \tag{C.2}$$

where $\mathbf{e_r}$ is a unit radial vector and $\mathbf{e_z}$ is a unit vector along z axis. The symmetry of the problem about z axis results in a cancellation of the radial component and, therefore, after integration the electric field intensity in the origin caused by the charged upper electrode is obtained:

$$\mathbf{E} = -\frac{\sigma r dr d\phi}{4\pi\epsilon_0(r^2+z^2)^{3/2}}\mathbf{e_z} = -\frac{\sigma}{2\epsilon_0}\left(1 - \frac{z}{\sqrt{a^2+z^2}}\right)\mathbf{e_z} \tag{C.3}$$

The electric field intensity $\tilde{\mathbf{E}}$ in the case of two circular sheets with uniform charge densities of opposite sign, as shown in Figure C.1, is found using already derived equation (C.3) :

$$\tilde{\mathbf{E}} = -\frac{\sigma}{2\epsilon_0}\left(1 - \frac{d/2}{\sqrt{a^2+(d/2)^2}}\right)\mathbf{e_z} + \frac{\sigma}{2\epsilon_0}\left(-1 - \frac{d/2}{\sqrt{a^2+(d/2)^2}}\right)\mathbf{e_z} \tag{C.4}$$

Finally, the electric field intensity in the origin between two charged plates of opposite polarities was found to be:

$$\tilde{\mathbf{E}} = -\frac{\sigma}{\epsilon_0}\left(1 - \frac{d}{\sqrt{4a^2+d^2}}\right)\mathbf{e_z} \tag{C.5}$$

Appendix D

Extinction ratio of the polarizers and sensor sensitivity

The effect of the polarizers on the temperature stability of the sensor has already been mentioned. Another characteristic which could influence the sensor performance is the extinction ratio of polarizers. Its effect on the sensor sensitivity is subject of this section.

A linear polarizer is an optical component that, when placed in a beam of light, produces a linearly polarized light. The direction of the electric field vibrations is called the direction of the principal transmittance. In the electrooptic sensor (Figure 4.1) the linear polarizer is used to define the linear polarization of the light at the beginning of the chain of optical components and, as an analyzer, to extract a linearly polarized component from the output light. The Jones matrix of an linear analyzer with the direction of the principle transmittance along x_1 axis, in x_1, x_2 plane, is:

$$\begin{pmatrix} k_1 & 0 \\ 0 & k_2 \end{pmatrix} = \begin{pmatrix} \sqrt{T_1} & 0 \\ 0 & \sqrt{T_2} \end{pmatrix} \tag{D.1}$$

where k_1, k_2 are square roots of the principle transmittances T_1, T_2 ($T_1 > T_2$). When two identical polarizers, with their directions of transmittance oriented at angle θ to each other, are placed in an unpolarized beam, the resulting transmittance is given

by:

$$T(\theta) = \frac{1}{2}(T_1^2 + T_2^2)\cos^2\theta + T_1 T_2 \sin^2\theta \tag{D.2}$$

The extinction ratio of a polarizer is defined by the principle transmittances as

$$er = \frac{T_2}{T_1} \approx 2\frac{T(90)}{T(0)} \tag{D.3}$$

where $T(90)$ and $T(0)$ are the transmittances obtained from (D.2) for angles 90 and 0°, respectively. The last result is suitable for practical measurements of the extinction ratios.

The effect of er on the sensor is investigated applying Jones calculus to the optical scheme from Figure 4.1. The output light vector $\mathbf{L}_{out}$ can be written in the form:

$$\mathbf{L}_{out} = \mathbf{A}_n\ \mathbf{C}_r\ \mathbf{Q}_{wp}\ \mathbf{P}\ \mathbf{L}_{in} \tag{D.4}$$

where $\mathbf{A}_n$, $\mathbf{C}_r$, $\mathbf{Q}_{wp}$ and $\mathbf{P}$ are the Jones matrices of the individual components in the sensor (analyzer, crystal, quarter-wave plate and polarizer), and $\mathbf{L}_{in}$ is the vector representing the input light. All the optical components excluding the polarizer and analyzer are considered to be ideal. The quarter-wave plate eigenaxes as well as the optical eigenaxes of the electrooptic crystal are at 45° to the x_1 axis. The polarizer and analyzer have the principle direction along x_1 and the input light beam is circularly polarized. Under these assumptions (D.4) becomes:

$$\begin{aligned}
\mathbf{L_{out}} &= \begin{pmatrix} k_{1a} & 0 \\ 0 & k_{2a} \end{pmatrix} \begin{pmatrix} \cos\frac{\Gamma}{2} & \sin\frac{\Gamma}{2} \\ \sin\frac{\Gamma}{2} & \cos\frac{\Gamma}{2} \end{pmatrix} \frac{1}{\sqrt{2}} \begin{pmatrix} 1 & i \\ i & 1 \end{pmatrix} \begin{pmatrix} k_{1p} & 0 \\ 0 & k_{2p} \end{pmatrix} \begin{pmatrix} 1 \\ i \end{pmatrix} = \\
&= \frac{1}{\sqrt{2}} \begin{pmatrix} k_{1a}k_{1p}(\cos\frac{\Gamma}{2} - \sin\frac{\Gamma}{2}) - k_{1a}k_{2p}(\cos\frac{\Gamma}{2} + \sin\frac{\Gamma}{2}) \\ ik_{2a}k_{1p}(\sin\frac{\Gamma}{2} + \cos\frac{\Gamma}{2}) + ik_{2a}k_{2p}(\cos\frac{\Gamma}{2} - \sin\frac{\Gamma}{2}) \end{pmatrix}
\end{aligned} \tag{D.5}$$

where Γ is the phase retardation introduced by the electrooptic crystal and the square roots of principle transmittances for analyzer and polarizer were distinguished by a subscripts a and p. The output light intensity is found using (4.9):

$$\begin{aligned}
I &= \frac{1}{2}(k_{1p}^2 + k_{2p}^2)(k_{2a}^2 + k_{1a}^2) + \\
&+ \frac{1}{2}\left[\sin\Gamma(k_{2p}^2 - k_{1p}^2)(k_{1a}^2 - k_{1p}^2) + 2k_{1p}k_{2p}(k_{2a}^2 - k_{1a}^2)\cos\Gamma\right]
\end{aligned} \tag{D.6}$$

Three special cases can be considered:

- Both polarizer and analyzer are ideal, ie.$k_{1a} = k_{1p} = 1$, $k_{2a} = k_{2p} = 0$. The intensity (D.6) becomes:

$$I = \frac{1}{2}(1 + sin\Gamma) \tag{D.7}$$

which is the transfer function of the ideal sensor.

- Both polarizer and analyzer are identical. Then the output intensity is:

$$I = \frac{1}{2}(k_1^2 + k_2^2)^2 + \frac{1}{2}(k_2^2 - k_1^2)[(k_2^2 - k_1^2)sin\Gamma - 2k_1 k_2 \cos\Gamma] \tag{D.8}$$

The relative sensitivity RS, defined as the sensitivity of the real sensor normalized by sensitivity of the ideal sensor, is obtained from (D.8):

$$RS = (k_2^2 - k_1^2)^2 = T_1^2(1 - e_r)^2 \tag{D.9}$$

where the equation (D.3) was used to express the relative sensitivity in terms of extinction ration of the polarizers.

In most commercially available polarizers the extinction ratio is much smaller that the principal transmittance T_1. It is, therefore, the absorption of the polarizer rather than the extinction ratio which influences the sensor sensitivity. Prism polarizers like Glan-Taylor, Glan-Thompson or Wollaston polarizers have relatively high principle transmittance (> 0.9 and low extinction ratio (typically 10^{-5}). Their another advantage is a large range of wavelength. Dichroic polarizers have slightly lower extinction ratio (typically 10^{-4}) and are quite lossy ($T_1 \approx 0.6 - 0.7$). They do not perform very well in the near infrared and are usually suitable for application below 800nm. Also there is concern about the performance of polymer films when the exposure to high temperatures is prolonged [27]. The Glan-Thompson polarizer were chosen for the application of DC field sensor because of their good performance in the infrared region.

Conclusions. The polarizers were found not to be the critical elements in the sensor. The extinction ratio was shown to influence the sensor sensitivity to very

small extent. The sensor sensitivity is mostly influence by the absorption of the polarizer (principle transmittance). However, in most cases the absorption may be compensated simply by an increase in the optical power of the beam or amplification of the photodetectors.

Bibliography

[1] George B.Arfken, Hans J.Weber, *Mathematical methods for physicist*, Academic Press, 4th edition, 1995

[2] M.Born, E.Wolf, *Principles of optics*

[3] J.A.Cross, *Electrostatics, Principles, Problems and Applications*, Adam Hilger, IOP Publishing Limited, Bristol 1987, chapters 2,3

[4] Ch.Kittel, *Introduction to solid state physics*

[5] M.V.Klein, *Optics*, John Wiley&Sons, Inc., New York, London, Sydney, Toronto, 1976, section 11.4

[6] P.Lorrain, D.Corson. *Electromagnetic fields and waves*, Willey&Sons, 2nd edition, p.163-175

[7] J.F.Nye, *Physical properties of crystals*

[8] Prokhorov, *Properties of Lithium Niobate*

[9] A.Yariv, P.Yeh, *Optical waves in crystals, Propagation and Control of Laser Radiation*, John Wiley&Sons, Inc., 1984, chapters 4,7,8

[10] A.Yariv, *Optical Electronics*, Saunders College Publishing, 4th edition, p.309-330, 1991

[11] A.von Engel, *Ionized gases*, second edition, Oxford University Press, p.5-10, 1965

[12] R.E.Aldrich, S.L.Hou, M.L.Harvill, *Electrical and optical properties of* $Bi_{12}SiO_{20}$, J.Appl.Phys., vol.42, p.493-494, 1971

[13] V.P.Avramenko, A.Yu.Kudzin, S.P.Reprentcheva, L.Ya.Sadovskaya, G.X.Sokolianskii, *Electric properties of* Bi_2TeO_5 *single crystals*, Ferroelectrics, Vol.82, p.173-178, 1988

[14] W.Balachandran, F.Cecelja, R.Jung, *A review of near field RF electric and magnetic field probes*, (in preparation)

[15] P.Bayvel, *Investigation of the electro-optic properties of* $Bi_{12}SiO_{20}$ *(BSO) and* $Bi_{12}GeO_{20}$ *(BGO)-Application to sensors*, J.Opt.Sensors, vol.2, no.6, p.413-419, 1987

[16] J.Bergman, A.Ashkin, A.A.Ballman, J.M.Dziedzic, H.J.Levinstein, R.G.Smith, *Curie temperature, birefringence, and phase-matching temperature variations in $LiNbO_3$ as a function of melt stoichiometry*, Appl.Phys.Lett., Vol.12, No.3, February 1968)

[17] K.M.Bohnert, J.Nehring, *Fibreoptic sensing of electric field components*, Appl.Opt., vol.27, no.23, p.4814-4818, Dec.1988

[18] E.Bonek, D.Hornbachner, E.RiedlBratengeyer, W.Hadrian and R.Jobst, *Electrooptic elf field sensor*, Electronics Letters, Vol.28, No.21, p.1994-1995, 8th Oct.1992

[19] M.Bordovsky, F.Cecelja, B.Balachandran *Comparative study of cubic crystals performance in bulk electro-optic sensor for DC and extra-low-frequency measurements*, SPIE Proc., Vol.2839, p.166-173, 1996

[20] D.P.Bortfeld, H.Meier, *REfractive indices and electro-optic coefficients of the eulitities $Bi_4Ge_3O_{12}$ and $Bi_4Si_3O_{12}$*, J.Appl.Phys., vol.43, no.12, p.5110-5111, Dec.1972

[21] C.F.Buhrer, L.Ho, J.Zucker, *Electrooptic effect in optically active crystals*, Appl.Opt., Vol.3, No.4, p.517-521, Apr.1964

[22] A.V.Bune, V.A.Pashkov, *Electron drift mobility in lithium niobate crystals*, Sov.Phys.Solid State, Vol.28, No.10, p.1701-1703, Oct.1986

[23] L.K.Bunina, E.P.Guenok, A.Yu.Kudzin, G.Kh.Sokolyanskii, A.S.Yudin, *Stimulated conductivity and optical absorption in lithium niobate crystals*, Sov.Phys.Solid State, Vol.33, No.8, p.1387-1388, Aug.1991

[24] Chang, C.N.Vittitoe, B.T.Neyer, W.P.Ballard, *Electrooptical technique for intense microwave measurements*, J.Appl.Phys., vol.57, no.11, p.4843-4848, June 1985

[25] Y.K.Choi, M.Sanagi, M.Nakajima, *Measurement of low frequency electric field using Ti : $LiNbO_3$ optical modulator*, IEE Proc.J, vol.140, no.2, p.137-140, Apr. 1993

[26] S.J.Czyzak, W.M.Baker, R.C.Crane, J.B.Howe, *Refractive indices of single synthetic Zinc Sulfide and Cadmium Sulfide crystals*, J.Opt.Soc.Am., vol.47, no.3, p.240-243, March 1957

[27] G.W.Day, P.D.Hale, M.Deeter, T.E.Milner, D.Conrad, S.M.Etzel, *Limits to the precision of electro-optic and magneto-optic sensors*, National Bureau of Standards Technical Note 1307, CODEN:NBTNAE, March 1987

[28] L.J.Donalds, W.G.French et al., *Electric field sensitive optical fibre using piezoelectric polymer coating*, Electr. Lett., vol.18, no.8, p.327-328, Apr.1982

[29] G.W.Day, P.D.Hale, M.Deeter, T.E.Milner, D.Conrad, S.M.Etzel, *Limits to the precision of electro-optic and magneto-optic sensors*, National Bureau of Standards Technical Note 1307, CODEN:NBTNAE, March 1987

[30] Yu.Gulyaev, Yu.L.Kopylov, V.B.Kravchenko, V.V.Kucha, V.V.Kutsaenko, V.T.Potapov, R.V.Shpilevskii, *Fiber optical electric field sensor*, Sov.Phys.Tech.Phys., vol.29, no.9, p.1064-1065, Sept.1984

[31] Y.Hamasaki, H.Gotoh, M.Katoh, S.Takeuchi, *OPSEF: an optical sensor for measurement of high electric field intensity*, Electr.Lett., vol.16, no.11, p.406-407, May 1980

[32] R.E.Hebner, E.C.Cassidy, *Measurement of 60 Hz voltages using the Kerr effect*, Rev.Sci.Instrum., vol.43, no.12, p.1839-1841, Dec.1972

[33] K.Hidaka, H.Fujita, *A new method of electric field measurements in corona discharge using Pockel's device*, J.Appl.Phys., vol.53, no.9, p.5999-6003, Sept.1982

[34] S.P.Hoernfeldt, *DC probes for electric field distribution measurements*, IEEE Power System Instrum.Measurement, p.524-529, 1991

[35] M.Imai, H.Tanizawa, Y.Ohtsuka, Y.Takase, A.Odajima, *Piezoelectric copolymer jacketed singlemode fibre for electricfield application*, J.Appl.Phys., vol.60, no.6, p.1916-1918, Sept.1986

[36] D.A.Jackson, *Monomode optical fibre interferometers for precision measurement*, J.Phys.E:Sci.Instrum., vol.18, p.981-1001, 1985

[37] N.A.F.Jaeger, L.Young, *High voltage sensor employing an integrated optics Mach-Zehnder interferometer in conjunction with a capacitive divider*, J.Lightw.Technol., vol.7, no.2, p.229-235, Feb.1989

[38] H.G.Jerrard, *Transmission of light through birefringent and optically active media: the Poicare sphere*, J.Opt.Soc.Am., Vol.44, No.8, p.634-640, 1954

[39] M.Kanda, *Standard Probes for Electromagnetic Field Measurements*, IEEE Trans.Anten.Propag., vol.41, no.10, p.1349-1364, Oct.1993

[40] M.Kanoi, et al., *Optical voltage and current measuring system for electric power systems*, IEEE Trans.Pow.Del., vol.1, no.1, p.91-97, Jan.1986

[41] M.Kiefer, A.Yariv, *Electro-optic characteristics of CdTe at 3.39 and 10.6 μm*, Appl.Phys.Lett., vol.15, no.1, p.26-27, July 1968

[42] S.A.Kingsley, S.Sriram, J.T.Boyd, D.H.Naghski, J.Latess *Photonic electrodeless passive electric field sensor*, 1994 Conference on precision electromagnetic measurements digest, 27 June- 1 July 1994

[43] K.P.Koo, G.H.Sigel, *An electric field sensor utilizing a piezoelectric Polivinylidene Fluoride (PVF2) film in a singlemode fibre interferometer*, IEEE J.Quant.Electr., vol.QE18, p.670, 1982

[44] Y.Kuhara, Y.Hamasaki, A.Kawakami,Y.Murakami, M.Tatsumi H.Takimoto, K.Tada, T.Mitsui, *BSO/Fibre optic voltmeter with excellent temperature stability*, Electr.Lett., vol.18, no.24, p.1055-1056, Nov.1982

[45] V.V.Kutsaenko, V.T.Potapov, R.V.Shpilevskii, *$Bi_{12}SiO_{20}$ fiber optic electric field sensor*, Sov.Phys.Tech.Phys., vol.30, no.7, p.790-792, July 1985

[46] N.Kuwabara, K.Tajima et al., *Development and analysis of electric field sensor using LiNbO3 optical modulator*, IEEE Trans.EMC, vol.34, no.4, p.391-396, Nov.1992

[47] K.Kyuma, S.Tai, M.Nunoshita, N.Mikami, Y.Ida, *Fibreoptic current and voltage sensor using a $Bi_{12}GeO_{20}$ single crystal*, J.Light.Technol., vol.LT1, no.1, p.93-97, March 1983

[48] K.S.Lee, *New compensation method for bulk optical sensors with multiple birefringence*, Appl.Opt., vol.28, no.11, p.2001-2011, June 1989

[49] K.S.Lee, *Electrooptic voltage sensor: birefringence effects and compensation methods*, Appl.Opt., vol.29, no.30, p.4453-4460, Oct.1990

[50] P.V.Lenzo, E.G.Spencer, A.A.Ballman, *Optical activity and electro-optic effect in Bismuth Germanium Oxide ($Bi_{12}GeO_{20}$)*, Appl.Opt., Vol.5, No.10, p.1688-1689, 1966

[51] D.T.Marple, *Refractive index of GaAs*, J.Appl.Phys., vol.35, no.4, p.1241-1242, Apr.1962

[52] D.T.F.Marple, *Refractive index of ZnSe, ZnTe, and CdTe*, J.Appl.Phys., vol.35, no.3, p.539-542, March 1964

[53] G.A.Massey, D.C.Erickson, R.A.Kadlec, *Electromagnetic field components: their measurement using linear electrooptic and magnetooptic effects*, Appl.Optics, vol.14, no.11, p.2712-2719, Nov.1975

[54] D.Mermelstein, *Optical fiber copolymer film electric field sensor*, Appl.Optics, vol.22, no.7, p.1006-1009, Apr.1983

[55] P.Meyrueix, D.Chatrefoe, *Pockel's effect voltage sensor. Construction of a VHV prototype*, NBS Workshop, 16/09/87-18/09/87

[56] Y.Murooka, T.Nakano, *Optical high sensitive field sensor using a Pockels crystal*, Rev.Sci.Instrum., vol.63, no.12, p.5582-5585, Dec.1992

[57] Y.Murooka, T.Nakano, Y.Takahashi, T.Kawakami, *Modified Pockels sensor for electric field measurements*, IEE Proc.Sci..Meas.Technol., vol.141, no.6, p.481-485, Nov. 1994

[58] S.Namba, *Electro-optical Effect of Zinc Blend*, J.Opt.Soc.Am., vol.51, no.1, p.76-79, Jan.1961

[59] S.Namba, *High voltage measurement by ADP crystal plate*, Rev.Sci.Instrum., vol.32, no.5, p.595-597, 1961

[60] J.A.Osborn, *Demagnetising factors of the general ellipsoid*, Phys.Rev., vol.67, no.11&12, p.351-357, June 1945

[61] PHOTOX Optical Systems datasheets

[62] T.S.Priest, G.B.Scelsi, G.A.Woolsey, *Optical fibre sensor for electric field and electric charge using low-coherence, Fabry-Perot interferometry*, Appl.Opt., vol.36, no.19, p.4505-4508, July 1997

[63] G.N.Ramachandran, S.Ramaseshan, *Magneto-optic rotation in birefringent media - Application of Poincare sphere*, J.Opt.Soc.Am., Vol.42, No.1, p.49-56, 1952

[64] S.M.Robertson, A.J.Rogers, *Measurement of DC electric field using the electrooptic effect*, IEE Proc., vol.132, Pt.J, no.3, p.195-198, June 1985

[65] K.Shibata, *A fibre optic electric field sensor using the electrooptic effect of* $Bi_4Ge_3O_{12}$, First International Conference on Optical Fibre Sensors, IEE Conference publication no.221, 164 (1983)

[66] R.T.Smith, F.S.Welsh, *Temperature dependence of the elastic, piezoelectric, and dielectric constants of Lithium Tantalate and Lithium Niobate*, J.Appl.Phys., Vol.42, No.6, pp.2219-2230, May 1971

[67] T.R.Sliker, J.M.Jost, *Linear electrooptic effect and refractive indices of cubic ZnTe*, J.Opt.Soc.Am., vol.35, p.130-131, 1966

[68] M.Tokuda, N.Kuwabara,i*Recent progress in fibre optic antennas for EMC measurement*, IEICE Trans.Commmun., vol.E75B, no.3, p.107-113, March 1992

[69] H.Trinks, G.Matz, H.Schilling, *Electrooptical system for EMP measurement*, IEEE Trans.Electromag.Compat., vol.EMC22, no.1, p.75-77, 1980

[70] S.T.Vohra, F.Buchholtz, A.D.Kersey, *Fibre optic dc and low frequency electric field sensor*, Optics Lett., vol.16, no.18, p.1445-1447, Sept.1991

[71] S.T.Vohra, F.Buchholtz, *Fibreoptic ac electric field sensor based on the electostictive effect*, Optics lett., vol.17, no.5, p.372-374, March 1992

[72] M.J.Walker, *Matrix calculus and the Stokes parameters of polarized radiation*, Am.J.Phys., p.170-173, 1954

[73] G.B.Dubrovskii, *Optical properties of CdTe*, Sov.Physics-solid state, vol.3, no.5, p.943946, Nov.1961

[74] Shurcliff, W.A., *Polarized light*, Princeton: Van Nostrand, 1964

[75] W.J.Tabor, F.S.Chen, *Electromagnetic wave propagation through materials possessing both Faraday rotation and birefringence*, J.Appl.Phys., vol.40, no.7, 1969

[76] M.Prutton, *Surface physics*, Oxford University Press, 4th edition, 1975

[77] C.C.Davis, *Lasers and Electrooptics, Fundamentals and Engineering*, Cambridge University Press, p.118, 309, 1996

[78] M.Bordovsky, W.Balachandran, *Electro-optic Sensor for Extra-low-frequency Electric Field Measurement*, Doctoral Research Conference, Brunel University, June 1996

[79] M.Bordovsky, W. Balachandran, *Electro-optic Electric Field Sensor for the Measurement of DC and Extra-low-frequency Fields*, Electrostatics Society of America 25th Annual Meeting Proceedings, 1997

[80] M.Bordovsky, W. Balachandran, *Effect of Circular Birefringence on the electro-optic electric field sensor*, (accepted for presentation at Bianisotropic98, June 98, Braunschweig, Germany)

[81] M.Bordovsky, W.Balachandran, F.Cecelja, *Bismuth Germanate and Lithium Niobate in DC and Extra-Low-Frequency Electrooptic Sensor*, (accepted for presentation at CPEM98, July 98, Washington, USA)

[82] M.Bordovsky, W. Balachandran, *Temperature Compensation of Quarter-wave Plate in DC Electro-optic Sensor* (to be published)